

UNIVERSITY OF OKLAHOMA

GRADUATE COLLEGE

CYCLIC TORNADOGENESIS AND HORIZONTAL VORTEX TUBES IN HIGH-
RESOLUTION IDEALIZED SIMULATIONS OF SUPERCELLS

A DISSERTATION

SUBMITTED TO THE GRADUATE FACULTY

in partial fulfillment of the requirements for the

Degree of

DOCTOR OF PHILOSOPHY

By

MAURÍCIO ILHA DE OLIVEIRA

Norman, Oklahoma

2021

CYCLIC TORNADOGENESIS AND HORIZONTAL VORTEX TUBES IN HIGH-
RESOLUTION IDEALIZED SIMULATIONS OF SUPERCELLS

A DISSERTATION APPROVED FOR THE
SCHOOL OF METEOROLOGY

BY THE COMMITTEE CONSISTING OF

Dr. Ming Xue, Chair

Dr. Louis J. Wicker

Dr. Alan Shapiro

Dr. Nusrat Yussouf

Dr. Naoko Sakaeda

Dr. Yan Zhang

© Copyright by MAURÍCIO ILHA DE OLIVEIRA 2021
All Rights Reserved.

Acknowledgements

This research project was primarily supported by the *Coordenação de Aperfeiçoamento de Pessoal de Nível Superior* (CAPES) under Grant number 88881.129505/2016-01 of the “*Programa de Doutorado Pleno no Exterior*” (DPE – 3830) under the Brazilian Ministry of Education. The Texas Advanced Computing Center (TACC) and National Institute for Computational Sciences (NICS) [through the Extreme Science and Engineering Discovery Environment (XSEDE) program] provided the computing resources for performing the simulations in this study. Computational resources from the Center for Analysis and Prediction of Storms (CAPS) and the University of Oklahoma (OU) Supercomputing Center for Education and Research (OSCER) are also acknowledged.

My interest in severe convective storms began during early childhood, when I witnessed my very first severe storms in my hometown (Santa Maria, Rio Grande do Sul) in southern Brazil, a land rife with these types of storms. Not long after that, my interest in severe storms would grow enormously, as my father would rent tornado documentary VHS tapes featuring U.S. tornadoes from the 1980s and 1990s, causing me to become further fascinated by storms. As I learned more about storms and tornadoes, it soon became clear that my journey should take me to the University of Oklahoma, located in the world’s most famous tornado hotspot and home to one of the best meteorology programs worldwide. The road to OU has been circuitous and I am eternally thankful to so many people that in several ways helped me fulfill my dream at OU.

I am indebted to my PhD advisor, Dr. Ming Xue, for the enormous support, patience, and continuous encouragement over these last four years. His mentorship, vast expertise with the ARPS model (created by himself during his own PhD), and rich knowledge of tornado dynamics were crucial to my academic and personal growth at OU. Oftentimes, our tornado discussions

would exceed our regular meeting times, as we discussed the most varied hypotheses for tornadogenesis. Those were surely very fun and motivational moments! I am indebted to my co-advisor, Dr. Louis Wicker, who always supported me with his outstanding knowledge of tornadic storms and numerical modeling, many times challenging me to push beyond my limits. Even more important, I am thankful to Lou and the Wicker Family (Kristy, Ben, and Laura) for taking me as an honorary member of their family since my early months at OU. Their immense kindness, empathy, and unmatched willingness to help others was the major highlight of my time in Oklahoma.

I cannot express enough how thankful I am to the members of PhD committee: Dr. Alan Shapiro, Dr. Nusrat Yussouf, Dr. Yan Zhang, and Dr. Naoko Sakaeda for all the support over these years. Your promptness to help and supportive attitude were paramount for my development as a scientist. In special, a number of exchanges with Dr. Shapiro since the fluid dynamics classes further clarified to me the kind of research that I enjoyed the most. Dr. Nusrat Yussouf is particularly thanked for the WRF numerical data of the 27 April 2011 used to obtain the base-state sounding used in this dissertation. Dr. Keith Brewster's expertise and aid with data assimilation using radar data in the ARPS model is deeply appreciated. Numerous discussions with Dr. Howie Bluestein, Dr. Derek Stratman, Dr. Evgeni Fedorovich, and Dr. Scott Salesky helped improve my skills considerably. Drs. Nathan Snook and Timothy Supinie are thanked for their support with the ARPS model.

I am very thankful for the many friendships that I've made at OU. In particular, I thank Dr. Brett Roberts, who I can say served as an additional advisor to me, closely watching over my progress while constantly sharing his coding expertise and tornado knowledge with endless patience and willingness to help. Dr. Hristo Chipilski is appreciated for being such a caring, funny,

and very supportive friend; it was an honor to walk alongside you on this journey. I am grateful to Dr. Mike Coniglio for our storm chasing adventures in the Plains and for all the tips and lessons regarding storm science. I thank Dr. Amanda Kis for being such a thoughtful person who has always sought to support me ever since we met, either by sharing her expertise on tornadoes or by encouraging me during my seminars. Dr. Eric Loken, Dr. Jon Labriola, Dr. Marcus Johnson, Ryan Pajela and several other friends (too many to list) are also appreciated for their sharing their experience at OU with me. The School of Meteorology staff: Christie Upchurch, Shelby Hill, Debra Farmer, Debra Barnhill, Danika Hines-Barnett, and Colleen Wilhelm are appreciated; having you to help us all in times of need has always been heartwarming. Also, I appreciate all the support with IT from Chris Cook and Shawn Riley.

My mentors and friends from Brazil were essential during my journey. I am indebted, in special, to my undergrad and Master's Degree advisor, Dr. Ernani de Lima Nascimento, also a former OU and CAPS student. He was a huge inspiration to this fellow Brazilian meteorologist, as his mentorship and countless stories and lessons about storm research and chasing in Oklahoma have shaped the scientist that I have become. My friends and fellow storm aficionados Vanessa, Eliton, Murilo, Diogo, Carolina, and Vitor are thanked for our collaborations and making this journey much more fun. I will forever be thankful to my dearest friends Daiane and Evandro (*in memoriam*) for their selfless nature to help others and for always encouraging and believing in me. I extend this appreciation to my friends Fernando, Natália, Stefanía, Felipe, Cristielen, and Franciano. My former mentors Dr. Otávio Acevedo and Dr. Gervásio Degrazzia are appreciated for their restless efforts to help their students; I am very glad to have had you by my side.

I dedicate this dissertation to my loving family. I am indebted to my father Antônio and my mother Carmen for their selfless efforts to give me a proper education, strict upbringing, and

absolute support for my career decisions. Continuous support and friendship from my brother Lucas (also a meteorologist and storm chaser) have always been instrumental over all these years; in the same sense, my little sister Isadora is also thanked. The person who has been key to my success is my aunt Elsa; her selfless and tireless efforts to help me played a fundamental role in my education and upbringing for which I will forever be grateful. I also thank my aunts Elide and Letícia, uncle Hugo, and my cousin Cândida, who have always provided all the encouragement I needed along the way.

I am extremely grateful to have met my girlfriend, my beloved Luciane, during our academic journey at the *Universidade Federal de Santa Maria* (UFSM, in Portuguese). Her unconditional love and support coupled with her bright mind and unbreakable will have always been a much-needed source of strength that I have relied on. You've always been an inspiration to me! As the two of us finally become the scientists we wished to be a decade ago, I can already see our long-awaited life together.

My gratitude is extended to Mr. Mike Wilhelm, Mr. John Brown, Mr. Kory Hartman (at SevereStudios.com), Mr. Tom Deelo, Mr. Ryne Chandler, Mr. Nate Hughett, Mr. Jason Rosolowski, and Dr. Christopher Karstens for generously providing the tornado footage used in the analysis presented in this study. Scott Pearse from NCAR is thanked for his support with VAPOR.

Finally, I dedicate this PhD dissertation to my dear and eternal friend Lincon Turcato Carabagialle (*in memoriam*). I cannot express how glad and honored I am to have been able to walk alongside you during our adventures in meteorology. The important lessons that you taught me and the valuable moments we shared continue to illuminate my path on a daily basis. Thank you, my friend!

Table of Contents

Acknowledgements.....	iv
List of Tables	xi
Abstract.....	xxvii
Chapter 1: Introduction.....	1
1.1. Cyclic tornadogenesis	2
1.2. Horizontal vortex tubes near tornadoes	3
1.3. Objectives of this study.....	5
Chapter 2: Review of Supercells, Tornadoes, and Horizontal Vortices	7
2.1 Supercell thunderstorms.....	7
2.2 Types of tornadoes	15
2.3 Tornadogenesis mechanisms in supercells	22
2.4 Horizontal vortex tubes near tornadoes	31
Chapter 3: Evolution of Storm- and Tornado-Scale Structures Leading to Cyclic Tornado Formation.....	34
3.1 Methodology.....	34
3.1.1 Experiment setup	34
3.1.2 Base-state environment and establishment of an initial balanced sounding.....	36
3.2 Simulation results.....	41
3.2.1 Overview of storm evolution and its attendant tornadoes	41
3.2.2 Low-level storm- and substorm-scale evolution associated with cyclic tornado development.....	51
3.2.2.1 Tornado 1	52

3.2.2.2 Tornadoes 2, 3, and 4.....	67
3.2.3 Relationship between tornado cycling and the nearby low-level inflow vorticity field	75
3.2.4 Evolution of midlevel updrafts and relationship with the low-level tornadoes	79
3.3 Summary and discussion.....	82
Chapter 4: The Evolution and Structure of Horizontal Vortex Tubes near Observed and Simulated Tornadoes.....	87
4.1 Methodology	87
4.2 HVs in the 100-m experiment.....	91
4.2.1 Overview of the simulated supercell and tornado.....	91
4.2.2 Evolution and kinematics of HVs near a tornado	97
4.2.2.1 3D vorticity structure and visual observations.....	97
4.2.2.2 Near-ground flow kinematics and potential HV formation mechanisms	103
4.3 HVs in the 30-m experiment.....	107
4.3.1 Overview of the simulated supercell and tornado.....	107
4.3.2 Visual characteristics of trailing HVs in the observed Tuscaloosa tornado	111
4.3.3 Simulated trailing HV	119
4.3.3.1 3D structure and evolution.....	119
4.3.3.2 Near-surface wind field.....	126
4.3 Summary and discussion.....	127
4.3.1 Behavior of small-scale HVs based on the 100-m simulation	127
4.3.2 Behavior of trailing HVs based on the 30-m simulation	132
Chapter 5: Summary and Future Work.....	137

References.....143

List of Tables

Table 3.1. Statistics of cyclic tornadogenesis for the 50-m supercell simulation.....	51
Table 4.1. Relevant information on the Tuscaloosa tornado used in this study.	112

List of Figures

- Fig. 2.1. Conceptual plan view of a cyclonic tornadic supercell at low levels. The thick line represents the radar echo. The finely stippled areas represent the updraft (UD), while the RFD and FFD are coarsely stippled. From Lemon and Doswell (1979). The frontal symbols illustrate the storm's gust front associated with each downdraft region. Ground-relative streamlines indicate the flow in and around the supercell. The tornado location is denoted by an encircled T..... 10
- Fig. 2.2. Cyclic mesocyclogenesis at low levels. Top panel: Occluding cyclic mesocyclogenesis; bottom panel: non-occluding cyclic mesocyclogenesis. Vertical vorticity maxima (low-level mesocyclones) are shaded in red. Updrafts are shaded in light blue and downdrafts are shaded in dark blue. The yellow contour outlines the boundary of the storm's rainy area. The black frontal symbols indicate the RFD and FFD gust fronts. From Adlerman and Droegemeier (2005). 14
- Fig. 2.3. Mechanisms of vertical vortex genesis in different convective modes. (a) Supercells: Blue (green) vortex lines represent vorticity that is produced baroclinically (frictionally). The large vertically pointing arrow represents a low-level updraft that tilts and stretches low-level horizontal vorticity into a low-level mesocyclone/tornado (indicated by the + symbol as cyclonic vertical vorticity) for air parcels traveling along the red trajectories. Red curved arrows denote the sense of rotation of the vortices. The gray frontal symbols represent the storm's surface gust fronts. From Yokota et al. (2018). (b) QLCSs: generation of a cyclonic-anticyclonic vortex pair through downward tilting of horizontal vorticity in westerly wind shear (typically available in the environmental; solid line) by a downdraft (large downward-pointing arrow). Dashed curved arrows indicate the sense of rotation of

the shear-induced vortex lines. (c) Similar to (b), but for upward tilting of horizontal vorticity in easterly wind shear (typically produced baroclinically along the QLCS' gust front) by an updraft. Both (b) and (c) from Weisman and Davis (1998). (d) Non-supercell local storms: (I & II): strong convergence along a surface wind shift line (in this schematic, a dry outflow boundary) initiates cumulus convection (represented by the cloud symbols above the black arrows, which denotes updrafts along the boundary) and misocyclones (circular arrows) through the release of vortex sheet instability. (III) Convection deepens and stretches misocyclones. (IV) As convective towers grow into cumulonimbus, misocyclones may be contracted into tornado, even before the onset of surface precipitation. (V) Cold outflow from the storm's rainy area encircles a mature tornado. (VI) Increased rainfall and cold outflow completely encircle the tornado, which weakens and moves into the cold air mass and dissipates within downdrafts (black downward-pointing arrows). From Lee and Wilhelmson (1997b)..... 21

Fig. 2.4. Mechanisms by which surface friction generates horizontal vorticity in supercell. (a) Friction produces horizontal vorticity (orange vectors) through low-level shear in the environmental (base-state) flow characterized as an Ekman spiral in a hodograph (inset). Blue curved arrow denotes a trajectory entering a pre-tornadic vortex (blue cylinder); dashed curved arrow in red represents the sense of rotation along the trajectory (which coincides with a vortex line in this case, since the vorticity is in the streamwise direction). (b) Production of near-ground horizontal crosswise vorticity in flow accelerating into a developing tornado (insets). The crosswise vorticity is exchanged into streamwise vorticity via a "riverbed effect" (green shaded area) as the flow curves cyclonically around the pre-tornadic vortex. (c) Frictional enhancement of low-level convergence and updrafts (shaded

in orange) along a supercell’s surface boundary (divergent flow behind the boundary is shaded in green) causing the contraction of a pre-tornadic vortex into a tornado (indicated by black arrows in opposing directions). From Roberts et al. (2016)..... 28

Fig. 3.1. (a) Skew T -log p diagram for the idealized tornadic supercell experiment. The red (green) solid line represents environmental temperature (dewpoint) in °C. The black dashed line denotes the temperature for an ascending surface-based parcel. Areas of positive (negative) buoyancy are highlighted by semi-transparent red (blue) shading. The black and blue dots represent the lifting condensation level and level of free convection, respectively. (b) Hodograph for storm-relative winds between the surface and 10 km AGL. Black dots are heights (in km AGL). The green vector indicates the ground-motion vector ($u = 11 \text{ m s}^{-1}$; $v = 17 \text{ m s}^{-1}$) originally subtracted from the wind profile to induce the storm to remain quasi-stationary in the simulation. Some relevant convective parameters are shown in the bottom right sector of the figure. 37

Fig. 3.2. Time-height plot of domain wide 0-5000 m (a) maximum updraft, (b) minimum perturbation pressure, and (c) maximum vertical vorticity, valid from 0 to 16200 s. 43

Fig. 3.3. Evolution of the simulated supercell for tornado 1 at the lowest grid level (1 m AGL) at (a) 7200 s, (b) 7500 s, (c) 7800 s, (d) 8100 s, (e) 8400 s, (f) 8700 s, (g) 9000 s, (h) 9300 s, and (i) 9600 s. Reflectivity is shaded in dBZ. The -1-K perturbation potential temperature contour is shown in magenta. Vertical vorticity is shaded in the foreground for $\zeta > 0.05 \text{ s}^{-1}$. Vectors represent storm-relative winds. 45

Fig. 3.4. Time series of maximum ground-relative wind (m s^{-1} ; black), minimum perturbation pressure (hPa; purple), and maximum vertical vorticity (s^{-1} ; golden) at 10 m AGL, valid

from 7600 to 10800 s. The semi-transparent horizontal bars in the background denote EF-scale wind speed ranges. (a) Tornado 1, (b) tornado 2, (c) tornado 3, and (d) tornado 4. 46

Fig. 3.5. Same as Fig. 3.3, but for tornado 2 (a) 9980 s, (d) 10280 s, (g) 10630 s, and (h) 11370 s; tornado 3 (b) 11980 s, (e) 12280 s, (h) 13160 s, (k) 13490 s; and tornado 4 (c) 13880 s, (c) 14180 s, (c) 14520 s, (c) 15030 s..... 48

Fig. 3.6. (a) Vertical velocity (shaded; $m s^{-1}$) at 500 m AGL, (b) density potential temperature perturbation (shaded; K) at 1 m AGL and perturbation pressure (regions shaded in orange for values < -3 hPa to highlight the tornado position, when it is present), (c) storm-relative wind speed at 500 m AGL (shaded; $m s^{-1}$) and perturbation pressure (hPa; dashed blue contours every 1 hPa, starting at -3 hPa), (d) volume rendered display of perturbation pressure (hPa) for values lower than 2.5 hPa. In (b), the solid blue denotes the RFGF and the dashed blue lines denote internal boundaries. The yellow star denotes the location of the camera in (d) relative to the tornado. In (a) and (c), the winds are storm relative, while in (b) the winds are ground relative. In all fields, the purple contour denotes the 10-dBZ reflectivity contour. All fields valid at 7500 s. 54

Fig. 3.7. (a) Vertical velocity (shaded; $m s^{-1}$) at 500 m AGL, (b) density potential temperature perturbation (shaded; K) at 1 m AGL and perturbation pressure (regions shaded in orange for values < -3 hPa to highlight the tornado position, when it is present), (c) storm-relative wind speed at 500 m AGL (shaded; $m s^{-1}$) and perturbation pressure (hPa; dashed blue contours every 1 hPa, starting at -3 hPa), (d) volume rendered display of perturbation pressure (hPa) for values lower than 2.5 hPa. In (b), the solid blue denotes the RFGF and the dashed blue lines denote internal boundaries. The yellow star denotes the location of the camera in (d) relative to the tornado. In (a) and (c), the winds are storm relative, while

in (b) the winds are ground relative. In all fields, the purple contour denotes the 10-dBZ reflectivity contour. All fields valid at 7800 s. 56

Fig. 3.8. 3D vorticity magnitude field ($> 0.15 \text{ s}^{-1}$), valid at (a) 7740 s, (c) 7770 s, (c) 7800 s, and (d) 7830 s. The green dashed lines denote the axis of the pretornadic vortex, while orange dashed lines denote axis of other vortices that interact with the pretornadic vortex. The solid blue line indicates the subjectively identified RFGF and the dashed blue line denotes the subjectively identified FFCB. 58

Fig. 3.9. (a) Vertical velocity (shaded; m s^{-1}) at 500 m AGL, (b) density potential temperature perturbation (shaded; K) at 1 m AGL and perturbation pressure (regions shaded in orange for values $< -3 \text{ hPa}$ to highlight the tornado position, when it is present), (c) storm-relative wind speed at 500 m AGL (shaded; m s^{-1}) and perturbation pressure (hPa; dashed blue contours every 1 hPa, starting at -3 hPa), (d) volume rendered display of perturbation pressure (hPa) for values lower than 2.5 hPa. In (b), the solid blue denotes the RFGF and the dashed blue lines denote internal boundaries. The yellow star denotes the location of the camera in (d) relative to the tornado. In (a) and (c), the winds are storm relative, while in (b) the winds are ground relative. In all fields, the purple contour denotes the 10-dBZ reflectivity contour. All fields valid at 8100 s. 60

Fig. 3.10. (a) Vertical velocity (shaded; m s^{-1}) at 500 m AGL, (b) density potential temperature perturbation (shaded; K) at 1 m AGL and perturbation pressure (regions shaded in orange for values $< -3 \text{ hPa}$ to highlight the tornado position, when it is present), (c) storm-relative wind speed at 500 m AGL (shaded; m s^{-1}) and perturbation pressure (hPa; dashed blue contours every 1 hPa, starting at -3 hPa), (d) volume rendered display of perturbation pressure (hPa) for values lower than 2.5 hPa. In (b), the solid blue denotes the RFGF and

the dashed blue lines denote internal boundaries. The yellow star denotes the location of the camera in (d) relative to the tornado. In (a) and (c), the winds are storm relative, while in (b) the winds are ground relative. In all fields, the purple contour denotes the 10-dBZ reflectivity contour. All fields valid at 8400 s. 61

Fig. 3.11. (a) Vertical velocity (shaded; m s^{-1}) at 500 m AGL, (b) density potential temperature perturbation (shaded; K) at 1 m AGL and perturbation pressure (regions shaded in orange for values < -3 hPa to highlight the tornado position, when it is present), (c) storm-relative wind speed at 500 m AGL (shaded; m s^{-1}) and perturbation pressure (hPa; dashed blue contours every 1 hPa, starting at -3 hPa), (d) volume rendered display of perturbation pressure (hPa) for values lower than 2.5 hPa. In (b), the solid blue denotes the RFGF and the dashed blue lines denote internal boundaries. The yellow star denotes the location of the camera in (d) relative to the tornado. In (a) and (c), the winds are storm relative, while in (b) the winds are ground relative. In all fields, the purple contour denotes the 10-dBZ reflectivity contour. All fields valid at 8700 s. 63

Fig. 3.12. (a) Vertical velocity (shaded; m s^{-1}) at 500 m AGL, (b) density potential temperature perturbation (shaded; K) at 1 m AGL and perturbation pressure (regions shaded in orange for values < -3 hPa to highlight the tornado position, when it is present), (c) storm-relative wind speed at 500 m AGL (shaded; m s^{-1}) and perturbation pressure (hPa; dashed blue contours every 1 hPa, starting at -3 hPa), (d) volume rendered display of perturbation pressure (hPa) for values lower than 2.5 hPa. In (b), the solid blue denotes the RFGF and the dashed blue lines denote internal boundaries. The yellow star denotes the location of the camera in (d) relative to the tornado. In (a) and (c), the winds are storm relative, while

in (b) the winds are ground relative. In all fields, the purple contour denotes the 10-dBZ reflectivity contour. All fields valid at 9000 s. 65

Fig. 3.13. (a) Vertical velocity (shaded; $m s^{-1}$) at 500 m AGL, (b) density potential temperature perturbation (shaded; K) at 1 m AGL and perturbation pressure (regions shaded in orange for values < -3 hPa to highlight the tornado position, when it is present), (c) storm-relative wind speed at 500 m AGL (shaded; $m s^{-1}$) and perturbation pressure (hPa; dashed blue contours every 1 hPa, starting at -3 hPa), (d) volume rendered display of perturbation pressure (hPa) for values lower than 2.5 hPa. In (b), the solid blue denotes the RFGF and the dashed blue lines denote internal boundaries. The yellow star denotes the location of the camera in (d) relative to the tornado. In (a) and (c), the winds are storm relative, while in (b) the winds are ground relative. In all fields, the purple contour denotes the 10-dBZ reflectivity contour. All fields valid at 9300 s. 66

Fig. 3.14. Vertical velocity (shaded; $m s^{-1}$), but for tornado 2 (a) 9980 s, (d) 10280 s, (g) 10630 s, and (h) 11370 s; tornado 3 (b) 11980 s, (e) 12280 s, (h) 13160 s, (k) 13490 s; and tornado 4 (c) 13880 s, (c) 14180 s, (c) 14520 s, (c) 15030 s..... 69

Fig. 3.15. Density potential temperature perturbation (shaded; K), but for tornado 2 (a) 9980 s, (d) 10280 s, (g) 10630 s, and (h) 11370 s; tornado 3 (b) 11980 s, (e) 12280 s, (h) 13160 s, (k) 13490 s; and tornado 4 (c) 13880 s, (c) 14180 s, (c) 14520 s, (c) 15030 s..... 70

Fig. 3.16. Storm-relative wind speed (shaded; $m s^{-1}$), but for tornado 2 (a) 9980 s, (d) 10280 s, (g) 10630 s, and (h) 11370 s; tornado 3 (b) 11980 s, (e) 12280 s, (h) 13160 s, (k) 13490 s; and tornado 4 (c) 13880 s, (c) 14180 s, (c) 14520 s, (c) 15030 s. 73

Fig. 3.17. Perturbation pressure (hPa; shaded for values less than -2.5 hPa), but for tornado 2 (a) 9980 s, (d) 10280 s, (g) 10630 s, and (h) 11370 s; tornado 3 (b) 11980 s, (e) 12280 s, (h) 13160 s, (k) 13490 s; and tornado 4 (c) 13880 s, (c) 14180 s, (c) 14520 s, (c) 15030 s... 75

Fig. 3.18. Total (3D) streamwise vorticity (shaded; s^{-1}) and perturbation pressure (dashed black contour for values less than -3 hPa), but for tornado 2 (a) 9980 s, (d) 10280 s, (g) 10630 s, and (h) 11370 s; tornado 3 (b) 11980 s, (e) 12280 s, (h) 13160 s, (k) 13490 s; and tornado 4 (c) 13880 s, (c) 14180 s, (c) 14520 s, (c) 15030 s..... 78

Fig. 3.19. Vertical velocity (shaded; $m\ s^{-1}$) and vertical vorticity (blue and red contours denote values less than $-0.02\ s^{-1}$ and greater than $0.02\ s^{-1}$, respectively, to indicate the approximate location of mesocyclones and mesoanticyclones), but for tornado 2 (a) 9980 s, (d) 10280 s, (g) 10630 s, and (h) 11370 s; tornado 3 (b) 11980 s, (e) 12280 s, (h) 13160 s, (k) 13490 s; and tornado 4 (c) 13880 s, (c) 14180 s, (c) 14520 s, (c) 15030 s..... 81

Fig. 4.1. (a) Skew T -log p diagram for the idealized tornadic supercell experiment. The red (green) solid line represents environmental temperature (dewpoint) in $^{\circ}C$. The black dashed line denotes the temperature for an ascending surface-based parcel. Areas of positive (negative) buoyancy are highlighted by semi-transparent red (blue) shading. The black and blue dots represent the lifting condensation level and level of free convection, respectively. (b) Hodograph for storm-relative winds between the surface and 10 km AGL. Black dots are heights (in km AGL). The green vector indicates the ground-motion vector ($u = 11\ m\ s^{-1}$; $v = 17\ m\ s^{-1}$) originally subtracted from the wind profile to induce the storm to remain quasi-stationary in the simulation. Some relevant convective parameters are shown in the bottom right sector of the figure. 89

Fig. 4.2. Select stages of the simulated supercell life cycle. (a) 3600.000 s, (b) 7200.000 s, (c) 10800 s, (d) 11888 s, (e) 12032 s, (f) 12930 s, (g) 13950 s, (h) 14274 s, and (i) 14608 s. Vertical vorticity (light shading; s^{-1}), horizontal wind (vectors; $m s^{-1}$), and the $0.3 g kg^{-1}$ rainwater mixing ratio contour. Vertical vorticity rivers [VVR, in (d)] are denoted by green arrows in (d)-(i). Pockets of strong vertical vorticity associated with the tornadoes in the center of the domain are shaded in the foreground, starting at $0.1 s^{-1}$. All fields at 158 m AGL. 92

Fig. 4.3. (a)-(f) 3D visualization of vertical vorticity with values greater (less) than $0.075 s^{-1}$ ($-0.075 s^{-1}$) indicating regions of cyclonic (anticyclonic) rotation in yellow (blue). Buoyancy (B ; in $m s^{-1}$) is displayed at 1 m AGL, with positively or neutrally (negatively) buoyant air in green (blue). The life cycle of the first tornado is shown at (a) 11888 s (tornadogenesis), (b) 12032 s (peak stage), and (c) 12930 s (demise). (d)-(f) Same as in (a)-(c), but for the second tornado at (d) 13950 s, (e) 14274 s, and (f) 14608 s. (g)-(i) The cloud field (sum of cloud water and cloud ice mixing ratios; in $g kg^{-1}$) corresponding to the second tornado in (d)-(f). All nonzero values are displayed. 94

Fig. 4.4. Vertical velocity field (light shading; $m s^{-1}$) throughout the life cycle of the simulated tornadoes at (a) 11888 s, (b) 12032 s, (c) 12930 s, (d) 13950 s, (e) 14274 s, and (f) 14608 s (compare with Figure 2d-i and Figure 3a-i). Horizontal wind (vectors; $m s^{-1}$) and the $0.3 g kg^{-1}$ rainwater mixing ratio contour are also plotted. Pockets of strong vertical vorticity associated with the tornadoes in the center of the domain are shaded in the foreground, starting at $0.1 s^{-1}$. All fields at 158 m AGL..... 95

Fig. 4.5. 3D visualization of vorticity magnitude, highlighting values greater than $0.15 s^{-1}$, at select time frames: (a) 14102 s, (b) 14170 s, (c) 14190 s, (d) 14230 s, (e) 14250 s, and (f) 14270

s. The viewpoint is that of an observer located at the southeast corner of the domain, looking toward the northwest corner. The green dashed line denotes the tornado vortex axis. Red arrows indicate vortices that form around the tornado and surrounding RFD outflow at the surface. Orange and black arrows indicate distinct vortices used for comparison with real vortices in Figure 4.6..... 98

Fig. 4.6. Visual observations of the 27 April 2011 Tuscaloosa tornado displaying several HVs. Video frames extracted from videos of (a) Mike Wilhelm (available online at: <https://www.youtube.com/watch?v=T0FHTG9VETY>) and (b) John Brown (available online at: <https://www.youtube.com/watch?v=9KjWtBrEYHY>), courtesy of Mike Wilhelm and Kory Hartman at SevereStudios.com, respectively. Red, orange and black arrows indicate key vortices discussed in the text. Other vortices are also evident in the figure. Tornado motion is due northeast (from left to right in the figure). Times in UTC are estimated. 100

Fig. 4.7. Tilting of HVs in the forward flank of tornadoes. (a) Visual observations of the 27 April 2011 Tuscaloosa tornado at 2206 UTC (extracted from Mike Wilhelm’s video, available online at: <https://www.youtube.com/watch?v=T0FHTG9VETY>; courtesy of M. Wilhelm). (b) Vertical cross section of x -vorticity component (ξ ; shaded in s^{-1}) along $x = 54.05$ km. Solid purple contours denote the $1 \times 10^{-3} \text{ g kg}^{-1}$ cloud water mixing ratio isopleth and dashed green contours denote downward motion regions where $w \leq -10 \text{ m s}^{-1}$. (c) DVR of perturbation pressure, highlighting values less than -9 hPa . (d) 3D visualization of vorticity magnitude, highlighting values greater than 0.15 s^{-1} . The dark orange arrows indicate the position of the HV and the vertical black line indicates the scale height of the tornado in

the DVRs. In all panels, the view is from the east-southeast. Tornado motion is due northeast (from left to right in the figure). All simulation fields are valid at 14100 s.... 103

Fig. 4.8. Horizontal vorticity (magnitude is light shaded and vectors are red; in s^{-1}) centered at the tornado at (a) 1 m AGL and (b) 158 m AGL valid at 14230 s (during the intensification phase of the tornado). Horizontal wind vectors are in black (in $m s^{-1}$) and vertical vorticity ζ is shaded in the foreground, starting at $0.1 s^{-1}$. The purple line indicates the $0.3 g kg^{-1}$ rainwater mixing ratio isopleth. 106

Fig. 4.9. Time-height cross section of 0-5000 m (a) maximum updraft, (b) minimum perturbation pressure, and (c) maximum vertical vorticity in the subdomain, valid from 0 to 10800 s. 108

Fig. 4.10. Evolution of the simulated supercell at the lowest grid level (1 m AGL) at (a) 7200 s, (b) 7800 s, (c) 7960 s, (d) 8670 s, (e) 9720 s, and (f) 10050 s. Reflectivity is shaded in dBZ. The -1-K perturbation potential temperature contour is shown in magenta. Vertical vorticity is shaded in the foreground for $\zeta > 0.05 s^{-1}$. Vectors represent storm-relative winds. The insets at the top corner of (b)-(d) highlight the evolution of the tornado's structure in the volume rendered perturbation pressure field, where $p' < -10$ hPa and the yellow stars denote the camera's location relative to the tornado. The small green, red, and blue arrows in the inset plots point to the north, east, and up, respectively. 110

Fig. 4.11. Time series of maximum ground-relative wind ($m s^{-1}$; black), minimum perturbation pressure (hPa; purple), and maximum vertical vorticity (s^{-1} ; golden) at 10 m AGL in the subdomain, valid from 7600 to 10800 s. The semi-transparent horizontal bars in the background denote EF-scale wind speed ranges. The vertical white lines are plotted at 9500

and 9850 s, respectively, to demark the formation and decay of the simulated trailing HV in Fig. 9. 111

Fig. 4.12. Early segment of the Tuscaloosa tornado damage path highlighting tree-fall damage (represented by small blue and red arrows). The figure is adapted from Fig. 13 of Karstens et al. (2013) to include the location of the video shown in Fig. 4.13 of this study. The camera icons are the location where the videos were taken. Image provided through the courtesy of Dr. Christopher Karstens. 113

Fig. 4.13. (a)-(h) Image sequence showing the Tuscaloosa tornado as it passed north of the observer, exhibiting a large trailing HV. The magenta dashed line in (a) and (b) outlines the trailing HV due to the poor contrast with the tornado. The orange arrows denote the spiraling vortices discussed in the text. Blue arrows show regular HVs advected by the tornado's outer flow. Times (MM:SS) are relative to the beginning of the video. Images provided through the courtesy of Tom Deelo. 115

Fig. 4.14. (a)-(h) Image sequence showing the Tuscaloosa tornado as it passed north of the observers, exhibiting a large trailing HV. The magenta dashed line in (a) and (b) outlines the trailing HV due to the poor contrast with the tornado. The orange arrows denote the spiraling vortices discussed in the text. The insets are zoomed-in views of the same spiraling vortices. Blue arrows show regular HVs advected by the tornado's outer flow. The green arrow in (h) indicates a band of accelerating flow toward the tornado around the position where the trailing HV was located in (a)-(g). Times (MM:SS) are relative to the beginning of the video. Images provided through the courtesy of Ryne Chandler and Nate Hughett. 116

Fig. 4.15. (a)-(d) Image sequence showing the Tuscaloosa tornado as it passed just north of the observer, exhibiting a large trailing HV. Yellow arrows show damage to buildings at the interface of the tornado and the trailing HV. The orange arrows denote the spiraling vortices discussed in the text. The frame shown in (b) was rotated counterclockwise by 7° to account for the unsteadiness of the footage. Times (MM:SS) are relative to the beginning of the video. Images provided through the courtesy of Jason Rosolowski..... 117

Fig. 4.16. Volume-rendered plots of three-dimensional vorticity magnitude where it exceeds 0.2 s^{-1} at (a) 9500 s, (b) 9550 s, (c) 9600 s, (d) 9650 s, (e) 9700 s, (f) 9750 s, (g) 9800 s, and (h) 9850 s. The orange dashed rectangle highlights the early stage of the trailing HV. The red dashed line subjectively denotes the tornado axis. Orange arrows indicate downward-bending tails of the trailing HV and the model equivalent of the observed small spiraling vortices shown in Figs. 4.13-4.15. The anticyclonic character of the spiraling vortices is highlighted in the insets in (f) and (h), where $\zeta < -0.1 \text{ s}^{-1}$ is shown in blue. The camera points to the southwest..... 121

Fig. 4.17. Top view of volume-rendered three-dimensional vorticity magnitude where it exceeds 0.2 s^{-1} at (a) 9500 s, (b) 9550 s, (c) 9600 s, and (d) 9650 s. The vorticity field is rendered only between the surface and 1 km AGL to avoid contamination by other intervening structures. The red dashed line subjectively denotes the tornado axis, with the red circle representing the base of the tornado. The camera is located at 5 km AGL. 123

Fig. 4.18. (a) Potential temperature perturbation (θ' ; shaded; K) and horizontal vorticity (ω_{hs} ; orange vectors; s^{-1}), (b) horizontal streamwise vorticity (shaded; s^{-2}) and (c) stretching of horizontal streamwise vorticity (shaded; s^{-2}). The red [green] contours in (a) and (b) [(c)] represent vertical vorticity in the tornado; the outermost contour denotes $\zeta = 0.75 \text{ s}^{-1}$, and

it increases at 0.25 s^{-1} intervals. Black vectors in all plots are storm-relative winds. The yellow dashed line indicates the wind-shift line associated with a RFD internal boundary.

Both fields are valid at 9650 s at 50 m AGL. 125

Fig. 4.19. Horizontal cross sections of (a) storm-relative horizontal wind speed (V_h ; shaded; m s^{-1}) and (b) vertical velocity (w ; shaded; m s^{-1}) valid at 9610 s at 10 m AGL. Vectors are storm-relative winds. The blue dashed line indicates the wind-shift line associated with an RFD internal boundary. The magenta AB line located along $y = 49.455 \text{ km}$ refers to the vertical cross sections shown in (b) and (c). (c) Vertical cross sections of storm-relative horizontal wind speed and (d) vertical velocity along the AB red line in (a) and (b). The red contours represent vertical vorticity in the tornado; the outermost contour denotes $\zeta = 0.75 \text{ s}^{-1}$, and it increases at 0.25 s^{-1} intervals. The magenta arrow in (c) and (d) denotes the rotor-type circulation. 127

Fig. 4.20. Conceptual model of evolution of HVs in the simulation from initial time t_0 through $t_0 + 2\Delta t$, at Δt time increments. Left column: 3D vorticity magnitude isosurfaces shaded in blue. The vertically-oriented vortex represents an intensifying or mature tornado while slantwise, detached vortex tubes represent more horizontally-oriented vortices in the periphery of the tornado. Regions of enhanced frictional generation of horizontal vorticity in strong, near-ground horizontal wind embedded in the RFD outflow are shaded in purple. Magenta arrows in the middle panel show the tilted circulation on the forward side of the tornado. Representative vortex lines associated with the HVs are displayed in light orange, with circular arrows indicating their sense of rotation. Strong surface RFD flow is indicated by the curved black arrows. Right column: The cloud field associated with a tornado producing HVs consistent with the vorticity field displayed in the right column and visual

observations. The RFD-related clear slot is annotated. The storm is moving to the northeast, as indicated by the red arrow the upper panel..... 131

Fig. 4.21. Conceptual model for the evolution of the trailing HV and spiraling vortices as related to surrounding storm-scale features. Top panel: top view of the three-dimensional vorticity magnitude field. Middle panel: three-dimensional vorticity magnitude field viewed from the northeast. Bottom panel: cloud field consistent with the visual observations viewed from the northeast. In all panels, time advances from the left to the right. All relevant symbols are defined in the bottom section of the figure. At t_0 , predominantly crosswise horizontal vorticity which is produced in the RFD outflow evolves into coherent HVs that align and accumulate in the vicinity of an internal boundary east-southeast of the tornado. As large and small HVs interact in that zone, their self-induced wind fields initiate an entangling process. By $t_0 + \Delta t$, the HVs have fully intertwined and grown into a complex vortex entanglement, visually observed as a large helical HV. As the entangling continues, some smaller HVs as well as the tails of the larger HVs may bend downward, producing small spiraling anticyclonic vortices in the outer edge of the HV. By $t_0 + 2\Delta t$, the entangling begins to disorganize, as seen by the increasingly distortion larger vortices composing the trailing HVs. Spiraling vortices continue to occur during this stage. 134

Abstract

Despite enormous progress in our understanding of tornadic supercells obtained over the last several decades, many aspects regarding the evolution of these storms and their attendant tornadoes require further investigation. High-resolution numerical simulations of tornadic supercells represent an important tool to shed light on a number of physical processes associated with supercell tornadogenesis. In recent years, numerical simulations have been used successfully to better understand the role of surface friction, strong low-level updrafts, internal momentum surges, and other types of storm-scale processes and/or structures in tornadogenesis. In this dissertation, idealized, high-resolution (horizontal grid spacing ranging from 30 to 100 m) numerical simulations of a tornadic supercell are performed using the Advanced Regional Prediction System (ARPS) in order to better understand some important aspects of the complex evolution of tornadic supercells at fine scales. These analyses focus on two aspects of tornado evolution. First, the cyclic nature of tornadogenesis is investigated, with emphasis on understanding how a supercell evolving in a horizontally homogenous, steady-state environment can produce significantly different tornadoes in each tornado cycle. Second, the evolution of horizontal vortex tubes sometimes observed near real tornadoes is also addressed. Given that surface friction can have a significant impact on the evolution of simulated tornadoes and surrounding storm structures, its effects are included in the simulations.

A 50-m grid spacing experiment is employed to address the questions regarding cyclic tornadogenesis. To avoid constant modification of the base-state wind profile by surface friction, a three-force balance between the horizontal pressure gradient, Coriolis, and frictional forces is enforced using the Geotriptic Wind Balance (GWB) technique, such that the wind profile remains quasi-steady over the course of the experiment away from storm-induced perturbations. The

simulated supercell produces four tornadoes in relatively regular periods during its life span, three of which attain Enhanced Fujita 5 (EF5) intensity, while one briefly attains EF3 winds. All tornadoes develop under intensifying low-level updrafts and lowering pressure aloft, but their ensuing evolution differs considerably. The first tornado, also the strongest one, moves along the interface between a rear-flank downdraft (RFD) and a forward-flank convergence boundary (FFCB), while highly tilted to the tornado. When the tornado's parent updraft sheds from the main updraft to the east, it moves under the midlevel updraft, strengthening to peak intensity until it is overtaken by cold outflow. After its dissipation, large amounts of precipitation in the rear-flank of the storm cause the subsequent tornadoes to have shorter life spans, as they tend to become "wrapped in rain" and detach from their parent low-level updraft too quickly. All tornadoes are preceded by a low-pressure lobe (LPL) associated with accelerating inflow into the tornado's parent updraft. A band of enhanced near-surface streamwise vorticity in conjunction with the LPL and enhanced inflow also develops and appears to feed into the low-level updraft, potentially intensifying upward motions dynamically. Unlike previous conceptual models of cyclic mesocyclogenesis, where midlevel updrafts move rearward relative to the storm and decay completely, occluded midlevel updrafts merge with newly developed updrafts and produce convoluted downdraft distribution at middle levels and near the rear-flank of the storm. This setup is at least partially responsible for inducing the transition of the supercell from a "classic" morphology into an HP mode, a condition that accounts for most of the individual differences among tornadoes in this simulation.

The interactions between HV and tornadoes are analyzed in a 100-m and a 30-m grid spacing simulations. For the 100-m grid spacing experiment (which is an early version of the 50- and 30-m simulations), visualizations of the three-dimensional (3D) flow field based on direct

volume rendering aided by visual observations of HVs in a real tornado reveal the existence of a complex distribution of 3D vortex tubes surrounding the tornadic flow throughout the simulation. A distinct class of HVs originates in two key regions at the surface: around the base of the tornado and in the RFD outflow and are believed to have been generated via surface friction in regions of strong horizontal near-surface wind. HVs around the tornado are produced in the tornado's outer circulation and rise abruptly in its periphery, assuming a variety of complex shapes, while HVs to the south-southeast of the tornado, within the RFD outflow, ascend gradually in the updraft.

A combination of visual observations of a violent tornado and 3D visualizations of the vorticity field near the tornado in the 30-m simulation (which based on the same observed tornado case) are used to document a distinct type of HV, which persistently trails the right flank of the tornado very close to the ground, hereafter referred to as "trailing HV". The analysis shows that trailing HVs are larger, stronger, and last longer than their small-scale counterparts. Still, their vorticity matches that of other smaller HVs previously documented in the literature, which is consistent with generation via frictional torques and baroclinity along warm RFD internal boundaries. Interestingly, in some instances, trailing HVs display smaller spiral vortices circulating their periphery, which may evolve into complex structures. Visualizations of the 3D vorticity field show that the trailing HV arises as an entanglement along an RFD internal boundary of large and small HVs originated in the RFD outflow during a period of tornado intensification. The RFD internal boundary also serves as focus for stretching of vorticity that is exchanged from originally crosswise into streamwise vorticity at the location of trailing HV, causing strengthening of the trailing HV. The spiral vortices result from the same entangling processes that gives rise to the trailing HV. Moreover, the analysis suggests that trailing HV may act as a rotor that reinforces the surface wind speed in the right flank of the tornado.

Chapter 1: Introduction

Over the past six decades, our understanding of tornadic supercells has seen enormous progress which, as a consequence, has led to more accurate tornado forecasts. Such progress can be traced back from the first detailed, observation-based description of supercell thunderstorms (Browning 1964) to today's impressive and increasingly more common high-resolution numerical simulations of deep moist convection capable of resolving tornadoes and their parent storms all together (Xue et al. 2014; Orf et al. 2017; Yokota et al. 2018; Orf 2019; Snook et al. 2019; Tao and Tamura 2020). In spite of the outstanding advancements made thus far, a number of aspects regarding supercell tornadogenesis remains elusive. For instance, it is still not possible to discern why two or more supercells forming in virtually identical tornado-prone environments (at least in terms of current observational capabilities) with very similar characteristics on a radar display, result in widely different outcomes in terms of tornado production. In this context, one such supercell may produce only brief, weak tornadoes or no tornadoes at all, while another nearly identical supercell may produce strong, long-lived tornadoes (Markowski 2020). These discrepancies suggest an extreme sensitivity of the tornadic potential of a supercell to small differences in initial and boundary conditions, such that tornadogenesis does have a stochastic component that is highly dependent on the evolution of internal structures of the storm, likely including very small-scale features (Coffer and Parker 2017; Coffer et al. 2017; Coffer and Parker 2018; Yokota et al. 2018; Snook et al. 2019; Flournoy et al. 2020). Although this is certainly a major issue for numerically predicting tornadoes (Markowski 2020), it also underscores the need for a better understanding of how the evolution of fine-scale structures of supercells (e.g., internal boundaries, individual updrafts and downdrafts, small-scale vortices) affects the overall evolution of the parent storm, and how these structures interact with developing tornadoes and their nearby

environment (Orf et al. 2017; Orf 2019). Fortunately, the ever-increasing capabilities of computers and observing platforms (such as mobile Doppler radars and lidars) continue to yield datasets of tornadic supercells at increasingly higher temporal and spatial resolutions (i.e., on the order of 2 s and less than 100 m, respectively), resulting in increasingly detailed fine-scale analyses of the airflow within these storms (Pazmany et al. 2013; Wurman and Kosiba 2013; Houser et al. 2015; Orf et al. 2017; Yokota et al. 2018; Bluestein et al. 2019; Orf 2019; Snook et al. 2019; Tao and Tamura 2020; Schueth et al. 2021).

In this dissertation, a set of high-resolution numerical simulations of a tornadic supercell (with horizontal grid spacing ranging from 30 to 100 m) are conducted to address two distinct but important aspects of supercell tornadoes that are intrinsically related to the fine-scale evolution of internal structures of the storm: cyclic tornadogenesis and horizontal vortex tubes near tornadoes. The motivation for studying these specific two aspects of supercell tornadoes is discussed below.

1.1. Cyclic tornadogenesis

Past idealized numerical simulations addressing specifically cyclic formation of rotation in supercells have been restricted to using horizontal grid spacing on the order of 500 m, which can resolve low-level mesocyclones, at most (Adlerman et al. 1999; Adlerman and Droegemeier 2002; Adlerman and Droegemeier 2005). These studies have shed light on the main aspects involved in the sequential formation of mesocyclones in a supercell and its dependence on smaller-scale storm features (gust fronts, occlusion downdrafts, two-celled updrafts, etc.) and, in general, show a regular trend for mesocyclones to evolve in a remarkably similar fashion over each cycle (Adlerman et al. 1999). In nature, however, tornadoes from different cycles of a supercell can be quite different in terms of intensity, duration, and structure (Bluestein 2009; Tanamachi et al. 2013;

Knupp et al. 2014; Houser et al. 2015; Wienhoff et al. 2020) and, occasionally, tornadoes from distinct cycles may interact with each other (French et al. 2015). In many circumstances, differences between tornado cycles may be caused by heterogeneities in the environment, such as, for example those associated with cell mergers (Wurman et al. 2007; Tanamachi et al. 2015). For observed supercells, intrinsic heterogeneities and natural evolution of the environments make it virtually impossible determine whether differences in tornado cycles arise due to storm-environment interactions or due to in-storm processes alone. In fact, large differences in terms of tornado characteristics between cycles in a supercell arise even without the complicating effects of a heterogeneous base-state environment, since tornado attributes or even the likelihood of tornadogenesis are volatile and extremely sensitive to initial and boundary conditions (Coffer et al. 2017; Markowski 2020). Understanding why these differences occur for a particular supercell and how they compare with existing observations and conceptual models of cyclic tornadogenesis can provide an improved understanding of these phenomena and perhaps better anticipate situations that may deviate from or add new information to long-established conceptual models.

1.2. Horizontal vortex tubes near tornadoes

High-resolution simulations of supercells display extremely turbulent cold pools, especially when the grid spacing employed is fine enough [$O(10-50\text{ m})$] to resolve very small structures. Three-dimensional visualizations of simulated supercell outflows (Orf et al. 2017; Orf 2019; Yao et al. 2019) have revealed complex vortex-vortex interactions, mostly prevalent in the vicinity of rear-flank downdrafts and low-level mesocyclones/tornadoes. Some of these vortices interact with the tornado, evolving into quasi-horizontal vortex tubes, colloquially referred to as *horizontal vortices* (Wurman and Kosiba 2013; Houser et al. 2016; Orf et al. 2017). Horizontal vortices are occasionally observed around the periphery of real tornadoes as condensation tubes,

whenever the pressure drop within their cores is large enough to induce condensation (Houser et al. 2016; Bai et al. 2017; Orf et al. 2017). Recent documentation of horizontal vortices in tornado footage, close-range mobile Doppler radar observations and visualizations of tornado-resolving simulations has provided some general insights into their typical behavior. In visual observations and visualizations of tornado simulations, horizontal vortices occur prominently in rear-flank downdrafts and appear to wrap around the tornado from the right-rear side (looking from behind the tornado) through the left-front low-level sectors (Bai et al. 2017; Orf et al. 2017). In Doppler radar observations, horizontal vortices also appear in the rear-flank downdraft region, in the vicinity of rear-flank downdraft internal boundaries during tornado intensification (Houser et al. 2016). Their vorticity vectors have a large component to the left of the cold pool outflow winds when near the surface (i.e., in the crosswise direction) or along the flow when ascending around the tornado (when the crosswise vorticity horizontally tilted into streamwise vorticity). This suggests that they can be generated by surface friction or by horizontal buoyancy gradients (baroclinity) along warm rear-flank downdraft internal boundaries behind a cooler surge (Houser et al. 2016). Since horizontal vortices are much weaker than the tornado itself, they apparently behave as passive coherent structures of the flow, being advected and distorted by the tornado's outer circulation and evolving into arcs around the tornado.

Although horizontal vortices have been documented more frequently in recent years, mostly based on observations, several aspects of their nature and importance in supercell dynamics remain unknown. For example, are horizontal vortices always simply passive features of the flow? Or, are there instances where horizontal vortices can have an impact on the flow field of the nearby tornado? Do the horizontal vortices contribute in any significant way to tornado and/or related mesocyclone circulations via vortex mergers? Can tornado-horizontal-vortex interactions enhance

damaging winds at the surface? Regarding the latter question, the only published report of ground-level damage associated with a horizontal vortex was that of Bai et al. (2017), who suggested that a downward-bending horizontal vortex far downstream of a typhoon-spawned tornado in Taiwan was responsible for damage to power lines. More studies are needed to better understand the behaviors and dynamics of horizontal vortices and whether/how they affect tornadoes and tornadic winds, especially near the surface where damage can occur.

During the 27 April 2011 devastating tornado outbreak in the southeast United States, several strong and violent tornadoes were accompanied by horizontal vortices (Knupp et al. 2014). Many of the most intriguing HV-tornado interactions observed on that day occurred during the early stages of the Tuscaloosa-Birmingham, Alabama, EF4 tornado¹, as it intensified over Tuscaloosa. During this stage of the tornado lifecycle, several Tuscaloosa residents video recorded the tornado from multiple locations, affording an opportunity to document some HV structures that have not been discussed much in the literature. More specifically, the visual observations reveal the existence of large, persistent horizontal vortices that closely trail the tornado's right flank very near the ground, producing strong wind fields (hereafter referred to as "trailing horizontal vortices" or "trailing HVs"). In addition, some of the videos suggest that these trailing HVs can themselves interact with smaller HVs to create complex three-dimensional vortical structures in the vicinity of the tornado, rendering these features even more interesting.

1.3. Objectives of this study

The purposes of this dissertation are twofold. First, we seek to better understand how and why a supercell evolving in a horizontally homogenous, steady-state environment can produce widely different tornadoes by contrasting the differences in storm structures that occur in each

¹ Hereafter, simply referred to as the Tuscaloosa tornado.

tornado cycle. This includes understanding how a previous tornado cycle affects the next to highlight the similarities and mainly discrepancies from previous conceptual models of cyclic that naturally arise for tornadic supercells simulated at high-enough resolution. Emphasis is given to understanding how tornadoes evolve relative to their parent updrafts, especially at low levels and how they relate to nearby storm structures. Second, this study seeks to better address questions posed in subsection 1.2 regarding horizontal vortices and their interactions with tornadoes. In particular, we seek to document and provide some preliminary understanding of the trailing HV structures identified in selected videos of the Tuscaloosa tornado, that are rarely observable by high-resolution mobile Doppler radar due to their small scale and relative rarity. In order to gain insight on the three-dimensional structure and evolution of trailing HVs beyond the limited clues available in the videos, we present visualizations and a brief qualitative analysis of a very high-resolution numerical simulation based on the Tuscaloosa tornado case, which contains vortical features with similar characteristics of visually observed trailing HVs. It is hoped that this study will highlight the potential importance of horizontal vortices and their interactions with tornadoes, as well as encourage more investigations on coherent vortical structures in supercell outflows may affect tornado dynamics.

Chapter 2: Review of Supercells, Tornadoes, and Horizontal Vortices²

The chief objectives of this dissertation are to further our knowledge of the processes conducive to tornado development in supercells and better understand how tornadoes interact with neighboring storm- and substorm-scale structures. In this context, it is appropriate to review what we do and do not know about these phenomena. In this section, a brief review of supercell thunderstorms is provided, followed by a review of the types of tornadoes and other relevant intense vortices produced by supercells. The mechanisms and modes tornadogenesis in supercells are also reviewed.

2.1 Supercell thunderstorms

Supercell thunderstorms are the rarest yet, oftentimes, the most severe manifestation of deep moist convection. The perception that supercells comprise a rather special subset of severe deep convection dates back from the late 1950s and early 1960s. Browning (1964), based on conventional radar observations, formally introduced the term supercell to refer to convective storms that persisted for prolonged periods (in some cases, several hours) and moved to the *right* of the pressure-weighted mean tropospheric wind to contrast with “ordinary” cells, i.e., those whose lifespan was merely on the order of the advective timescale and tended to move *along* with the mean wind. Early studies (Browning and Ludlam 1962; Browning and and 1963; Marwitz 1972a, 1972b, 1972c; Schlesinger 1973) correctly determined that the roots for supercell longevity lied in the presence of strong environmental vertical wind shear through a deep layer of the troposphere (e.g., 0-6 km AGL). In such environments, precipitating hydrometeors produced in a storm’s updraft are redistributed downwind by the intense wind shear allowing the main updrafts

² Some parts are direct excerpts from Oliveira et al. (2019) and Oliveira et al. (2022; entitled: Trailing Horizontal Vortices in Observed and Numerically Simulated Tornadoes, submitted to the Bulletin of the American Meteorological Society, in review at the time of this writing).

and downdrafts to coexist symbiotically for extended periods. This is opposed to ordinary cell dynamics in which precipitation falls directly over the updraft within 40-60 min of storm formation due to the lack of strong wind shear, ultimately cutting off the supply of unstable air for updraft maintenance and causing its decay (Byers and Braham 1949). However, it was also noted at the time that longevity and deviant motion were not features exclusive to supercells necessarily; for example, multicellular storms tended to regenerate and propagate also to the right of the mean-tropospheric wind due to the interaction of their cold pools with the environmental wind shear, when the latter was substantial and had southerly component (Marwitz 1972b). Based primarily on conventional radar, limited surface observations, and early numerical modelling efforts, Fujita and Grandoso (1968) hypothesized that not only the longevity and deviant motion of supercells, but their splitting behavior into anticyclonic and cyclonic storms was related to the presence of persistent midlevel rotation [about 3-8 km above ground level (AGL)] in their updrafts. These rotating updrafts, later referred to as *midlevel mesocyclones* and *mesoanticyclones* (e.g., Davies-Jones 1984), would eventually become the defining characteristic of supercells that distinguishes from other modes of deep convection.

Much of our current knowledge of supercells can be traced back to pioneering studies combining of observations (e.g., from surface station, sounding, radar, aircraft, storm-chaser footage), theory, and numerical modeling conducted during the early 1970s through the mid-to-late 1980s (Barnes 1978b, 1978a; Klemp and Wilhelmson 1978b, 1978a; Wilhelmson and Klemp 1978; Lemon and Doswell 1979; Ray et al. 1981; Rotunno 1981; Wilhelmson and Klemp 1981; Rotunno and Klemp 1982; Klemp and Rotunno 1983; Klemp and Weisman 1983; Davies-Jones 1984; Rotunno and Klemp 1985; Vasiloff et al. 1986; Brandes and Johnson 1988). The seminal work of Lemon and Doswell (1979) illustrates the success of combining radar, instrumented

aircraft, visual, and surface observations to construct conceptual models of the main structures composing a tornadic supercell (Fig. 2.1). In their model, the low-level structure of a supercell, such as that seen in a low plan position indicator (PPI) of a radar display, contains a main updraft (UD) accompanied by two main downdrafts regions. One such downdraft is located downwind of the updraft in the storm's forward flank (termed *forward-flank downdraft* or FFD), whereas the other downdraft is located in the rear flank (termed *rear-flank downdraft* or RFD), each of these downdrafts associated with its own surface gust front. In this mature stage of a tornadic supercell, a *low-level mesocyclone* (around 0-3 km AGL) is situated near the interface between the updraft and the RFD and at the tip of a *hook* in the low-level radar reflectivity field, such that the mesocyclone exhibits a "divided structure" or, correspondingly, the updraft has a "horseshoe" shape. Tornadoes are typically located around the center of the low-level mesocyclone also near the updraft-RFD interface. A "*flanking line*" of cumulus towers is commonly observed along the *rear-flank gust front* (RFGF). The conceptual model of Lemon and Doswell (1979) has endured to this day with only minor modifications. Perhaps the most notable modification is the modern notion that FFDs are not typically associated with well-defined surface gust fronts; rather, the forward-flank region of supercells usually contains confluent boundaries (sometimes rather diffuse), such as left-flank convergence boundaries (LFCBs) and/or forward-flank convergence boundaries (FFCBs; Beck and Weiss 2013).

The first-order understanding that midlevel mesocyclones (and mesoanticyclones) originate from tilting of horizontal vorticity available in the environmental wind shear was established through numerical modelling and theoretical work in the late 1970s and 1980s. Davies-Jones (1984) performed an elegant mathematical derivation of the origin of midlevel rotation in supercells, where he demonstrated that upward tilting of streamwise horizontal vorticity by an

updraft in an environment characterized by clockwise-curved hodographs (veering shear vectors with height) yields a high spatial correlation between positive vertical velocity and vertical vorticity in rising air parcels, thus producing for net cyclonic midlevel rotation in supercell updrafts.

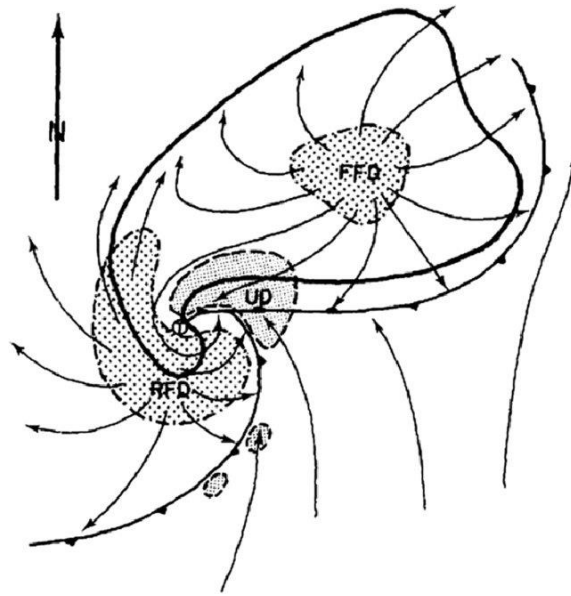


Fig. 2.1. Conceptual plan view of a cyclonic tornadic supercell at low levels. The thick line represents the radar echo. The finely stippled areas represent the updraft (UD), while the RFD and FFD are coarsely stippled. From Lemon and Doswell (1979). The frontal symbols illustrate the storm's gust front associated with each downdraft region. Ground-relative streamlines indicate the flow in and around the supercell. The tornado location is denoted by an encircled T.

Inspired by the landmark realistic numerical simulations of supercells by Klemp and Wilhelmson (1978b, 1978a), Rotunno and Klemp (1985) demonstrated in a numerical study how an updraft developing in an environment rich in environmental wind shear tilts initially horizontally oriented vortex lines upward to produce midlevel rotation. As a storm develops midlevel rotation, its motion and persistence become intrinsically associated with such rotation. The presence of a midlevel rotation (localized zones of lowered pressure aloft) in a storm induces nonlinear vertical dynamic pressure gradient accelerations on the flanks of the convective cloud in a way that it continually grows along those flanks; for clockwise-curved hodographs, favorable dynamic vertical pressure gradients are induced on the right flank of storms such that they

propagate to the right of the mean-tropospheric winds (Weisman and Klemp 1982, 1984). In addition to investigating midlevel mesocyclogenesis, Rotunno and Klemp (1985) built upon their previous research (Klemp and Rotunno 1983) to demonstrate near-surface vertical rotation in supercells develops as the storm's updraft tilts and stretches horizontal vorticity that is augmented by baroclinicity along horizontal buoyancy gradients in the rain-cooled downdraft portion of the storm. A more detailed discussion of baroclinic vortex genesis modes will be provided in subsection 2.4.

A key aspect of supercells that is particularly challenging to forecast accurately is their ability to produce several mesocyclones and tornadoes sequentially during their life cycle (Darkow and Roos 1970; Lemon and Doswell 1979; Johnson et al. 1987; Adlman and Droegemeier 2002; Dowell and Bluestein 2002a, 2002b). Under certain environmental setups, supercells can produce tornadoes periodically for long periods, occasionally longer than 7 hours (e.g., Knupp et al. 2014). The processes of sequential mesocyclone production in supercells has been referred to as *cyclic mesocyclogenesis*, while the process of repeated tornado formation has been referred to as *cyclic tornadogenesis*; cyclic mesocyclogenesis does not imply cyclic tornadogenesis, but cyclic tornadogenesis occurs in association with cyclic mesocyclogenesis (Darkow and Roos 1970; Johnson et al. 1987; Adlman et al. 1999; Dowell and Bluestein 2002a, 2002b; Wurman et al. 2007; French et al. 2008; Houser et al. 2015). The dangers posed by cyclic tornadic supercells have attracted considerable attention since the 1970s (Darkow and Roos 1970; Lemon and Doswell 1979), mainly due to some notorious tornado outbreaks that occurred in that decade and earlier (e.g., Fujita et al. 1970; Agee et al. 1976; Locatelli et al. 2002). As a result, much has been learned about the processes by which supercells produce tornadoes repeatedly.

The first conceptual models of cyclic mesocyclogenesis were constructed on comprehensive analyses of observational data. Lemon and Doswell (1979) produced a model where cyclic mesocyclogenesis resulted from the discrete production of mesocyclones and updrafts following the occlusion of an initial mesocyclone and updraft. The occlusion of mesocyclones is an analogy to the occlusion process that occurs in well-developed extratropical cyclones. Utilizing a dataset of approximately 100 radar-observed supercells, Burgess et al. (1982) conceived a conceptual model of cyclic mesocyclogenesis in which the authors describe how mesocyclones are undercut from their source of potentially unstable environmental air by outward-surging RFGFs that occlude the mesocyclones. Undercut mesocyclones move rearward relative to the storm motion (or leftward for cyclonic supercells in the Northern Hemisphere) as they weaken and disintegrate within the storm's precipitation area, while new mesocyclones/updrafts tend to develop at the occlusion point because of the locally enhanced convergence in that region. A wide range of mesocyclone lifespans were identified in their study, ranging approximately from 45 to 90 min.

Adlerman et al. (1999) conducted a detailed analysis of an idealized numerical simulation of a cyclic supercell initialized with a sounding associated with the 20 May 1977 Del City, Oklahoma, storm, finding good agreement with previous observation-based models of cyclic supercells. Their simulation shows that an initial low-level mesocyclone is cut off from its source of potentially buoyant environmental air by an outward-surging RFD, reinforced by an occlusion downdraft induced by a downward pressure gradient force due to rotation becoming stronger at low levels (Klemp and Rotunno 1983). Further outward motion of the downdraft air causes the original mesocyclone to occlude and detach from the RFGF, soon moving into the storm's outflow and attaining maximum intensity under a deep, vertically stacked updraft; after its peak stage, the mesocyclone decays embedded in cold outflow and downdrafts. Enhanced surface convergence

along a bulging RFGF triggers new updraft pulses downshear from the decaying mesocyclone, which eventually develop into new mesocyclones. The entire process of cyclic mesocyclogenesis in their simulation takes 60 min, 20 min longer than the typical cycling period documented by Burgess et al. (1982). In a subsequent study, Adlerman and Droegemeier (2002) found that cycling frequency (among other mesocyclone characteristics) is quite sensitive to a variety of model parameters, including parameterizations of microphysics and surface friction, grid spacing, and diffusion coefficients; this suggests that some cyclic aspects of supercells may be difficult to accurately predict using numerical models. Additionally, Adlerman and Droegemeier (2005) found that cyclic mesocyclogenesis is remarkably sensitive to the environmental wind shear characteristics (i.e., hodograph shape) in which the supercell is embedded, commonly resulting in two main modes of cyclic mesocyclogenesis. The first mode was described in Adlerman et al. (1999) and other radar-based studies, and is termed *occluding cyclic mesocyclogenesis* (Fig. 2.2; top panel), to refer to mesocyclones that move rearward relative to the storm after occlusion. The second mode consists of decaying mesocyclones that propagate southward (in a storm-relative sense) along the gust fronts without occluding, with new mesocyclones forming along kinks in the gust front farther north repeatedly; this mode is referred to as *non-occluding cyclic mesocyclogenesis* (Fig. 2.2; bottom panel).

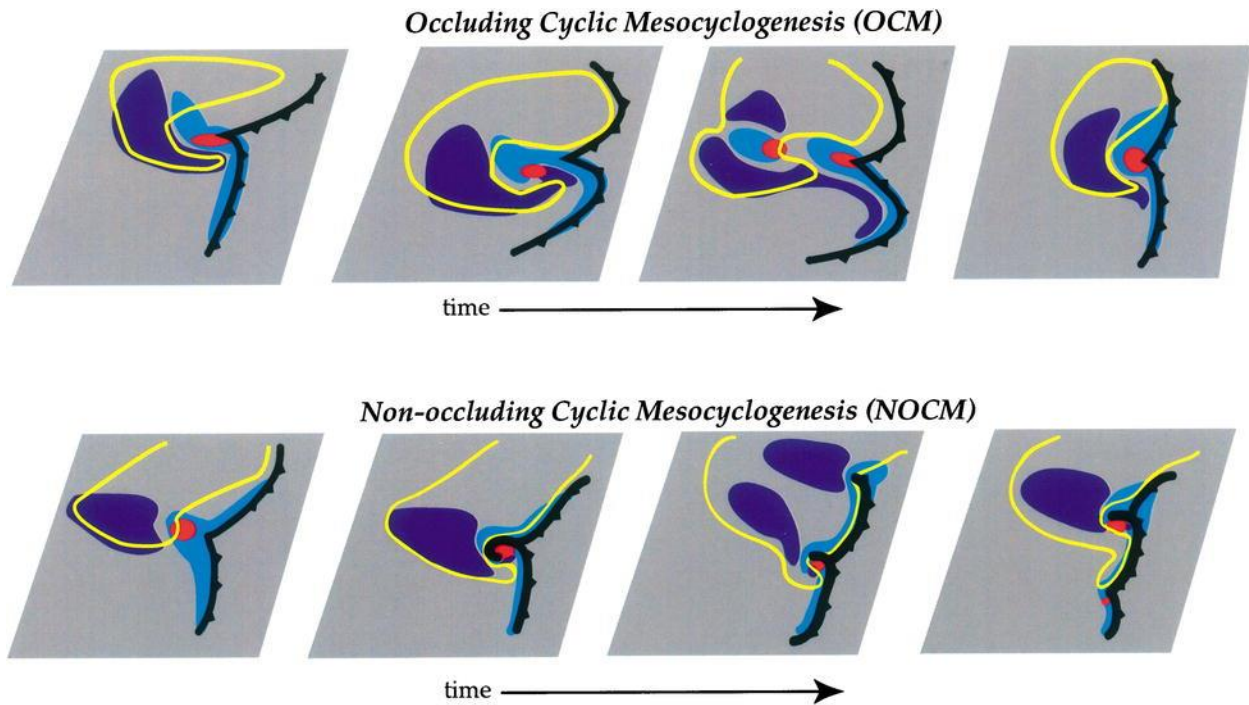


Fig. 2.2. Cyclic mesocyclogenesis at low levels. Top panel: Occluding cyclic mesocyclogenesis; bottom panel: non-occluding cyclic mesocyclogenesis. Vertical vorticity maxima (low-level mesocyclones) are shaded in red. Updrafts are shaded in light blue and downdrafts are shaded in dark blue. The yellow contour outlines the boundary of the storm's rainy area. The black frontal symbols indicate the RFD and FFD gust fronts. From Adlerman and Droegemeier (2005).

In subsequent years, studies utilizing higher resolution Doppler radar data further refined existing models of cyclic mesocyclogenesis and tornadogenesis and discussed how particular cases can deviate from the models. Dowell and Bluestein (2002a, 2002b) analyzed Doppler radar data of a cyclic tornadic supercell collected by an aircraft from the Verification of the Origins of Rotation in Tornadoes Experiment (VORTEX; Rasmussen et al. 1994) to formulate a refined conceptual model of cyclic tornadogenesis. Their model, which is based on the model of Burgess et al. (1982), illustrates how a portion of the horseshoe updraft is “shed” during the occlusion process and moves rearward relative to the storm motion, whereas the other portion of the updraft remain attached to the RFGF. As the tornado-bearing updraft is shed further rearward into the storm's cold pool, increasing tilting and stretching of low-level horizontal vorticity (both originated in the environment or augmented by in-storm processes) at the bulge of the RFGF

fosters new mesocyclone and tornado development downshear of the old tornado in a process that can persist for hours. Beck et al. (2006) used high-resolution mobile Doppler radar of nontornadic cyclic supercell to determine that hook-echo regeneration downshear of old occluding mesocyclones depends on a surging RFGF to produce low-level deformation field that is a favorable for new mesocyclone development. Using high-resolution mobile Doppler radar data of a distinct cyclic supercell, French et al. (2008) hypothesized that for mesocyclones to persist and intensify, strong rear-flank outflow needs to develop in order to balance strong storm-relative inflow winds that tend to advect newly develop circulations into the cold pool to rapidly. More recently, Betten et al. (2018) constructed nearly continuous wind retrievals over a 90-min period from mobile Doppler radar observations of a cyclic high-precipitation supercell (Moller et al. 1990) to address interactions between the storm's boundaries, vertical drafts, and mesocyclones. Although the authors found an overall storm evolution similar to previous studies of cyclic supercells, the interaction between gust fronts, internal boundaries, and updrafts differed markedly between cycles, with RFD internal surges playing a major role in modulating these differences.

2.2 Types of tornadoes

Tornadoes are defined as violently rotating columns of air pendant from cumulonimbus clouds or growing cumulus towers, which make contact with the surface (Glickman 2000; Agee 2014). Because of the intense winds in and around tornadoes and their relatively small diameter, obtaining in situ measurements of their wind field has proven extremely difficult over the years. Indeed, even obtaining *indirect* measurements of tornadic winds near the surface through mobile Doppler radars is challenging given that such observations must be taken at a considerable close range (Bluestein et al. 2007a; Bluestein et al. 2013; Kosiba and Wurman 2013; Wurman and Kosiba 2013; Houser et al. 2015, 2016; Bluestein et al. 2018, 2019). In order to acquire reasonable

post-storm estimates of tornado intensity, Fujita (1971) devised a six-category scale ranging from 0 to 5 to assign tornado strength ratings according to the degree of damage caused by tornadoes. The Fujita (F) scale remained as the primary tool to estimate tornado intensity in the U.S. for around three decades until early 2007 when it was replaced by the Enhanced Fujita scale (EF) scale (WSEC 2006), a refinement that continues to employ the same 0-5 categories. Elaborated through a combined efforts of engineers and meteorologists, the EF scale assigns more accurate and consistent wind speed estimates according to the degree of damage to man-made structures and vegetation than the F scale, most notably for the upper damage categories, which had long been recognized to represent overestimates of actual tornadic winds (e.g., Edwards et al. 2013).

Convective storms can generate a myriad of surface vortices which may or may not qualify as tornadoes. Building upon previous tornado categorizations (Davies-Jones et al. 2001; Agee and Jones 2009), Agee (2014) proposed a tornado classification scheme divided into three main tornado types. Tornadoes of Type I comprise those produced by mesocyclones (or, equivalently, mesoanticyclones) within supercells. As such, tornadoes spawn from low-topped continental mini-supercells and mini-supercells in landfalling tropical cyclones are included in this category as well. Type II tornadoes generally refer to tornadoes generated by mesovortices within larger, organized multicellular convective systems, such as quasi-linear convective systems (QLCSs). Finally, tornadoes of Type III designate localized or shear-induced vortices pendant from a cumuliform updraft and in contact with the ground, such as landspouts (Bluestein 1985) and waterspouts (Golden 1971). Although gustnadoes are also strong shear-induced vortices generated in convective storms, they are no longer considered tornadoes according to the classification system of Agee (2014) because of their lack of connection to the parent convective cloud. The tornado taxonomy presented by Agee (2014) is used herein to discuss the types of tornadoes.

Of all three type of tornadoes, Type I or mesocyclonic tornadoes are generally the ones capable of attaining strong-to-violent (EF2-EF5) strength and, thus, cause significant damage (Church et al. 1993; Davies-Jones et al. 2001; Smith et al. 2012); as a result, this type of tornado has rightly received vast attention in the severe storms research community. Type I tornadoes form as the result of persistent stretching of low-level mesocyclone-scale vorticity [$O(0.01 \text{ s}^{-1})$] under the storm's parent updraft, usually within a rotating wall cloud near the interface between the RFD and the updraft (Klemp 1987; Wicker and Wilhelmson 1995; Davies-Jones et al. 2001; Markowski et al. 2002; Markowski and Richardson 2009; Markowski et al. 2012b; Markowski et al. 2012a; Kosiba et al. 2013; Markowski and Richardson 2014; Davies-Jones 2015). In the absence of preexisting vertical vorticity at the ground, the mesocyclone-scale vorticity that is eventually contracted into a tornado develops via tilting of low-level horizontal vorticity that is produced either barotropically (i.e., contained in the pre-storm environmental wind shear; e.g., Mashiko et al. 2009), baroclinically in downdrafts and along outflow boundaries (Markowski et al. 1998; Atkins et al. 1999; Rasmussen et al. 2000; Markowski et al. 2008; Markowski et al. 2012b; Markowski et al. 2012a; Dahl et al. 2014; Dahl 2015; Marquis et al. 2016; Boyer and Dahl 2020), frictionally (Schenkman et al. 2014; Markowski 2016; Roberts et al. 2016; Roberts and Xue 2017; Tao and Tamura 2020), or most likely, a combination of all the above processes (Markowski 2016; Mashiko 2016a, 2016b; Yokota et al. 2018) (Fig. 2.3a). The last two mechanisms have been considered to play a more relevant role in tornadogenesis (Dahl 2015; Roberts et al. 2016). In some situations, anticyclonic tornadoes may form in association with mesoanticyclones on the trailing end (with respect to storm motion) of the hook echo and RFGF near strong mesocyclones or cyclonic tornadoes (Brown and Knupp 1980; Fujita 1981; Bluestein et al. 2007a; Wurman and Kosiba 2013; Bluestein et al. 2016). Such tornadoes have been shown to form due to upward tilting

of horizontal vortex lines into arcs straddling the hook echo; the horizontal vorticity is produced baroclinically along the leading edge of the colder RFD and tilting occurs as the air parcels descend in the RFD (Straka et al. 2007; Markowski et al. 2008; Markowski et al. 2012b; Kosiba et al. 2013; Markowski and Richardson 2014). The branch of the vortex line arc in the trailing end of the hook is responsible for the anticyclonic vortex, while the opposite end of the vortex line reinforces the low-level mesocyclone. Given that the main focus of this dissertation pertains to mesocyclonic tornadoes, a more in-depth discussion of the formation mechanisms of tornadoes in supercells will be provided in subsection 2.4.

As previously discussed, Type II tornadoes are produced by mesovortices in QLCSs, such as squall lines or bow echoes. These mesovortices usually develop on the north (south) sector of the QLCS apex in the Northern Hemisphere (Southern Hemisphere), such that they are sometimes referred to as “bookend vortices” (Weisman 1993; Atkins et al. 2004). The perception that QLCSs can produce tornadoes may be traced back to the late 1950s with Nolen (1959), who associated the occurrence of tornadoes to undulated patterns seen in radar reflectivity displays of squall lines, which became known as “line-echo wave patterns” or LEWPs. Smith et al. (2012) constructed a climatology of significant severe storms based on storm reports from 2003 to 2011 in the contiguous U.S., where the authors partitioned storm classification based on convective mode; they demonstrated that QLCSs can account for as much as 14% of all reported tornadoes. More recently, Ashley et al. (2019) used image classification and machine learning techniques to elaborate a climatology of QLCSs; among their results, the authors show that in certain regions of the U.S., such as the area west of the Appalachians, extending from the lower Great Lakes to the mid-South, QLCS tornadoes can remarkably account for 50%-73% of all regional tornado reports. Some particular QLCS tornado events may be quite efficient at producing tornadoes, especially in

the presence of strong low-level shear (Forbes and Wakimoto 1983; Schenkman et al. 2012; Knupp et al. 2014). As with Type I tornadoes, existing theories regarding the sources of horizontal vorticity for the production of tornado-producing mesovortices in QLCSs rely on barotropic, baroclinic, and/or frictional processes. Weisman and Davis (1998) proposed that, for a QLCS moving eastward, downward tilting of horizontal vortex lines associated with westerly environmental shear (typical of midlatitude pre-storm environments) by storm-scale downdrafts can produce cyclonic-anticyclonic vortex couplets at the tail-end of QLCSs, with the cyclonic (anticyclonic) member on the northern (southern) end of the convective line in the Northern Hemisphere (Fig. 2.3b). The authors demonstrated that the inclusion of the Coriolis force acts to favor the cyclonic member of the couplet over a few hours, consistent with the observed predominance of cyclonic bookend vortices. In the same context, Weisman and Davis (1998) also show that upward tilting of horizontal vortex lines associated with easterly shear (produced baroclinically in the cold pool and along the leading edge of the QLCS) can also produce a vortex couplet of the same sign of the one described by the barotropic mechanism (Fig. 2.3c). In recent years, high-resolution numerical simulations of QLCS have shed light on the role of surface friction in the formation of mesovortices. In a high-resolution (100-m grid spacing), real-data simulation of a tornadic mesovortex that occurred on 8-9 May 2007 in Minco, Oklahoma, Schenkman et al. (2012) found that surface friction was responsible for producing a horizontal rotor around their mesovortex, which acted to enhance low-level updrafts and vortex stretching, eventually resulting in tornadogenesis. The importance of surface friction is also reinforced by Xu et al. (2015), who showed that meso- γ scale QLCS vortices can form through the upward tilting of horizontal crosswise vorticity produced frictionally ahead of the QLCS environment and also within descending rear-inflow jets.

Finally, tornadoes of Type III develop in mesoscale environments containing abundant preexisting vertical vorticity in the boundary layer, most commonly along convergent zones, such as outflow boundaries and fronts, but usually with weak vertical wind shear (Fig. 2.3d). Based on a large set of observed landspout events in Colorado, Wakimoto and Wilson (1989) concluded that this type of tornado originates via a vortex sheet instability along a surface convergence boundary, which breaks up into discrete mesocyclones. Some of the resulting mesocyclones may then become collocated with growing convective updrafts along the boundary, eventually intensifying to tornadic strength via vortex stretching. This mechanism was later confirmed in numerical simulations by Lee and Wilhelmson (1997a, 1997b). Although Type III tornadoes are usually not as strong as Type I (and some Type II) tornadoes, they may occasionally attain EF2 intensity (Wakimoto and Wilson 1989).

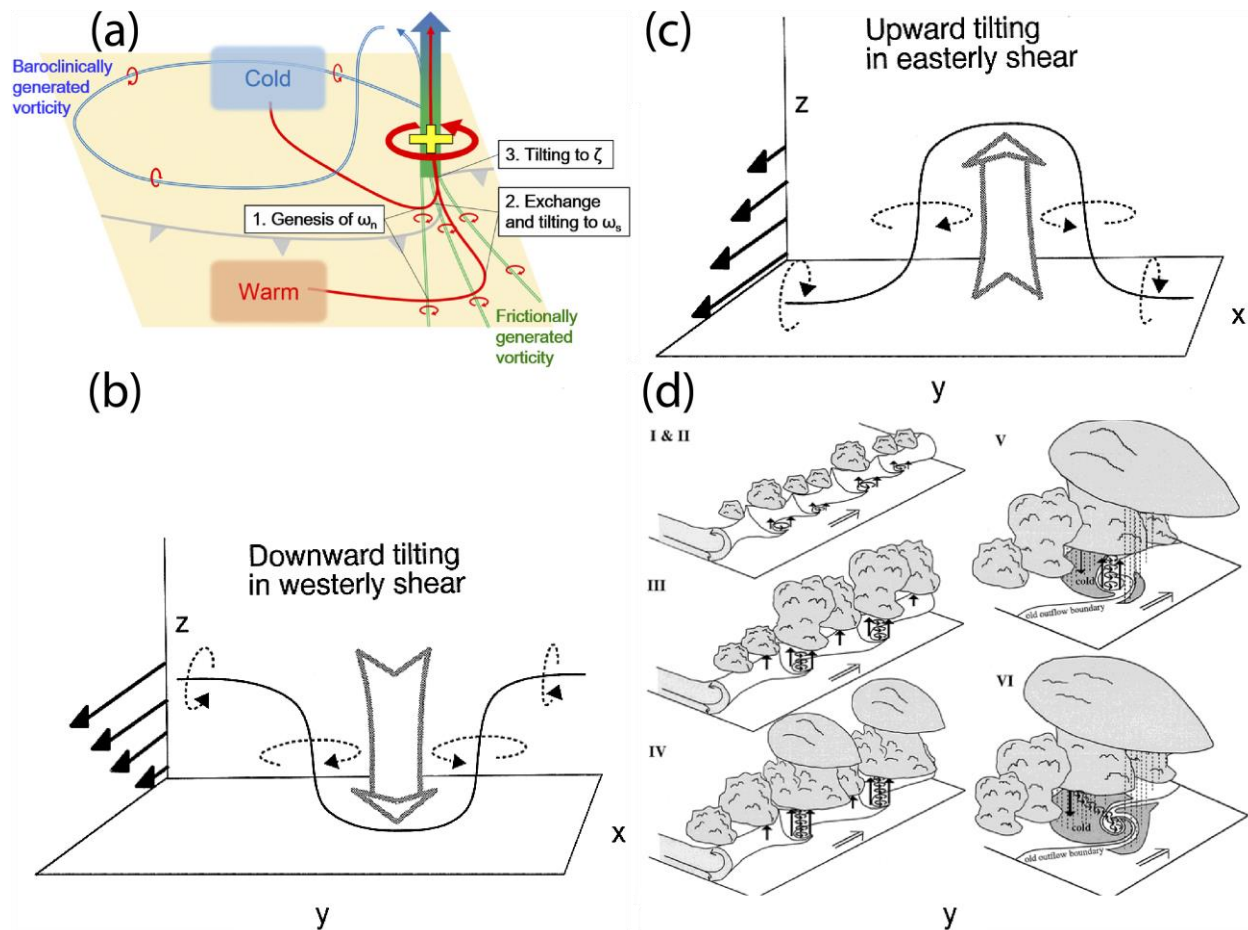


Fig. 2.3. Mechanisms of vertical vortex genesis in different convective modes. (a) Supercells: Blue (green) vortex lines represent vorticity that is produced baroclinically (frictionally). The large vertically pointing arrow represents a low-level updraft that tilts and stretches low-level horizontal vorticity into a low-level mesocyclone/tornado (indicated by the + symbol as cyclonic vertical vorticity) for air parcels traveling along the red trajectories. Red curved arrows denote the sense of rotation of the vortices. The gray frontal symbols represent the storm's surface gust fronts. From Yokota et al. (2018). (b) QLCSs: generation of a cyclonic-anticyclonic vortex pair through downward tilting of horizontal vorticity in westerly wind shear (typically available in the environmental; solid line) by a downdraft (large downward-pointing arrow). Dashed curved arrows indicate the sense of rotation of the shear-induced vortex lines. (c) Similar to (b), but for upward tilting of horizontal vorticity in easterly wind shear (typically produced baroclinically along the QLCS' gust front) by an updraft. Both (b) and (c) from Weisman and Davis (1998). (d) Non-supercell local storms: (I & II): strong convergence along a surface wind shift line (in this schematic, a dry outflow boundary) initiates cumulus convection (represented by the cloud symbols above the black arrows, which denotes updrafts along the boundary) and misocyclones (circular arrows) through the release of vortex sheet instability. (III) Convection deepens and stretches misocyclones. (IV) As convective towers grow into cumulonimbus, misocyclones may be contracted into tornado, even before the onset of surface precipitation. (V) Cold outflow from the storm's rainy area encircles a mature tornado. (VI) Increased rainfall and cold outflow completely encircle the tornado, which weakens and moves into the cold air mass and dissipates within downdrafts (black downward-pointing arrows). From Lee and Wilhelmson (1997b).

2.3 Tornadogenesis mechanisms in supercells

In spite of remarkable advancements in our understanding of supercell tornadogenesis over the past several decades, the knowledge on storm- and substorm-scale dynamics involved in tornado formation remains incomplete. Overall, supercell tornadogenesis has been commonly defined as a three-stage process (e.g., Davies-Jones 2015). In the first stage, a developing updraft acquires vertical vorticity at mid-levels (about 3-8 km AGL) by tilting environmental streamwise horizontal vorticity associated with large-scale (base-state) vertical wind shear. As previously discussed, however, this mechanism cannot be invoked to explain the development of near-ground mesocyclone-scale vorticity [$O(0.01 \text{ s}^{-1})$] since rising air parcels carry their vorticity *away* from the surface (Davies-Jones 1984). As such, the second stage of tornadogenesis relies on tilting of near-ground horizontal vorticity (augmented via in-storm processes) by a *downdraft*, such that parcels develop vertical vorticity while they descend toward the surface (Davies-Jones and Brooks 1993). The third and final stage of tornadogenesis consists of the amplification of vertical vorticity produced in stage two into tornadic intensity [$O(0.1-1 \text{ s}^{-1})$] through stretching under the storm's updraft. While there is general consensus in the severe storms research community regarding the mechanism responsible for midlevel mesocyclogenesis, the development of near-ground rotation in supercells persists as a matter of debate. Over the last three decades, considerable effort has been devoted to unraveling the mechanisms by which low-level horizontal vorticity is generated within supercells as well as the roles played by the storm's vertical drafts in the tilting and stretching of such vorticity into low-level mesocyclones and tornadoes.

The landmark numerical studies of Klemp and Rotunno (1983) and Rotunno and Klemp (1985) conspicuously indicated that baroclinic generation of low-level horizontal vorticity along supercells' outflow boundaries was the primary contributor to the development of intense near-

surface rotation. Based on the notion that updrafts alone could not tilt horizontal vorticity to produce vertical vorticity at ground level, Davies-Jones and Brooks (1993) used numerical simulations to demonstrate how downdrafts could efficiently produce cyclonic vertical vorticity at the surface. They showed that near-ground cyclonic vorticity develops due to a “slippage” process, where horizontal vorticity and velocity vectors along air parcel trajectories descending in a downdraft detach from one another due to continued baroclinic generation of horizontal vorticity. This causes air parcels initially containing quasi-streamwise horizontal vorticity first to acquire anticyclonic vorticity during their initial descent through tilting; upon nearing the ground, however, the velocity vectors along air parcel trajectories become quasi-horizontal, while the vorticity vectors acquire an upward (cyclonic) component due to the combined effects of baroclinity and tilting. The key role of baroclinity in tornadogenesis has been widely substantiated by a large body of literature (Wicker and Wilhelmson 1995; Markowski et al. 1998; Rasmussen et al. 2000; Markowski et al. 2008; Markowski and Richardson 2009; Markowski et al. 2012b; Markowski et al. 2012a; Beck and Weiss 2013; Dahl et al. 2014; Markowski and Richardson 2014; Dahl 2015; Parker and Dahl 2015; Rotunno et al. 2017; Boyer and Dahl 2020; among many others).

Despite efficient at producing near-surface vorticity, baroclinity can become a hindrance to tornadogenesis, if excessive. Based on mobile mesonet collected around tornadic and nontornadic hook echoes from 1994 to 1999, Markowski et al. (2002) found that the likelihood of tornadogenesis decreased considerably for supercells containing rear-flank outflows that were too cold. Several other studies have corroborated these results (Shabbot and Markowski 2006; Grzych et al. 2007; Hirth et al. 2008; Lerach et al. 2008; Markowski et al. 2008; Snook and Xue 2008; Lee et al. 2011; Lee et al. 2012; Lerach and Cotton 2012; Markowski et al. 2012b; Dawson et al. 2015; Marquis et al. 2016). On one hand, when the outflow is too cold, air parcels may acquire

appreciable vorticity baroclinically, yet fail to amplify that vorticity into a tornado through stretching under a low-level updraft due to excessive convective inhibition. On the other hand, when outflow buoyancy is too warm, air parcels may not develop enough baroclinic vorticity for amplification under a low-level updraft. This conundrum has led tornadogenesis to be considered a “Goldilocks” problem (Markowski et al. 2008; Markowski and Richardson 2009), in which the outflow must possess some intermediate strength to sustain considerable baroclinic vorticity production and still retain enough buoyancy such that vorticity-rich parcels can be stretched by a low-level updraft (Markowski and Richardson 2014; Fischer and Dahl 2020).

Barotropic horizontal vorticity has also been considered as a potential source of tornadic vorticity. It has been shown through idealized, axisymmetric simulations that downdrafts in the vicinity of updrafts (such as RFDs) can produce ground-level vertical vorticity by reorienting initially horizontal environmental vortex lines at the edge of the downdraft (Davies-Jones et al. 2001; Markowski et al. 2003a; Davies-Jones 2008; Parker 2012). Furthermore, sounding-based climatologies of severe convective parameters in the late 1990s and early 2000s (Rasmussen and Blanchard 1998; Brooks et al. 2003; Markowski et al. 2003b; Rasmussen 2003) showed that the likelihood of supercells tornadogenesis was higher for environments containing larger low-level (0-1 km) shear [or, similarly, storm-relative helicity (SRH)]. In order to investigate the relative roles of barotropic and baroclinic processes in tornadogenesis, Markowski (2012) conducted a detailed Lagrangian circulation analysis along material circuits for the 5 June 2009 Goshen County, Wyoming, tornadic low-level mesocyclone based on dual-Doppler data collected during the second Verification of the Origins of Rotation in Tornadoes Experiment [VORTEX2; Wurman et al. (2012)]. Their results suggested that only a relatively small amount of circulation acquired by the circuits came from environmental vorticity (at most, 10-30%); baroclinicity was implied to

have contributed much more to the circulation of the circuits. More recently, idealized supercell simulations by Dahl et al. (2014) employed a Lagrangian approach to track vortex line segments within downdrafts, where the authors found a much more significant contribution of baroclinity to near-ground vertical vorticity production relative to environmental vorticity. Their results were reinforced in a subsequent study by Dahl (2015) for environments containing crosswise vorticity. The collective outcome of the abovementioned studies strongly indicates that baroclinic vorticity usually dominates over environmental vorticity as a source of near-surface rotation³.

In recent years, the potential role played by surface friction in generating near-ground horizontal vorticity for supercell tornadogenesis has become a central topic in the severe storm research community. This source of vorticity has been mostly neglected in many numerical studies addressing tornadogenesis because of their use of free-slip lower boundary conditions and the challenges associated with realistically parameterizing surface drag (Wicker and Wilhelmson 1995; Markowski and Bryan 2016; Markowski et al. 2019). A number of studies employing realistic heterogeneous (observation-based) initial and boundary conditions suggests that surface friction can be a dominant contributor to the vorticity budget of tornadoes. Schenkman et al. (2014) performed a real-case, high-resolution (50-m grid spacing) simulation of the 8 May 2003 Oklahoma City F4 tornado (Xue et al. 2014), in which two tornadoes developed. A Lagrangian vorticity budget analysis for backward trajectories initialized in the tornadoes indicated that both tornadoes formed predominantly due to tilting and subsequent stretching of horizontal vorticity generated frictionally near the ground. In a similar context, Mashiko (2016b) and Mashiko (2016a) performed real-case simulations of the 6 May 2012 Tsukuba tornado, Japan; by also integrating material circuits and trajectories initialized around the low-level mesocyclone and tornado

³ Unless, perhaps, in extremely sheared environments, such as in landfalling tropical cyclones (Mashiko et al. 2009). In that case, environmental vorticity may dominate the vorticity budget of tornado-entering parcels.

backward in time, the authors found a dominant contribution of baroclinic effects for the total circulation of the material circuits around the mesocyclone and vorticity budgets for the tornado, though friction did play a secondary role. In turn, Yokota et al. (2018) performed a 33-member ensemble experiment of the same Tsukuba tornado, in which friction was predominantly the main contributor to pretornadic circulation in their backward-integrated material circuits that traveled near the surface. However, depending on the times and positions that the circuits were analyzed, baroclinic production of circulation could be as large as friction. Recently, Tao and Tamura (2020) also performed simulations of the Tsukuba tornado, where they found a dominant contribution of frictionally generated horizontal vorticity to the tornado's vorticity budget.

The mechanisms by which surface friction instigate tornadogenesis in supercells were investigated in detail by Roberts et al. (2016). The authors performed and compared a pair of idealized, horizontally homogeneous supercell simulations initialized via a warm bubble, differing by how surface drag was applied to the simulated winds. In one of their simulations, surface drag was applied to the full wind (referred to as FWFRIC), while in the other experiment, surface drag was applied to the environmental wind only (referred to as EnvFRIC). Overall, their FWFRIC simulation produced a tornado very early in the life cycle of the storm (by 1500 s) before a mature cold pool was established. On the other hand, the EnvFRIC simulation never developed a tornado, only subtornadic vorticity maxima. A Lagrangian trajectory analysis of the FWFRIC experiment determined that frictionally generated vorticity was paramount for the genesis of the tornado, since strong baroclinicity was still weak at that early stage of the storm's evolution. Based on the experiments, Roberts et al. (2016) summarized how that surface friction affects tornadogenesis in three collective ways (Fig. 2.4). First, surface friction is responsible for producing Ekman-type hodographs in the boundary layer, thus enhancing low-level shear (and thereby, horizontal

vorticity) in the base-state environment (Fig. 2.4a). Second, surface friction acts on inflow winds accelerating into a developing tornado to abruptly generate near-ground (0-200 m AGL) horizontal *crosswise* vorticity, which is exchanged into horizontal *streamwise* vorticity via a “riverbend effect”, as parcels turn cyclonically around the low-level circulation (Fig. 2.4b). The resulting vorticity is then readily available for tilting and stretching into the developing tornado. Third, surface friction enhances cross-isobaric flow at low-levels, leading to strong convergence and an enhanced low-level updraft (Fig. 2.4c). Using the same set of experiments, Roberts and Xue (2017) showed that the circulation in the pretornadic low-level mesocyclone of FWFRIC was fundamentally produced via frictionally generated vorticity. In a subsequent study, Roberts et al. (2020) also showed how the potential for tornadogenesis, timing, and other tornado characteristics varied as a function of a set drag coefficients typical of continental environments. In short, tornadogenesis was favored (hampered) in their experiments with drag coefficients set to nonzero values (zero) and tended to occur more prominently for drag coefficients in an intermediate range.

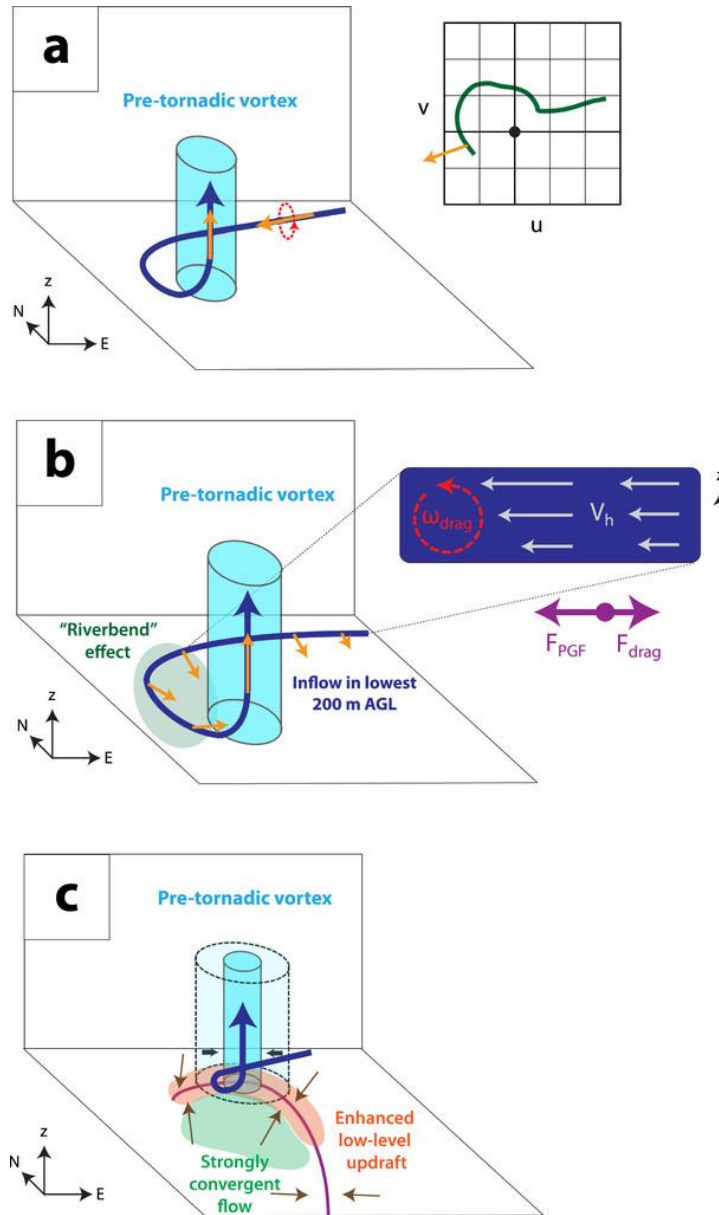


Fig. 2.4. Mechanisms by which surface friction generates horizontal vorticity in supercell. (a) Friction produces horizontal vorticity (orange vectors) through low-level shear in the environmental (base-state) flow characterized as an Ekman spiral in a hodograph (inset). Blue curved arrow denotes a trajectory entering a pre-tornadic vortex (blue cylinder); dashed curved arrow in red represents the sense of rotation along the trajectory (which coincides with a vortex line in this case, since the vorticity is in the streamwise direction). (b) Production of near-ground horizontal crosswise vorticity in flow accelerating into a developing tornado (insets). The crosswise vorticity is exchanged into streamwise vorticity via a “riverbed effect” (green shaded area) as the flow curves cyclonically around the pre-tornadic vortex. (c) Frictional enhancement of low-level convergence and updrafts (shaded in orange) along a supercell’s surface boundary (divergent flow behind the boundary is shaded in green) causing the contraction of a pre-tornadic vortex into a tornado (indicated by black arrows in opposing directions). From Roberts et al. (2016).

While the sources of tornadic vorticity (related to stage 2 in the tornadogenesis process) have been a central topic in tornado research as discussed above, a growing body of literature has stressed the importance of intense low-level updrafts to tornadogenesis (Markowski and Richardson 2014; Coffey and Parker 2015; Coffey and Parker 2017; Coffey et al. 2017; Orf et al. 2017; Roberts and Xue 2017; Yokota et al. 2018; Fischer and Dahl 2020; Flournoy et al. 2020; Goldacker and Parker 2021). The notion that dynamically induced low-level lifting is likely key to tornadogenesis was underscored in the numerical study of Wicker and Wilhelmson (1995). In their idealized supercell simulations, pretornadic low-level mesocyclones (formed via tilting of both barotropic and baroclinic horizontal vorticity) was shown to dynamically reduce the pressure field above cloud base (via the “spin” term in the Poisson equation for perturbation pressure; Klemp and Rotunno 1983; Rotunno and Klemp 1985), resulting in locally enhanced vertical perturbation pressure gradient accelerations and stretching of mesocyclonic vorticity to tornadic strength. This type of process was also found in the numerical simulations of Grasso and Cotton (1995). More recently, in an in-depth analysis of the 5 June 2009 Goshen County tornadic supercell during VORTEX2, Markowski et al. (2012a) hypothesized that the role of strong wind shear in pretornadic environments was to promote midlevel mesocyclones with lowered bases (e.g., 1 km AGL), in turn, favoring strong low-level upward accelerations. Their hypothesis was later corroborated through highly idealized, dry simulations of supercell-like “pseudostorms” initialized with artificial heat sources and sinks (Markowski and Richardson 2014). Tornadogenesis was shown to become more likely when the environment contained *strong* low-level shear and mild cold pools (i.e., those produced by heat sinks of an intermediate strength in their range of heat sinks) due to tilting and stretching of baroclinally generated vorticity under persistent, dynamically driven low-level updrafts at the base of the mesocyclone.

The fundamental relevance of strong low-level updrafts in tornadogenesis were discussed by Coffey and Parker (2017), who performed a pair idealized supercell simulations initialized with composite base-state environments obtained from VORTEX2. One of the experiments composite environments was derived from the tornadic events sampled by upper-air sounding during the field campaign, whereas the other was produced from the nontornadic events. They showed that low-level updrafts formed dynamically and organized in the tornadic case because the wind profile contained large low-level (0-500 m AGL) environmental streamwise vorticity. Conversely, the nontornadic simulations had disorganized low-level updrafts due to significant low-level crosswise environmental vorticity in the wind profile. Remarkably, simulation initialized with the tornadic simulations remarkably. The results of Coffey and Parker (2017) were further substantiated by subsequent numerical studies utilizing ensemble analyses (Coffey et al. 2017; Flournoy et al. 2020) and sensitivity experiments (Coffey and Parker 2018) derived from the same VORTEX2 dataset. A collective outcome of the abovementioned studies is the notion that environmental streamwise vorticity (SRH 0-500 m) in layer shallower than previously thought can better predict tornadoes (Coffey et al. 2019).

Coffey et al. (2019) show that strong environmental near-ground horizontal streamwise vorticity calculated for very shallow layers such as 0-500 or even 0-100 m AGL has high skill at predicting tornadogenesis in supercells. More recently, Goldacker and Parker (2021) have shown through idealized simulations initialized with real-data wind profiles that the low-level updrafts in supercell-like storms that tilt large environmental near-surface streamwise vorticity can intensify further via a feedback process, in which vertical vorticity is produced in the low-level updraft, accompanied by localized pressure lowering. As a consequence, upward accelerations are

augmented via vertical perturbation pressure gradients, leading to enhanced stretching of vertical vorticity and so on, eventually resulting in tornadogenesis.

2.4 Horizontal vortex tubes near tornadoes

Supercells produce a wide spectrum of vortical structures with length scales ranging from the large, midlevel mesocyclone (5–10 km in diameter; Brandes 1984; Wakimoto et al. 2004) down to vortices on the order of only a few meters, such as suction vortices (e.g., Fujita 1981; Fiedler 2009; Wurman and Kosiba 2013). One such manifestation of strong vorticity in supercells occurs in the form of three-dimensional (3D), elongated vortex tubes that are typically observed near tornadoes or in the periphery of their parent low-level mesocyclones (Bluestein et al. 2007b; Knupp et al. 2014; Bai et al. 2017). They can occasionally be visually observed as condensation tubes or severely slanted funnels, given high-enough relative humidity and/or intense-enough cyclostrophic pressure drop inside them (Houser et al. 2016; Orf et al. 2017). These vortex tubes are anecdotally referred to as “horizontal vortices” (hereafter, referred to as HVs) since, in contrast to tornadoes that are defined as vertical vortices, the axis of rotation of these vortex tubes is oriented primarily parallel to the ground.

Given the small scale and transient nature of HVs, they are hard to observe in Doppler radar data or to resolve in high-resolution numerical simulations; most evidence for their existence relies on videos or photographs (Knupp et al. 2014; Houser et al. 2016; Bai et al. 2017; Orf et al. 2017). Among the few existing observations, Wurman and Kosiba (2013) provide evidence for large HVs south-southeast of two large tornadoes sampled by the DOW radar. In both cases, the HVs are located outside of the tornadic circulation but their sense of rotation (inferred from radial velocity plan position indicators at two levels; see their Figure 14) is different; in one case the inferred horizontal vorticity vector points to the southwest while in the other it points to the north-

northeast. This suggests different mechanisms may control HV formation. Houser et al. (2016) provided an analysis of an HV interacting with the violent El Reno-Piedmont tornado on 24 May 2011 based on Rapid-scan X-Polarimetric Doppler (RaXPo1) data and videographic observations. The HV, which is collocated with a weak-reflectivity band in reflectivity data, has a horizontal vorticity vector orientation similar to the Canton tornado case from Wurman and Kosiba (2013), which pointed to the northeast and originated in a rear-flank downdraft (RFD) internal momentum surge (RFDIS) to the south-southeast of the tornado, close to the surface. The HV wraps around the intensifying tornado, ascending in its circulation. The authors suggest possible mechanisms for the formation of the HV consistent with the observed horizontal vorticity vector orientation, which include: (i) baroclinic production along a warm RFD surge behind the primary RFD gust front, (ii) frictional torques in outflow air also behind the primary RFD gust front and (iii) reorientation of vertical vorticity associated with the tornado into a horizontal axis. Regardless of the mechanism, horizontal stretching of the vortex tube into the intensifying tornado is responsible for strengthening the HV to the point that cyclostrophic pressure drop in its core caused condensation to form.

Using a numerical simulation employing 30-m isotropic grid spacing to investigate the 24 May 2011 El Reno supercell and tornado, Orf et al. (2017) were the first to describe simulated HVs similar to visual observations. In their simulation, vortices ascend as funnel clouds on the periphery of the simulated tornado, in a similar manner to that described in Houser et al. (2016).

As discussed by Houser et al. (2016), surface friction is a plausible mechanism that can produce strong near-surface horizontal vorticity in the RFD outflow. This mechanism was shown earlier by Schenkman et al. (2014) to have a significant impact on the vorticity budget of a developing tornado in a real case simulation of the 8 May 2003 Oklahoma City tornadic storm

(Xue et al. 2014). In that study, surface friction acts on outflow and inflow parcels to produce strong near-surface horizontal vorticity that is abruptly tilted and stretched to produce pre-tornadic vertical vorticity centers that eventually coalesce into a tornado. This mechanism was explored in detail by Roberts et al. (2016) and Roberts and Xue (2017) in an idealized, single-sounding simulation of the 3 May 1999 Bridge Creek-Moore tornado. In summary, the authors show that surface friction acting on storm-induced flow produces near-surface crosswise horizontal vorticity that can be exchanged into streamwise vorticity as the flow bends cyclonically when converging toward a developing tornado (i.e., the river bend effect, e.g., Davies-Jones et al. 2001). The vorticity-rich parcels can then be tilted abruptly and stretched to produce strong near surface vertical vorticity.

Although recent studies have shed some light on the behavior of HVs near tornadoes, overall, the typical behavior of HVs around tornadoes remains poorly understood. For instance, an important question that remains unclear is whether HVs are simply passive features of the flow surrounding tornadoes (i.e., merely distorted and advected by tornadic winds) or they can, in some circumstances, interact with the tornado somehow to locally enhance (or disrupt) each other. To address these questions, high-resolution simulations of tornadoes and HVs are key since they can provide a reasonable depiction of the 3D flow in and around tornadoes. As such, Section 4 will be dedicated to better understanding how HVs interact with tornadoes, making use of high-resolution simulations of tornadoes and visual observations of tornado-HV interactions in real tornadoes.

Chapter 3: Evolution of Storm- and Tornado-Scale Structures Leading to Cyclic Tornado Formation

3.1 Methodology

3.1.1 Experiment setup

The three-dimensional, nonhydrostatic Advanced Regional Prediction System (ARPS; Xue et al. 2000; Xue et al. 2001; Xue et al. 2003) is used for the numerical experiments used in this dissertation. The ARPS was designed with the purpose of simulating convective-scale phenomena and has been used extensively in studies concerned with the dynamics and prediction of tornadoes (Snook and Xue 2008; Schenkman et al. 2014; Xue et al. 2014; Dawson et al. 2015; Roberts et al. 2016; Roberts and Xue 2017; Snook et al. 2019; Roberts et al. 2020). In order to resolve fine-scale storm structures at low levels, a horizontal grid spacing of 50 m is used along with a vertical grid spacing that stretches from 2 m at the surface to 200 m above 10 km above ground level (AGL). This grid setup yields three levels of scalar variables (as well as horizontal wind components) below 20 m AGL (1, 6, and 16 m AGL) and an average vertical grid spacing of 30.8 m below 650 m AGL. Placing the lowest scalar level very close to the model surface is also an attempt to increase the sample size of parcel trajectories that do not fall below the lowest scalar level, thus, avoiding the need to rely on extrapolated kinematic quantities (Guchte and Dahl 2018). Vorticity budgets along Lagrangian trajectories for the tornadoes in the simulations presented herein will be examined in a future study. A drawback of using very small near-surface grid spacing is that the time step used in the explicit vertical advection scheme must also be very small; otherwise, the linear stability condition can be easily violated, especially when tornadoes are present. Due to the very small grid spacing used, both the large and small time steps used by mode-splitting time

integration (Klemp and Wilhelmson 1978a; Xue et al. 2000) are set to 0.05 s to ensure time integration stability in the presence of tornadic wind speeds⁴.

The domain size and total number of grid points are $100 \text{ km} \times 100 \text{ km} \times 18.2 \text{ km}$ and $2003 \times 2003 \times 93$, respectively, with open radiative lateral boundary conditions. The bottom boundary is flat. The experiment is integrated forward in time for 4 h 30 min (16200 s) to encompass the entire lifecycle of four tornadoes that form cyclically in the simulated supercell. History files are saved at 60 s intervals for the first 5700 s of model integration (period corresponding to the nontornadic phase of the storm) and every 2 s for the remaining integration window to sample the life cycle of the tornadoes at considerably high temporal resolution.

For the microphysics parameterization, the National Severe Storm Laboratory double-moment scheme (NSSL2M; Mansell et al. 2010) is used. Fourth-order advection is used in the horizontal and vertical along with fourth-order horizontal and vertical computational mixing coefficients. Subgrid-scale turbulence is parameterized with a 1.5-order turbulent kinetic energy (TKE)-based scheme (Moeng and Wyngaard 1988).

In order to account for the effects of surface friction in this study, a semi-slip lower boundary condition is employed. In the ARPS model, surface drag is parameterized through the horizontal momentum stresses at the surface:

$$-\tau_{13}(z = 0) = \rho C_d V_h u, \quad (3.1)$$

$$-\tau_{23}(z = 0) = \rho C_d V_h v, \quad (3.2)$$

where τ_{13} and τ_{23} represent the Reynolds stress tensor contained in the subgrid-scale turbulence scheme, ρ is density, C_d is the drag coefficient (dimensionless) valid at 1 m AGL, u and v represent the ground-relative horizontal wind components, respectively, and V_h denotes the ground-relative

⁴ When the vertical Courant number is large and $\max(u, v, w) \sim$ sound speed, the advantages of using time splitting are lost. More specifically, time splitting becomes less advantageous once the Mach number ~ 0.3 - 0.4 .

horizontal wind speed. Through this formulation, surface drag acts on the total wind field (base state wind + storm-induced perturbation wind). This experiment and all others to be addressed in later chapters employ $C_d = 0.028$. This C_d value corresponds to a roughness length ~ 9.16 cm, which roughly corresponds to roughness lengths in between the $C_d = 0.005$ and 0.01 experiments used in Roberts et al. (2020), whose first model level AGL is 10 m.

To obtain a more complete depiction of 3D features of interest in this study, 3D visualizations of simulated storm structures extensively. The visualizations mainly use the volume rendering feature of the Visualization and Analysis Platform for Ocean, Atmosphere, and Solar Researchers (VAPOR; Li et al. 2019) software.

3.1.2 Base-state environment and establishment of an initial balanced sounding

The base-state environment of the tornadic supercell simulation by a single sounding shown in Fig. 3.1. The profile is obtained from a full-physics 3-km grid spacing Weather Research and Forecasting (WRF) model ensemble-mean analysis nested within a 15 km grid covering the contiguous U.S. for the 27 April 2011 devastating tornado outbreak in Mississippi-Alabama (Yussouf et al. 2015). In that study, conventional and radar observations were assimilated on the 15 and 3 km grids, respectively, using ensemble Kalman filter. The model sounding is extracted approximately 40 km southeast of the predicted storm corresponding to the Tuscaloosa-Birmingham tornadic supercell (Knupp et al. 2014) at the 2100 Universal Time Coordinated (UTC) analysis time. The analysis time is 1 h before the observed and predicted storms struck Tuscaloosa (at around 2200 UTC). The thermodynamic profile is obtained from a grid point over the city of Tuscaloosa (32.9° N; 85.6° W) and the wind profile is averaged over a 0.2° latitude-longitude box centered on that grid point.

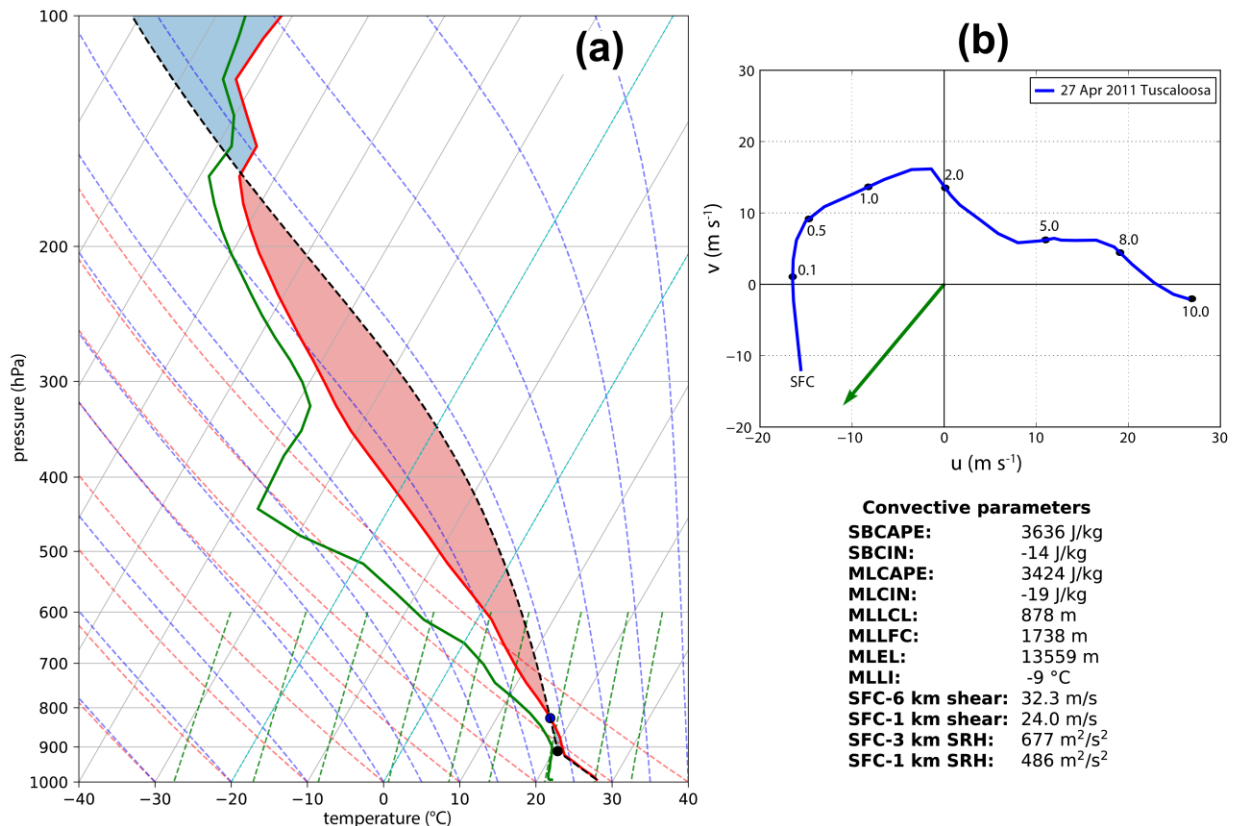


Fig. 3.1. (a) Skew T -log p diagram for the idealized tornadic supercell experiment. The red (green) solid line represents environmental temperature (dewpoint) in °C. The black dashed line denotes the temperature for an ascending surface-based parcel. Areas of positive (negative) buoyancy are highlighted by semi-transparent red (blue) shading. The black and blue dots represent the lifting condensation level and level of free convection, respectively. (b) Hodograph for storm-relative winds between the surface and 10 km AGL. Black dots are heights (in km AGL). The green vector indicates the ground-motion vector ($u = 11 \text{ m s}^{-1}$; $v = 17 \text{ m s}^{-1}$) originally subtracted from the wind profile to induce the storm to remain quasi-stationary in the simulation. Some relevant convective parameters are shown in the bottom right sector of the figure.

A comparison of the surface air and dew-point temperatures at the Tuscaloosa airport (28.0 °C and 21.0 °C, respectively) with the WRF profile (27.8 °C and 21.9 °C, respectively) revealed a good agreement between the observations and WRF-generated analysis. The location and time of the model-extracted sounding match the spatial and temporal ranges for proximity sounding suggested by Potvin et al. (2010) and minimize contamination from the predicted storm. A constant wind speed ($u = 11 \text{ m s}^{-1}$; $v = 17 \text{ m s}^{-1}$) is subtracted from the sounding to keep the simulated supercell quasi-stationary during its tornadic phase. For this 50-m experiment, the winds in Fig.

3.1b are ~20 % stronger relative to those used in the original profile below 2 km AGL [the original profile was used in the experiment of Oliveira et al. (2019); to be presented in Chapter 4]. This modification was obtained via sensitivity experiments in order to obtain a strongly tornadic supercell, given that the initial experiments using the same sounding of Oliveira et al. (2019) failed to yield intense tornadoes. This discrepancy is likely a result of the current experiment using a different model configuration from Oliveira et al. (2019), which include an updated version of the ARPS model, a larger domain, smaller grid spacing, and double-moment microphysics.

The base-state environment features a combination of high conditional instability and extreme values of low-level shear [e.g., 3424 J kg⁻¹ mean-layer Convective Available Potential Energy (MLCAPE) and 486 m² s⁻² 0-1-km SRH], a setup known to be conducive to violent tornadoes (Rasmussen 2003; Coffey et al. 2019; Taszarek et al. 2020) and consistent with observations and mesoscale model analyses for 27 April 2011 around the time of the Tuscaloosa tornado (Knupp et al. 2014). In our test early simulations, convective initiation was easily achieved in this environment by releasing a 3-4 K warm thermal bubble due to the negligible mean-layer convective inhibition (MLCIN; -2 J kg⁻¹) environment. A drawback seen in these experiments, however, was that numerous spurious storms formed in the inflow of the developing supercell of interest, contaminating its ensuing evolution. To avoid this problem, a temperature increment was added to the sounding in the 720–2900 m layer, with a maximum 1.8 K added to the top of atmospheric boundary layer AGL. This increment rapidly decreases following a fourth-degree polynomial function such that at the bottom (top) of the modified layer, the perturbation is 0.2 K (0.5 K). The depth of the layer and the magnitude of the temperature increment were chosen by trial and error and were found to be the best option to eliminate spurious inflow convection while sustaining a vigorous tornadic supercell storm in the simulation. This procedure artificially mimics

the often-present top-of-boundary-layer inversion, and its direct effect was to reduce the MLCAPE and increase the magnitude of MLCIN from 2 to 19 J kg⁻¹. Convection is initiated with an ellipsoidal thermal bubble perturbation centered at ($y = 16$ km; $x = 55$ km) with a horizontal (vertical) radius of 10 km (1.5 km). The maximum potential temperature perturbation at the center of the bubble is 6 K. This larger than typical (and usually undesired) thermal amplitude is needed to develop a sustained supercell because of the larger inhibition added to the sounding as well as the strong low-level wind shear in the environment.

The straightforward inclusion of surface drag in idealized convective storm simulations has the undesired effect of constantly slowing down the initial near-ground wind profile (Roberts 2017), thus modifying the base-state kinematic environment as the storm evolves and complicating analyses of storm evolution of chief interest in this study. In order to avoid this issue, the ‘‘Geotriptic Wind Balance’’ (GWB) technique presented by Dawson et al. (2019) is used. The key idea of this technique is to allow the initial base-state environment to remain quasi-steady by enforcing a three-way balance among the horizontal pressure gradient, Coriolis, and frictional forces in the model. A brief description of the technique is now provided.

For any arbitrary initial sounding that is assumed to be subject to a three-force balance:

$$0 = -\frac{1}{\rho_z} \frac{\partial p_z}{\partial x} + f v + F_x[u], \quad (3.3)$$

$$0 = -\frac{1}{\rho_z} \frac{\partial p_z}{\partial y} - f u + F_y[v], \quad (3.4)$$

where F denotes the frictional terms computed from the u and v wind components. For a simulation initialized using an arbitrary sounding, the Coriolis force (second term on the RHS) and the parameterized frictional force (third term on the RHS) can be readily computed in the model since both terms are direct functions of the known local wind profile. Thus, the only unknown term in equations (3.3) and (3.4) based on the initial arbitrary sounding is the horizontal pressure

gradient force (PGF; first term on the RHS). In turn, the horizontal PGF can be readily calculated from (3.3) and (3.4) by assuming that the frictional and Coriolis forces in the observed (initial) sounding are representative of the frictional and Coriolis forces in the model:

$$P_x = fv + F_x[u], \quad (3.5)$$

$$P_y = -fu + F_y[v], \quad (3.6)$$

where P is a pseudo-PGF force denoting the estimated horizontal PGF from the initial sounding, i.e., the “real” PGF. In the model, the RHS of (3.5) and (3.6) is simply calculated from the rate of change of u and v following the first time step of model integration, usually computed at the southwesternmost grid column of the domain. This computation is performed very early in the simulation and away from the initial thermal perturbation to ensure that the only forces acting on the wind profile are the frictional and Coriolis forces. In the model, this computation appears as:

$$fv + F_x[u] = \frac{u_1 - u_0}{\Delta t}, \quad (3.7)$$

$$-fu + F_y[v] = \frac{v_1 - v_0}{\Delta t}, \quad (3.8)$$

where the u_0 and v_0 are the wind components at the initial time, while u_1 and v_1 are the wind components computed after the first model time step Δt has elapsed. Following the first model time step integration, the vertical pseudo-PGF profile is calculated using (3.7) and (3.8) at each model grid column and then added to the momentum equations for all subsequent time steps in the simulation. The outcome of this procedure is that the wind profile remains virtually steady over time away from storm-induced perturbations. This is particularly advantageous in this study since our goal is to understand why and how tornadoes vary between cycles due to storm-induced structural differences, such that an environment constantly modified by surface drag would further complicate the analysis of the results. (This was one of the major reasons for employing the GWB method in the first place.)

A recent paper by Davies-Jones (2021) suggests that the use of the GWB technique to maintain a steady-state environment in the presence of surface friction idealized storm simulations can introduce an artificial source of near-ground horizontal vorticity into the simulation, which can affect the vorticity budget of tornadoes and other vortices. In addition, Davies-Jones (2021) also discusses how storm initiation in idealized simulations using very warm initial perturbations may upset the initial environment and trigger potentially unrealistic storm processes, such as barotropic tornadogenesis modes early in a storm's lifecycle. As Davies-Jones (2021) was published after the simulations presented in this study were completed and analyzed, it was not possible to address those issues for this work. In all simulations presented herein, though, in spite of the initial peak updrafts triggered after the release of the thermal bubbles, no tornadoes formed early in the storm's life cycle, such that the deleterious effects of the very warm bubble might have been less severe in these simulations. Moreover, it is believed the fundamental *qualitative* aspects of the evolution of supercells and tornadoes analyzed in this dissertation are not invalidated by this issue, as will be discussed in subsequent chapters. Nonetheless, the issues raised by Davies-Jones (2021) and its impacts on the storm simulations in this study deserve more in-depth analysis and should quantitatively be addressed in future work.

3.2 Simulation results

3.2.1 Overview of storm evolution and its attendant tornadoes

Before beginning a detailed evolution of the supercell during cyclic tornadogenesis, it is relevant to present the overall evolution of the storm and the main features associated with the tornadoes it spawns. This is illustrated in Fig. 3.2, which shows a time-height plot of domainwide maximum vertical velocity (w_{max}), minimum perturbation pressure (p'_{min}), and maximum vertical vorticity (ζ_{max}) for the entire duration of the simulation. Since the focus of our analysis is the

evolution of the supercell during its tornadic phase, the initial nontornadic development of the simulation is briefly described. Following an initial updraft peak associated with the release of the thermal bubble, intense (but short-lived) updrafts develop over the first 3600 s of the storm's life cycle, displaying oscillations in strength due to the initial cell split into right- and left-moving storms (Klemp and Wilhelmson 1978b; Rotunno and Klemp 1982). The right-moving cell, which is the storm of interest in this study, migrates toward the center of the domain as it intensifies, while its left-moving counterpart weakens as it moves toward the northern border of the domain (not shown). Shortly after 3600 s, the midlevel updraft has developed ζ_{max} values well in excess of 0.01 s^{-1} associated with $p'_{min} < -5 \text{ hPa}$ above 1 km AGL, evidencing the presence of a midlevel mesocyclone and characterizing the storm as a supercell. Between 3600 and 6600 s, despite oscillations in the intensity of low-to-midlevel updrafts, the supercell steadily matures while still moving toward the center of the domain, where it eventually minimizes its grid-relative motion by 6600 s.

Significant changes in the storm's behavior ensue after 6600 s. Very strong updrafts ($w_{max} > 40 \text{ m s}^{-1}$) and pressure deficits ($p'_{min} < -10 \text{ hPa}$) develop in the layer between 1 and 2 km AGL and build upward, reaching 3 km AGL by 7200 s, while also extending toward the surface (with $w_{max} > 20 \text{ m s}^{-1}$). At this time, the storm displays a "classic" supercell morphology on the surface reflectivity field (Fig. 3.3a), which includes a well-defined hook echo in the reflectivity field and an attendant RFGF [seen as an arc in the -1-K density potential temperature perturbation (θ'_ρ) isotherm], and heavy rainfall accompanied by divergent flow in the FFD northwest of the hook echo.

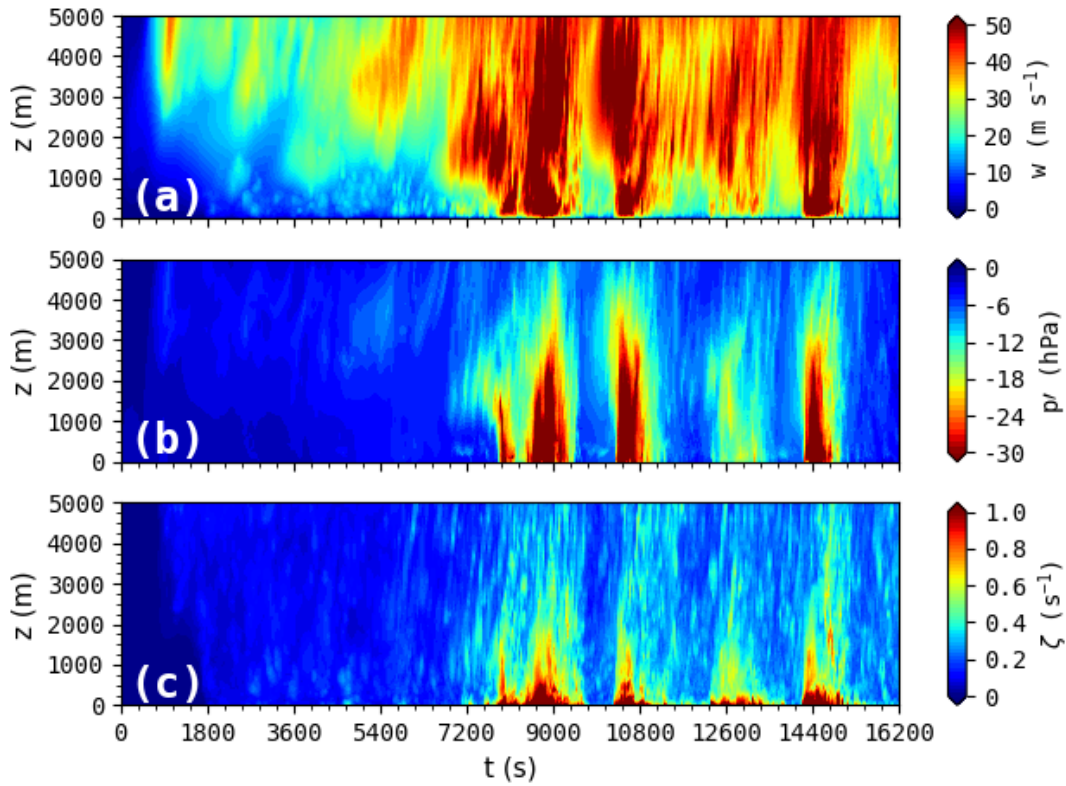


Fig. 3.2. Time-height plot of domain wide 0-5000 m (a) maximum updraft, (b) minimum perturbation pressure, and (c) maximum vertical vorticity, valid from 0 to 16200 s.

Between 7200 and 7500 s, the low-level updraft and low pressure abruptly build downward below 1 km AGL. Near the surface, transient pulses of w_{max} , p'_{min} , and ζ_{max} occur simultaneously (Fig. 3.2a-c), indicating that the intensification of the low-level updraft results in stretching of vertical vorticity maxima within the storm in the vicinity of the tightening hook echo (Fig. 3.3b). Simultaneously, the RFGF bulges northeastward and vertical vorticity increases in the hook echo, further evidencing an intensification of the low-level circulation (Fig. 3.3c). The persistence of these processes eventually culminates in tornadogenesis⁵ shortly after 7800 s (more precisely, at 7830 s). In this study, tornadogenesis is subjectively defined as the formation of a deep ($z > 1$ km),

⁵ Since the Reynolds number of the numerical simulation is orders of magnitude less than the actual atmosphere, the term “tornado” here is synonymous with “tornado-like vortex”.

persistent (lasting > 2 min) vortex exhibiting maximum ground-relative wind speed (V_{hmax}) exceeding (29 m s^{-1} ; i.e., the lowest bound for EF0 damage), $\zeta_{max} > 0.3 \text{ s}^{-1}$, and $p'_{min} < -10 \text{ hPa}$ at 10 m AGL⁶, respectively (Fig. 3.4a). The initial 300-s period of the tornado's life cycle is characterized by rapid tornado intensification (V_{hmax} exceeds 80 m s^{-1} , which corresponds to EF4 intensity; Fig. 3.4a) and deepening ($z > 2.5 \text{ km}$; Fig. 3.2a). This initial strong phase is sharply followed by a weakening phase from 8100 s to 8400 s, when the tornado's 10-m AGL winds drop to EF2 strength and p'_{min} increases to $\sim -15 \text{ hPa}$ (Figs. 3.2 and 3.4a). The weakening phase occurs in conjunction with a noteworthy erosion of the western side of the hook echo and an initially northeastward and then northwestward (Figs. 3.3d,e) motion of the tornado along the RFGF. As will be discussed later in this chapter, this evolution is influenced by a dynamically induced RFD internal surge. After undergoing the weakening stage, the tornado again intensifies and deepens, this time attaining its peak intensity between 8600-8850 s, with $V_{hmax} > 100 \text{ m s}^{-1}$ (i.e., EF5 strength), $\zeta_{max} > 2 \text{ s}^{-1}$, $p'_{min} < -70 \text{ hPa}$ (Fig. 3.4b-c), in addition to a depth $> 5 \text{ km}$ AGL through which $w_{max} > 50 \text{ m s}^{-1}$ extends. (Fig. 3.2a-c). The remarkable intensification of the tornado occurs as it occludes and detaches from the RFGF, causing it to move rearward relative to the supercell and closer to its precipitating core (Figs. 3.3f). The tornado maintains EF4 strength until 9000 s (Fig. 3.4a), when it begins to become encircled by larger amounts of precipitation from a newly developed hook echo (Fig. 3.3g). Increasing precipitation around the tornado and further rearward motion (Fig. 3.3h) eventually lead to its definitive weakening and dissipation by 9460 s (Fig. 3.4a). Concomitant with the decay of the first tornado, a new hook echo forms to the east-northeast of the remnants of the first circulation along the primary RFGF at 9600s (Fig. 3.3i), in agreement

⁶ These thresholds are defined at the 10 m AGL to be consistent with conventional measurements of wind speed used for EF scale ratings.

with previous conceptual models of occluding cyclic tornadogenesis (Burgess et al. 1982; Adlerman et al. 1999; Dowell and Bluestein 2002a; Beck et al. 2006).

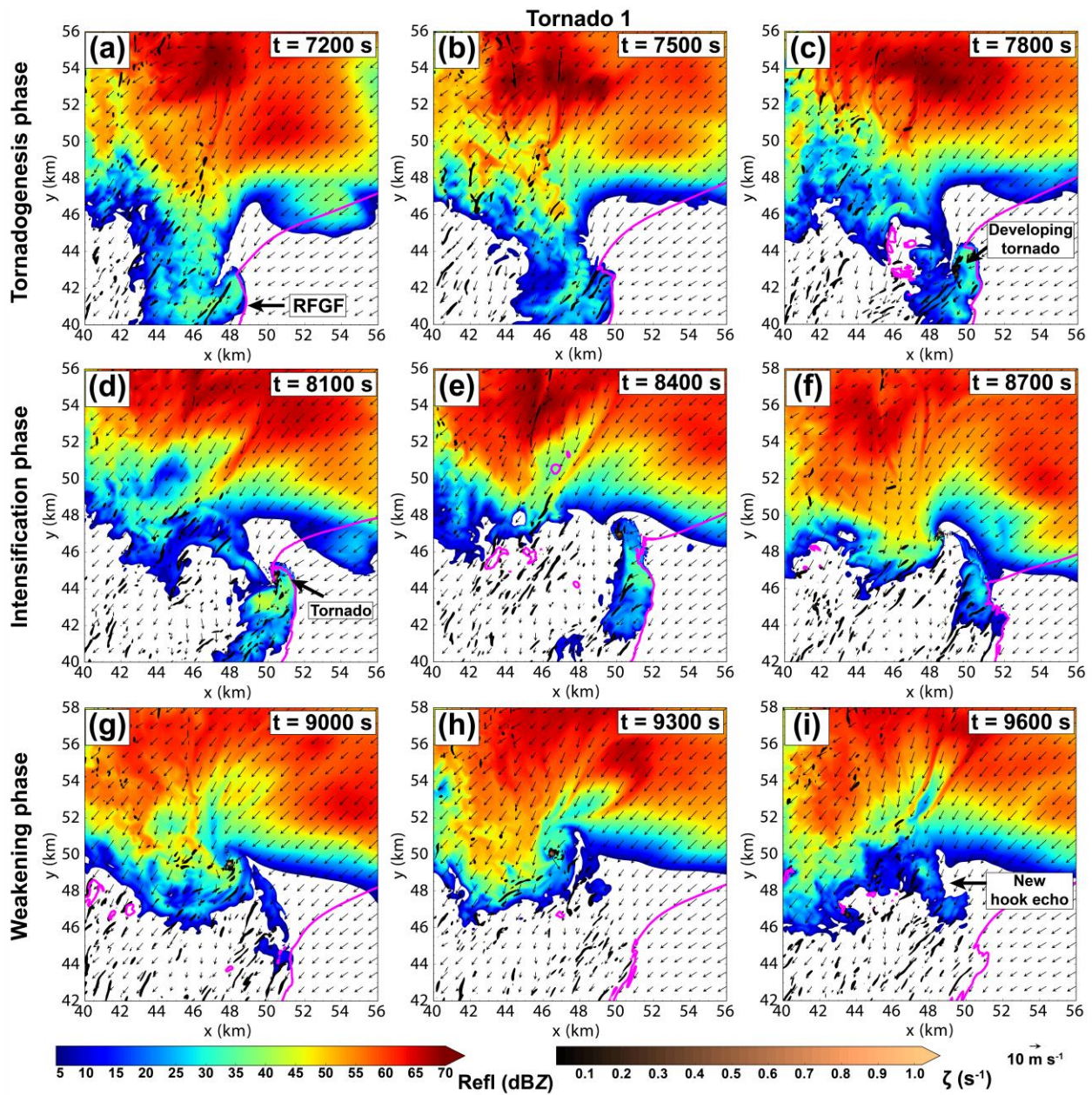


Fig. 3.3. Evolution of the simulated supercell for tornado 1 at the lowest grid level (1 m AGL) at (a) 7200 s, (b) 7500 s, (c) 7800 s, (d) 8100 s, (e) 8400 s, (f) 8700 s, (g) 9000 s, (h) 9300 s, and (i) 9600 s. Reflectivity is shaded in dBZ. The -1-K perturbation potential temperature contour is shown in magenta. Vertical vorticity is shaded in the foreground for $\zeta > 0.05 \text{ s}^{-1}$. Vectors represent storm-relative winds.

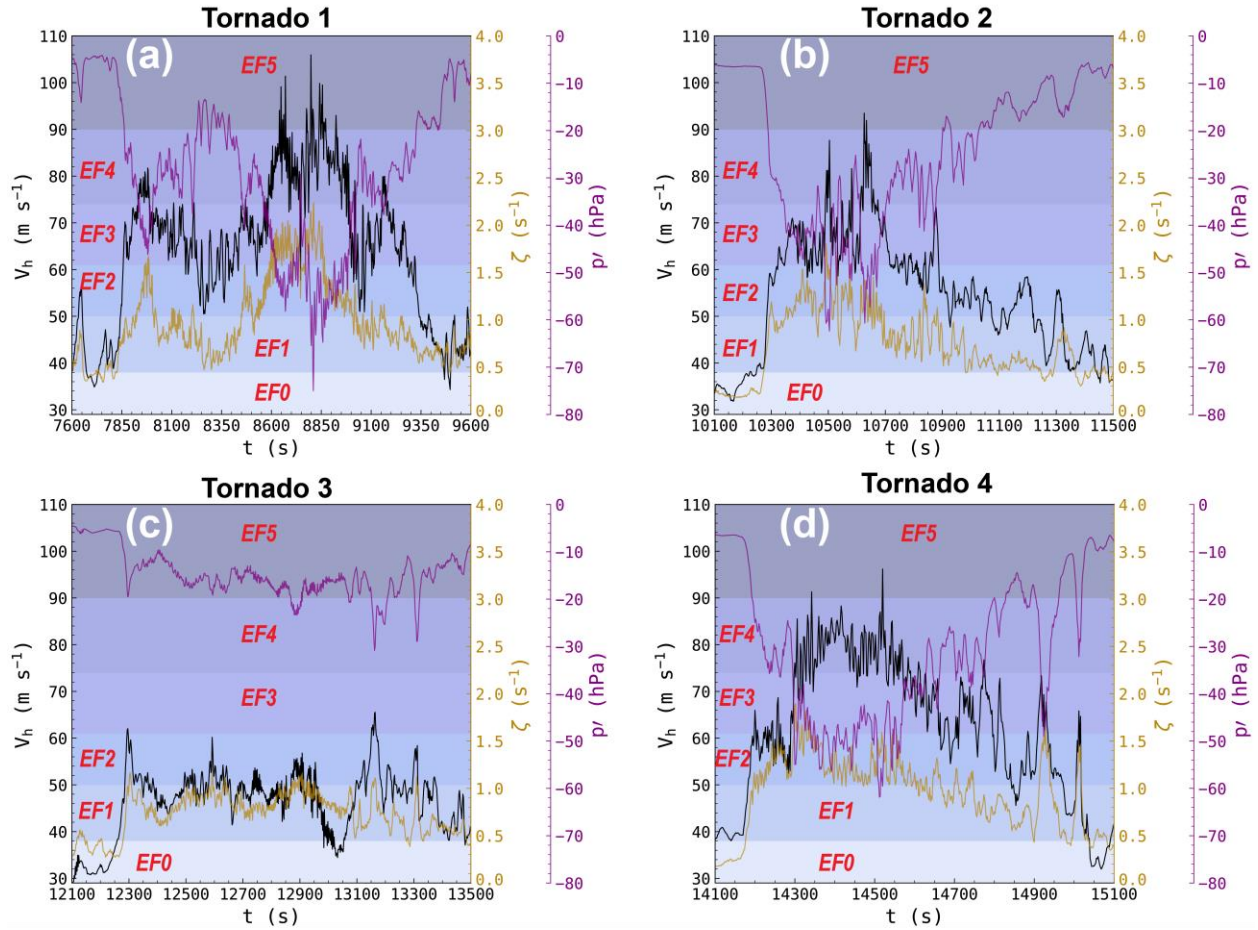


Fig. 3.4. Time series of maximum ground-relative wind (m s^{-1} ; black), minimum perturbation pressure (hPa; purple), and maximum vertical vorticity (s^{-1} ; golden) at 10 m AGL, valid from 7600 to 10800 s. The semi-transparent horizontal bars in the background denote EF-scale wind speed ranges. (a) Tornado 1, (b) tornado 2, (c) tornado 3, and (d) tornado 4.

Immediately following the dissipation of the first tornado, new intensification of the low-level updraft and pressure lowering take place above 1.5 km AGL, eventually penetrating downward below 1 km AGL, as the new hook echo expands (Figs. 3.2a and 3.5a, respectively). As with the first tornado, the persistence of this trend results in a second tornado by 10280 s (Figs. 3.4b and Fig. 3.5d). The second tornado deepens much more abruptly than the first tornado, growing higher than 3 km in less than a minute (Fig. 3.2), while attaining EF2-strength winds by 10300 s (Fig. 3.4b). Unlike the first tornado, however, the second tornado forms more than 1 km to the west of the northern tip of the RFGF and into the precipitation of the hook (Fig. 3.5b). The

tornado reaches peak intensity by 10630 s (Fig. 3.5g) when it briefly displays instantaneous $V_{hmax} > 92 \text{ m s}^{-1}$. After this period, precipitation increases in the hook echo as the tornado travels rearward relative to the storm (Fig. 3.5d), resulting in its weakening and dissipation at 11370 s. The growing amount of precipitation in the supercell's rear-flank denotes the onset of its transition into a high-precipitation (HP) morphology (Moller et al. 1990; Doswell and Burgess 1993; Moller et al. 1994).

Following the demise of the second tornado, the supercell enters a more disorganized phase, highlighted by a large hook echo reminiscent of the second low-level mesocyclone and transient updraft pulses and pressure perturbations above 1 km AGL in Fig. 3.2a. In spite of the updraft pulses, strong w_{max} ($15\text{-}25 \text{ m s}^{-1}$) persists continuously just above the surface ($z > 100 \text{ m}$). These updrafts are accompanied by shallow, transient vertical vorticity maxima seen in Fig. 3.2c, which reside within a broad, lingering low-level mesocyclone (Fig. 3.5b). By 12280 s, a third tornado forms just west of the RFGF at the reflectivity gradient of a poorly defined hook echo (Fig. 3.5e). This tornado is much weaker and smaller than its predecessors (Fig. 3.2c), remaining mostly at EF1-EF2 strength, but briefly attaining EF3 intensity by 13160 s (Figs. 3.4c and 3.5h). Once again, another increase in precipitation in the hook echo and storm-relative rearward motion induce the tornado to be absorbed into the lingering low-level mesocyclone of the second tornado and dissipate by 13490 s (Fig. 3.5k). The evolution of the third tornado reflects the disorganized state of the supercell at this stage.

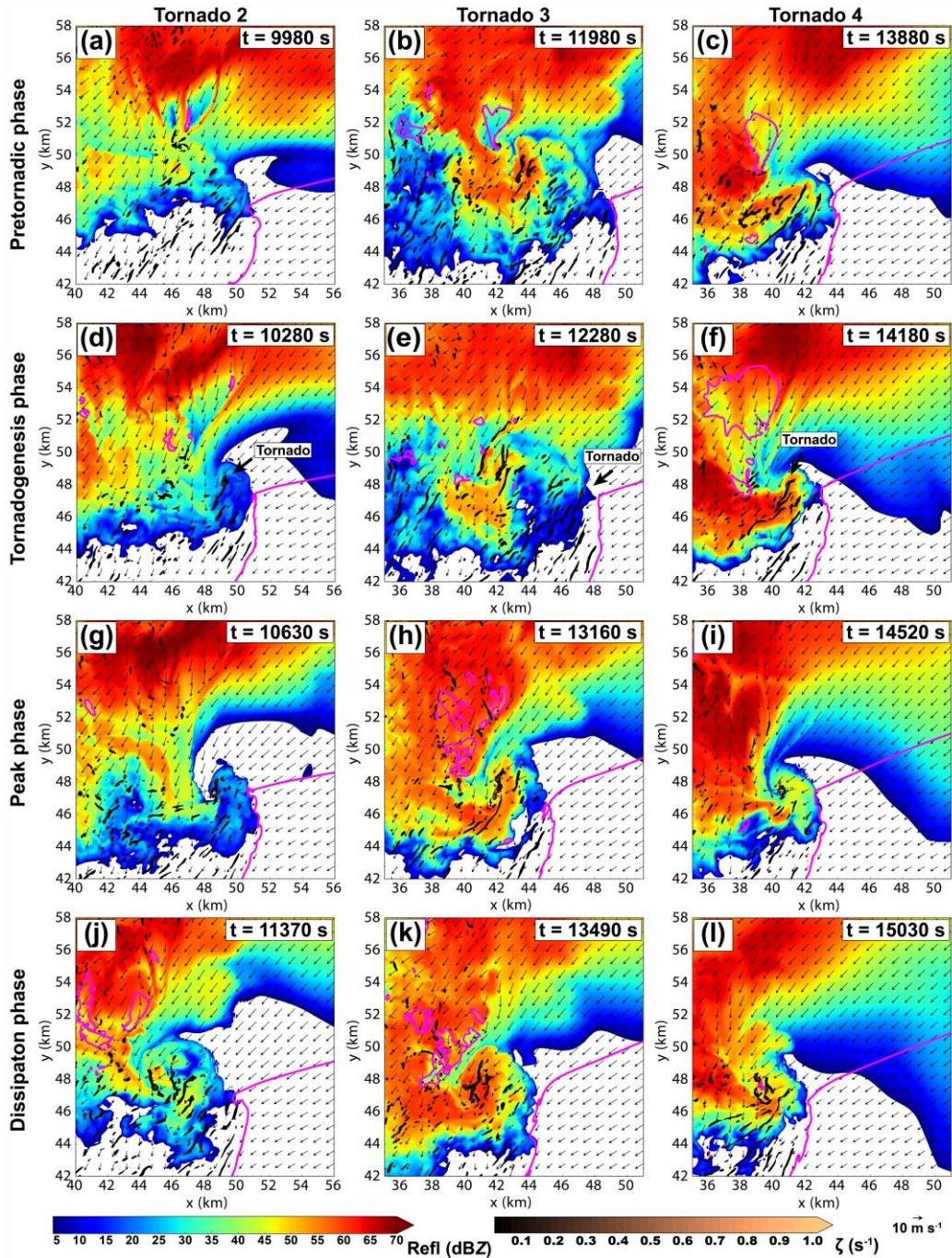


Fig. 3.5. Same as Fig. 3.3, but for tornado 2 (a) 9980 s, (d) 10280 s, (g) 10630 s, and (h) 11370 s; tornado 3 (b) 11980 s, (e) 12280 s, (h) 13160 s, (k) 13490 s; and tornado 4 (c) 13880 s, (c) 14180 s, (c) 14520 s, (c) 15030 s.

In the subsequent 400 s following the dissipation of the third tornado, the lingering low-level mesocyclone finally decays and new low-level updraft intensification and pressure lowering take place below 500 m AGL (Fig. 3.2b,c), resulting in the formation of a new hook echo and a

fourth tornado by 13880 (Figs. 3.5c,f). Fig. 3.2 shows that the tornado forms and grows abruptly similar to the second tornado, growing higher than 3 km and intensifying to EF3 intensity in less than a minute (Fig. 3.4d). Similar to the second and third tornadoes, the fourth tornado also forms and attains its peak intensity (instantaneous V_{hmax} briefly exceeds 95 m s^{-1} at 14520 s) to the west of the RFGF (Fig. 3.5i), thus embedded in heavy precipitation since its genesis. By 15030 s, the tornado also dissipates by moving rearward relative to the storm into the rear-flank high-precipitation core (Fig. 3.5l). Following the decay of the fourth tornado, no additional tornadoes develop in the simulation until the end of model integration (16200 s).

To summarize the overall evolution of the supercell, Table 3.1 shows some statistics of cyclic tornadogenesis. In a radar-based study of cyclic mesocyclogenesis, Beck et al. (2006) determined mesocyclone cycling frequency by adapting the method devised by Burgess et al. (1982), where cycling frequency is defined as the amount of time elapsed between the beginning of the mature phases of subsequent mesocyclones. A mesocyclone was subjectively determined to attain its mature phase when its hook echo became equally divided into updraft and downdraft. In this study, this method is adapted by determining the time elapsed between two tornadogenesis events since, during this phase, the parent low-level mesocyclones are already divided into updrafts and downdrafts, though not necessarily equally divided (analyses of the vertical velocity fields will be presented in the next subsection). Although the first tornado takes over 2 h 10 min to form, subsequent tornadogenesis events occur much more rapidly at later stages. This result is in agreement with Adlerman et al. (1999), who showed that, once a supercell successfully undergoes its first cycle, it develops a structure that is more prone to the formation of new low-level mesocyclones/tornadoes. The average cycling frequency of simulated and observed cyclic supercells in previous studies ranges from a few minutes (6 min; Beck et al. 2006) to more than an

hour (Burgess et al. 1982) because it is highly sensitive to the environment the storm is embedded (Adlerman and Droegemeier 2005), interactions with other storms (Wurman et al. 2007), and model parameters (Adlerman and Droegemeier 2002), thus, varying significantly from storm to storm. The cycling frequency for the simulated supercell in this study fits well in between other simulated and observed supercells, with an average cyclic frequency of 35.2 min.

In spite of the tendency for the supercell to produce tornadoes more frequently with time, not surprisingly perhaps, there is no clear relationship between the intensity and duration of the tornadoes with progressing cycles. This is mainly because the third tornado (the weakest tornado) persists longer than the second and fourth tornadoes. In addition, the two longest-lived tornadoes, tornadoes 1 and 3, take the longest time to attain their peak phases, while tornadoes 2 and 4 attain peak strength rather rapidly (less than 6 min). Furthermore, there is also no clear relationship between cycling progression and the amount of time elapsed from the peak to demise phases of tornadoes, although later tornadoes (tornadoes 3 and 4) do dissipate faster after reaching their peak phases. These differences among cycles seem to be largely influenced by the supercell transition from a classic structure into an HP mode (Fig. 3.5), where, for example, increasing amounts of precipitation and turbulent outflow in the rear-flank of the storm, drastically affect the evolution and interrelationship between successive cycles and individual characteristics of each tornado. Therefore, it becomes evident that the complex evolution of internal storm-scale features has a major effect in determining the ultimate characteristics of cyclic tornadogenesis, as one might expect (Coffer et al. 2017). Such complex storm-scale evolution and their impacts on cyclic tornadogenesis warrant a more detailed assessment.

Table 3.1. Statistics of cyclic tornadogenesis for the 50-m supercell simulation.

Tornado	Duration (min)	Interval from previous cycle (min)	Interval from genesis to peak (min)	Interval from peak to demise (min)	Interval without tornado (min)
Tornado 1	27.1	—	16.1	11.0	—
Tornado 2	18.1	40.7	5.8	12.3	16.6
Tornado 3	20.0	33.4	14.6	5.4	15.3
Tornado 4	14.1	31.6	5.6	8.5	11.6

3.2.2 Low-level storm- and substorm-scale evolution associated with cyclic tornado development

In order to better compare the role of storm- and substorm-scale structures in modulating each tornado cycle in the simulation, a more detailed analysis of key components of the supercell’s low-level structure is now provided. The analysis addresses the four tornadoes (hereafter referred to as tornadoes 1, 2, 3, and 4, respectively), but emphasizes tornado 1 because it denotes the transition of the supercell into its tornadic mode and also because it is the longest lived and strongest of the four tornadoes. Additionally, emphasis is given to the evolution of low-level updrafts and features related to them given their well-known relevance to tornado dynamics (Markowski and Richardson 2014; Coffey and Parker 2017; Coffey et al. 2017; Yokota et al. 2018; Fischer and Dahl 2020; Goldacker and Parker 2021). The focus herein is to inspect how the interaction between low-level updrafts and surrounding storm structures affects the tornadoes throughout their life span and, consequently, clarify the differences between cycles by taking advantage of the high spatiotemporal resolution of the present dataset, as compared previous studies of cyclic supercells (Adlerman et al. 1999; Adlerman and Droegemeier 2002; Dowell and Bluestein 2002a; Beck et al. 2006; French et al. 2008; Betten et al. 2018).

3.2.2.1 Tornado 1

The pretornadic phase of tornado 1 is illustrated in Fig. 3.6 at 7500 s. The 300-s period preceding tornadogenesis will be referred to herein as the pretornadic phase of each tornado⁷. Fig. 3.6a presents the vertical velocity field (w) at 500 m AGL to show the structure of low-level updrafts and downdrafts accompanying the developing tornado. At this stage, a narrow band of the RFD near the tip of the hook and behind the RFGF likely consisting of a small-scale occlusion downdraft (Klemp and Rotunno 1983; Klemp 1987; Markowski 2002) begins to protrude into the south side of the low-level updraft and produce a well-known horseshoe shape or a “divided mesocyclone structure” (Lemon and Doswell 1979; Klemp and Rotunno 1983; Klemp 1987; Markowski 2002; Skinner et al. 2014; Betten et al. 2018). The low-level updraft is initially north-south oriented, containing the strongest and more compact updrafts ($w > 20 \text{ m s}^{-1}$) in the northern portion at the tip of the hook and gentler ascent of southeasterly environmental inflow just east of the hook. At the surface (Fig. 3.6b), in addition to the RFGF, a left-flank convergence boundary (LFCB; Beck and Weiss 2013; Coffey and Parker 2017) separates colder outflow from the storm’s core from cooler air to the east. Also at 500 m AGL, a broad area of storm-relative inflow winds (V_{hSR}) in excess of 25 m s^{-1} flanks the eastern side of the low-level updraft (Fig. 3.6c). The winds in the inflow band enter the updraft directly from the southeast and northeast. This inflow band bears striking resemblance to a radar-sampled northeasterly inflow band northeast of a low-level mesocyclone in a cyclic supercell documented by French et al. (2008). Smaller areas of locally strong V_{hSR} can be seen far northwest of the low-level updraft collocated with dipoles of upward and downward motion, and are located at the leading edge of intense small-scale downdrafts (Figs.

⁷ For tornado 1, specifically, tornadogenesis occurs actually shortly after 7800 s, at 7830 s. The simulated fields are shown every 300 s to provide a more detailed analysis of this tornado.

3.6a) and heterogeneous outflow buoyancy (Figs. 3.6b) near the storm's core. More importantly, the inflow band contains a core of stronger winds ($V_{hSR} > 30 \text{ m s}^{-1}$) 3 km east of the low-level updraft that is collocated with an area of locally lower pressure ($p' < -3 \text{ hPa}$). Fig. 3.6d shows a 3D view of the p' field from the southeast of the hook in which the low pressure area appears as a low-pressure lobe (LPL), extending from the surface upward and connecting to the pretornadic low-level mesocyclone aloft. Collectively, the LPL and broad inflow band represent a 3D manifestation of the well-known inflow low structure typically found in the inflow regions of supercells, where the environmental low-level winds accelerate into the storm producing low pressure via the Bernoulli effect (e.g., Fig. 8.23 on page 221 of Markowski and Richardson 2010). Other high-resolution supercell simulations using 3D visualizations, such as Orf et al. (2017), have also shown LPLs associated with concentrated bands of inflow around low-level updrafts. However, the LPL shown by Orf et al. (2017) lies on the cool side the FFCB and is associated with an streamwise vorticity current (Schueth et al. 2021), unlike the one shown in the present study, which primarily originates in the environment or along the forward-flank reflectivity gradient. Visualizations of the 3D p' field at earlier times (not shown) indicate that the appearance of the LPL antecedes the appearance of the low-level mesocyclone aloft and account for the expanding pressure deficit in the 1-3 km layer AGL seen in the time-height plot (Fig. 3.2b) beginning at 6600 s.

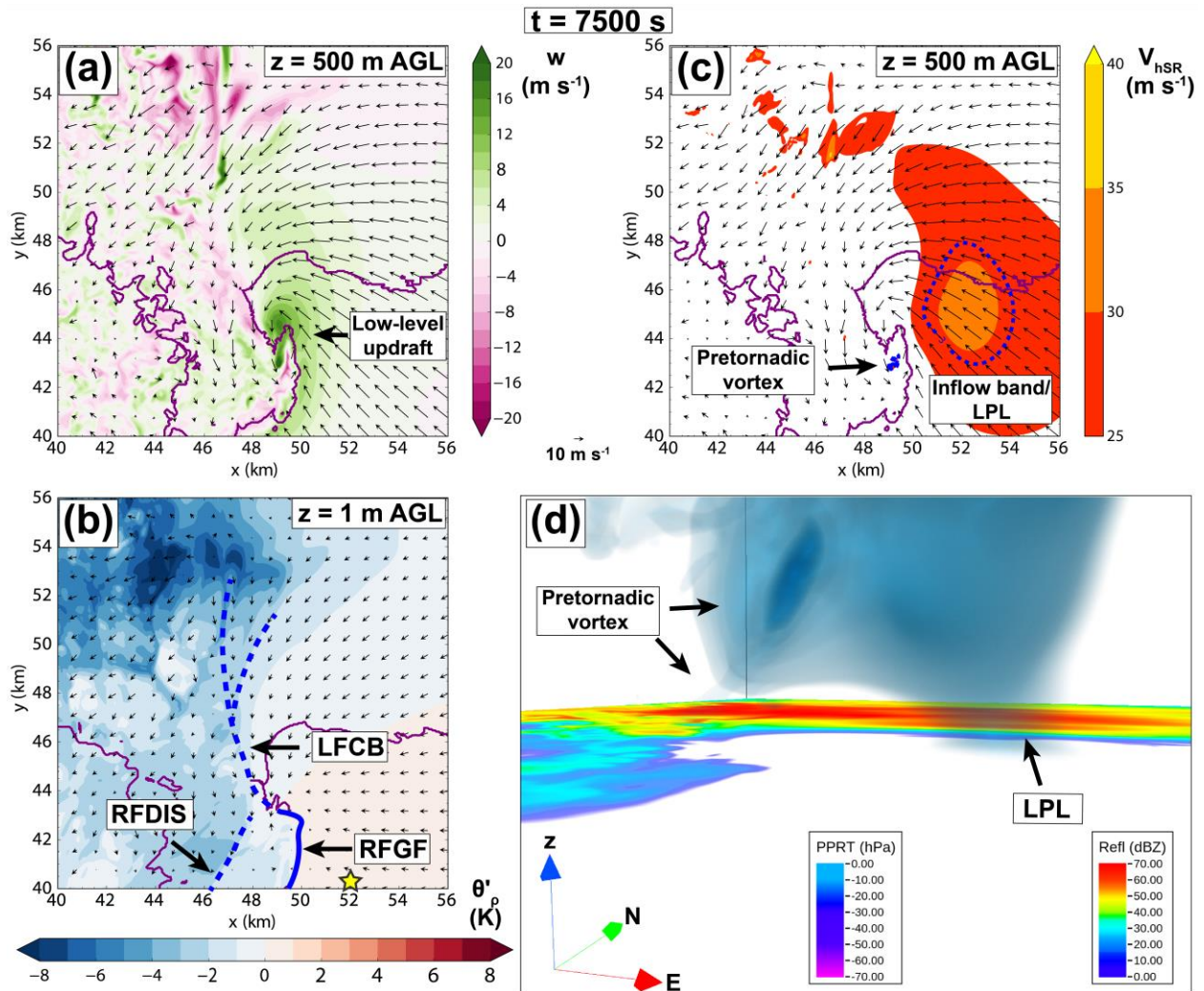


Fig. 3.6. (a) Vertical velocity (shaded; m s^{-1}), (b) density potential temperature perturbation (shaded; K) at 1 m AGL and perturbation pressure (regions shaded in orange for values < -3 hPa to highlight the tornado position, when it is present), (c) storm-relative wind speed at 500 m AGL (shaded; m s^{-1}) and perturbation pressure (hPa; dashed blue contours every 1 hPa, starting at -3 hPa), (d) volume rendered display of perturbation pressure (hPa) for values lower than 2.5 hPa. In (b), the solid blue denotes the RFGF and the dashed blue lines denote internal boundaries. The yellow star denotes the location of the camera in (d) relative to the tornado. In (a) and (c), the winds are storm relative, while in (b) the winds are ground relative. In all fields, the purple contour denotes the 10-dBZ reflectivity contour. All fields valid at 7500 s.

By 7800 s, 30 s before tornadogenesis, the low-level updraft becomes stronger, with $w > 20 \text{ m s}^{-1}$ occupying a larger area at the northern tip of the hook that is bounded by a more protruding occlusion downdraft to its southeast (Fig. 3.7a). The RFD also strengthens to the northwest of the low-level updraft and acquires northwesterly momentum; this configuration demarks the onset of

the hook echo erosion previously shown in Figs. 3.3d and 3.3e. Fig. 3.7b shows that the RFDIS reaches the surface containing higher θ'_p air than the surrounding outflow, suggesting that the RFD is dynamically forced downward from higher altitudes (above 1 AGL) and relatively drier (Nascimento et al. 2014; Skinner et al. 2014; Skinner et al. 2015; Schenkman et al. 2016). As a consequence, the erosion of the hook echo appears to result from hydrometeor evaporation/melting caused by dry air entrainment into the RFD. Considering the RFDIS reached the low-level circulation just around the time of tornadogenesis, it seems reasonable to speculate that strong convergence (not shown) along its leading edge acted to instigate tornadogenesis (Kosiba et al. 2013). Nonetheless, given the steady intensification of the pretornadic low-level updraft well before the arrival of the RFDIS, it appears more likely that the RFDIS might have served as a catalyst to tornadogenesis rather than an instigator in this case. To the east of the low-level updraft, the broad inflow band increases in aerial coverage to the northwest toward the storm's core (Fig. 3.7c). The LPL accompanying the inner core of stronger inflow winds also stretches northwestward, but becomes more concentrated and connects to the low-level mesocyclone within the hook echo. This is also shown in Fig. 3.7d, which also reveals that the LPL becomes stronger but concentrated at higher levels to the northwest of the low-level mesocyclone/incipient tornado.

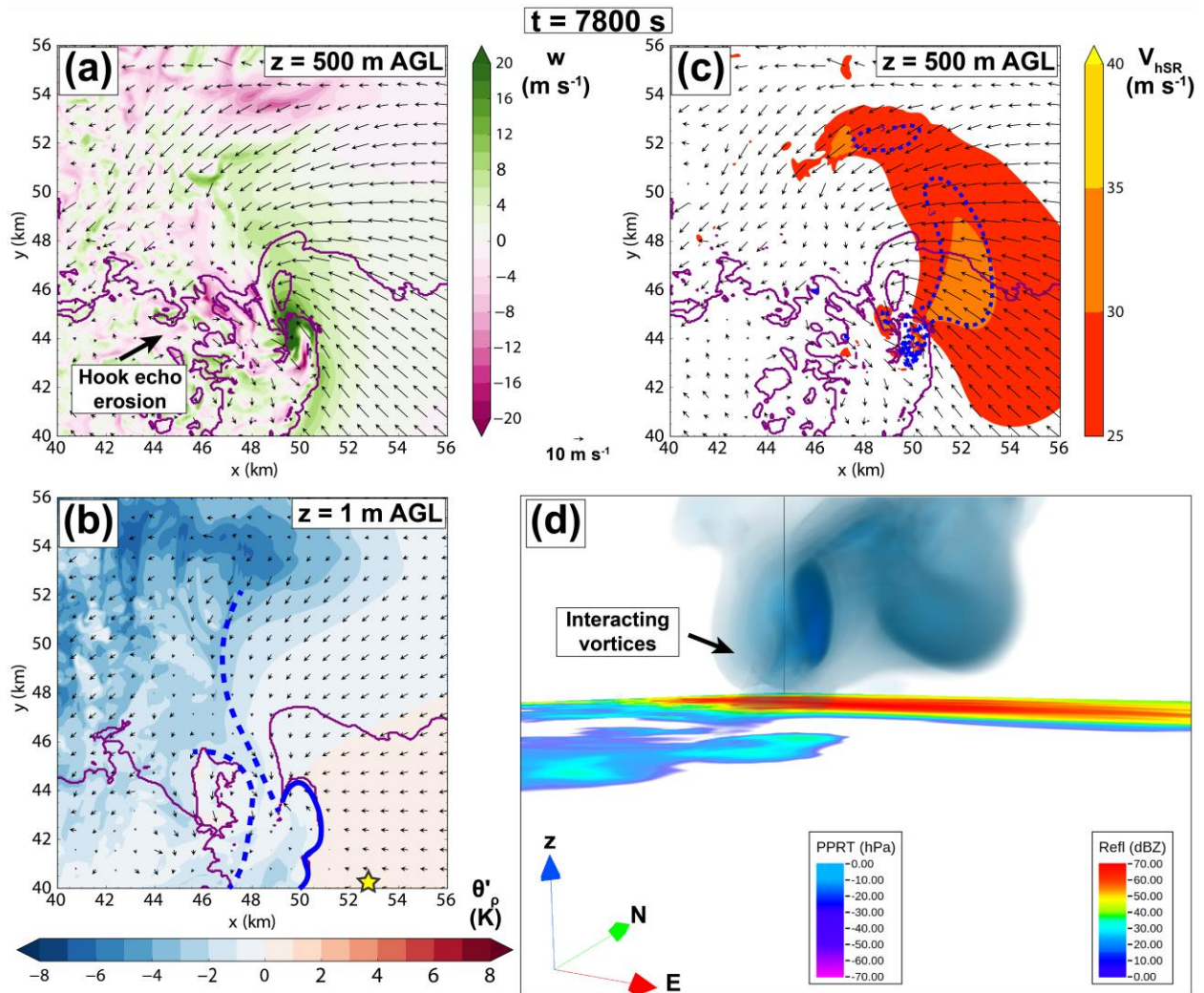


Fig. 3.7. (a) Vertical velocity (shaded; m s^{-1}) at 500 m AGL, (b) density potential temperature perturbation (shaded; K) at 1 m AGL and perturbation pressure (regions shaded in orange for values < -3 hPa to highlight the tornado position, when it is present), (c) storm-relative wind speed at 500 m AGL (shaded; m s^{-1}) and perturbation pressure (hPa; dashed blue contours every 1 hPa, starting at -3 hPa), (d) volume rendered display of perturbation pressure (hPa) for values lower than 2.5 hPa. In (b), the solid blue denotes the RFGF and the dashed blue lines denote internal boundaries. The yellow star denotes the location of the camera in (d) relative to the tornado. In (a) and (c), the winds are storm relative, while in (b) the winds are ground relative. In all fields, the purple contour denotes the 10-dBZ reflectivity contour. All fields valid at 7800 s.

The vortex dynamics leading up to the formation of tornado 1 is rather complex and unsteady. A closer inspection of Fig. 3.6d shows that the intensifying low pressure perturbation attending the pretornadic vortex aloft comprises other vortices revolving around the main axis of the low-level mesocyclone. This evolution is better visualized in the 3D vorticity magnitude field

around the time of tornadogenesis (Fig. 3.7). Several vortices from the rear-flank outflow with a variety of different orientations (main axes denoted by the dashed orange lines) approach and interact with the main pretornadic vortex at the RFGF-FFCB intersection (main axis denoted by the green dashed lines; Fig. 3.7a). The pretornadic vortex, which is highly tilted toward the north (due to rapid forward motion in a ground-relative sense), becomes distorted, disconnects and reconnects with the ground as it intertwines and merges with some of the vortices (Fig. 3.7b,c). As this vortex intertwining process proceeds, the pretornadic vortex eventually congeals into a tornado by 7830 s (Fig. 3.7d). This mode of tornadogenesis involving a highly tilted, fast-moving tornado differs from the more steady vortex accumulation presented by Orf et al. (2017), where a parade of mesocyclones emerges from the SVC at the surface and gradually congeal into a tornado under the low-level updraft in a more organized fashion. In fact, the complex mode of tornadogenesis mode seen in the present simulation shares similarities to the more unsteady genesis mode observed in several tornadoes of the 27 April 2011 tornado outbreak (from which the original sounding is derived), such as the Cullman and Cordova tornadoes, in addition to the Tuscaloosa tornado itself (Knupp et al. 2014).

Following genesis, the tornado begins to move northeastward influenced the RFDIS to its west shortly after undergoing a brief weakening period (Fig. 3.9a; also shown in Fig. 3.4a). At the surface, the tornado, still located at the RFGF-LFCB intersection and far removed from coldest outflow air, ingests air that is neutrally or weakly negatively buoyant ($\theta'_\rho \sim -1$ to 0 K; Fig. 3.9b), a favorable configuration to tornado formation and maintenance (Markowski et al. 2002; Shabbot and Markowski 2006; Grzych et al. 2007; Marquis et al. 2011; Lee et al. 2012; Markowski and Richardson 2014; Marquis et al. 2016; Flournoy et al. 2020). The core of strong inflow winds and

the LPL further intensify and expand, producing a large zone of low pressure that connects with the tornado to the southwest (Fig. 3.9c).

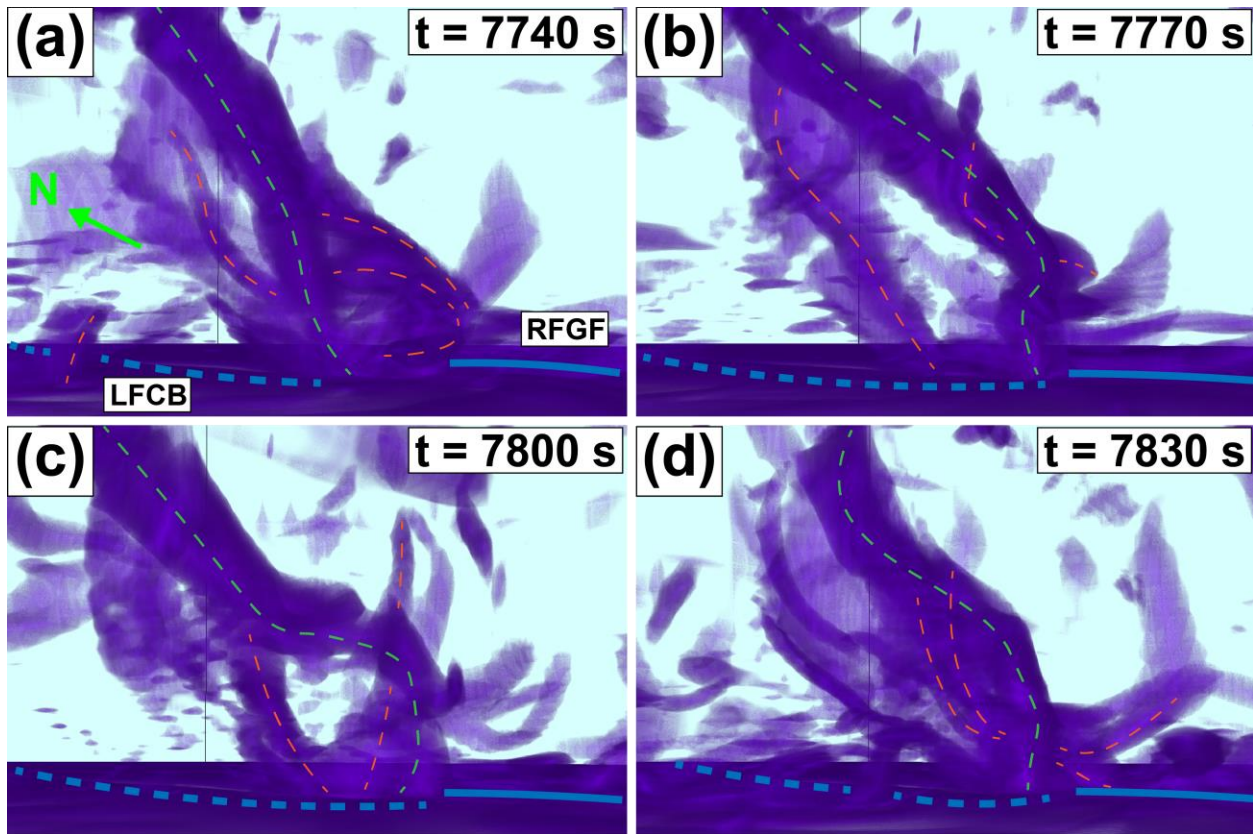


Fig. 3.8. 3D vorticity magnitude field ($> 0.15 \text{ s}^{-1}$), valid at (a) 7740 s, (c) 7770 s, (c) 7800 s, and (d) 7830 s. The green dashed lines denote the axis of the pretornadic vortex, while orange dashed lines denote axis of other vortices that interact with the pretornadic vortex. The solid blue line indicates the subjectively identified RFGF and the dashed blue line denotes the subjectively identified FFCB.

The 3D view presented in Fig. 3.9d shows that the LPL also develops upward to form a tilted deep column downstream of the tornado. Such growth of the LPL results from the intensification of the parent midlevel updraft located 2-3 km northwest of the surface tornado; the evolution of the midlevel updrafts will be explored in more detail in subsection 3.2.4. Fig. 3.9d shows that, at low levels, the tornado is nearly vertically stacked but tilts sharply toward the north and toward the upper portion of the LPL. Animations of the p' field (not shown) show that, in addition to the pronounced northward tilt, the upper portion of the tornado exhibits a spiral

structure during this stage. The presence of this structure together with the strong downdraft near the center of the tornado at 500 m AGL in Fig. 3.9a are characteristic of vortex breakdown aloft due to a downward dynamic perturbation pressure gradient acceleration in the core of the low-level tornado (Church et al. 1979; Rotunno 1979; Pauley and Snow 1988; Lewellen and Lewellen 2007; Fiedler 2009; Dahl 2021). Also in Fig. 3.9d, a small-scale low-pressure tube can be seen attached to the tornado's east side at the surface (also noticeable in Fig. 3.9b). This structure corresponds to an HV beginning to wrap around the tornado circulation. A detailed analysis of HVs will be provided in Chapter 4.

The tornado enters a second period intensification by 8400 s (recall Fig. 3.4a) when its motion shifts from northeastward to northwestward, denoting the onset of the rearward storm-relative motion typical of occluding mesocyclones/tornadoes (Burgess et al. 1982; Adlerman et al. 1999; Dowell and Bluestein 2002b, 2002a; French et al. 2008; Bluestein 2009). From this period on, the low-level updraft “sheds” into two parts that evolve differently, as in the conceptual models of Adlerman and Droegemeier (2000) and Dowell and Bluestein (2002a, 2002b). One of the low-level updrafts is associated with the occluded tornadic circulation and will hereafter be referred to as an *occlusion updraft* following Betten et al. (2018), while the other portion of the updraft, which is weaker, remains attached to the RFGF to the southeast of the tornado, hereafter referred to as *RFGF updraft*. The occlusion is better illustrated in Fig. 3.10b, which shows that the tornado shifts to a position ~ 0.5 km northwest of the RFGF-FFCB intersection. Despite the occlusion, θ_ρ perturbations surrounding the tornado remain small ($-1 \text{ K} < \theta'_\rho < 0 \text{ K}$). Figs. 3.10c and 3.10d show that the inflow band and LPL intensify in a narrow zone just north-northeast of the tornado as a response to the strong occlusion updraft suggesting the upward mass flux associated with the

occlusion updraft becomes rather substantial. Interestingly, another HV encircles the near-ground sector northeast of the tornado, a situation also seen in observed tornadoes (Houser et al. 2016).

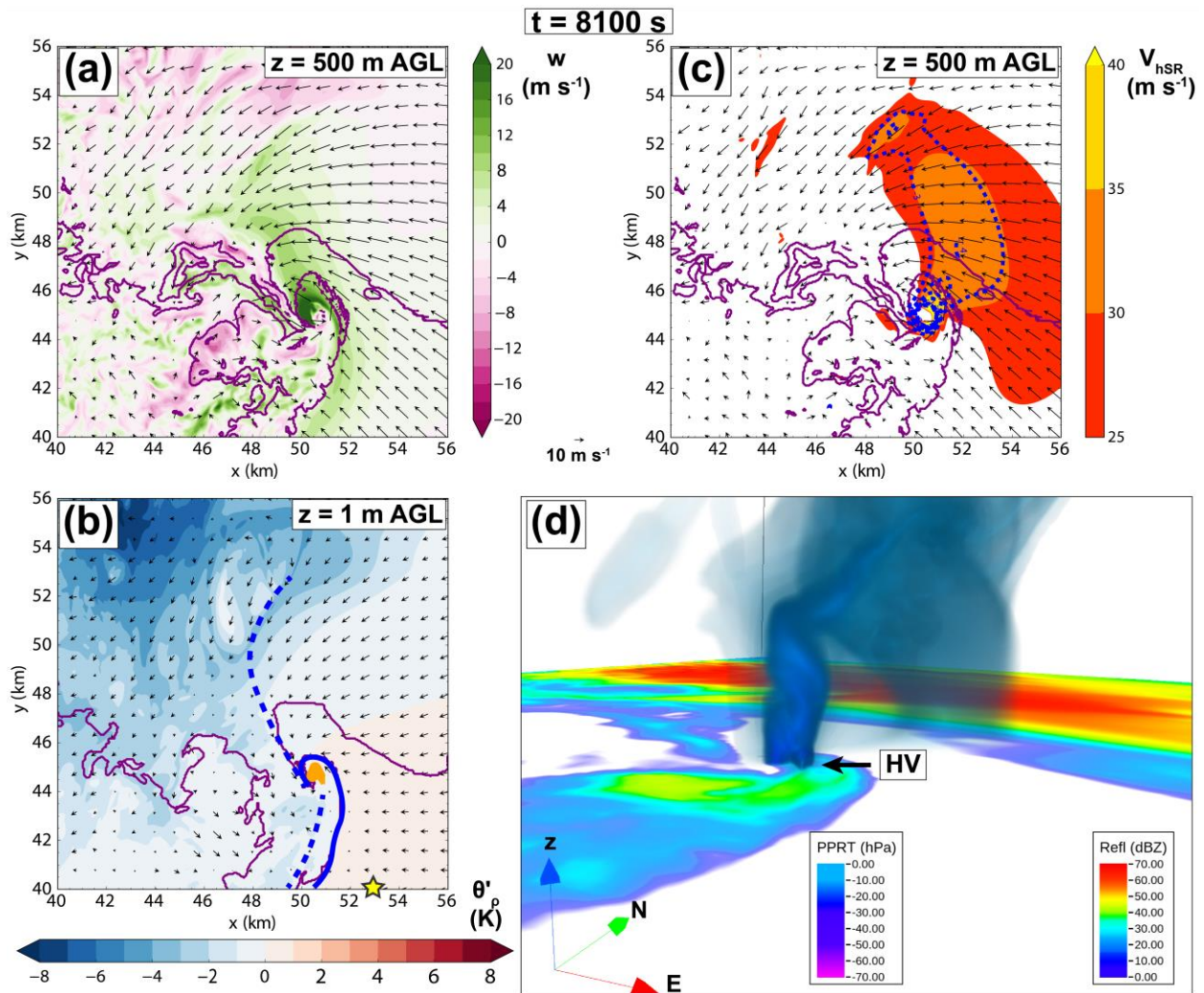


Fig. 3.9. (a) Vertical velocity (shaded; m s⁻¹) at 500 m AGL, (b) density potential temperature perturbation (shaded; K) at 1 m AGL and perturbation pressure (regions shaded in orange for values < -3 hPa to highlight the tornado position, when it is present), (c) storm-relative wind speed at 500 m AGL (shaded; m s⁻¹) and perturbation pressure (hPa; dashed blue contours every 1 hPa, starting at -3 hPa), (d) volume rendered display of perturbation pressure (hPa) for values lower than 2.5 hPa. In (b), the solid blue denotes the RFGF and the dashed blue lines denote internal boundaries. The yellow star denotes the location of the camera in (d) relative to the tornado. In (a) and (c), the winds are storm relative, while in (b) the winds are ground relative. In all fields, the purple contour denotes the 10-dBZ reflectivity contour. All fields valid at 8100 s.

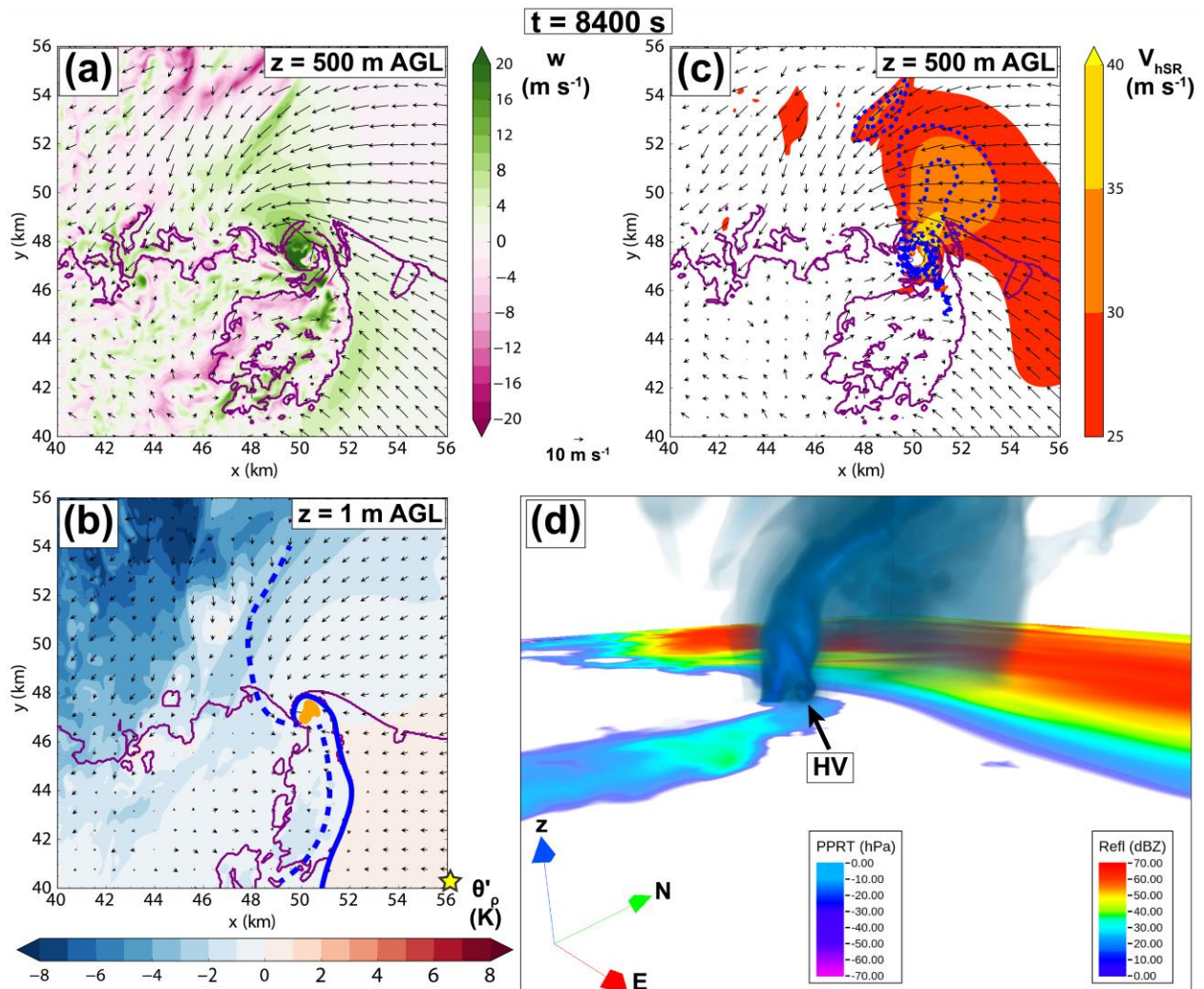


Fig. 3.10. (a) Vertical velocity (shaded; m s⁻¹) at 500 m AGL, (b) density potential temperature perturbation (shaded; K) at 1 m AGL and perturbation pressure (regions shaded in orange for values < -3 hPa to highlight the tornado position, when it is present), (c) storm-relative wind speed at 500 m AGL (shaded; m s⁻¹) and perturbation pressure (hPa; dashed blue contours every 1 hPa, starting at -3 hPa), (d) volume rendered display of perturbation pressure (hPa) for values lower than 2.5 hPa. In (b), the solid blue denotes the RFGF and the dashed blue lines denote internal boundaries. The yellow star denotes the location of the camera in (d) relative to the tornado. In (a) and (c), the winds are storm relative, while in (b) the winds are ground relative. In all fields, the purple contour denotes the 10-dBZ reflectivity contour. All fields valid at 8400 s.

At 8700 s, the tornado is nearing its peak phase as shown in Fig. 3.4a. Unlike previous times when the tornado was capped by a strong downdraft aloft, its structure at 500 m AGL is almost entirely dominated by a strong, compact updraft situated directly above the surface tornado (Figs. 3.11a,b). Indeed, during this phase, the tornado evolves into a deep coherent vortex (Fig. 3.11d) consistent with the time-height plot (Fig. 3.2b) that gradually tilts to the north into the low pressure area under the parent midlevel updraft/mesocyclone. The continuous rearward storm-relative motion of the tornado places it closer to the coldest portion of the rear-flank outflow, with another RFDIS and new hook echo wrapping around its south sector, though colder outflow does not feed into the tornado yet (Fig. 3.11b). Previous studies attribute tornado/mesocyclone intensification and deepening following the occlusion process, such as in tornado 1, to enhancement of vertical vorticity stretching under a deep low-to-midlevel updraft (Adlerman et al. 1999; Betten et al. 2018) and to “blocking” of low angular momentum warm-sector air out of the low-level circulation (Markowski et al. 2012b; Markowski et al. 2012a). The increasing separation between the occlusion and RFGF updrafts also reflects in the characteristics of the inflow features. Figs. 3.11c and 3.11d show a nearly complete detachment of the LPL (now located along the forward-flank reflectivity gradient) from the tornado coupled with a dramatic weakening of the storm-relative inflow in the same region. This suggests that the upward mass flux is becoming more concentrated in the contracting tornado itself.

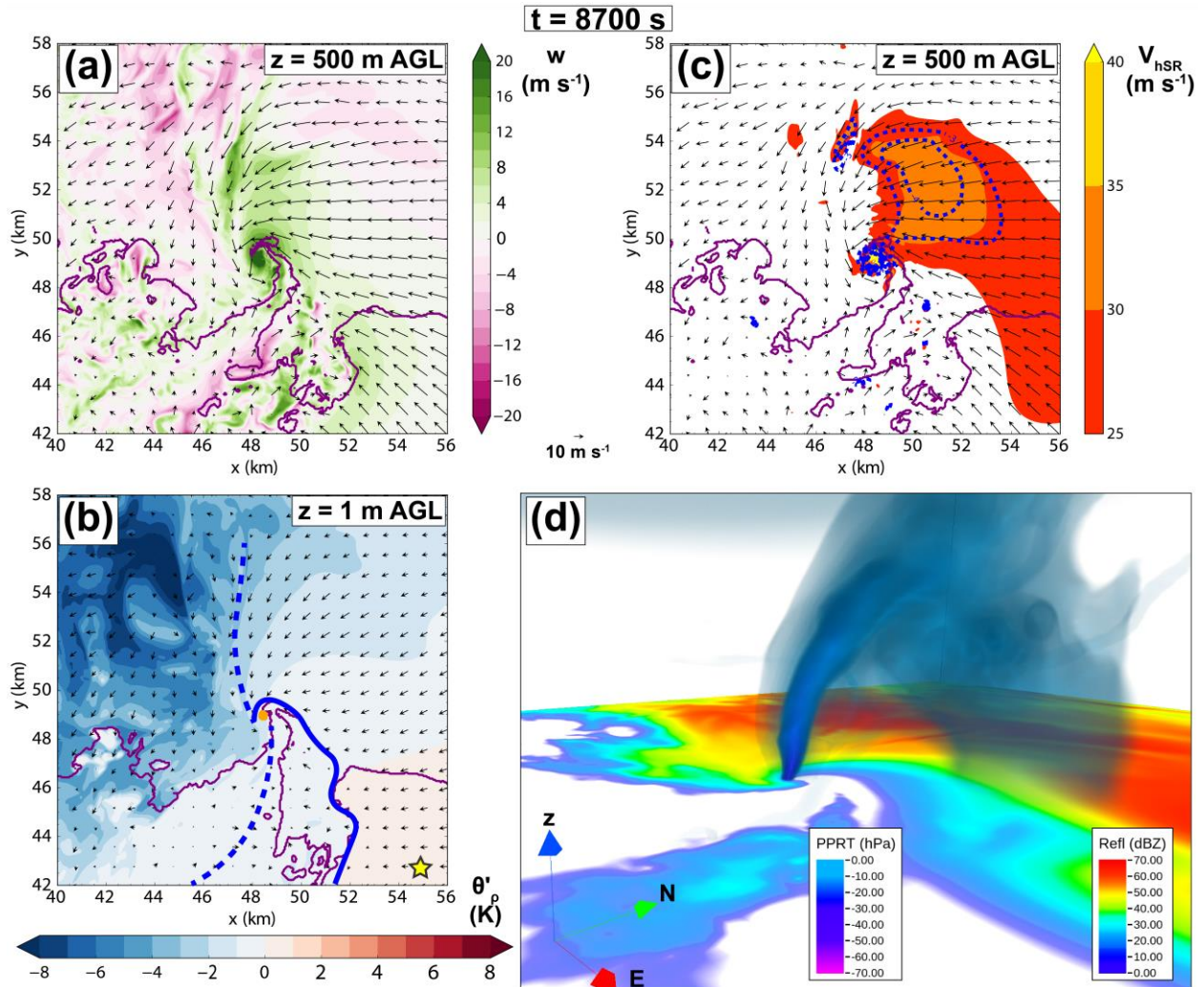


Fig. 3.11. (a) Vertical velocity (shaded; m s⁻¹) at 500 m AGL, (b) density potential temperature perturbation (shaded; K) at 1 m AGL and perturbation pressure (regions shaded in orange for values < -3 hPa to highlight the tornado position, when it is present), (c) storm-relative wind speed at 500 m AGL (shaded; m s⁻¹) and perturbation pressure (hPa; dashed blue contours every 1 hPa, starting at -3 hPa), (d) volume rendered display of perturbation pressure (hPa) for values lower than 2.5 hPa. In (b), the solid blue denotes the RFGF and the dashed blue lines denote internal boundaries. The yellow star denotes the location of the camera in (d) relative to the tornado. In (a) and (c), the winds are storm relative, while in (b) the winds are ground relative. In all fields, the purple contour denotes the 10-dBZ reflectivity contour. All fields valid at 8700 s.

Key changes in the supercell's low-level structure occur after the peak phase of the tornado.

Fig. 3.12a shows that the tornado becomes overtaken by an occlusion downdraft at 500 m AGL accompanying the cold ($\theta'_p < -4$ K) surface RFDIS, which finally impinges on the west and south

sides of the tornado (Fig. 3.12b). A new hook echo, previously shown in Figs. 3.3g-i (and later associated with tornado 2), forms in association with the gradual expansion and intensification of the RFGF updraft. The inflow band core and LPL shrink in size, detaching completely from the tornado (Figs. 3.12c,d). In turn, new zones of strong inflow begin to form approximately 6 km east of the tornado. Fig. 3.12d also reveals that the tornado, although still deep and strong at the surface (Fig. 3.4a), becomes highly tilted to the west near the surface and toward the north above aloft. By 9300 s, the tornado becomes mostly embedded in downdraft and cold outflow (Figs. 3.13a,b). Undulations along the vortex and increasing northward tilt (Fig. 3.13d) denote the “rope out” stage of the tornado, which retains considerably high (EF2) winds at the surface (Fig. 3.4a). While the tornado decays, the RFGF updraft continues to gradually expand and intensify, occupying the inflow notch area east of the incipient hook echo with $w > 8 \text{ m s}^{-1}$. With the ongoing demise of the occlusion updraft, the inflow band core east of the hook and low-level updraft broadens and becomes collocated with a new LPL (Figs. 3.13c,d). The morphology of the LPL is quite similar to the original LPL associated with tornado 1. A separate nearly horizontal tube-like structure is also observed in Fig. 3.13d just above, but not fully attached to the LPL; this feature is associated with the new midlevel mesocyclone. The development of the low-level updraft downstream of the old occlusion updraft accompanied by a new midlevel mesocyclone, inflow band, LPL, and hook conform well to long-established conceptual models of occluding cyclic tornadogenesis (Burgess et al. 1982; Adlerman et al. 1999; Dowell and Bluestein 2002a, 2002b; Adlerman and Droegemeier 2005; Beck et al. 2006).

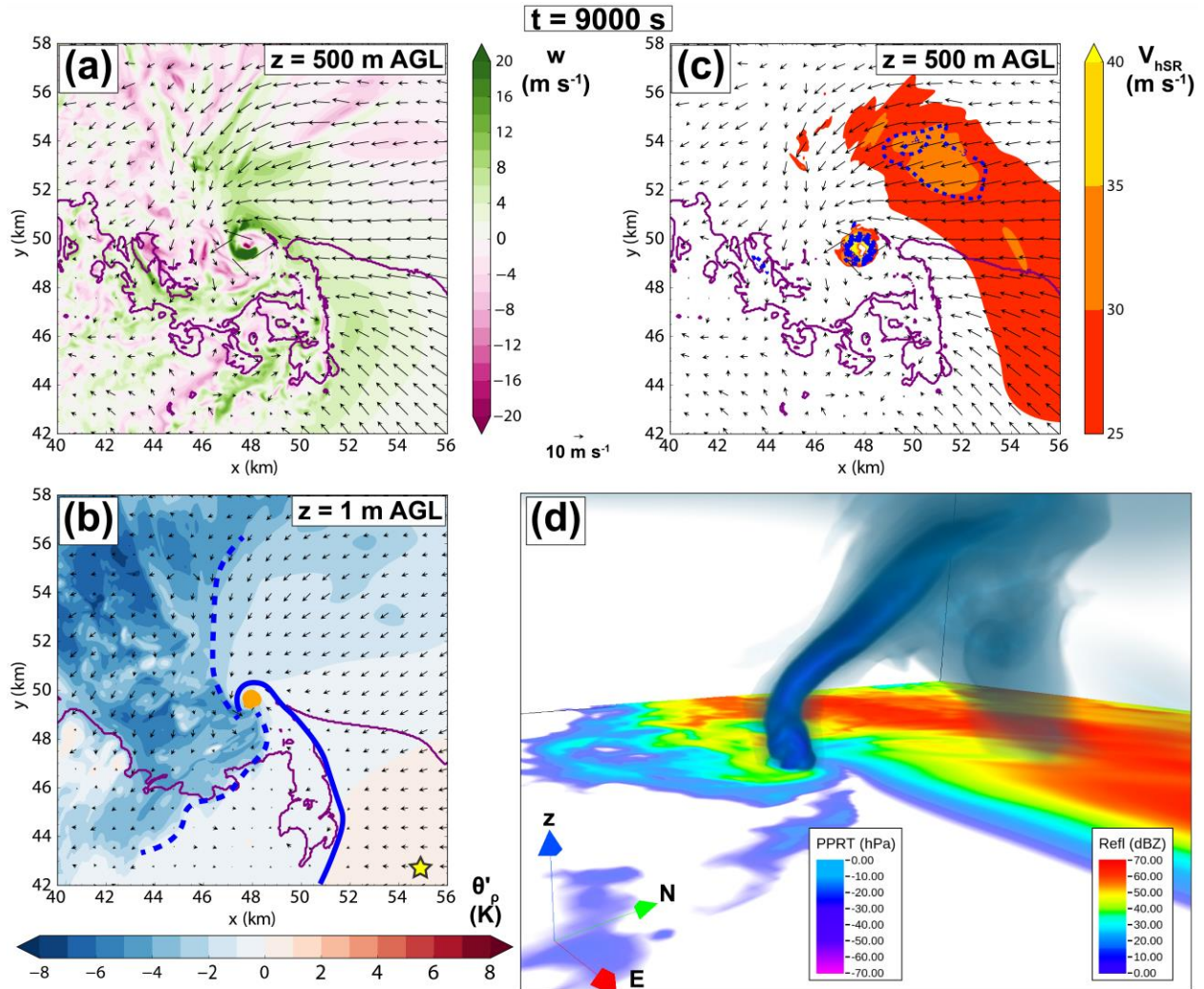


Fig. 3.12. (a) Vertical velocity (shaded; m s^{-1}) at 500 m AGL, (b) density potential temperature perturbation (shaded; K) at 1 m AGL and perturbation pressure (regions shaded in orange for values < -3 hPa to highlight the tornado position, when it is present), (c) storm-relative wind speed at 500 m AGL (shaded; m s^{-1}) and perturbation pressure (hPa; dashed blue contours every 1 hPa, starting at -3 hPa), (d) volume rendered display of perturbation pressure (hPa) for values lower than 2.5 hPa. In (b), the solid blue denotes the RFGF and the dashed blue lines denote internal boundaries. The yellow star denotes the location of the camera in (d) relative to the tornado. In (a) and (c), the winds are storm relative, while in (b) the winds are ground relative. In all fields, the purple contour denotes the 10-dBZ reflectivity contour. All fields valid at 9000 s.

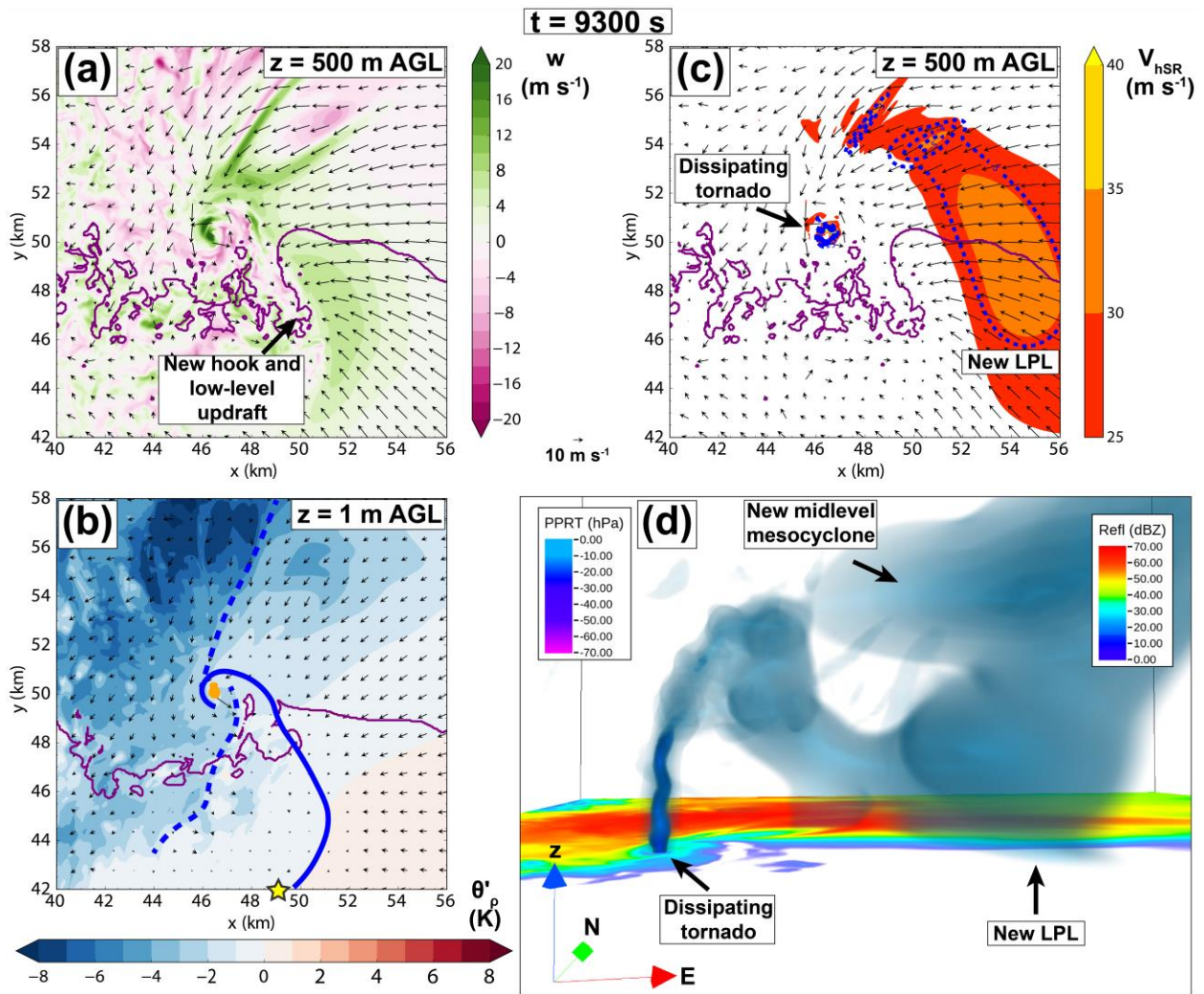


Fig. 3.13. (a) Vertical velocity (shaded; m s^{-1}) at 500 m AGL, (b) density potential temperature perturbation (shaded; K) at 1 m AGL and perturbation pressure (regions shaded in orange for values < -3 hPa to highlight the tornado position, when it is present), (c) storm-relative wind speed at 500 m AGL (shaded; m s^{-1}) and perturbation pressure (hPa; dashed blue contours every 1 hPa, starting at -3 hPa), (d) volume rendered display of perturbation pressure (hPa) for values lower than 2.5 hPa. In (b), the solid blue denotes the RFGF and the dashed blue lines denote internal boundaries. The yellow star denotes the location of the camera in (d) relative to the tornado. In (a) and (c), the winds are storm relative, while in (b) the winds are ground relative. In all fields, the purple contour denotes the 10-dBZ reflectivity contour. All fields valid at 9300 s.

3.2.2.2 Tornadoes 2, 3, and 4

Overall, the cycling tendency of tornadoes 2, 3, and 4 is similar to that of tornado 1 in terms of the conceptual models of cyclic supercells (i.e., they all exhibit regeneration of hook echoes east-northeast of old ones, low-level updraft shedding and occlusion of low-level circulation). However, the individual characteristics of each of these features differs remarkably between each cycle, thus, resulting in rather different tornado characteristics.

Similar to tornado 1, the pretornadic stage of each tornado exhibits a well-defined horseshoe updraft at 500 m AGL located in the inflow notch east-northeast of the hook (Figs. 3.14a-c). The low-level updrafts of each tornado all form to the east southeast of the previous tornado's location, similar to the cycling mode of tornado 1. Yet, low-level updraft differences between the subsequent tornadoes to tornado 1 are notable and result mainly from the large amount of precipitation and RFD outflow in the hook region due to the later HP character of the supercell (Figs. 3.15a-c; Figs. 3.3 and 3.5a-c). Tornadoes 2 and 4, i.e., the ones which form and deepen most rapidly (Figs. 3.14a and 3.14c; also Fig. 3.2), have weaker maximum low-level updrafts ($w \sim 12$ and $w \sim 10 \text{ m s}^{-1}$, respectively) than tornado 1 during the pretornadic phase. In addition, there is no indication of small-scale occlusion downdrafts related to incipient vortices at 500 m AGL. In turn, the core of the 500-m AGL updraft of tornado 3 (near $x = 48 \text{ km}$, $y = 49 \text{ km}$) lies just west of the 10-dBZ reflectivity contour and at the leading edge of an RFDIS associated with the outflow-dominated circulation of tornado 2 (Figs. 3.14b and 3.14j). Of the four tornadoes, tornado 3 is the only directly one affected by a circulation from a previous cycle. At the surface (Figs. 3.15a-c), θ_p deficits are as small as those for tornado 1, within -1 K and 0 K under the pretornadic low-levels updrafts; in the same context, θ'_p gradients are also weak in the northeast inflow into the low-level updrafts, generally smaller than -1 K km^{-1} . Such conditions may indeed facilitate the ongoing

intensification of the pretornadic low-level updrafts, as they may be in a “Goldilocks” regime, where θ_ρ deficits are small enough so that air parcels retain large buoyancy and small, but not negligible baroclinic generation of horizontal vorticity (Markowski and Richardson 2009). During genesis, all three tornadoes form in an occlusion updraft accompanied by occlusion downdrafts, thus, detached to the west from the RFGF-FFCB intersection (Figs. 3.14d-f and 3.15c-d). This situation does not imply that the tornadoes develop surrounded by RFD, though; indeed, tornado 2 is the one mostly surrounded by downdraft, including the occlusion downdraft to its east-southeast and the broader RFD just to the west. Tornadoes 3 and 4 are mostly embedded in updrafts, both associated with the parent occlusion updrafts and updrafts bands due to RFDIS in their vicinity. In spite of the differences in the low-level updrafts and downdrafts, tornadoes 2 and 4 begin to ingest some cooler air to their east ($\theta'_\rho < -2$ K) that is enveloped in the hook; θ'_ρ gradients also increase slightly to the northeast. On the other hand, the scenario for tornado 3 is quite similar to its pretornadic phase, without a notable θ'_ρ hook or any other feature that is deviant from the previous phase, partly due to the smaller and weaker character of developing tornado 3 not significantly influencing the neighboring storm structures. During both the pretornadic and tornadogenesis phases of the three tornadoes, the coldest portion of the outflow remained favorably far west of the developing tornadoes as for tornado 1 and in agreement with the results of Flournoy et al. (2020).

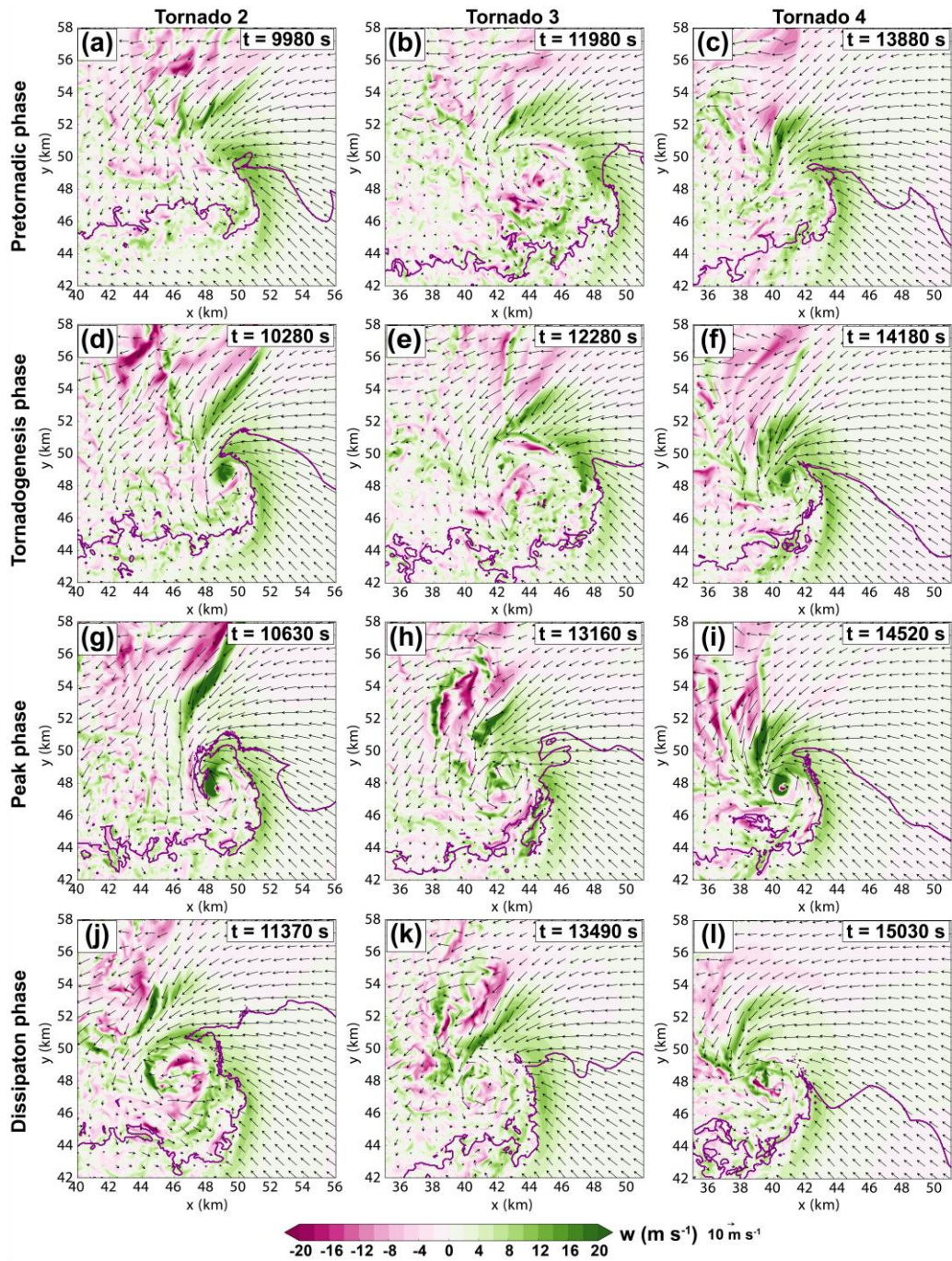


Fig. 3.14. Vertical velocity (shaded; m s^{-1}), but for tornado 2 (a) 9980 s, (d) 10280 s, (g) 10630 s, and (h) 11370 s; tornado 3 (b) 11980 s, (e) 12280 s, (h) 13160 s, (k) 13490 s; and tornado 4 (c) 13880 s, (c) 14180 s, (c) 14520 s, (c) 15030 s.

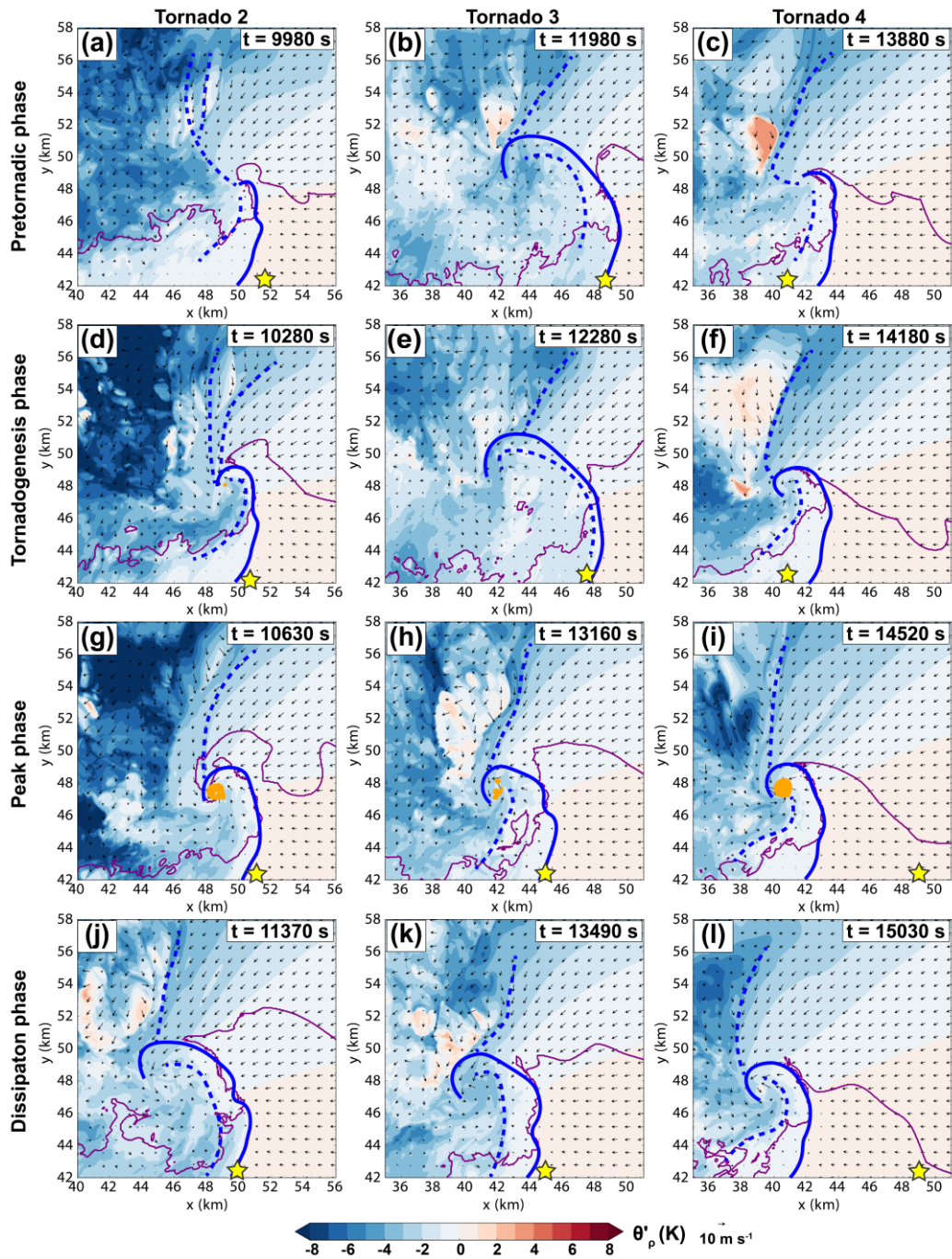


Fig. 3.15. Density potential temperature perturbation (shaded; K), but for tornado 2 (a) 9980 s, (d) 10280 s, (g) 10630 s, and (h) 11370 s; tornado 3 (b) 11980 s, (e) 12280 s, (h) 13160 s, (k) 13490 s; and tornado 4 (c) 13880 s, (c) 14180 s, (c) 14520 s, (c) 15030 s.

During the peak phase of the three tornadoes, the RFGF surges eastward and northward leading up to an increased separation between the occlusion updraft and RFGF updrafts (Figs. 3.15g-i). Such separation (or shedding) is equivalent or slightly smaller than that observed during the peak phase of tornado 1, which was attained well after the occlusion and when the tornado began to become embedded in precipitation near the core of the storm (Figs. 3.3f, 3.11a and 3.11b). Tornadoes 2 and 4 are able to maintain strong, organized occlusion updrafts (even containing strong central downdrafts) as they move rearward into the outflow (Figs. 3.14g and 3.14i); tornado 3, on the other hand, is advected into the chaotic outflow-dominated circulation of tornado 2 by the strong easterly storm-relative flow at the northern part of the low-level updraft (Figs. 3.14h). Despite moving deeper into the precipitating core of the supercell, the rain-cooled air ingested by the three tornadoes is not particularly cold, with within $\theta'_p \sim -3$ K to -2 K (Figs. 3.15g and 3.15i). The θ'_p gradients also do not increase significantly for tornadoes 2 and 4, but increase notably for tornado 3, reaching ~ -2 K km⁻¹ just north of the tornado (Fig. 3.15h), implying a more important role of baroclinic vorticity generation for tornado 3 at peak stage. Similar to tornado 1, the later tornadoes reach their demise when removed several kilometers from the RFGF and into the colder rear-flank outflow (Figs. 3.14j-l). Dissipation of tornado 2 occurs when it is overtaken by the heavy precipitation and downdrafts/divergence in the hook (Fig. 3.14j), decaying into a broad, persistent circulation which later “ingests” tornado 3, facilitating its decay in colder air, in turn (Figs. 3.14k and 3.15k), as previously described. The dissipation of tornado 4 resembles more that of tornado 1, where the tornado simply moves farther rearward into the colder outflow, leaving behind a reorganizing RFGF updraft for the next tornado cycle (Figs. 3.14l and 3.15l).

Similar to the tornado 1, the subsequent tornadoes are each preceded by a broad inflow band collocated with an LPL bounding the low-level updraft to the east-northeast, despite not

having a pretornadic vortex to their southwest at this stage (Fig. 3.16). The pretornadic inflow bands and LPLs of tornadoes 2 and 4 bear remarkable resemblance, while exhibiting the strongest winds ($V_{hSR} > 35 \text{ m s}^{-1}$) and low pressure ($p' < -6 \text{ hPa}$) at 500 m AGL, although the LPL of tornado 2 occupies more of its inflow core area (Figs. 3.16a and 3.16c). The 3D view provided in Figs. 3.17a and 3.17c show that the pretornadic LPLs of tornadoes 2 and 4 are also broader and deeper than that of tornado 1. The pretornadic inflow band and LPL of tornado 3 are much weaker than both tornadoes 2 and 4, but larger than tornado 1 (Figs. 3.16b and 3.17b). Other low- p' structures can also be seen in Figs. 3.17a-c for each tornado and correspond to their midlevel mesocyclones. As for tornado 1, the inflow band of each of the later tornadoes exceeds $V_{hSR} > 35 \text{ m s}^{-1}$ (even $> 40 \text{ m s}^{-1}$ for tornado 4) and encircle the west side of the developing tornadoes (Figs. 3.16d-f); this evolution is more noticeable for tornadoes 3 and 4, while for tornado 2 the core of high winds barely changes and the LPL weakens slightly (Figs. 3.16e). These differences in the LPLs are also visualized in Figs. 3.17d-f. The three tornadoes form well to the southwest of the LPL and exhibit a northward tilt toward the core of the LPL aloft, similar to tornado 1.

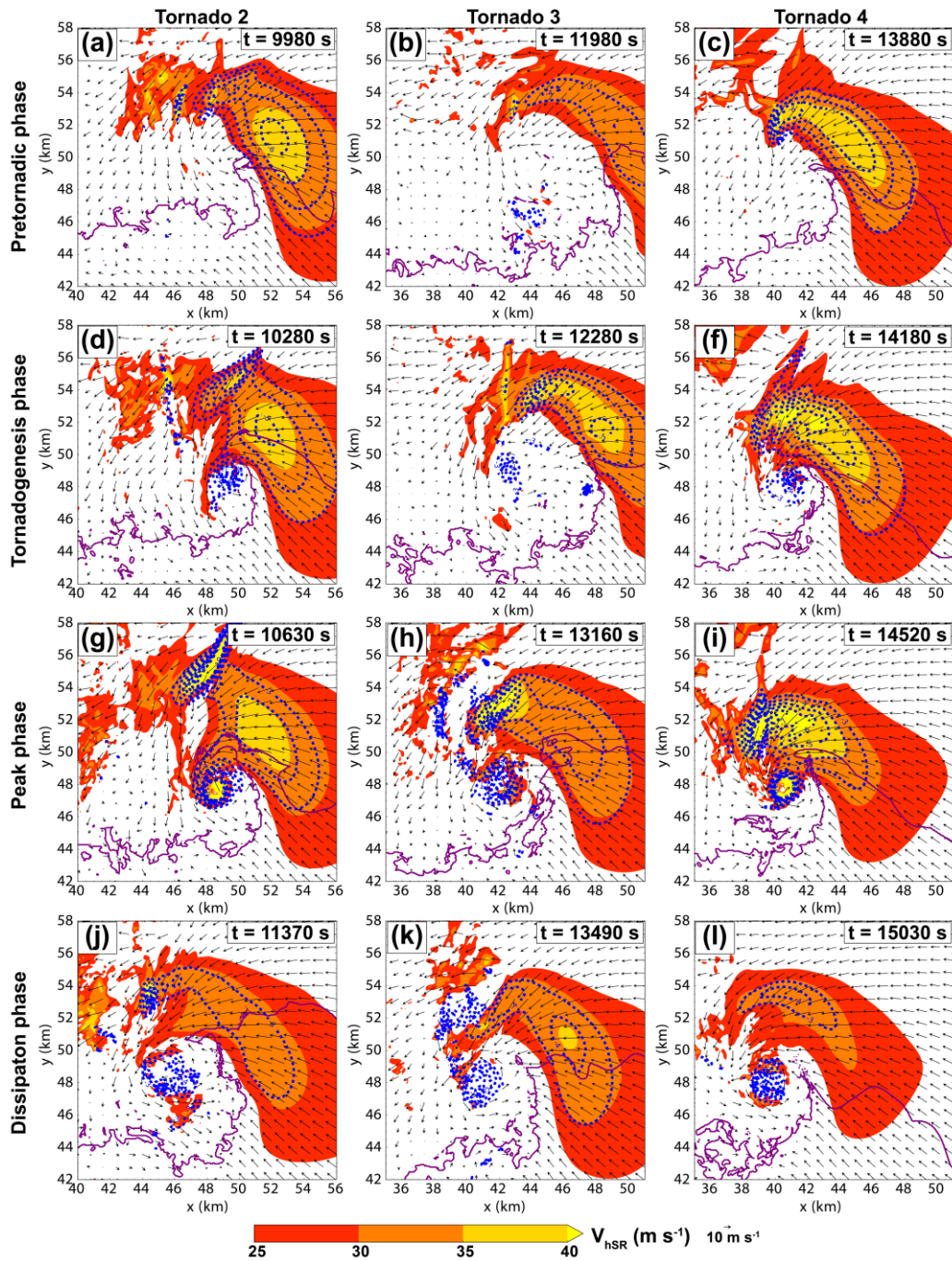


Fig. 3.16. Storm-relative wind speed (shaded; $m s^{-1}$), but for tornado 2 (a) 9980 s, (d) 10280 s, (g) 10630 s, and (h) 11370 s; tornado 3 (b) 11980 s, (e) 12280 s, (h) 13160 s, (k) 13490 s; and tornado 4 (c) 13880 s, (c) 14180 s, (c) 14520 s, (c) 15030 s.

During the peak phase, the process of detachment from the inflow band and LPL is underway for each tornado, again, similar to tornado 1 (Figs. 3.16g-i and 3.17g-i). The process is more noticeable in tornadoes 2 and 3 (Figs. 3.16g,h and 3.17g,h) which move further rearward and away from the core of high inflow winds and into the cold pool. Upon becoming encircled by precipitation, the tilt of the tornado toward the north increases considerably. The top portions of tornadoes 2 and 4 remain attached to the LPL aloft (Figs. 3.17g and 3.17i), while tornado 3 fully separates from its parent LPL and merges with other low pressure features within the turbulent outflow-dominated circulation of tornado 2 (Figs. 3.17h). This separation trend persists until the dissipation phase when the original inflow band core and LPL of each tornado weakens and is located more than 6 km to the east-northeast of the decaying tornadoes (Figs. 3.16j-i). The only inflow band that shows signs of re-intensification for the next cycle is that of tornado 3 since the next cycle occurs much more rapidly than the previous one (Figs. 3.16k). Still, all tornadoes leave a residual LPL to the east of their previous position under a separate low pressure area associated with a new midlevel, which will be the precursor of the next tornado cycle. Unlike tornado 1, later tornadoes do not decay through a “rope out” process. Rather, the tornadoes tend to dissipate while interacting with other turbulent vortices in the rear-flank outflow, occasionally displaying a multiple-vortex structure. Such mode of tornado dissipation was also reported in the high-resolution simulation of Orf et al. (2017)

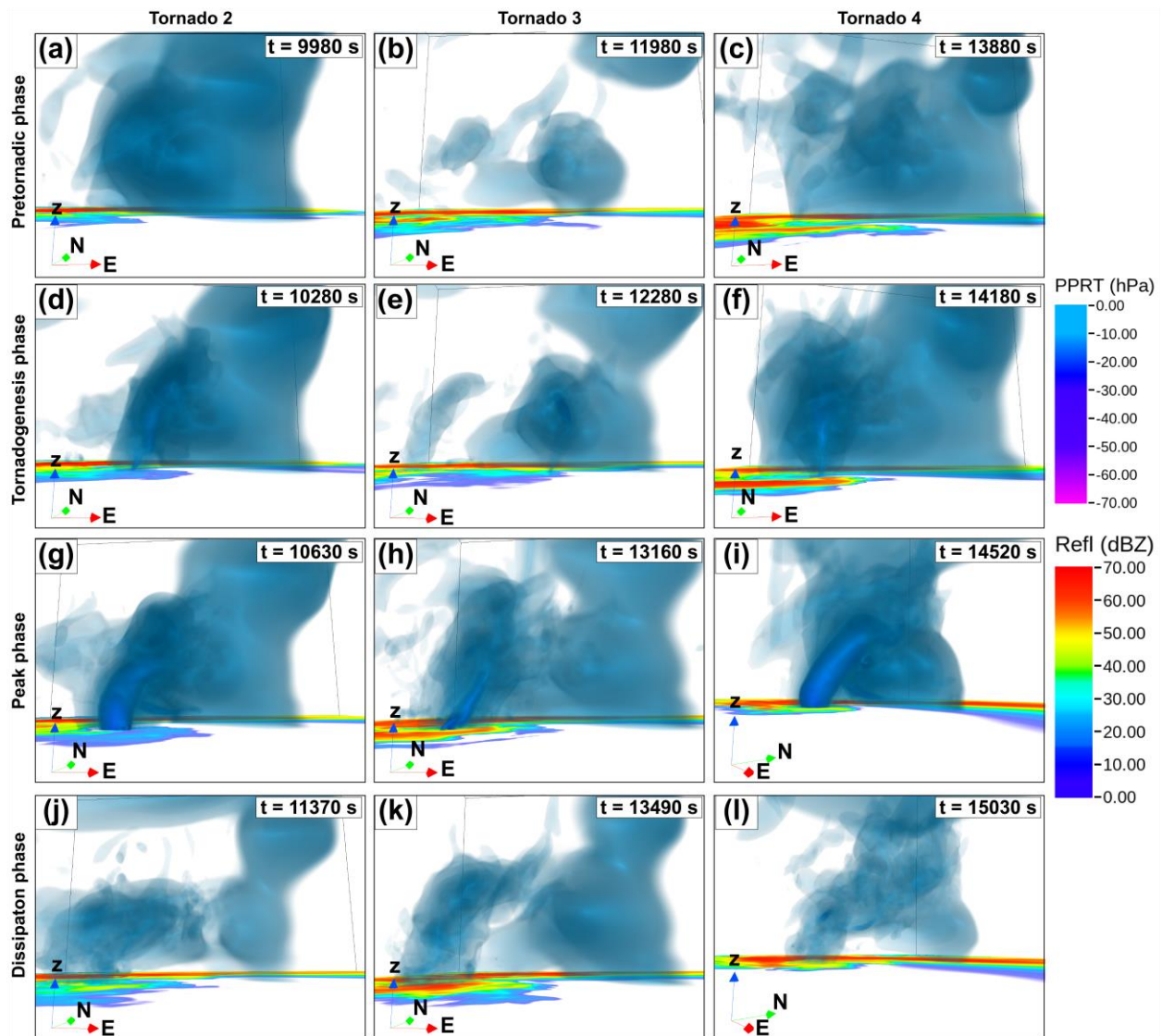


Fig. 3.17. Perturbation pressure (hPa; shaded for values less than -2.5 hPa), but for tornado 2 (a) 9980 s, (d) 10280 s, (g) 10630 s, and (h) 11370 s; tornado 3 (b) 11980 s, (e) 12280 s, (h) 13160 s, (k) 13490 s; and tornado 4 (c) 13880 s, (f) 14180 s, (i) 14520 s, (l) 15030 s.

3.2.3 Relationship between tornado cycling and the nearby low-level inflow vorticity field

So far, it has been shown that each cycle of the tornadic supercell is associated with a band of enhanced low-level inflow winds to the east of and into the storm's updraft accompanied by an LPL. These features undergo well-defined cycles of strengthening, maturity, and weakening that follow closely each updraft/ tornado cycle. As a consequence, this type of pattern reflects on other kinematic quantities in the same region of the storm, which may be even more relevant to the

development of the tornadic supercell, such as the near-surface vorticity field. Very large environmental streamwise vorticity near the surface (in the 0-500 or even 0-100 m AGL layers) indicates a heightened tornado potential given that all atmospheric conditions are favorable to supercells (Coffer et al. 2019). Furthermore, the interaction of the strong near-surface streamwise horizontal vorticity with supercell low-level updrafts may dynamically induce feedbacks that enhance the updraft further and may result in tornado formation Goldacker and Parker (2021). Hence, it is relevant to assess the surrounding streamwise vorticity in the inflow sector of the supercell and how it evolves during each tornadic cycle.

Fig. 3.18 shows the evolution of total (3D) streamwise vorticity at 100 m AGL for all simulated tornadoes through their life cycles⁸. Total streamwise vorticity is shown here in an attempt to better highlight in-storm vortical features (other than tornadoes themselves), which may have a considerable vertical components (Orf et al. 2017). As expected, similar to the enhanced inflow band and LPL features discussed previously, the inflow streamwise vorticity field at 100 m also displays a clear pattern of intensification, maturation, and weakening following the life cycle of each tornadic updraft. During the pretornadic phase of tornado 1 (Fig. 3.18a), a broad corridor of enhanced streamwise vorticity is seen just east of the hook echo and collocated with the near-surface LPL, a pattern that persists during the tornadogenesis phase of the tornado (Fig. 3.18e). From the tornadogenesis into the dissipating phase, the enhanced area of streamwise vorticity detaches into two bands, one very strong and small oriented in the north-south direction that accompanies the occlusion updraft and the other one accompanying the RFGF updraft (Fig. 3.18e,i,m). The streamwise vorticity band associated with the tornado persists with it until its

⁸ The times of the pretornadic, tornadogenesis, peak, and dissipation phase of tornado 1 are not exact as for the other tornadoes in order to keep consistency and facilitate comparisons with previous fields shown for tornado 1 at 300-s intervals.

dissipation phase, where the tornado has already moved far rearward into the storm's cold pool. Just east of the RFGF updraft, the other branch of the enhanced streamwise vorticity region gradually reattaches to the strengthening LPL (and RFGF updraft) during the weakening stage of tornado 1 (Figs. 3.18i,m), and fully develops into a new, single streamwise vorticity band when tornado 2 forms (Figs. 3.18b,f), clearly in conjunction with the newly established low-level updraft

The same general evolution is also observed for tornadoes 2, 3, and 4, though the details of the streamwise vorticity band vary widely among these tornadoes. For example, though tornadoes 2 and 4 share a number of similarities (strength, structure, rapid development), the enhanced streamwise accompanying these tornadoes do not present any particularly similar structure, except for the general pattern described for tornado 1 and strong LPLs (Figs. 3.18 b,f,j,n and 3.18d,h,l,p). Tornado 3, the weakest tornado, has the broadest enhanced inflow region but it is the first tornado to detach from it, due to rapid occlusion and absorption into the lingering low-level mesocyclone of tornado 2 (Figs. 3.18 c,g,k,o).

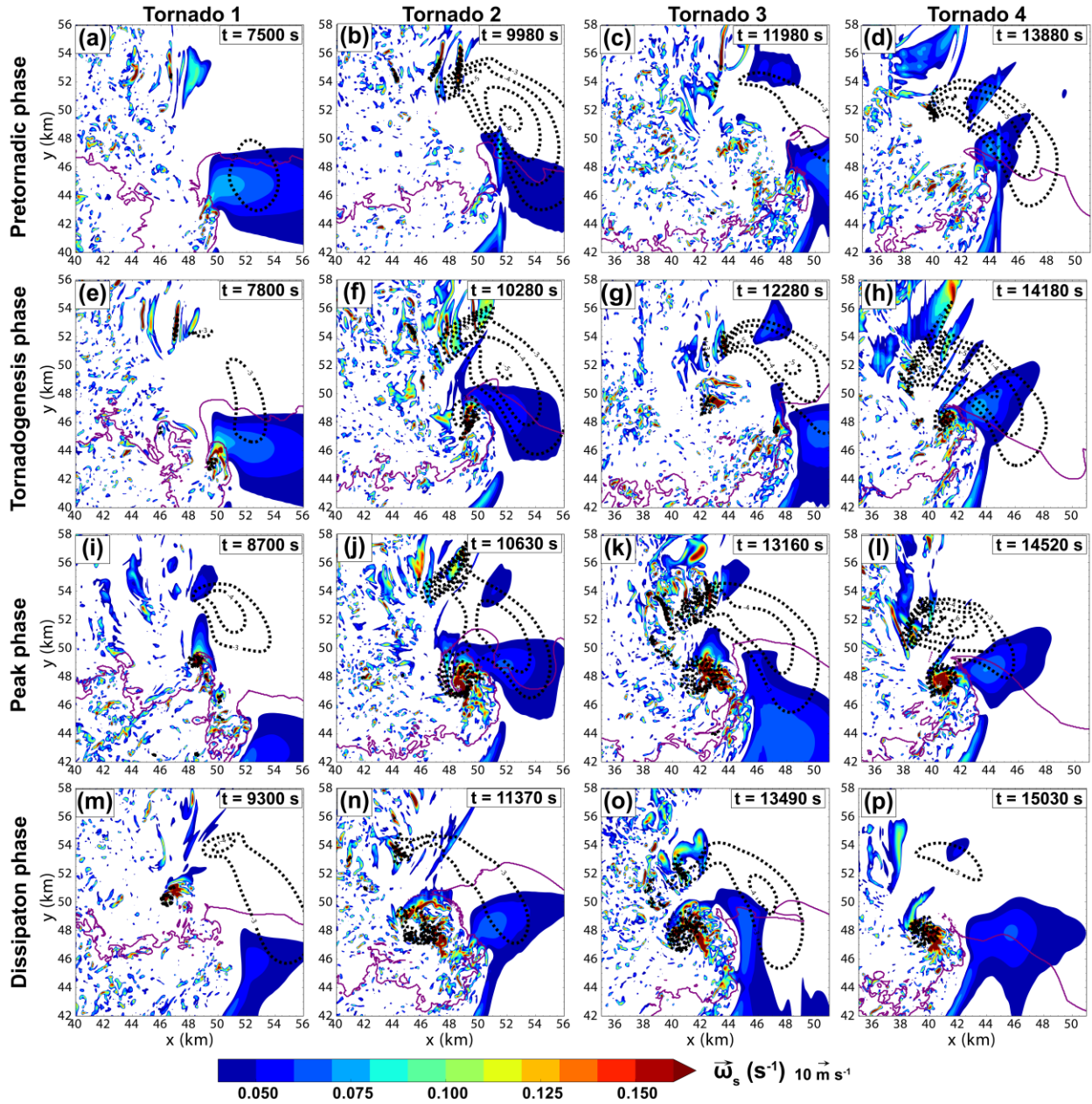


Fig. 3.18. Total (3D) streamwise vorticity (shaded; s^{-1}) and perturbation pressure (dashed black contour for values less than -3 hPa), but for tornado 2 (a) 9980 s, (d) 10280 s, (g) 10630 s, and (h) 11370 s; tornado 3 (b) 11980 s, (e) 12280 s, (h) 13160 s, (k) 13490 s; and tornado 4 (c) 13880 s, (c) 14180 s, (c) 14520 s, (c) 15030 s.

3.2.4 Evolution of midlevel updrafts and relationship with the low-level tornadoes

The previous analysis of the vertical velocity field at low levels highlighted a rather organized pattern of tornado cycling at low levels, where an updraft associated with a tornado intensifies, occludes, and moves rearward relative to the storm in its decay phase, while the updraft at the RFD weakens during the “shedding” process, to later intensify and become the dominant low-level updraft (Adlerman et al. 1999; Dowell and Bluestein 2002a; French et al. 2008). Most structural differences among the low-level updrafts occur due to increasing precipitation and downdraft in the rear flank of the storm as each cycle progresses.

The transition of the storm into an HP mode is related to a complex evolution of its midlevel updrafts. Unlike the low-level vertical velocity field, the midlevel updrafts of the supercell evolve in quite unorganized morphologies as the storms cycle. Classic conceptual models of occluding cyclic mesocyclogenesis (or tornadogenesis), such as that of Adlerman et al. (1999), emphasize how occluding midlevel mesocyclones move rearward relative to the storm and into the cold pool as they dissipate and a completely new midlevel updraft develops to the east-northeast of the old one, triggered by the a surging RFGF. In the simulation shown herein, however, new and old midlevel updrafts often interact before an old updraft is able to decay completely, producing structures that significantly differ from Adlerman’s conceptual model. This is illustrated in Fig. 3.19, which presents the vertical velocity (shaded) and vertical vorticity fields (blue and red contours) at 4 km AGL. The evolution of the midlevel updrafts associated with tornado 1 follows the conceptual model of Adlerman et al. (1999) during its life cycle, first shedding from an intensifying RFGF updraft (i.e., directly above the RFGF underneath) during the tornado formation phase (Figs. 3.19a,e) until it is completely separated from the RFGF updraft during the peak and decay phases (Fig. 3.19i,m). Most of the strongest downdrafts related to the occluded midlevel

updraft at this stage are located far northwest from the intensifying updraft to its southeast. Nonetheless, during the life cycle of tornado 2 (Figs. 3.19b,f,j,n), the occluding midlevel updraft of cycle 1 does not decay completely and eventually merges with tornado 2's midlevel updraft, producing a broad area of upward motion with embedded areas of downdraft to its west (the difference becomes evident by comparing the tornadogenesis phases of tornadoes 1 and 2; Figs 3.19e and 3.19f). Other robust updrafts form west of $x = 46$ km near and between $y = 46$ and 48 km atop the southern extent of surface rear-flank cold pool, also merging with the preexisting midlevel updrafts. This configuration becomes more convoluted during the life cycle of tornado 3 (Figs. 3.19c,g,k,o), with downdrafts extending as far south as $y = 46$ km and new updrafts still merging to the main updraft between $y = 46$ and 48 km. The expanding downdrafts are directly related to the copious amounts of precipitation and outflow previously shown in Figs. 3.3 and 3.5, and account for the disorganized structure of the lingering mesocyclone associated with tornado 2 that absorbs tornado 3. During the life cycle of tornado 4 (Figs. 3.19c,g,k,o), most of the turbulent downdrafts predominant during the life cycle of tornado 3 are displaced to the northwest of the tornadic updraft, such that the tornadic updraft is able to organize into a larger and stronger structure than tornado 3's updraft.

In summary, for this particular simulated supercell, despite persistent tendency for low-level updrafts to evolve into relatively organized cycles, the evolution of their corresponding midlevel updrafts is rather complicated due to mergers with other developing updrafts of the same supercell, which result in disorganized downdraft patterns nearby, which in turn, affect the precipitation field at the surface and the evolving tornadoes. This scenario with decaying tornadic midlevel updrafts interacting with new tornadic updrafts has similarities with that documented by Houser et al. (2015) for the 24 May 2011 El-Reno-Piedmont tornadoes, although in that case the

authors describe the evolution of the low- and midlevel mesocyclone to be a hybrid between occluding and non-occluding modes of Adlerman and Droegemeier (2005). In this simulation, all tornado cycles undergo the occluding mode.

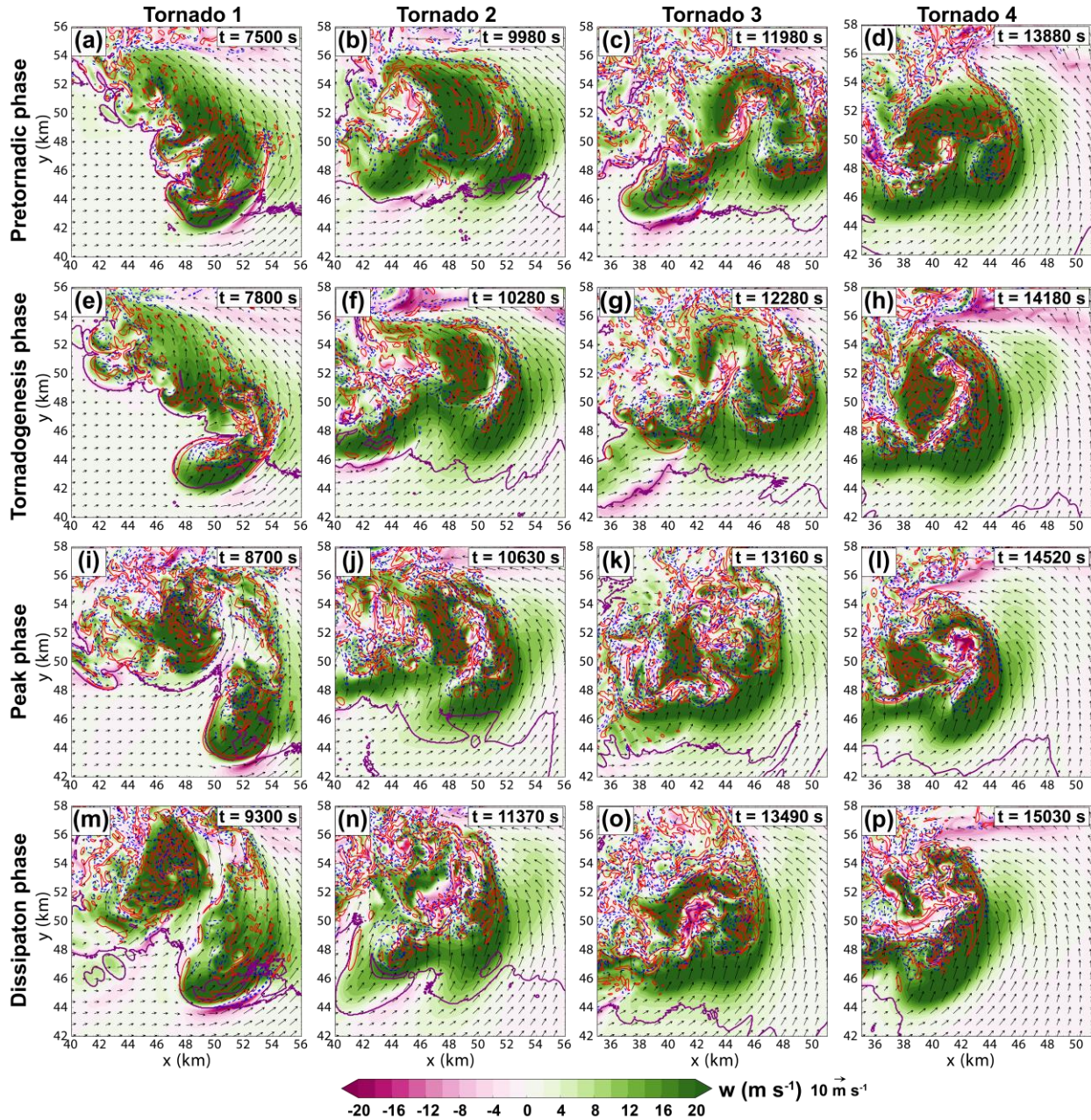


Fig. 3.19. Vertical velocity (shaded; m s^{-1}) and vertical vorticity (blue and red contours denote values less than -0.02 s^{-1} and greater than 0.02 s^{-1} , respectively, to indicate the approximate location of mesocyclones and mesoanticyclones), but for tornado 2 (a) 9980 s, (d) 10280 s, (g) 10630 s, and (h) 11370 s; tornado 3 (b) 11980 s, (e) 12280 s, (h) 13160 s, (k) 13490 s; and tornado 4 (c) 13880 s, (c) 14180 s, (c) 14520 s, (c) 15030 s.

3.3 Summary and discussion

In this study, a 50-m grid spacing idealized numerical simulation of a cyclic tornadic supercell was conducted to assess the impact of certain storm-scale structures on the evolution of tornadoes. The simulations includes the effects of surface friction, which have been shown to be important for the development of tornadoes. In order to mitigate the continuous decelerating of near-surface winds in the base-state wind profile caused by surface friction that would otherwise introduce undesired extra degrees of freedom in our analyses (via an evolving base-state wind field), the initial base-state initial profile was artificially balanced using the Geotriptic Wind Balance (GWB) method (Dawson et al. 2019). Overall, four tornadoes develop in the simulated supercell after 2 h of model integration until the end of the experiment (4 h 30 min). Three of the tornadoes (tornadoes 1, 2, and 4) attain EF5 intensity (though briefly for tornadoes 2 and 4), while one of the tornadoes is weaker, briefly attaining EF3 strength. Each of the tornadoes formed as strong low-level updrafts (with $w_{\max} > 40 \text{ m s}^{-1}$ below $< 1 \text{ km AGL}$) and low pressure aloft developed several minutes before their genesis, causing continuous stretching of near-surface vertical vorticity into tornadic intensity. Such process has been extensively documented in the literature and attributed to dynamically induced updraft at low altitudes resulting from tilting of near-surface environmental streamwise vorticity or frictionally or baroclinally augmented horizontal vorticity from within the convective storm (Coffer and Parker 2017; Goldacker and Parker 2021). The chaotic evolution of the storm itself did not preclude the occurrence of cyclic tornadogenesis at relatively regular intervals. After the first tornado formed, the supercell proceeded to produce tornadoes repeatedly, as the overall storm structure became prone to reestablishing intense low-level updrafts (along new hook echoes) and develop new tornadoes to the east-northeast of the decaying tornadoes, in a way that is similar to well-established conceptual

models of cyclic supercells (Burgess et al. 1982; Adlerman et al. 1999; Dowell and Bluestein 2002a, 2002b; Beck et al. 2006).

Nevertheless, the chaotic evolution of the supercell did cause each tornado to behave in rather particular ways. Tornado 1, which was the longest lived, formed through complex small-scale vortex-vortex interactions and remained near the RFGF-FFCB intersection during its initial development stage, while moving northeastward and subsequently northwestward (in a storm-relative sense), influenced by an RFDIS. The interaction of the RFDIS with the tornado also caused horizontal vortex tubes to wrap around the low-level of the tornado at times, in agreement with high-resolution observation of tornadoes (Houser et al. 2016). Though tornado 1 was always located within its parent low-level updraft, its initial development occurred considerably far south from its parent midlevel updraft, causing the top portion of the tornado to be poorly connected to the midlevel updraft. As the tornado occluded (i.e., became completely surrounded by cool outflow and detached from the RFGF), its parent low-level updraft separated into two parts, an occlusion updrafts (associated with the tornado) and a reminiscent updraft at the RFGF far east of the tornado. This type of evolution is well documented in both observed and simulated tornadoes/mesocyclones (Burgess et al. 1982; Adlerman et al. 1999; Dowell and Bluestein 2002a, 2002b; Beck et al. 2006). When the tornado moved further rearward relative to the storm, its tilt with height decreased and the tornado intensified to its peak intensity as a deep coherent vortex. However, constant rearward motion and a surge of cold outflow caused the tornado to decay. Before its dissipation phase, though, the air surrounding the tornado had only small density potential temperature deficits (-2 to 0 K), a condition favorable for tornado maintenance (Markowski et al. 2002; Marquis et al. 2012).

The evolving structure of the supercell from a “classic” morphology in the surface reflectivity field to a high-precipitation (HP) mode had a major effect in determining the characteristics of subsequent tornadoes. While tornado 1 took several minutes to become embedded in the precipitating core of the storm, tornado 2, 3, and 4 occluded quickly, even before genesis (Markowski et al. 2012b; Markowski et al. 2012a). A large amount of precipitation that developed at the rear flank of the storm developed when tornado 1 dissipated was rapidly encircled by the evolving circulation of tornado 2. A similar scenario occurred for tornado 4. Interestingly, tornadoes 2 and 4 displayed were rather similar in terms of structure, intensity, duration, and the time they took to form (on the order of 20 s). One reason that these two tornadoes formed so rapidly is that they were not as tilted with height as tornado 1 during genesis, such that vertically vorticity stretching may have intensified these tornadoes more readily through a significant depth. The occlusion process itself may have blocked low angular momentum air from the warm sector of these tornadoes, causing the area-average circulation around them to increase quickly (Markowski et al. 2012a). The reason why tornado 3 was the weakest tornado is related to why it also persisted longer than tornadoes 2 and 4: the lingering rain-wrapped mesocyclone of tornado 2. Just after forming at the RFGF updraft, tornado 3 occluded and moved into the rain-wrapped mesocyclone of tornado 2. Unlike previous tornadoes, tornado 3 did not spend time growing (i.e., intensifying via vertical vorticity stretching) along with its parent low-level updraft, as it quickly shed into the rain-wrapped circulation. Nonetheless, once within the rain-wrapped mesocyclone, tornado 3 remained within disorganized areas of intense upward motion, which helped maintain the tornado for as long the rain-wrapped mesocyclone persisted. A more detailed analysis of these results may benefit from Lagrangian vorticity budget along trajectories or circulation analysis along material circuits. Attempts to perform vorticity budget calculations along forward or backward integrated

trajectories were frustrated in the present study because most often parcels trajectories passing through the cold pools and flowing into the tornadoes were not reliable due to strong flow and strong gradients in the turbulent flow in those regions. In addition, any vorticity budget analysis for these simulations should address the spurious vorticity source issues raised by Davies-Jones (2021) due to the use of the GWB technique, a problem that was not covered in this study. This type of investigation is left for a future study.

The transition of the supercell from a “classic” to an HP morphology seems to be caused, at least partially, by a disorganized evolution of midlevel updrafts. Unlike previous conceptual models of cyclic mesocyclogenesis (Adlerman et al. 1999) that predict a general rearward motion and decay of the midlevel updraft away from the newly evolving updraft, midlevel updrafts in the tornadoes analyzed in this supercell often merged to the newly developed updrafts while other updraft formed on back side of the surface cold pool, also merging the new tornadic updrafts. This process creates a convoluted distribution of precipitation that falls closer to the rear-flank of the storm and is more readily advected around the new tornadoes.

A feature that preceded each of the four tornadoes was a low-pressure lobe (LPL) collocated or in close proximity to the core of enhanced inflow winds to the east of the low-level updrafts. This structure evolved in close relationship with the intensifying pretornadic updrafts and is related to accelerating winds into the updraft (Markowski and Richardson 2010). The LPL forms at low levels, initially between 500-2000 m AGL, but later expands upward and downward, eventually merging with the midlevel mesocyclone low pressure volume. Related to the enhanced inflow winds, zones of enhanced near-ground streamwise vorticity develop to the east of low-level updrafts. These zones develop during the genesis and intensification phases of the tornadoes and detach from the low-level updrafts when the occlusion updrafts are shed and move rearward into

the core of the storm. Storm environments feedbacks are known to locally modify the environment in the vicinity of a supercell, including local increases in SRH near the storm (Wade et al. 2018). In some situations, such enhancements may be measured to heights as deep as 1-2 km AGL (M. Coniglio, personal communication). Given the importance of high streamwise vorticity for the development of dynamically induced low-levels updrafts in supercells, the presence of such enhancements in the immediate vicinity of the storm may perhaps foster tornadogenesis by further augmenting dynamics feedbacks between the low-level updrafts and the environmental vorticity field (Goldacker and Parker 2021). This hypothesis can be investigated in future numerical studies and perhaps based on field campaign data near supercells.

One encouraging result from this simulation for numerical prediction purposes is the tendency of the supercell to undergo cycling at relatively regular intervals, despite differences between cycles. Britt et al. (2020) found that ensemble forecasts of supercells at 1-km grid spacing do have skill in providing useful guidance on the likelihood and cycling frequency of supercells. Based on the single simulation presented here, it is possible that numerical forecasts at much finer (< 250 m) grid spacing may be able to predict well cycling frequency and likelihood. To test this, further assessments must be conducted, preferentially using an ensemble framework.

Chapter 4: The Evolution and Structure of Horizontal Vortex Tubes near Observed and Simulated Tornadoes⁹

4.1 Methodology

In order to analyze the evolution and structure of HVs near simulated tornadoes, two idealized simulations are employed. The configuration of these simulations, which are conducted using the ARPS model, are quite similar to that presented in Chapter 3, and a brief description of each of them is provided here. Some features that are common to both simulations include fourth advection along with fourth-order computational mixing in the horizontal and vertical directions (with mixing coefficients adjusted to correspond to the vertical and horizontal grid spacing of each experiment). The environment is horizontally homogeneous; lateral boundary conditions are open radiative and the lower boundary is flat. Also, both simulations employ the previously described GWB technique (Dawson et al. 2019) to maintain the base-state environment in the presence of surface drag, which is enabled by applying the drag coefficient $C_d = 0.028$ in the 1.5-order TKE turbulence closure scheme (Moeng and Wyngaard 1988) at the lowest scalar level of the vertical grid (at 1 m AGL). In addition, visualizations of the 3D wind field concerning the vorticity features addressed in this section are compared to visual observations of HVs in real tornadoes to better understand the behavior of the observed vortices.

4.1.1 100-m grid spacing experiment

The 100-m simulation is an early version of the 50-m experiment described in Section 3 and the 30-m experiment to be addressed in subsection 4.1.1. The simulation employs a horizontal grid spacing of 100 m, which is marginal for resolving tornadoes and even more HV structures.

⁹ As in Chapter 2, some parts of this chapter are direct excerpts from Oliveira et al. (2019) and Oliveira et al. (2022; entitled: Trailing Horizontal Vortices in Observed and Numerically Simulated Tornadoes, submitted to the Bulletin of the American Meteorological Society, in review at the time of this writing).

Nevertheless, visualizations of this simulation are still able to capture some relevant interactions between tornadoes and HVs, as will be discussed.

The domain extent for this simulation is $84 \text{ km} \times 84 \text{ km} \times 16 \text{ km}$ ($843 \times 843 \times 83$ grid points). A Rayleigh sponge layer is applied above 12 km AGL to damp vertically propagating disturbances within the domain. As with the 50-m experiment in Chapter 3, the vertical grid spacing stretches from 2 m to 200 m above 10 km AGL, placing the lowest scalar level at 1 m AGL. Due to the very small near-surface grid spacing and aspect ratio, the large and small time steps are set to initially 0.075 s and 0.05, respectively. Model integration is carried out using mode splitting, with the leapfrog (forward-backward) scheme for the slow (fast acoustic) modes. The model is integrated until 14270.175 s using the 0.075 s large step. However, at this time, a tornado with strong near-surface updrafts is underway, and the vertical advection stability limit is violated since the first model layer is very shallow. From this time on, the simulation is restarted and run until 4 h 20 min using a large time step of 0.025 s while the small time step size is kept at 0.05 s. This is possible because vertical acoustic wave propagation is treated implicitly in the ARPS so that the small time step size is limited by horizontal grid spacing only. The large time step size is on the other hand limited by the very small vertical grid spacing in the case of large vertical velocity. The acoustic wave models are integrated using forward-backward integration schemes with time step size $\Delta\tau$, starting from the past time level $t - \Delta t$ and ending the future time level $t + \Delta t$, in n number of “small” time steps. When $n = 1$, $\Delta\tau = 2\Delta t$, hence the ‘small’ time step size is twice as large as the ‘large’ time step size (Skamarock and Klemp 1992; Xue et al. 1995).

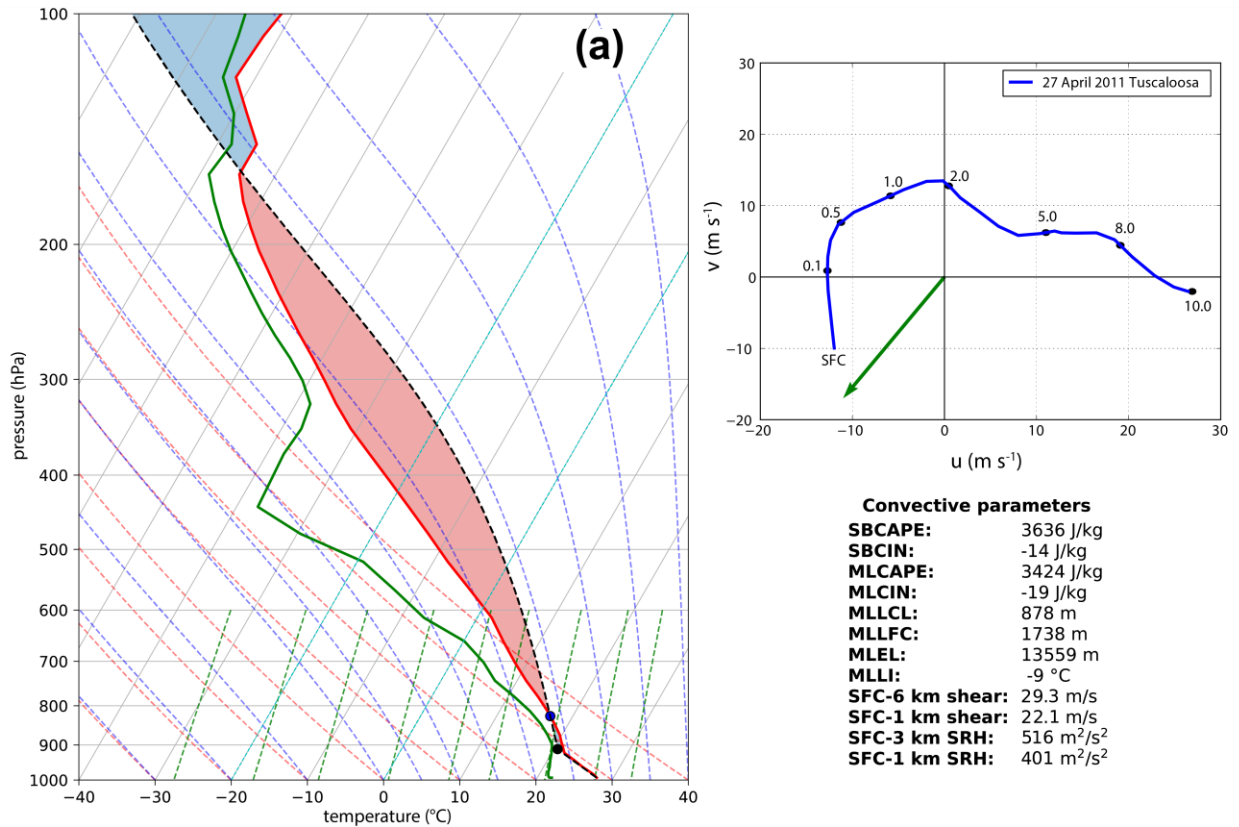


Fig. 4.1. (a) Skew T -log p diagram for the idealized tornadic supercell experiment. The red (green) solid line represents environmental temperature (dewpoint) in °C. The black dashed line denotes the temperature for an ascending surface-based parcel. Areas of positive (negative) buoyancy are highlighted by semi-transparent red (blue) shading. The black and blue dots represent the lifting condensation level and level of free convection, respectively. (b) Hodograph for storm-relative winds between the surface and 10 km AGL. Black dots are heights (in km AGL). The green vector indicates the ground-motion vector ($u = 11 \text{ m s}^{-1}$; $v = 17 \text{ m s}^{-1}$) originally subtracted from the wind profile to induce the storm to remain quasi-stationary in the simulation. Some relevant convective parameters are shown in the bottom right sector of the figure.

The microphysics scheme of Lin et al. (1983) [modified by Tao and Simpson (1991)] is used with the rain intercept parameter N_{0r} set to $2 \times 10^{-6} \text{ m}^{-4}$, rather than the default value of $8 \times 10^{-6} \text{ m}^{-4}$. The reduced value can produce more realistic cold pools and sustained tornadic vortices (Snook and Xue 2008; Dawson et al. 2010; Roberts et al. 2016; Roberts and Xue 2017; Roberts et al. 2020).

The initially horizontally homogeneous environment defined by the same single sounding used in Chapter 3, which was obtained from the 27 April 2011 real-case numerical forecast of

Yussouf et al. (2015). The artificial modifications to the thermodynamic profile are applied to this original sounding to damp spurious convection in the domain, but no alterations to the wind profile are applied here. As such, Fig. 4.1 shows the initial environment; notice the different hodograph and shear parameter values as compared to those presented in Fig. 3.1 in the previous chapter). Storm initiation is triggered by a 6-K thermal perturbation placed at ($x = 55$ km; $y = 16$ km). Data are saved every 60 s (2 s) before (after) 10800 s of model time.

4.1.2 30-m grid spacing experiment

This experiment is nearly identical to the 50-m experiment presented in Section 3, except for variations in the horizontal grid spacing and the domain extent. This 30-m simulation addressed in this chapter is used to analyze the feature described in the Introduction as a “trailing HV”, a larger-scale, more complex and energetic type of HV that may potentially interact with a nearby tornado. In order to better resolve fine-scale HV structures at low levels, a horizontal grid spacing of 30 m is used along with the same vertical grid spacing of 2 m at the surface, which stretches to 200 m above 10 km AGL. The average vertical grid spacing in this simulation is 30.8 m below 650 m AGL. As in the previous simulations, the very small grid spacing used at the surface requires very small large and small time steps in the mode-splitting time integration scheme due to the high tornadic winds; thus, the large and small time step sizes are set to 0.05 s to ensure stability during time integration. The domain extent is 90 km \times 90 km \times 18.2 km (3003 \times 3003 \times 93 grid points), with a Rayleigh sponge layer applied above 14 km AGL. The experiment is integrated forward in time for 3 h (10800 s) to encompass the entire lifecycle of a simulated tornado.

Very high-resolution simulations of tornadic supercells produce massive amount of data that need to be storage on disk for analyzing tornado dynamics. Given that this study focuses on analyzing vortex structures around the tornado and surrounding storm-scale features, to save disk

space, we keep only three-dimensional data in an $18 \text{ km} \times 18 \text{ km} \times 18.2 \text{ km}$ box that follows the storm's low-level (0-3 km AGL) mesocyclone. Data are saved every 60 s during the storm's nontornadic phase (0-6600 s) and every 2 s for the remainder of simulation, including the pretornadic phase and the tornado's full tornado lifecycle (6602-10800 s).

The base-state environment of the tornadic supercell simulation is exactly the same (modified) sounding used in Chapter 3 (Fig. 3.1). The 6-K warm bubble used to trigger convection in the environment is initially located at ($x = 55 \text{ km}$; $y = 16 \text{ km}$). Microphysical processes are parameterized using the NSSL 2-moment scheme (Mansell et al. 2010).

4.2 HVs in the 100-m experiment

4.2.1 Overview of the simulated supercell and tornado

The simulated storm is fully developed into a supercell (e.g., with a hook-like appendage in the rainwater field and well-defined forward- and RFD gust fronts; Fig. 4.2a) after 1 h of model integration as it gradually moves northwestward within the domain. This northwestward motion persists (but slows down) during the first 3 h of simulation. During this period, the storm develops only mesocyclone-scale vertical vorticity of $O(10^{-2} \text{ s}^{-1})$ at low levels (Fig. 4.2a–c), with multiple low-level mesocyclone cycles taking place. However, tornado-intensity vortices do not develop until later in the simulation, a behavior that differs from the observed supercells in the 27 April 2011 tornado outbreak which were prolific tornado producers during a significant fraction of their life span.

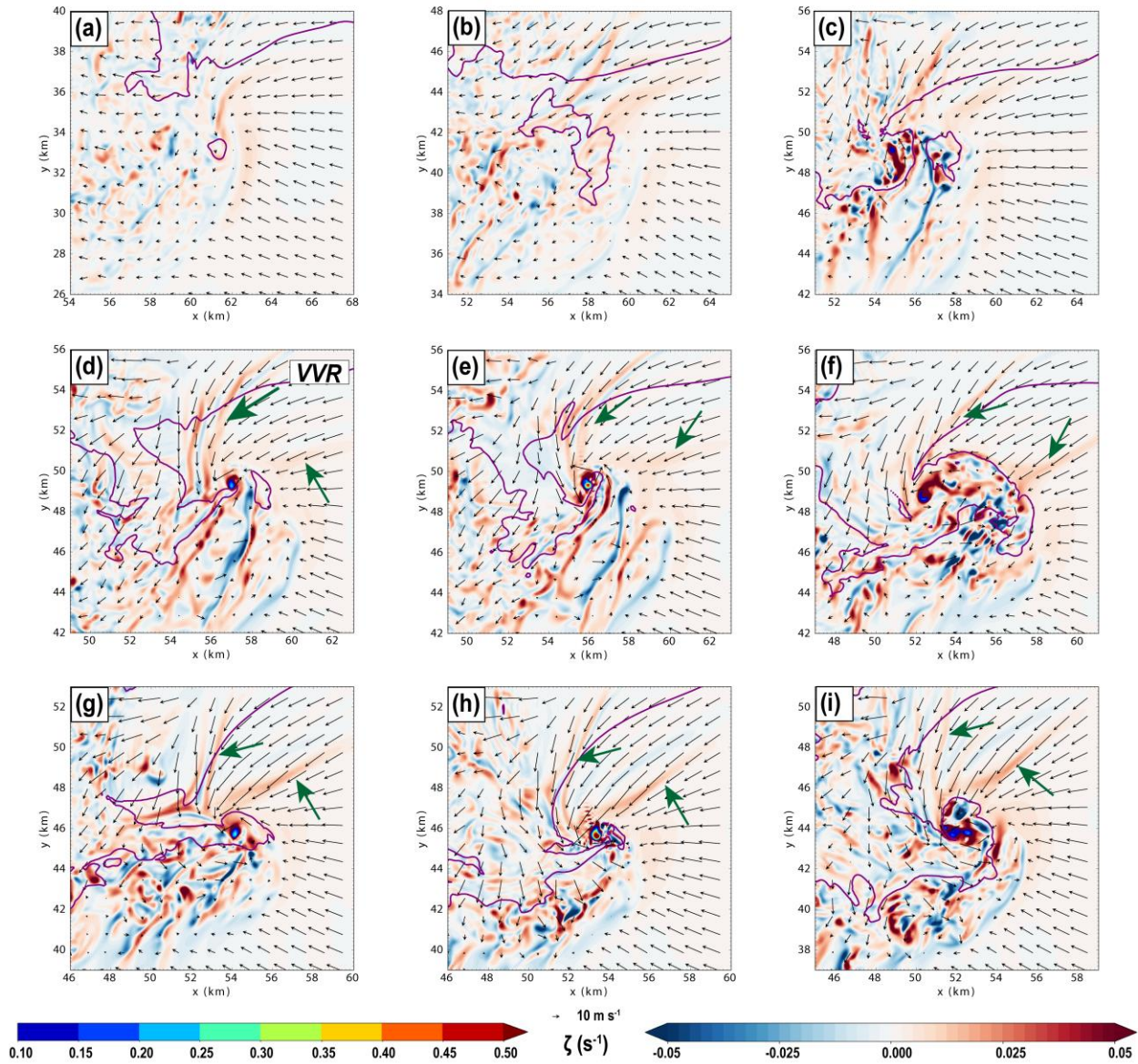


Fig. 4.2. Select stages of the simulated supercell life cycle. (a) 3600.000 s, (b) 7200.000 s, (c) 10800 s, (d) 11888 s, (e) 12032 s, (f) 12930 s, (g) 13950 s, (h) 14274 s, and (i) 14608 s. Vertical vorticity (light shading; s^{-1}), horizontal wind (vectors; m s^{-1}), and the 0.3 g kg^{-1} rainwater mixing ratio contour. Vertical vorticity rivers [VVR, in (d)] are denoted by green arrows in (d)-(i). Pockets of strong vertical vorticity associated with the tornadoes in the center of the domain are shaded in the foreground, starting at 0.1 s^{-1} . All fields at 158 m AGL.

After 3 h 16 min, significant structural changes occur in the supercell. Rapid strengthening of the low-level updraft at the tip of the hook (not shown) occurs coincidentally with a sharpening (i.e., increase in confluence) of an LFCB. The increase in the degree of organization of the LFCB results

in the formation of “vertical vorticity rivers” oriented along the y -axis (Dahl et al. 2014; Parker and Dahl 2015; Coffey and Parker 2017), which first appear at the base of downdrafts northwest of the low-level circulation (Fig. 4.2d). These features, along with enhanced vertical vorticity in an RFD internal boundary, are thought to be the primary storm-scale sources of vertical vorticity to the developing low-level rotation in other simulations in the literature (Beck and Weiss 2013; Dahl et al. 2014; Parker and Dahl 2015; Coffey and Parker 2017). At 11888 s, the first tornado forms at the tip of the hook as seen in the vertical vorticity field (Fig. 4.2d, Fig. 4.3a, and Fig. 4.4a). In this relatively coarse grid spacing simulation, a tornado is defined as a deep (> 1 km), persistent (lasting > 2 min), concentrated vortex with vertical vorticity exceeding 0.1 s^{-1} and wind speed greater than 29 m s^{-1} (the minimum wind threshold of an EF0 tornado) at 10 m AGL¹⁰.

As the tornado matures, it briefly attains a maximum EF3 intensity at 12032 s (Fig. 4.2e, Fig. 4.3b, and Fig. 4.4b), with peak ground-level wind speeds of 62.2 m s^{-1} at 10 m AGL and surface core width (roughly estimated based on the highly-asymmetric radius of maximum wind at 1 m AGL) of about 200 m. After this short period of intensification, however, the tornado maintains only EF1 wind speeds during most of its life cycle. Throughout its life cycle, the tornado exhibits significant northeastward tilt with height (Griffin et al. 2019) and is stronger near the ground during the tornadogenesis and maintenance phases (Fig. 4.3a,b). In fact, nearly all the violent tornadoes on the 27 April 2011 tornado outbreak displayed pronounced northeastward tilt with height in addition to the almost ubiquitous presence of HVs (Knupp et al. 2014). The condensation funnel of this first tornado never touches the ground, a result of the insufficient cyclostrophic pressure drop within the tornado vortex (also likely due to the relatively coarse horizontal grid spacing).

¹⁰ No minimum pressure perturbation threshold was imposed in this initial experiment, though a tornado is usually present in the simulation when surface $p'_{min} < -10$ hPa or so.

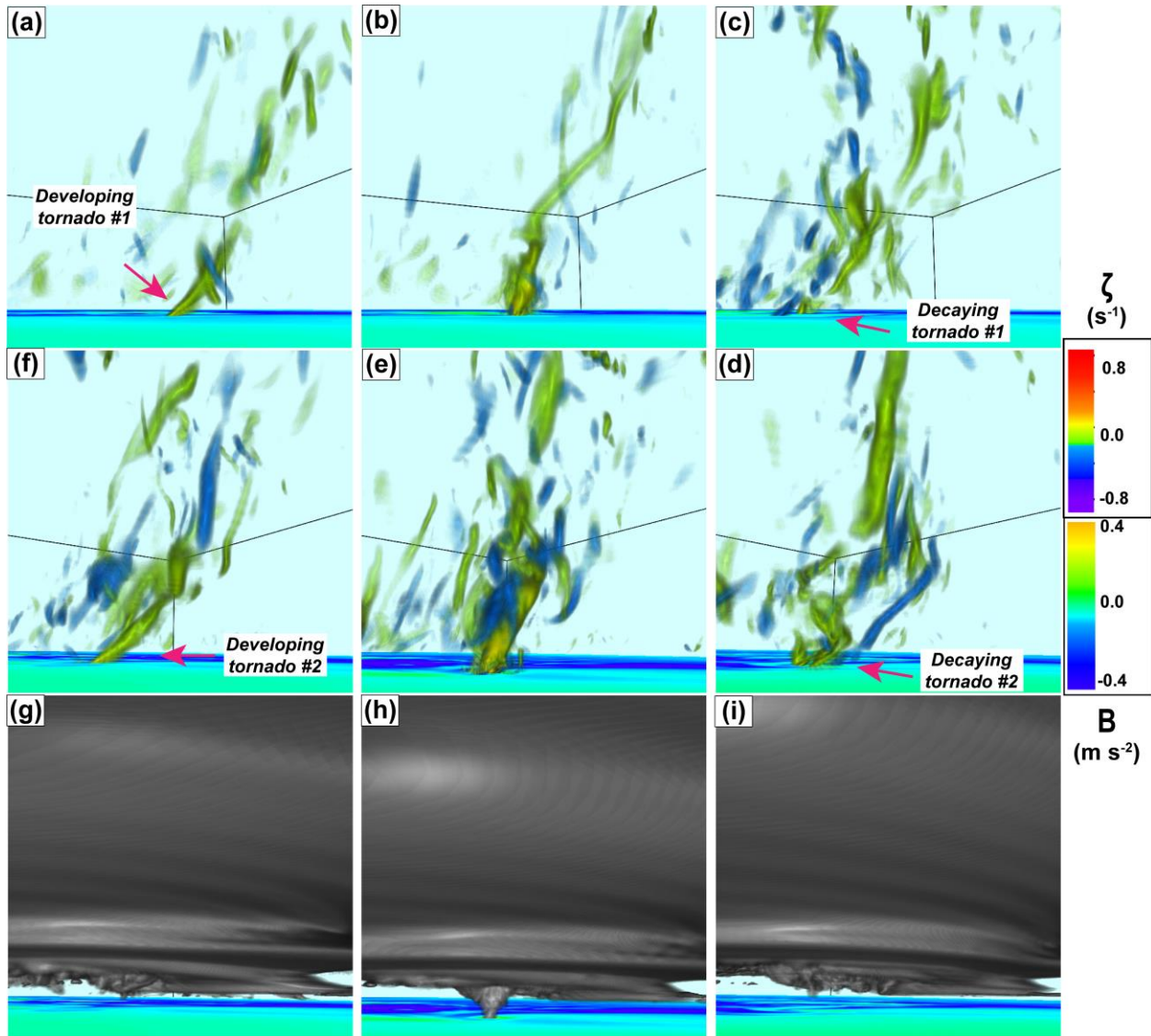


Fig. 4.3. (a)-(f) 3D visualization of vertical vorticity with values greater (less) than 0.075 s^{-1} (-0.075 s^{-1}) indicating regions of cyclonic (anticyclonic) rotation in yellow (blue). Buoyancy (B ; in m s^{-2}) is displayed at 1 m AGL, with positively or neutrally (negatively) buoyant air in green (blue). The life cycle of the first tornado is shown at (a) 11888 s (tornadogenesis), (b) 12032 s (peak stage), and (c) 12930 s (demise). (d)-(f) Same as in (a)-(c), but for the second tornado at (d) 13950 s, (e) 14274 s, and (f) 14608 s. (g)-(i) The cloud field (sum of cloud water and cloud ice mixing ratios; in g kg^{-1}) corresponding to the second tornado in (d)-(f). All nonzero values are displayed.

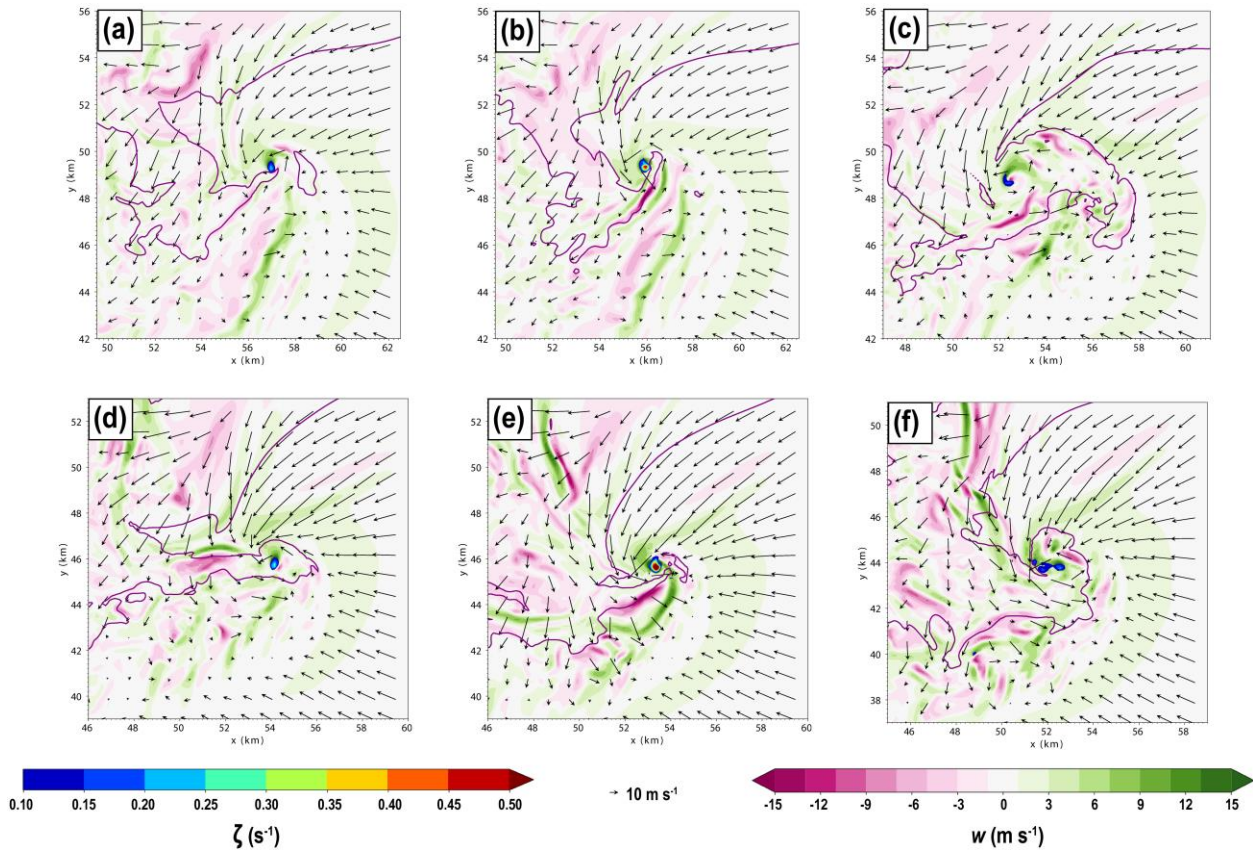


Fig. 4.4. Vertical velocity field (light shading; m s^{-1}) throughout the life cycle of the simulated tornadoes at (a) 11888 s, (b) 12032 s, (c) 12930 s, (d) 13950 s, (e) 14274 s, and (f) 14608 s (compare with Figure 2d-i and Figure 3a-i). Horizontal wind (vectors; m s^{-1}) and the 0.3 g kg^{-1} rainwater mixing ratio contour are also plotted. Pockets of strong vertical vorticity associated with the tornadoes in the center of the domain are shaded in the foreground, starting at 0.1 s^{-1} . All fields at 158 m AGL.

In addition to the abovementioned LFCB vorticity river, less prominent rivers exist northeast of the tornado (Figure 4.2e), possibly associated with forward-flank convergence boundaries (FFDBs; Beck and Weiss 2013). The FFCB merges with the LFCB just north-northwest of the tornado and may contribute to the vertical vorticity budget of the tornado (Beck and Weiss 2013; Dahl et al. 2014; Parker and Dahl 2015; Coffey and Parker 2017).

After approximately 17 min on the ground, the first tornado becomes completely occluded and wrapped in rain, resulting in broadening of the hook as the dissipating tornado moves rearward (southwestward) relative to the parent supercell (Fujita et al. 1970; Dowell and Bluestein 2002b;

French and Kingfield 2019) (Figs. 4.4f and 4.4c). The near ground vortex becomes completely detached from its upper portion and gradually decays (Fig. 4.3c). The remnant vortex persists as a shrinking area of vertical vorticity embedded in precipitation that eventually mixes out within the turbulent downdraft outflow in the rear part of the storm. Despite that, the hook persists as a large low-level circulation, with an anticyclonic flare (Markowski et al. 2008; Bluestein et al. 2016) to its southeast (Fig. 4.2f).

As the occluding downdrafts gradually weaken, new vertical vorticity rivers form at the FFDB and LFCB as well as smaller feeders at the edge of a downdraft surge northwest of the low-level mesocyclone. A second tornado then forms at 13950 s (Adlerman et al. 1999) (Fig. 4.2g, Fig. 4.3d,g, and Fig. 4.4d). The second tornado, unlike the first one, becomes large (400 m wide at the surface) and strong enough such that the pressure drop within its core is able to produce a condensation funnel that extends all the way to the ground during its most intense phase (Fig. 4.3h). As this tornado matures (Fig. 4.2h), it reaches ground-relative wind speeds at 10 m AGL of 86.7 m s^{-1} , corresponding to high-end EF4 intensity. The vortex is also tilted to the northeast but is wider at low levels than the first tornado at its maintenance phase (compare Fig. 4.3b,e). Note also the well-defined “divided mesocyclone” structure (Lemon and Doswell 1979) in Fig. 4.4e, with the development of an occlusion downdraft east of the tornado.

Similar to the first tornado, the occlusion process wraps precipitation around the tornado, which eventually also becomes completely embedded in rain (Figs. 4.2i and 4.4f). The circulation also broadens and becomes asymmetric, resulting in detachment of tornado and its associated LFCB and FFCB vorticity rivers, which now surround the occluded low-level mesocyclone. The decaying circulation then moves southwestward into the heavy precipitation of the hook and dissipates. Unlike the first tornado, however, as the second tornado becomes detached from its

upper portion, multiple surface vertical vorticity centers (Figs. 4.2i and 4.3f,i) associated with updraft pockets (Fig. 4.4f) persist in the decaying broad surface circulation.

After the second tornado dissipates, the simulated supercell maintains a well-defined hook in the rainwater field but no additional tornado forms until the end of model integration at 4 h 20 min (not shown).

4.2.2 Evolution and kinematics of HVs near a tornado

Throughout the development of the tornadoes in the simulation, the presence of HVs surrounding the tornadic circulations is ubiquitous, with striking similarities with the HVs presented in Orf et al. (2017). Using direct volume rendering (DVR), we now investigate the evolution, types and different structures of HVs exclusively focusing on the second simulated tornado since it is stronger and associated with a greater variety of HVs.

4.2.2.1 3D vorticity structure and visual observations

During the intensification and maintenance phases of the tornado, there is enhanced activity of HVs near its outer circulation. It is also during this phase that these structures are more prominent and well defined. This is shown in a visualization of the 3D vorticity magnitude field in Fig. 4.5, which highlights regions of vorticity magnitude $> 0.15 \text{ s}^{-1}$, prior to and around the time the tornado attained EF4 strength. The general appearance of the vorticity magnitude field reveals a complex distribution of elongated vortices surrounding the tornado and its parent low-level mesocyclone. A wide spectrum of length scales is evident that includes vortices of nearly the same dimensions of the tornado down to scales near the grid spacing resolvability limit. This observation is supported by videographic evidence (Fig. 4.6), which indicates that the width of some HVs can be as small as a few meters. [Note that the width of condensation tubes should be smaller than the actual HV circulation, e.g., Atkins et al. (2014)]. The broad spectrum of HV scales (as well as

other small-scale vortices in Fig. 4.5) is a reflection of the turbulent nature of the storm’s cold pool where they reside primarily, as also seen in the visualizations of Orf et al. (2017).

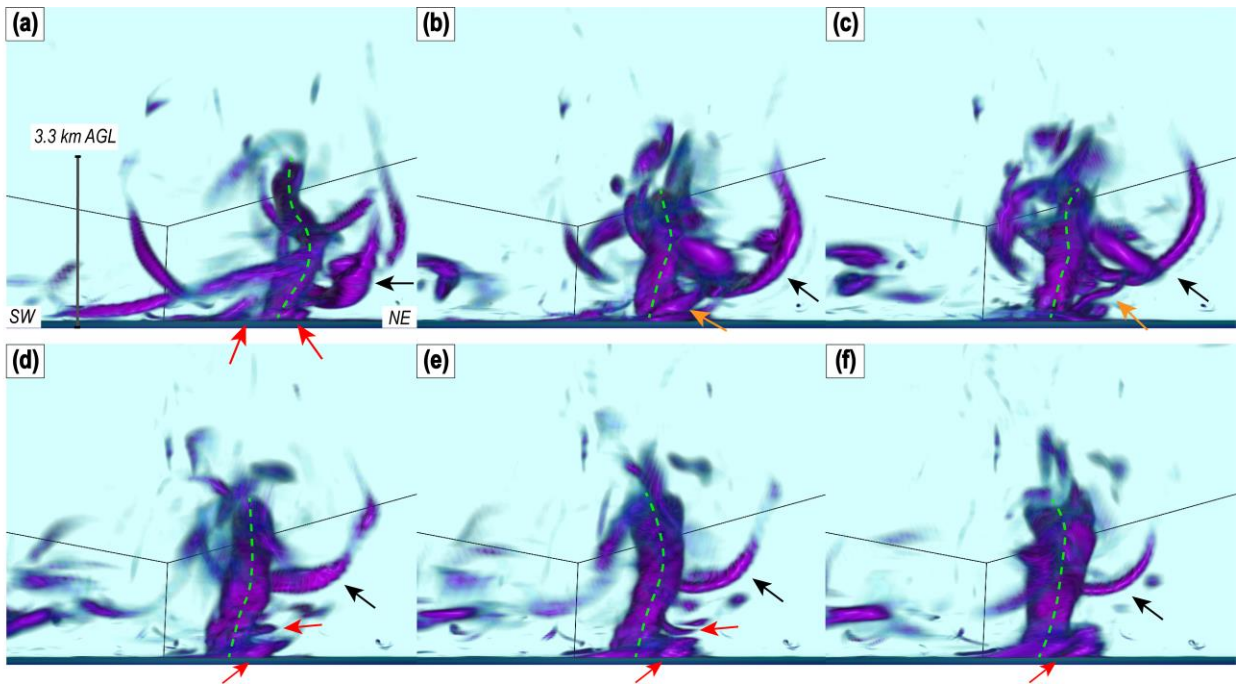


Fig. 4.5. 3D visualization of vorticity magnitude, highlighting values greater than 0.15 s^{-1} , at select time frames: (a) 14102 s, (b) 14170 s, (c) 14190 s, (d) 14230 s, (e) 14250 s, and (f) 14270 s. The viewpoint is that of an observer located at the southeast corner of the domain, looking toward the northwest corner. The green dashed line denotes the tornado vortex axis. Red arrows indicate vortices that form around the tornado and surrounding RFD outflow at the surface. Orange and black arrows indicate distinct vortices used for comparison with real vortices in Figure 4.6.

In order to assess the similarity of the simulated vorticity structure with real-world observations of HVs, Fig. 4.6 presents visual observations from video frames of the 27 April 2011 Tuscaloosa-Birmingham EF4 tornado, when several HVs were orbiting the tornado simultaneously. In both Figures 4.6a and 4.6b, the storm-relative viewpoint of the observers is approximately similar to that shown in Figure 4.5, looking from the southeast through the RFD region, but turning north and northwest (Figure 4.6c) as the tornado moved northeast. In both observed and simulated tornadoes, the HVs revolve counter-clockwise in the tornadic outer wind field and tend to align azimuthally around (but outside) the tornado core, thus forming ring-like

structures encircling the tornado. Although in a different context, this behavior bears remarkable resemblance to the process by which elongated vortices in isotropic homogeneous turbulence, the so-called “worms” [e.g., Jiménez et al. (1993)], interact with a large, sustained columnar vortex in the visualizations of Takahashi et al. (2005). In their study, the interaction of the sustained vortex and the worms is shown to induce disturbances in the larger vortex core flow that can affect its dynamics. Given the vorticity arrangement shown in Figure 4.5, it seems plausible to hypothesize that vortex-vortex interactions analogous to those shown by Takahashi et al. (2005) may occur among tornadoes and surrounding HVs.

Both observed and simulated HVs have a tendency to form in preferred storm-relative regions. The majority of the vortices appear or become well defined (as large tubes in Fig. 4.5 or condensation funnels in Fig. 4.6) to the rear (south and southeast) and right (east) sides of the tornadoes as they ascend in the outer circulation updraft. In fact, many HVs first appear *close to the ground* in an arc extending from the rear through the right side of the tornado. This is seen in the convoluted vorticity distribution surrounding the simulated tornado (Fig. 4.5a–c) and in the large, ascending vortex attached to the right flank of the observed Tuscaloosa tornado condensation funnel, shown in the leftmost arrows in Figures 4.6a and 4.6b.

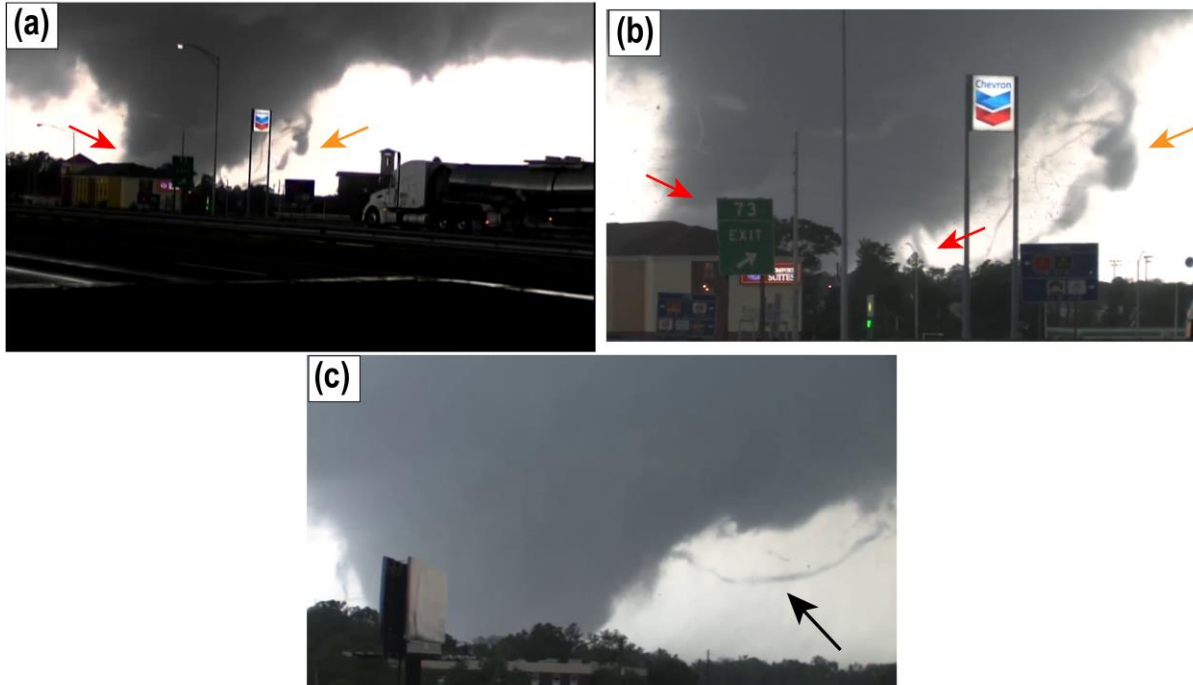


Fig. 4.6. Visual observations of the 27 April 2011 Tuscaloosa tornado displaying several HVs. Video frames extracted from videos of (a) Mike Wilhelm (available online at: <https://www.youtube.com/watch?v=T0FHTG9VETY>) and (b) John Brown (available online at: <https://www.youtube.com/watch?v=9KjWtBrEYHY>), courtesy of Mike Wilhelm and Kory Hartman at SevereStudios.com, respectively. Red, orange and black arrows indicate key vortices discussed in the text. Other vortices are also evident in the figure. Tornado motion is due northeast (from left to right in the figure). Times in UTC are estimated.

The evolution of HVs shown in Fig. 4.5 highlights the diversity of structures and shapes the HVs can assume when interacting with the tornado. Large HVs close to the tornado initially tend to maintain their tornado-relative position (bottommost red arrow in Fig. 4.5e and the leftmost red arrows in Fig. 4.6a,b), then eventually become detached from the surface as they are tilted by the updraft and finally spiral and evolve into complex shapes (e.g., uppermost red arrow in Fig. 4.5e). Smaller vortices near the tornado edge, on the other hand, are rapidly captured in the tornado outer circulation and spiral upward, either maintaining their horizontal orientation or becoming severely distorted into a variety of shapes. Two such examples of complex shapes include the coil spring and U-shaped vortices in the forward sector of the tornado in Fig. 4.5b,c and 4.6a,b, denoted by the orange and black arrows, respectively. Clearly, the strong vertical motion gradients in the

leading edge of the tornado (especially in forward-tilted tornadoes, as in both observed and simulated tornadoes presented here) and sinking motion ahead it must be involved in the creation of these highly-distorted vortex shapes (this aspect is further discussed later). We also note that vortices located farther away from the tornado core tend to be moved around with less change in shape or orientation (e.g., the U-shaped vortex in Fig. 4.5d–f and Fig. 4.6c). This suggests that the rate of distortion of HVs is a function of the 3D shear strain rate surrounding the tornado core. Therefore, the length scale of the HVs and their distance to the parent tornado are both key to determining how their shapes and structures evolve near the tornadic wind field.

The behavior of the most prominent HV in the simulation, i.e., the one highlighted by the black arrow in Fig. 4.5, is further compared with visual observations in Fig. 4.7. In the real Tuscaloosa tornado, a large HV is tilted upward in the right flank of the tornado as it revolves around it and then attaches to the cloud base in its forward flank (Fig. 4.7a). A vertical cross section along the y -axis at 14100.075 s in the simulation (Fig. 4.7b) reveals the corresponding HV already located in the front sector of the tornadic circulation with horizontal vorticity predominantly oriented along the x -direction. In that sector, a lowering in the cloud base can be seen collocated with the HV. Although HVs are crudely resolved in the simulation, condensation driven by cyclostrophic pressure drop is still able to form when the HV nears the cloud base because of the nearly saturated air at that level. The simulated perturbation pressure (Fig. 4.7c) and vorticity magnitude (Fig. 4.7d) fields bear a striking resemblance with the visual observation in Fig. 4.7a, despite the more evident horizontal orientation of the HV in the simulation fields. The region where the HV attaches to the tornado in the perturbation pressure field (Fig. 4.7c) denotes a region where the upward tilting of the HV is reduced or even slightly tilted downward ahead of the tornado in the vorticity magnitude field (Fig. 4.7d). Such reduced upward (or downward) tilt appears to be

due to weaker updraft or downward motion in the secondary vertical circulation ahead of the tornadic circulation where the HV resides which, in this case, is enhanced by the pronounced northeastward tilt of the tornado. Thus, as this particular HV rotates around the tornado, it is affected by a minimum in upward motion (or downdraft) ahead of the tornado (i.e., along the tornado motion vector) and stronger updrafts at its northwestern and southeastern tips (transverse to the tornado motion vector; see Fig. 4.4e). This pattern of horizontal gradient of vertical motion (∇_{hW}) may result in the U-shape of the HV later in its life cycle (Figs. 4.5b–e and 4.6c).

The general evolution of the HV shown in Fig. 4.7 also suggests that, once the HV reaches the regions of strong ∇_{hW} ahead of the tilted tornado, it aligns perpendicularly to ∇_{hW} and attaches to this region. Ultimately, the HV becomes part of the horizontal vorticity field associated with the tornado-relative ∇_{hW} . This does not occur for weak, small HVs: as previously stated, they are quickly distorted by the strong velocity gradients as they approach the tornado outer edge. Therefore, the visualizations indicate that strong HVs can form far outside the tornado core via processes, such as frictional or baroclinic torques, and eventually become embedded in regions of sharp tornado-relative ∇_{hW} and attendant horizontal vorticity field.

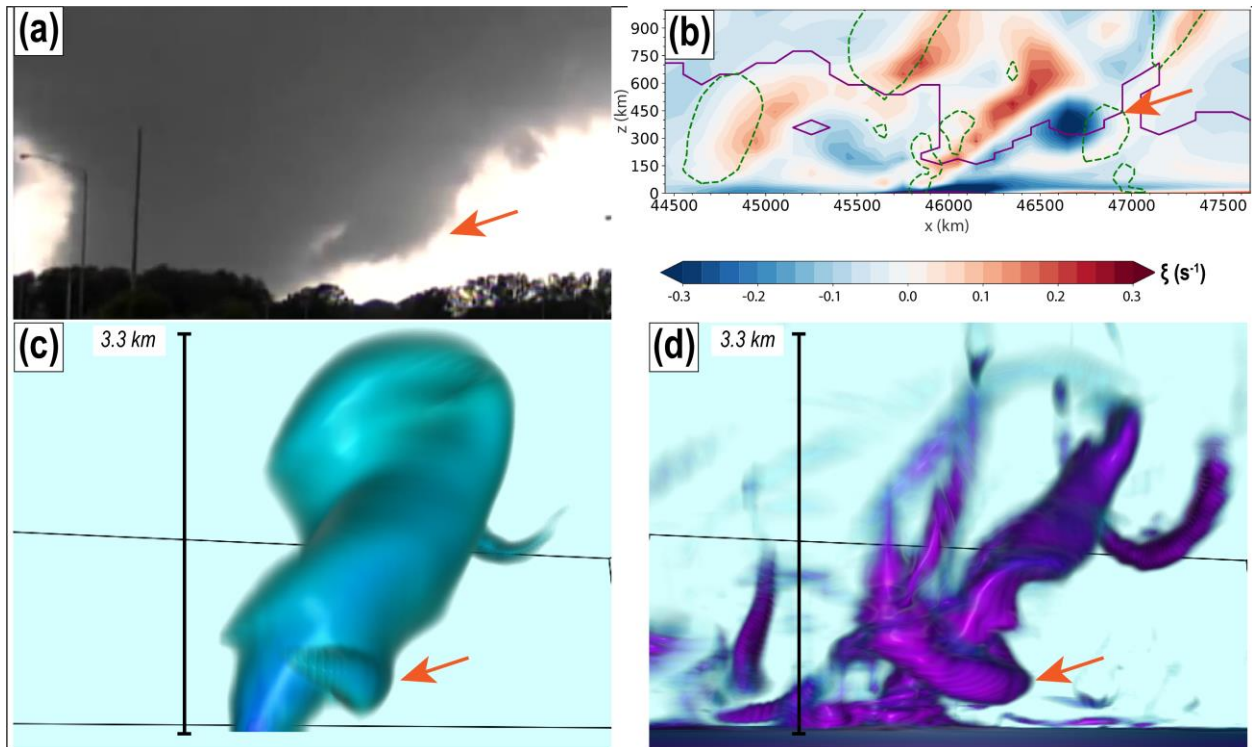


Fig. 4.7. Tilting of HVs in the forward flank of tornadoes. (a) Visual observations of the 27 April 2011 Tuscaloosa tornado at 2206 UTC (extracted from Mike Wilhelm’s video, available online at: <https://www.youtube.com/watch?v=T0FHGTG9VETY>; courtesy of M. Wilhelm). (b) Vertical cross section of x -vorticity component (ξ ; shaded in s^{-1}) along $x = 54.05$ km. Solid purple contours denote the $1 \times 10^{-3} \text{ g kg}^{-1}$ cloud water mixing ratio isopleth and dashed green contours denote downward motion regions where $w \leq -10 \text{ m s}^{-1}$. (c) DVR of perturbation pressure, highlighting values less than -9 hPa . (d) 3D visualization of vorticity magnitude, highlighting values greater than 0.15 s^{-1} . The dark orange arrows indicate the position of the HV and the vertical black line indicates the scale height of the tornado in the DVRs. In all panels, the view is from the east-southeast. Tornado motion is due northeast (from left to right in the figure). All simulation fields are valid at 14100 s.

4.2.2.2 Near-ground flow kinematics and potential HV formation mechanisms

Having analyzed the structure and types of HVs presented in the simulation, a brief assessment of the near-ground wind field surrounding the tornado and its associated horizontal vorticity is now presented. Even though vorticity budget analysis are not carried out in this study, the near-ground kinematic patterns around the tornado can provide valuable information about potential HV formation mechanisms and help guide future dynamical analyses.

As discussed earlier, among the variety of vortices observed in the simulation, a group of HVs is known to form near the ground in two key regions: in a circle around the base of the tornado

and in an arc extending from rear through the right flanks of the tornado. The vortices near the base of the tornado continuously form and rapidly rise just outside the tornado core flow, while the ones in the rear and right flanks form longer near-surface tubes before accelerating toward the right side of the tornado and revolving around it, as previously described. One of the potential mechanisms for the rapid generation of HVs is via the Leibovich and Stewartson (1983) instability. An in-depth discussion of this mechanism can be found in Nolan (2012). Regardless of the genesis region, what is special about this class of vortices is that they typically erupt from the near-surface pool of enhanced horizontal vorticity. This shallow pool of horizontal vorticity that exists close to the ground (dark purple at the ground in Fig. 4.5) is a direct result of surface drag and the resulting large near-surface vertical shear (Schenkman et al. 2014; Roberts et al. 2016; Roberts and Xue 2017)¹¹. The tornado acts as a pump pulling the near-surface horizontal vorticity field upward: the vortices near the base of the tornado are abruptly displaced and/or tilted upward by the updraft while the ones in the right and rear flanks rise more gently along slantwise paths.

The idea that surface drag can be responsible for the generation of HVs can be linked to the predominant sense of rotation displayed by the vortices. In our 3D visualizations, virtually *all* large HVs, either embedded in the tornado outer circulation or RFD outflow, rotate around a horizontal axis with *sinking* motion ahead of them and trailing *rising* motion, as they orbit the tornado in the same way the HV presented by (Houser et al. 2016). An analysis of the videos presented in Fig. 4.5 also shows that the observed vortices in the Tuscaloosa tornado, as well as other tornado events (Knupp et al. 2014; Houser et al. 2016; Bai et al. 2017), consistently display the same behavior. This suggests that HVs near the surface have horizontal vorticity vectors that

¹¹ Though a fraction of this vorticity may have artificial origins considering the arguments of Markowski and Bryan (2016) regarding the lack of turbulent eddies in the inflow region and Davies-Jones (2021) regarding the introduction of spurious vorticity sources due the GWB technique.

point to the left of the horizontal wind vector at large angles, implying considerable crosswise horizontal vorticity (Schenkman et al. 2014; Roberts et al. 2016; Roberts and Xue 2017; Yokota et al. 2018; Tao and Tamura 2020). This can be seen in Fig. 4.8a, which shows the horizontal vorticity field at 1 m and 158 m AGL. Immediately outside the tornado core, in predominantly rotational flow, near-surface horizontal vorticity vectors, consistent with the near-surface HVs, point to the left of the prevailing horizontal wind in which they are embedded, thus having a large crosswise component. Above the surface (i.e., farther from the lower boundary; Fig. 4.8b) the vorticity vectors become more streamwise, suggesting that HVs that arise from the near-ground pool of enhanced horizontal vorticity tend to exchange their crosswise vorticity into the streamwise direction, as they spiral around and upward near the tornado. This observation is consistent with generation of crosswise horizontal vorticity via surface friction in strong, accelerating horizontal flow (Schenkman et al. 2014; Houser et al. 2016; Roberts et al. 2016; Yokota et al. 2018; Tao and Tamura 2020).

Another possibility for the horizontal vorticity of near-surface HVs is generation by baroclinic torques (Davies-Jones et al. 2001; Markowski et al. 2008; Dahl et al. 2014; Markowski and Richardson 2014; Dahl 2015; Parker and Dahl 2015; Fischer and Dahl 2020). However, if the horizontal vorticity in the HVs were mainly created baroclinically at the leading edge of a negatively buoyant RFD, the generated horizontal vorticity would point to the right of the downdraft and cold pool flows, giving an opposite sense of rotation than observed (Markowski et al. 2008; Wurman and Kosiba 2013). Yet baroclinity can still yield the observed vorticity if it is produced at the leading edge of an RFD warm surge, as suggested by Orf et al. (2017). Thus vorticity generated may not be confined to be very close to the ground surface. This aspect is an important difference between Orf et al. (2017) and the present study since the former employed a

free-slip lower boundary condition while we include surface drag to capture the effects of surface frictional generation of horizontal vorticity. Recent studies have found that surface-friction-generated vorticity can be an important or dominant source of vorticity that feeds a tornado vortex near the ground (Schenkman et al. 2014; Roberts et al. 2016; Roberts and Xue 2017; Yokota et al. 2018; Tao and Tamura 2020). This process appears likely the main source of vorticity of the HVs observed in this study. Nevertheless, quantitative analyses of the simulation data are needed to address this question with any degree of certainty and also quantify any sources of vorticity for HVs.

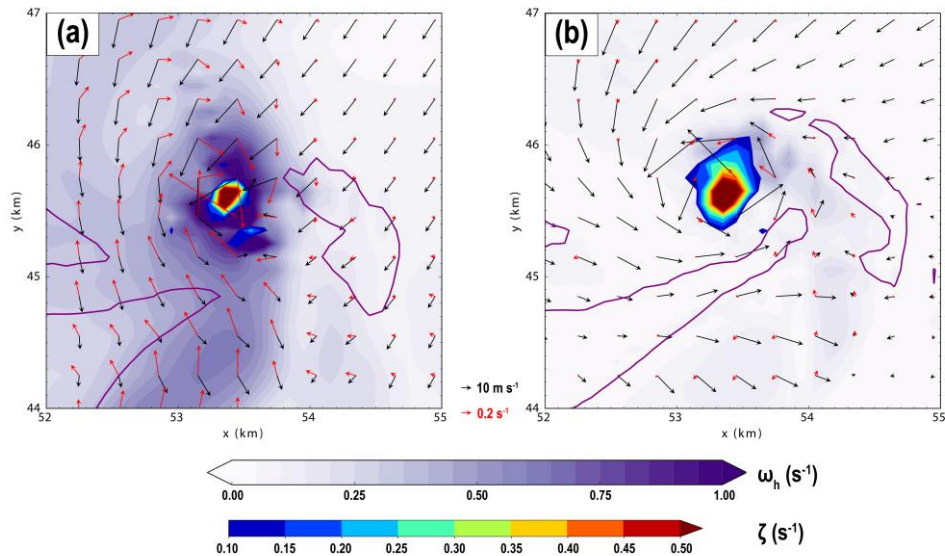


Fig. 4.8. Horizontal vorticity (magnitude is light shaded and vectors are red; in s⁻¹) centered at the tornado at (a) 1 m AGL and (b) 158 m AGL valid at 14230 s (during the intensification phase of the tornado). Horizontal wind vectors are in black (in m s⁻¹) and vertical vorticity ζ is shaded in the foreground, starting at 0.1 s⁻¹. The purple line indicates the 0.3 g kg⁻¹ rainwater mixing ratio isopleth.

4.3 HVs in the 30-m experiment

4.3.1 Overview of the simulated supercell and tornado

Before presenting an analysis of trailing HVs, it is relevant to provide a general assessment of the simulated storm and its attendant tornado, similar to the analysis presented in Section 3.1 of the previous chapter. The general evolution of the supercell is depicted in Fig. 4.9 in terms of time-height cross sections of 0-5000 m AGL domainwide w_{max} , p'_{min} , ζ_{max} . Overall, the first 2 h of storm evolution are quite similar to the storm simulated in the 50-m experiment. The initial updraft impulse develops into deep convection by 1800 s and splits into left-moving and right-moving cells by 2400 s (not shown). The right-moving cell, i.e., the storm of interest in this study, moves to the northwest, while the left-moving cell moves to the north and eventually exits the simulation domain (not shown). By 3600 s, the storm's midlevel updraft has developed ζ_{max} values exceeding 0.01 s^{-1} in the 2-5 km AGL layer, characterizing the storm as a supercell. The storm moves northwestward between 3600 and 6600 s, eventually slowing its northwestward movement so that the storm's updraft becomes nearly centered in the domain. At 7200 s, the storm displays a "classic" supercell morphology, with well-defined forward- and rear-flank precipitation cores, a hook echo, and a RFGF (denoted by the eastward arcing of the θ'_p -1-K contour between $43 \text{ km} < y < 45 \text{ km}$ in Fig. 4.10a). During the 3600-7200 s period, the supercell updraft cycles a few times, as indicated by transient pulses in w_{max} and ζ_{max} in Figs. 2a and c, respectively. However, no tornado-like vortex develops in the first 2 h of model integration.

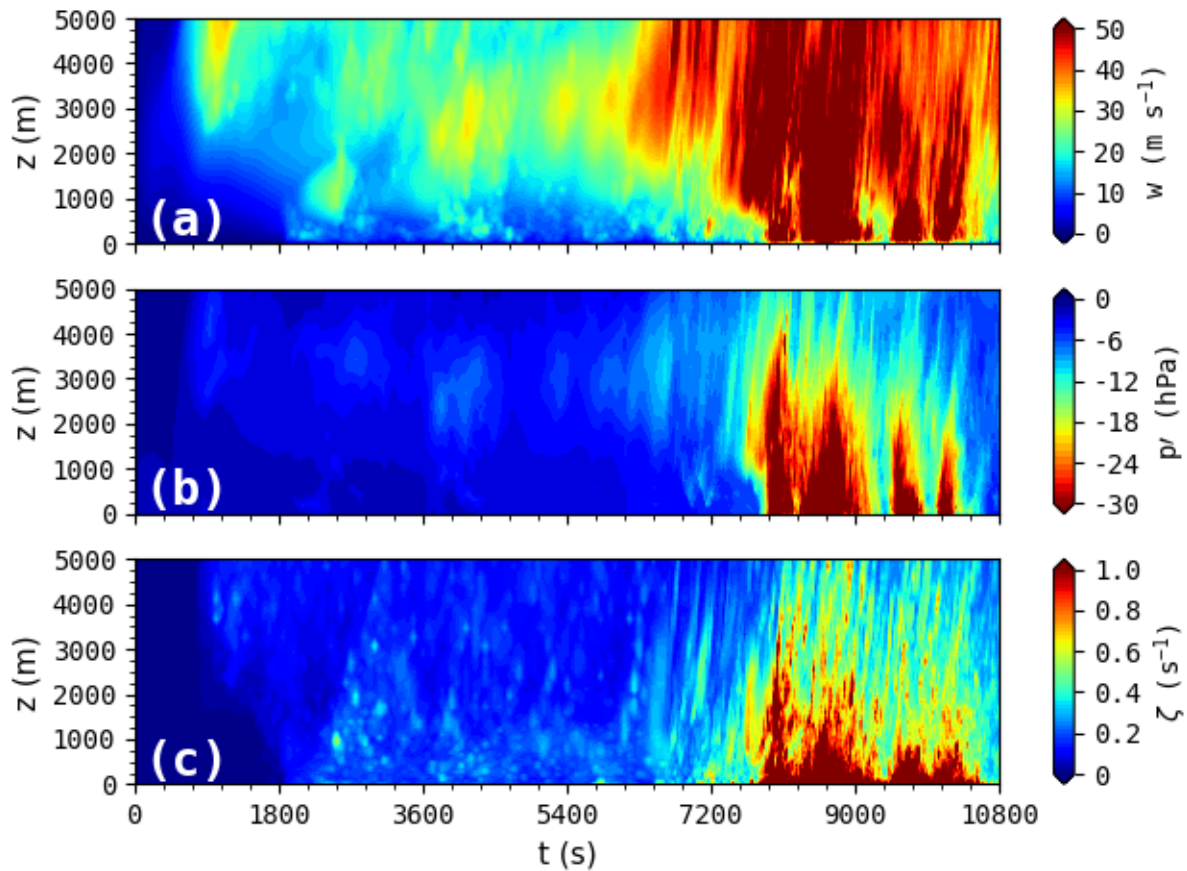


Fig. 4.9. Time-height cross section of 0-5000 m (a) maximum updraft, (b) minimum perturbation pressure, and (c) maximum vertical vorticity in the subdomain, valid from 0 to 10800 s.

Dramatic changes in the storm's behavior commence around 7200 s and precede tornadogenesis. Strong updraft and pressure deficit develop simultaneously in the 1-3 km AGL layer and build downward toward the surface in the following minutes (Fig. 4.9a,b). As this trend continues, small, short-lived pockets of high ζ_{max} begin to form and intensify rapidly near the surface, indicating that the strengthening low-level updraft is enhancing stretching of low-level ζ (Fig. 4.9c). This behavior has been extensively described in previous numerical simulations of tornadic supercells and is attributed to the generation of strong dynamic vertical perturbation pressure gradient acceleration (DVPPGA) within low-level mesocyclones during the pretornadic

phase (Grasso and Cotton 1995; Wicker and Wilhelmson 1995; Markowski and Richardson 2014; Coffey and Parker 2017; Coffey et al. 2017; Orf et al. 2017; Roberts and Xue 2017; Yokota et al. 2018; Flournoy et al. 2020). These studies attribute the generation of low-level DVPPGA to rotationally induced nonlinear effects resulting from tilting and stretching of large low-level streamwise horizontal vorticity available in the storm environment (Markowski and Richardson 2014; Coffey and Parker 2017; Coffey et al. 2017; Goldacker and Parker 2021), later augmented by baroclinic (Wicker and Wilhelmson 1995; Orf et al. 2017) or frictional (Roberts and Xue 2017) processes within the parent supercell. Further intensification of the low-level updraft eventually culminates in tornadogenesis¹² by 7800 s (Fig. 4.10b), illustrated in Figs. 4.9b and 4.9c as an explosive development of a high- ζ_{max} , low- p'_{min} column extending up to 5 km AGL.

Shortly after formation, the tornado intensifies rather rapidly, attaining *instantaneous* ground-relative wind speeds of 100 m s⁻¹ (above the EF5 threshold) by 7960 s (Fig. 4.11) and displaying a spiral vortex breakdown (Fiedler 2009; Dahl 2021) just above the surface in the visualized perturbation pressure (inset in Fig. 4.10c). After its initial intensification, the strength and structure of the tornado fluctuates considerably throughout the remainder of its life span (Fig. 4.11), reaching EF5 intensity (10 m wind speed reaches 90 m s⁻¹) several times during the period. During its third intensification stage, the tornado, recently occluded and located 1-1.5 km to the west of the RFGF (Fig. 4.10d), attains its highest intensity around 8670 s, with instantaneous surface winds in excess of 120 m s⁻¹, p'_{min} lower than -110 hPa and ζ_{max} of nearly 4 s⁻¹. Such extreme values are consistent with the presence of a near-ground vortex breakdown seen in Fig. 4.10d.

¹² A “tornado” is defined herein as in Chapter 3, i.e., persistent (lasting > 2 min), deep ($z > 1$ km), strong ($\zeta_{max} > 0.3$ s⁻¹, $p'_{min} < -10$ hPa) coherent vortex with wind speeds exceeding the minimum criteria for EF0 strength at 10 m AGL, the level at which wind speeds are assessed for EF-scale rating.

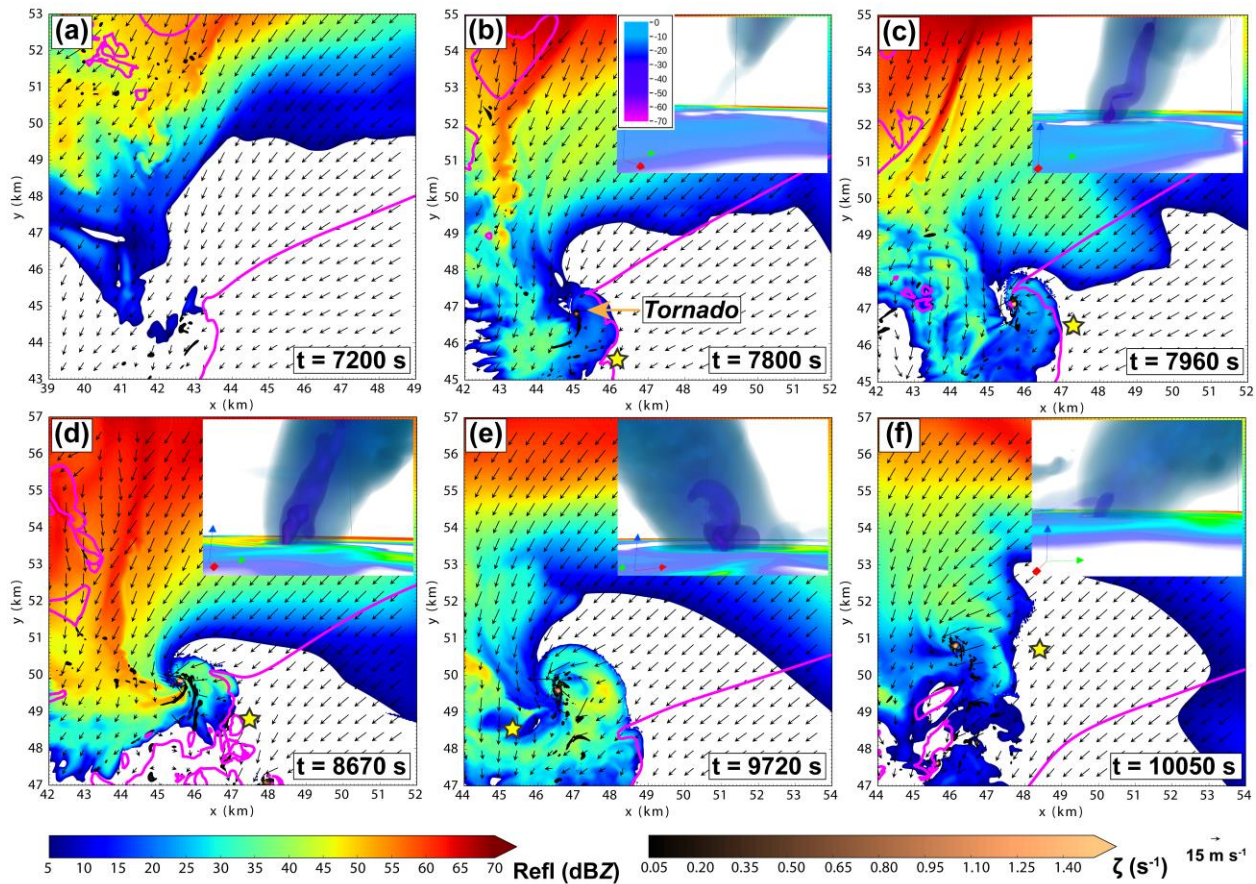


Fig. 4.10. Evolution of the simulated supercell at the lowest grid level (1 m AGL) at (a) 7200 s, (b) 7800 s, (c) 7960 s, (d) 8670 s, (e) 9720 s, and (f) 10050 s. Reflectivity is shaded in dBZ. The -1 -K perturbation potential temperature contour is shown in magenta. Vertical vorticity is shaded in the foreground for $\zeta > 0.05$ s^{-1} . Vectors represent storm-relative winds. The insets at the top corner of (b)-(d) highlight the evolution of the tornado's structure in the volume rendered perturbation pressure field, where $p' < -10$ hPa and the yellow stars denote the camera's location relative to the tornado. The small green, red, and blue arrows in the inset plots point to the north, east, and up, respectively.

Following its peak stage, hook-echo precipitation fully encircles the tornado causing its complete occlusion and a gradual weakening trend in the subsequent 600 s concomitant. Though embedded in rain, a fourth intensification phase begins at 9300 s, when the tornado again reaches EF5 strength and a new spiral breakdown structure (Fig. 4.10e). It is during this stage, specifically from 9500 to 9850 s, that the trailing HV (seen as a large curling horizontal low- p' lobe south of

the tornado in Fig. 4.10e) to be analyzed in the next section develops. Finally, the tornado intensifies one last time by 10050 s as a shallow single-celled vortex (Fig. 4.10f) before finally dissipating by 10500 s in the storm's precipitating core. The total duration of the tornado is ~ 45 min.

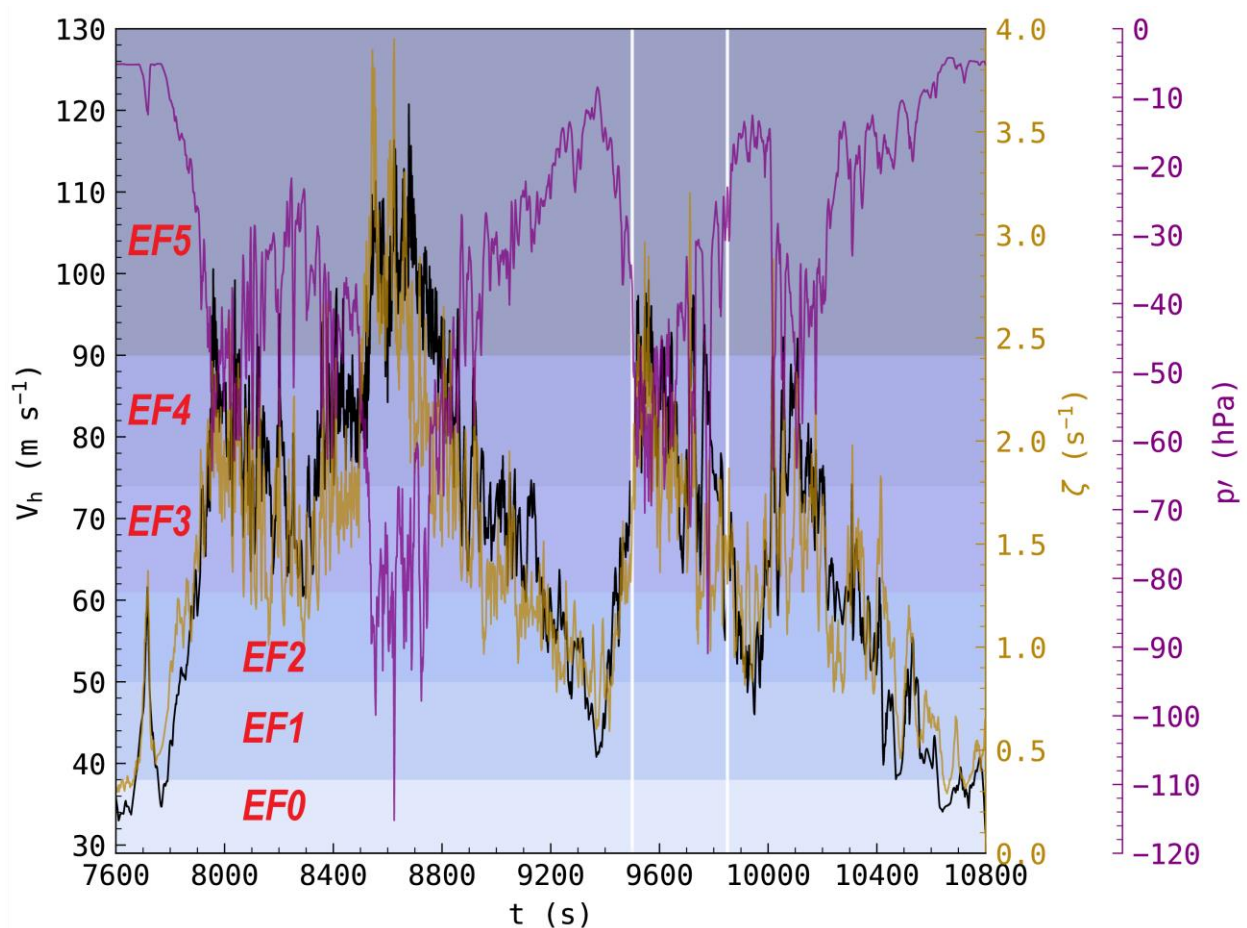


Fig. 4.11. Time series of maximum ground-relative wind (m s^{-1} ; black), minimum perturbation pressure (hPa; purple), and maximum vertical vorticity (s^{-1} ; golden) at 10 m AGL in the subdomain, valid from 7600 to 10800 s. The semi-transparent horizontal bars in the background denote EF-scale wind speed ranges. The vertical white lines are plotted at 9500 and 9850 s, respectively, to demark the formation and decay of the simulated trailing HV in Fig. 9.

4.3.2 Visual characteristics of trailing HVs in the observed Tuscaloosa tornado

There were numerous social media (Youtube) posts of videos capturing the Tuscaloosa tornado as it formed and tracked through the city. Three videos of the early stages of the Tuscaloosa tornado highlighting the trailing HVs are used in our analysis. These videos were taken by Ryne

Chandler and Nate Hughett (hereafter referred to as “Chandler/Hughett video”), Jason Rosolowski (“Rosolowski video”), and Tom Deelo (“Deelo video”), who kindly granted permission for use in this study. Two of the videos, the Chandler/Hughett and Rosolowski videos, were also used and geolocated by Karstens et al. (2013) in their assessment of tree fall damage patterns induced by the Tuscaloosa tornado. An independent geolocation procedure using spatial matches to video frames of all three videos is conducted to ascertain the precise location where the videos were taken using Google Maps (maps.google.com). Both Chandler/Hughett and Rosolowski video locations matched accurately those shown in Karstens et al. (2013); in addition, the Deelo video location was determined successfully using the location information available in the video’s description. The geolocated video sites relative to the tornado’s early damage path are shown in Fig. 4.12, which is adapted from Fig. 13 of Karstens et al. (2013). The video’s names, observer’s locations, their distances to the tornado’s center line (determined from Fig. 4.12) as well as the hyperlinks to the videos URLs are shown in Table 4.1.

Table 4.2. Relevant information on the Tuscaloosa tornado used in this study.

Videographer(s)	Location (lat, lon)	Aprox. distance to tornado (m)	Video’s online address
R. Chandler/ N. Hughett	33.17979°N, 87.55692°W	500-600 m	https://www.youtube.com/watch?v=TIx26tN6pCk
T. Deelo	33.17589°N, 87.55421°W	1000 m	https://www.youtube.com/watch?v=I8FceUTsJ84
J. Rosolowski	33.19472°N, 87.52420°W	150-200 m	https://www.youtube.com/watch?v=5ohIVzIZLuQ

The trailing HVs occurred during two instances of the early life cycle of the Tuscaloosa tornado. The first instance was filmed at close range (Table 4.1) in both Deelo’s and

Chandler/Hughett’s videos, from which selected frames are shown in Figs. 4.13 and 4.14, respectively. In both figures, the camera initially points to the northwest and gradually shifts to the north-northeast to follow the northeastward-moving tornado. The main aspects of trailing HVs can be gained by a combined analysis of Figs. 4.13 and 4.14. In Fig. 4.13, despite the contamination by backlighting, the trailing HV can be discerned in the foreground, as a large, near-surface quasi-horizontal tube tangent to the outer edge of the tornado’s condensation funnel and present in all panels. The trailing HV is oriented from the rear (southwest) toward the forward flank (northeast) of the tornado, with its forward sector wrapping around the tornado.

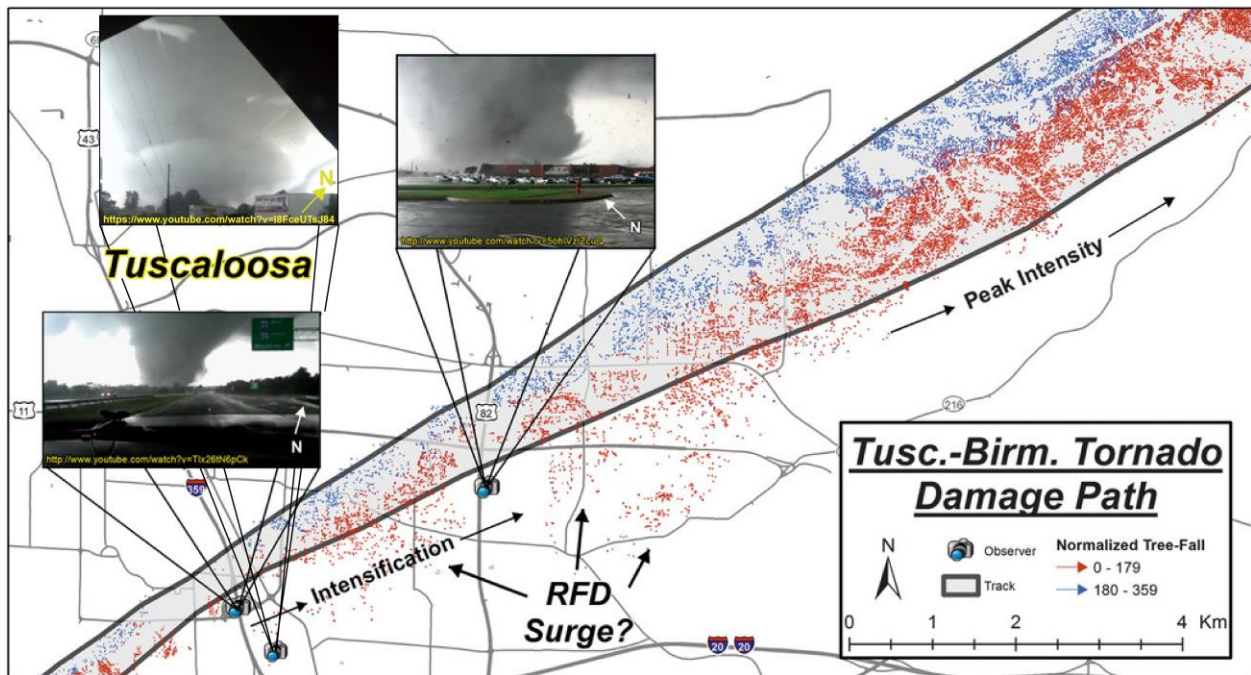


Fig. 4.12. Early segment of the Tuscaloosa tornado damage path highlighting tree-fall damage (represented by small blue and red arrows). The figure is adapted from Fig. 13 of Karstens et al. (2013) to include the location of the video shown in Fig. 4.13 of this study. The camera icons are the location where the videos were taken. Image provided through the courtesy of Dr. Christopher Karstens.

These observations are better illustrated by the wider perspective shown in Fig. 4.14, despite the poor contrast between the tornado and the trailing HV in Figs. 4.13a and b. The rotation

of the trailing HV is characterized by extremely intense helical flow with the associated rotation vector directed from its tail into the forward flank of the tornado, as denoted by the hypothetical streamlines in Fig. 4.13b. The vertical motion field in this flow configuration contains strong upward motion superimposed on the tornado's updraft and downward motion on the external edge of the trailing HV just above the surface.

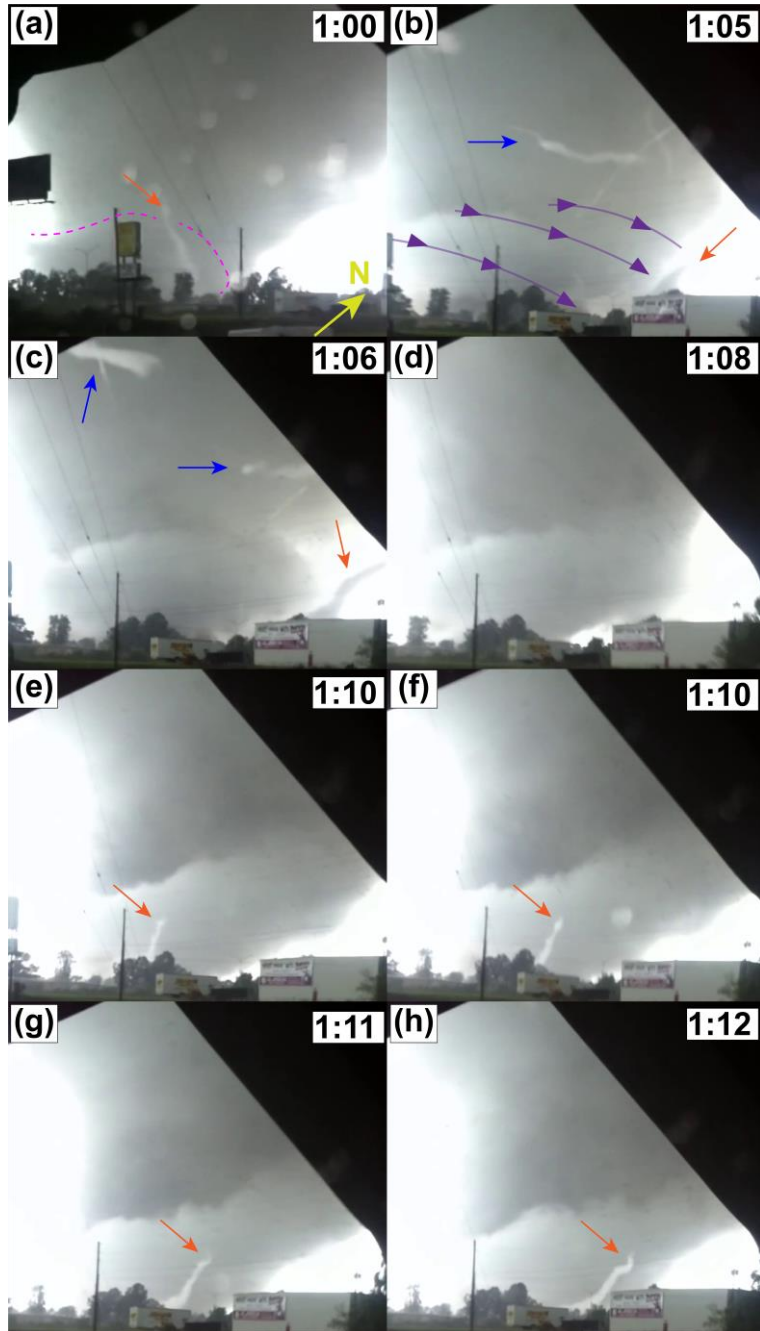


Fig. 4.13. (a)-(h) Image sequence showing the Tuscaloosa tornado as it passed north of the observer, exhibiting a large trailing HV. The magenta dashed line in (a) and (b) outlines the trailing HV due to the poor contrast with the tornado. The orange arrows denote the spiraling vortices discussed in the text. Blue arrows show regular HVs advected by the tornado's outer flow. Times (MM:SS) are relative to the beginning of the video. Images provided through the courtesy of Tom Deelo.

The longevity of the trailing HV relative to smaller HVs can also be seen in Figs. 4.13 and 4.14. Smaller-scale HVs are seen moving rapidly around the tornado in Figs. 4.13b and c and in Fig. 4.13a and b (indicated by blue arrows). Conversely, the trailing HV approximately preserves its size, intensity, and position relative to the tornado throughout the entire period shown in Figs. 4.13 and 4.14a-g (12 and 13 s, respectively). This shows that, unlike small-scale HVs, trailing HVs may be associated with larger, more persistent storm-scale structures, such as RFD internal boundaries in the right-rear sector of the tornado (notice the accelerating flow toward the tornado denoted by the green arrow in Fig. 4.14h around the earlier location trailing HV). It is interesting to notice, though, that the downstream portion of the trailing HV eventually tilts upward into the forward flank of the tornado (Figs. 4.13d-h and Figs. 4.14d-g).

The second instance of a trailing HV in the Tuscaloosa tornado occurred approximately 3 min after the one shown in Figs. 4.13 and 4.14 and is shown in Fig. 4.15 (Rosolowski's video; also seen in Fig. 4.12). In Fig. 4.15, the tornado has just passed to the north of the observer, who is watching the tornado moving due northeast and is located immediately to the southeast of the tornado. The trailing HV is seen as a horizontal condensation funnel attached to the right-forward edge of the tornado in Fig. 8, with its tail closer to the observer. From this perspective, not only is the strong helical flow of the trailing HV more evident, but also the upward motion at the interface between the vortex and the tornado just above the ground. In fact, the strong upward jet in this region can be seen violently lifting off building materials in Figs. 4.15b and c (yellow arrows). The still images and the video suggest that the HV, which is likely to be outside the radius of

maximum winds from the tornado, can also create damaging winds. The potential for HVs to enhance damage near the periphery of the tornado should be studied further.



Fig. 4.14. (a)-(h) Image sequence showing the Tuscaloosa tornado as it passed north of the observers, exhibiting a large trailing HV. The magenta dashed line in (a) and (b) outlines the trailing HV due to the poor contrast with the tornado. The orange arrows denote the spiraling vortices discussed in the text. The insets are zoomed-in views of the same spiraling vortices. Blue arrows show regular HVs advected by the tornado's outer flow. The green arrow in (h) indicates a band of accelerating flow toward the tornado around the position where the trailing HV was located in (a)-(g). Times (MM:SS) are relative to the beginning of the video. Images provided through the courtesy of Ryne Chandler and Nate Hughett.



Fig. 4.15. (a)-(d) Image sequence showing the Tuscaloosa tornado as it passed just north of the observer, exhibiting a large trailing HV. Yellow arrows show damage to buildings at the interface of the tornado and the trailing HV. The orange arrows denote the spiraling vortices discussed in the text. The frame shown in (b) was rotated counterclockwise by 7° to account for the unsteadiness of the footage. Times (MM:SS) are relative to the beginning of the video. Images provided through the courtesy of Jason Rosolowski.

The visual aspects of the trailing HV collectively provide clues regarding their formation mechanisms. The sense of rotation of trailing HVs, their vertical motion pattern, and position relative to the tornado match other radar-detected and numerically simulated HVs observed to the south and east of intensifying tornadoes and near RFD internal boundaries (Houser et al. 2016), who suggested that HVs are produced via frictional torques and/or baroclinity along a relatively warm RFD internal boundaries, with the former likely being more effective near the ground. The tree fall pattern found outside the tornado's damage path observed at the times of Chandler/Hughett's and Deelo's videos were taken and just before Rosolowski's video (Fig. 4.12) suggests the occurrence of RFD internal boundaries and/or strong inflow winds into the tornado; this further substantiates the potential role of frictional processes in the formation of HVs, and

possibly also contribution of baroclinic vorticity generation at the leading edge of internal surge (whose leading edge is the internal boundary; Skinner et al. 2011; Schenkman et al. 2016), if the internal surface is warmer than its surrounding.

An additional intriguing aspect present in both trailing HVs is that they episodically exhibit smaller vortices wrapping around their outer edges. This phenomenon occurs twice in the first trailing HV. In the first situation, a thin, quasi-vertical condensation tube appears near the tail of the trailing HV and moves along its external periphery, as it rotates around the base of the tornado (orange arrows in Figs. 4.13a-c and Figs. 4.14a-c). The “head” of the vortex rotates under the trailing HV while its tail leans outward with height, such that their vertically vorticity component is clockwise. With time, the combined wind fields of the tornado and the trailing HV deform this vortex into an “S”-shaped structure and subsequently into a “coil-spring structure¹³” that spirals upward toward the cloud base (Figs. 4.14d-g). A few seconds later, a similar (but smaller) vortex appears near the tail of the trailing HV and also moves along its outer edge and around the tornado (Figs. 4.13e-h and Figs. 4.14e-g). This second vortex develops a spiral structure at its tail in Figs. 4.13e-h and Figs. 4.14e-g. Multiple thin, wave-like vortices are also observed twisting around the tail of the second trailing HV (Figs. 4.15a,c,d). The systematic appearance of small vortices twisting around trailing HVs is, perhaps, a clue of the vortex dynamics involved in the formation of the latter. The formation mechanism of the trailing HV is discussed in the next section with the aid of the numerical simulation.

¹³ The “coil-spring vortex” is indeed the same as shown in Figs. 6a and b of Oliveira et al. (2019) or Figs. 4.6 and 4.7 of this chapter.

4.3.3 Simulated trailing HV

4.3.3.1 3D structure and evolution

The previous section provided evidence for the existence of trailing HVs based on videos of the Tuscaloosa tornado. Nevertheless, analyses relying solely on visual observations are inherently limited to features revealed by air motion tracers (in this case, condensation) and, thus, cannot afford more comprehensive assertions about the structure and origins of trailing HVs. In this section, visualizations of a trailing HV in the supercell simulation are employed to substantiate the visual observations and further unravel the three-dimensional morphology of trailing HVs.

Fig. 4.16 shows volume-rendered plots of three-dimensional vorticity magnitude throughout the lifecycle of the simulated trailing HV during the fourth intensification and peak stage of the tornado (9500-9850 s; see also Fig. 4.10e and Fig. 4.11). This field is used because it better reveals the fine-scale aspects of the complex wind field around the trailing HV. It would be relevant to visualize the resolved HV features as condensation tubes for straightforward comparison with the observed HVs. However, HVs do not appear when the cloud water field is visualized; in fact, the tornado itself appears merely as an elevated funnel cloud; a similar issue also occurs in the tornado-resolving simulation of Finley et al. (2018). The causes for the underestimation of condensation in the simulated vortices are unclear and are currently subject of further investigation, but it is believed that the cause of this issue resides in the NSSL2M version in the ARPS used in this study.

At 9500 s (Fig. 4.16a), the tornado is seen from the northeast as a northward-leaning tube, with its main axis denoted by the dashed red line. As is typical of high-resolution supercell simulations, several vortex tubes exist in the cold pool and around the tornado, but more prominently in the low levels of the RFD region (in the orange rectangle). Some of these vortices

are longer and located adjacent to the ground, extending horizontally far north into the east side of the tornado, where they gently tilt upward. Between 9550 and 9600 s (Figs. 4.16b,c), other vortices originating in the RFD outflow impinge on the incipient trailing HV, resulting in a larger, more complex structure. The position of the trailing HV relative to the tornado and the upward tilt near the tornado's forward sector are consistent with observed trailing HVs in Figs. 4.13 and 4.14, although the length of the vortices is much larger (~1.5-2 km) than that noticed in the visual observations; this is due to condensation only revealing the strongest section of the trailing HV in the vicinity of the tornado. Also similar to the real trailing HVs (Figs 4.13-4.15), the rotation in the vortices constituting the simulated trailing HV is dominated by strong helical flow directed from its tail into the tornado's forward flank.

From 9650 s to 9750 s (Figs. 4.16d-f), more vortices interact with the trailing HV, causing its structure to evolve from initially quasi-horizontal vortices into a large, complex entanglement of vortex tubes, extending further into the rear-flank area, but preserving similar orientation relative to the tornado. The entangled vortex is composed of a mixture of large, quasi-horizontal vortices and smaller, three-dimensional vortices, with the large vortices contributing mostly to the structure of the trailing HV. As the tornado becomes completely wrapped in rain and weakens (Figs. 4.10e,f and 4.11), the structure of the trailing HV falls apart into a disorganized three-dimensional structure of intertwined vortices (Figs. 4.16f,h). Entangling of quasi-parallel vortex tubes has been described in simulations of turbulent flows (Jiménez et al. 1993) and occurs as a result of the self-induced velocity fields of the individual vortices via the Biot-Savart law (Wu et al. 2007; Davidson 2015). Similar dynamics accounts for the structure of the trailing HV.

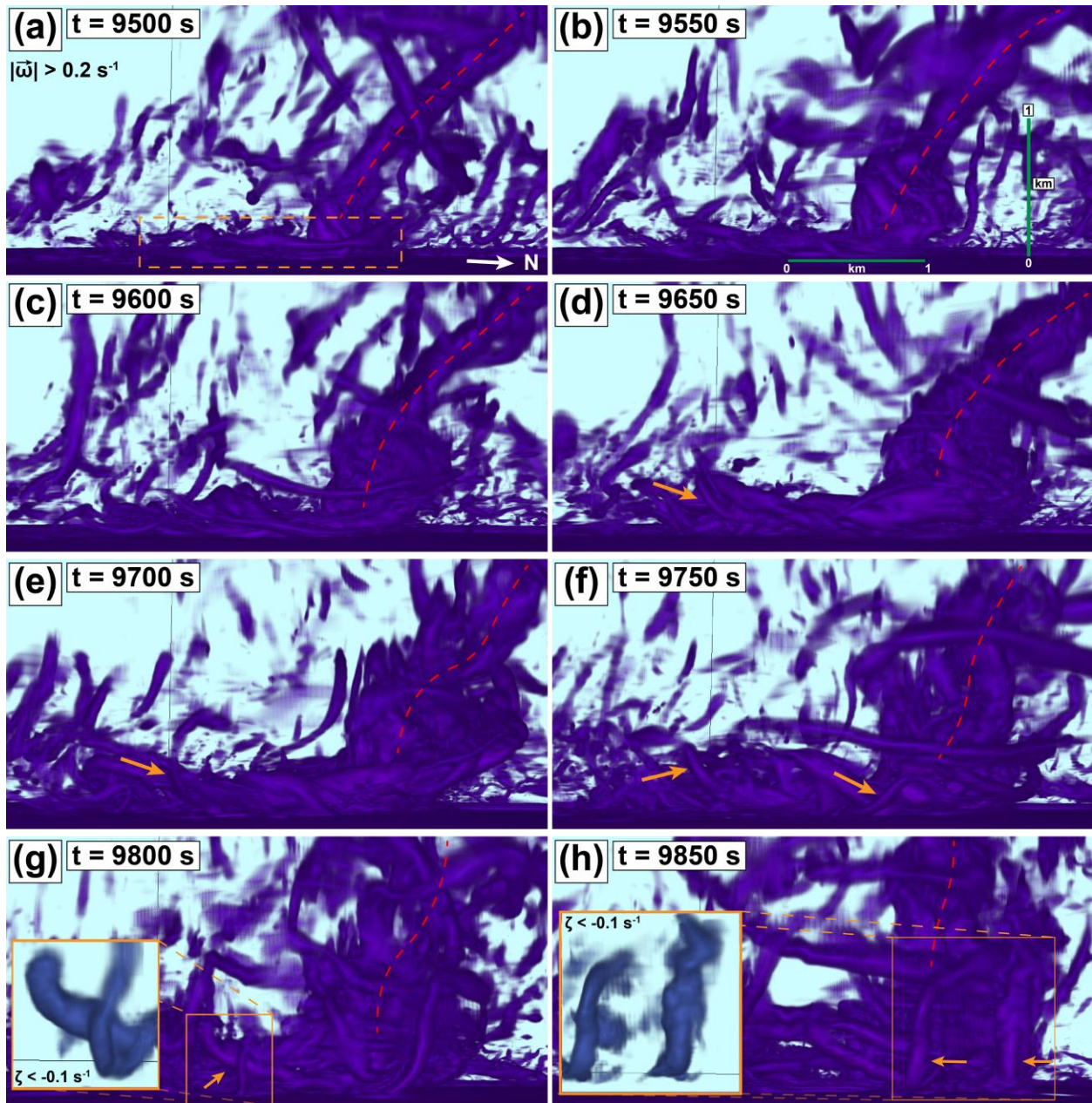


Fig. 4.16. Volume-rendered plots of three-dimensional vorticity magnitude where it exceeds 0.2 s^{-1} at (a) 9500 s, (b) 9550 s, (c) 9600 s, (d) 9650 s, (e) 9700 s, (f) 9750 s, (g) 9800 s, and (h) 9850 s. The orange dashed rectangle highlights the early stage of the trailing HV. The red dashed line subjectively denotes the tornado axis. Orange arrows indicate downward-bending tails of the trailing HV and the model equivalent of the observed small spiraling vortices shown in Figs. 4.13-4.15. The anticyclonic character of the spiraling vortices is highlighted in the insets in (f) and (h), where $\zeta < -0.1 \text{ s}^{-1}$ is shown in blue. The camera points to the southwest.

The entangled nature of trailing HVs is also responsible for the formation of the small spiraling vortices observed in Figs. 4.13-4.15. From 9650 to 9850 s (Figs. 4.16d-h), smaller vortices (orange arrows) form near the tail of the trailing HV and move along it, until they rotate around the tornado, similar to the thin vortices in Figs. 4.13-4.15. Being smaller and weaker than the larger vortices composing the trailing HV, the smaller vortices are twisted by the bulk rotation of the trailing HV, causing their tail to lean outward and their “head” to move under the trailing HV. This tilts the small, initially quasi-horizontal vortices into a nearly vertical orientation dominated by anticyclonic vorticity (seen in insets in Figs. 4.16d-h), distorting them into “S”-shaped or spiral structures (Figs. 4.16g-h; also seen in Fig. 4.13c and 4.14). These small vortices, when eventually absorbed into the trailing HV, head first, can however still contribute positively to the vertical vorticity when the leading part of the trailing HV is lifted off ground.

Further insight into the structure of the simulated trailing HV and its association with nearby storm-scale features is provided in the top view of the volume-rendered vorticity field (Fig. 4.17). At 9500 s, the large HVs constituting the trailing HV are located to the east and southeast of the tornado, surrounded by smaller HVs. The large HVs are located immediately rearward of a northeast-southwest-oriented RFD internal boundary (blue dashed line). This boundary serves as a focus for accumulation of vortex tubes originating in the RFD outflow to the west. This is seen in the following 250 s (Figs. 4.17b-f), as more HVs continue to form in the RFD outflow and in the vicinity of the boundary and progressively intertwine around the largest vortices, giving rise to the complex entangled structure that constitutes the trailing HV. The RFD internal boundary also acts as a corridor of strong rear inflow toward the tornado as the westerly internal flow turns northward near and at the boundary; as a result, the originally left-pointing crosswise horizontal vorticity just west of the boundary becomes streamwise (Fig. 4.18a). As previously discussed, the

initially crosswise horizontal vorticity is likely attributed to frictional torques or baroclinity along warm RFD surges (both mechanisms act constructively along the warmer tongue between $46.6 \text{ km} < x < 46.7 \text{ km}$ and $49.2 \text{ km} < y < 49.6 \text{ km}$).

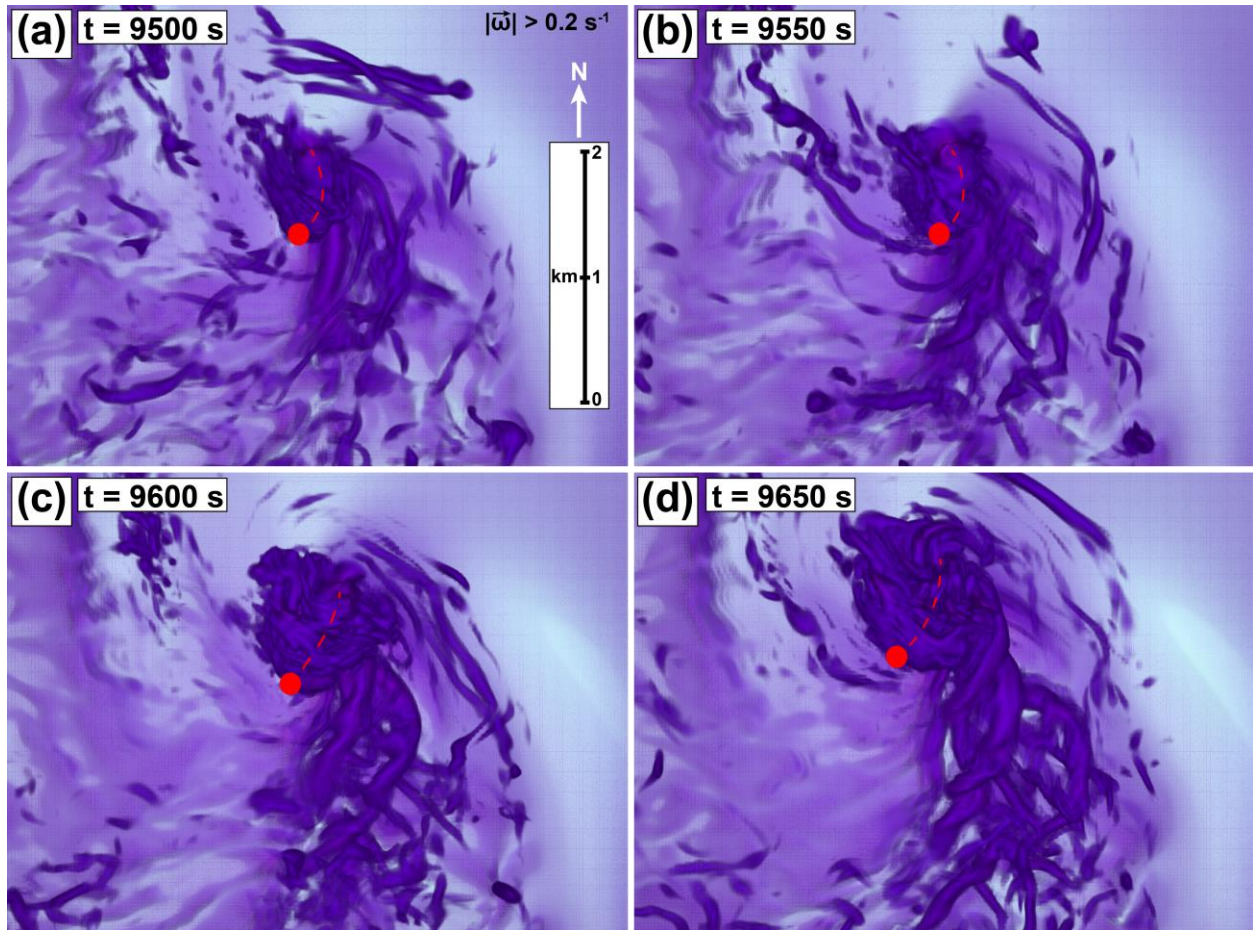


Fig. 4.17. Top view of volume-rendered three-dimensional vorticity magnitude where it exceeds 0.2 s^{-1} at (a) 9500 s, (b) 9550 s, (c) 9600 s, and (d) 9650 s. The vorticity field is rendered only between the surface and 1 km AGL to avoid contamination by other intervening structures. The red dashed line subjectively denotes the tornado axis, with the red circle representing the base of the tornado. The camera is located at 5 km AGL.

The internal boundary is also a favorable region for intensification of the trailing HV, as the HVs accumulate and are stretched along the boundary. This is evidenced by horizontal cross sections of horizontal streamwise vorticity and its stretching term shown in Fig. 4.18b and c. The trailing HV is located just to the west of the boundary-related wind shift, where flow rapidly

accelerates toward the east sector of the tornado, resulting in a corridor of intense streamwise vorticity (Fig. 4.18b) due to stretching (Fig. 4.18c). The relationship between the trailing HV and the RFD internal boundary corroborates the inferences made using the visual observations (Figs 4.13-4.15) and the visualizations of vorticity (Fig. 4.16).

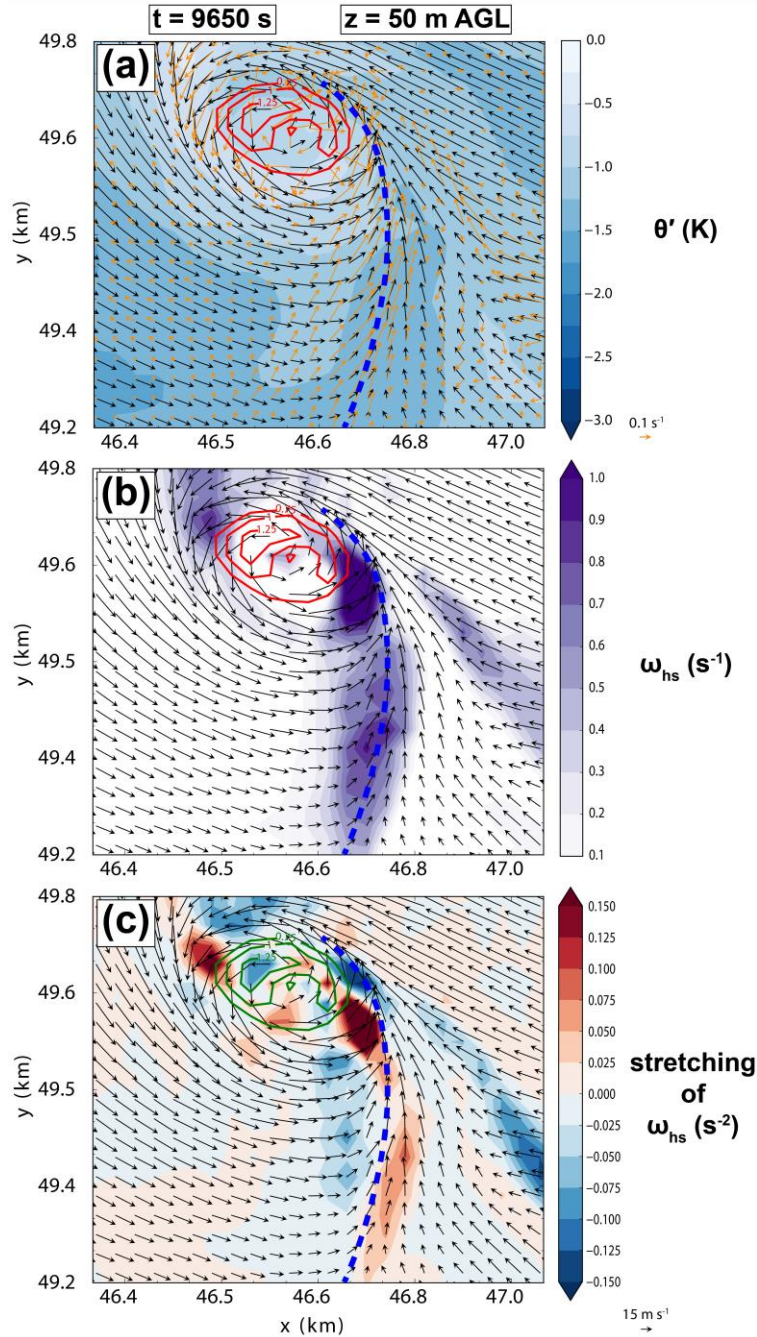


Fig. 4.18. (a) Potential temperature perturbation (θ' ; shaded; K) and horizontal vorticity ($\overline{\omega}_{hs}$; orange vectors; s^{-1}), (b) horizontal streamwise vorticity (shaded; s^{-2}) and (c) stretching of horizontal streamwise vorticity (shaded; s^{-2}). The red [green] contours in (a) and (b) [(c)] represent vertical vorticity in the tornado; the outermost contour denotes $\zeta = 0.75 s^{-1}$, and it increases at $0.25 s^{-1}$ intervals. Black vectors in all plots are storm-relative winds. The yellow dashed line indicates the wind-shift line associated with a RFD internal boundary. Both fields are valid at 9650 s at 50 m AGL.

4.3.3.2 Near-surface wind field

A question raised in the Introduction was: “Can tornado-HV interactions enhance damaging winds at the surface?” The observed damage at the interface between the tornado and the trailing HV in Figs. 4.15b and c suggest this may occur. We now further address this question by inspecting the intensity of the near-surface horizontal and vertical velocity fields near the interface between the simulated tornado the trailing HV. Figs. 4.19a and b show horizontal cross sections of storm-relative horizontal wind and vertical velocity on a $400 \text{ m} \times 400 \text{ m}$ area encompassing the tornado and the trailing HV at 10 m AGL at 9610 s, during the mature phase of the trailing HV. Storm-relative winds are stronger at the eastern periphery of the tornado, where the trailing HV is located (Fig. 4.19a; seen also in Figs. 4.17 and 4.18a). The area of enhanced horizontal winds is also collocated with the northern tongue of a band of intense upward motion (Fig. 4.19b), just to the southeast of the tornado. This is the area where the tornado draws in and stretches horizontal streamwise vorticity along the internal boundary, as identified in Figs. 4.18b. The superposition of the trailing HV and the tornado wind fields induces a rotor-type circulation containing extremely strong winds ($> 80 \text{ m s}^{-1}$ between 10 and 70 m AGL, with small-scale areas exceeding above 90 m s^{-1} just to the north; Fig. 4.19c) and updrafts ($> 20 \text{ m s}^{-1}$ at 20 m AGL; Fig. 4.19d) just above the surface through the vortex. Hence, the analysis based on Fig. 4.19 suggests that trailing HVs are associated with both enhanced storm-relative horizontal and upward flow at the right edges of tornadoes to some extent. Unfortunately, however, such conclusions based on a single simulated event are, at most, circumstantial, since it is impossible to know exactly how the unsteady, highly asymmetric tornado (notice the multiple-vortex structure in the vertical vorticity contours in Figs. 4.19a and b) would have evolved in the absence of the trailing HV. More studies addressing the interactions of trailing HVs and tornadoes are necessary to confirm this possibility.

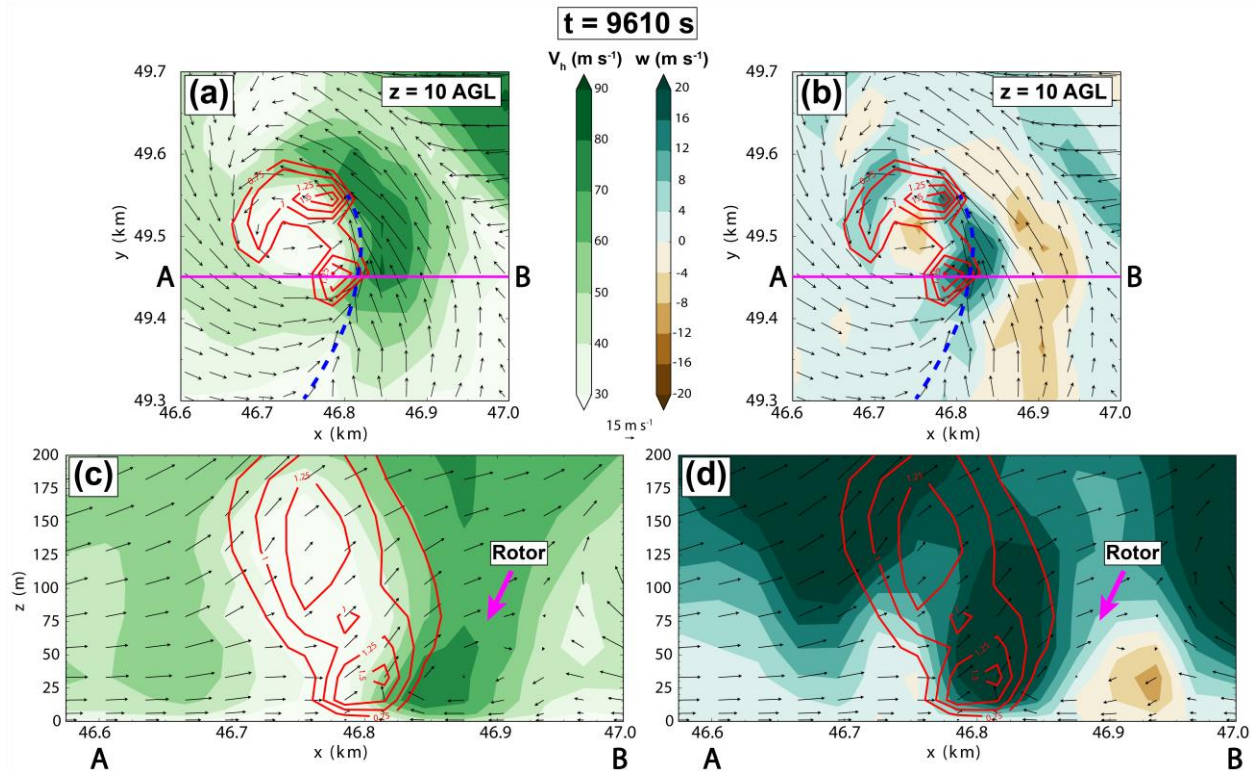


Fig. 4.19. Horizontal cross sections of (a) storm-relative horizontal wind speed (V_h ; shaded; $m s^{-1}$) and (b) vertical velocity (w ; shaded; $m s^{-1}$) valid at 9610 s at 10 m AGL. Vectors are storm-relative winds. The blue dashed line indicates the wind-shift line associated with an RFD internal boundary. The magenta AB line located along $y = 49.455$ km refers to the vertical cross sections shown in (b) and (c). (c) Vertical cross sections of storm-relative horizontal wind speed and (d) vertical velocity along the AB red line in (a) and (b). The red contours represent vertical vorticity in the tornado; the outermost contour denotes $\zeta = 0.75 s^{-1}$, and it increases at $0.25 s^{-1}$ intervals. The magenta arrow in (c) and (d) denotes the rotor-type circulation.

4.3 Summary and discussion

4.3.1 Behavior of small-scale HVs based on the 100-m simulation

An idealized numerical simulation of a tornadic supercell is produced with the ARPS model at 100-m grid spacing and visualized with VAPOR; the data are analyzed, with the aid of 3D visualizations, to qualitatively determine the 3D structure, types and evolution of HVs near simulated tornadoes. The simulation includes surface drag with a semi-slip lower boundary condition in order to capture the effects of surface friction on the production of near-ground horizontal vorticity. Furthermore, the first scalar model level is placed at 1 m AGL to augment

vertical resolution close to the surface to resolve near-surface vertical shear, and to facilitate future trajectory-based analyses. The simulated parent supercell remains nontornadic during the first 3 h of life cycle, producing only mesocyclone-scale low-level vertical vorticity. After 3 h 16 min, the supercell transitions to its tornadic mode, producing two significant tornadoes. The first tornado lasts for 17 min and briefly attains EF3 strength, while maintaining EF1 winds for most of its life cycle. The second tornado is shorter lived but stronger, with peak winds reaching a high-end EF4 threshold. Both tornadoes exhibit significant tilt to the northeast with height.

HVs exist near the simulated tornadoes throughout their entire life cycle but are more prominent during the strengthening and maintenance phases of the tornadoes, consistent with the case study of Houser et al. (2016). A comparison of volume-rendered 3D vorticity magnitude fields and visual observations shows that the most significant HVs appear near the surface in an arc extending from the south toward the east sides of the tornadic circulation, embedded in both tornado outer flow and RFD outflow behind the gust front. Larger HVs tend to maintain their shape and position relative to the tornado longer than their smaller-scale counterparts, which quickly become distorted and are advected around and upward outside the tornado. Moreover, HVs farther away from the tornado tend to keep their shape and revolve around the parent circulation more slowly. This may be a result of reduced 3D shear strain rates outside and farther away from the tornado core flow. Once HVs are captured in the near-tornado, accelerating flow, very strong stretching occurs, which can occasionally form condensation inside the vortex tube via cyclostrophic pressure deficits, as shown in Figs. 4.6 and 4.7, and also discussed by Houser et al. (2016).

A closer inspection of a strong simulated HV reveals that the vortex is advected cyclonically toward the forward flank of the tornado at low levels. Because the tornado tilts

forward with height, strong horizontal gradients of vertical motion exist ahead of it. Our visualizations suggest that strong HVs can form within the storm cold pool and later become attached to the zone of strong horizontal gradient of vertical motion ahead of a forward-tilted tornado. Thus, HVs can occasionally be absorbed in the horizontal vorticity field associated with tornado-relative vertical motion gradients. In fact, many of the fast moving, forward-tilted tornadoes observed on the 27 April 2011 tornado outbreak displayed HVs in their forward sectors during a significant portion of their life cycle (Knupp et al. 2014).

Another relevant aspect seen in both 3D visualizations and videos of the Tuscaloosa tornado is the tendency for HVs to have horizontal vorticity vectors with a large crosswise component at low levels, similar to the 24 May 2011 El Reno tornado studied by Houser et al. (2016). Regions of large horizontal near-ground vorticity collocated with and pointing to the left of strong near-surface horizontal winds strongly suggest a possible role by surface friction in the production of HVs. Recent studies have shown that surface friction can produce significant near-ground horizontal vorticity within RFD outflows (Schenkman et al. 2014) and in the storm's inflow (Roberts et al. 2016; Roberts and Xue 2017; Roberts et al. 2020; Tao and Tamura 2020) that is ultimately tilted and stretched to produce tornadic vortices. It may well be possible that the HVs described in this study are coherent-structure manifestations of the vorticity-generation processes discussed by Schenkman et al. (2014) and Roberts et al. (2016), revealed here owing to the use of 3D visualizations and comparisons with real tornado footage. Recently, 3D visualizations of simulated tornadic supercells have provided crucial insights into storm- and tornado-scale processes involved in tornado formation and dynamics (Orf et al. 2017; Orf 2019). Mechanisms other than surface friction, such as baroclinity along RFD warm surges behind their primary gust fronts and reorientation of near-tornado vertical vorticity into the horizontal (Houser et al. 2016),

may also be important for the generation of the variety of 3D vortex tubes in the vicinity of a tornadic wind field. The complex distribution of HVs near the simulated tornadoes in the RFD outflow suggest all these mechanisms may be acting together. A conceptual model of the 3D structure, relevant flow features and what we believe to be the most plausible mechanisms for HV formation is presented in Figure 4.20.

We want to point out that the 100-m horizontal grid spacing used in this study is certainly coarse to resolve the vast spectrum of HVs that may exist in nature, which possibly includes HVs of only a couple of meters of length scale. Consequently, we may be resolving only the larger, more energetic HVs in the initial portion of the inertial subrange, implying that only a small part of the HV spectrum is represented here. With an isotropic grid spacing of 30 m, Orf et al. (2017) was able to resolve a broader spectrum of 3D vortical structures in their supercell's cold pool and around the tornado. Such grid spacing was enough to allow condensation to form inside the HV as happens in nature, which suggests that, to properly address the dynamics of HVs, grid spacing on the order of a few meters is desirable.

Takahashi et al. (2005) show that turbulent worm-type vortices that interact with a dominant large vortex can affect the dynamics of the latter. Although we did not address the impacts of HVs on the parent tornado itself, the interaction is clearly seen in the volume rendered movies. Given the highly nonlinear nature of these vortex-vortex interactions, it would be plausible to speculate that the most energetic HVs can have some influence on the tornado vortex. These questions were partially addressed in the 30-m experiment, but a more sophisticated approach to study this type of very small-scale structures is needed. Future work including detailed vorticity and circulation budget analyses and perhaps in real-data simulations of violent tornadoes at very

high-resolution (grid spacing 10-30 m) may be able to provide a clearer picture of the dynamics of HVs.

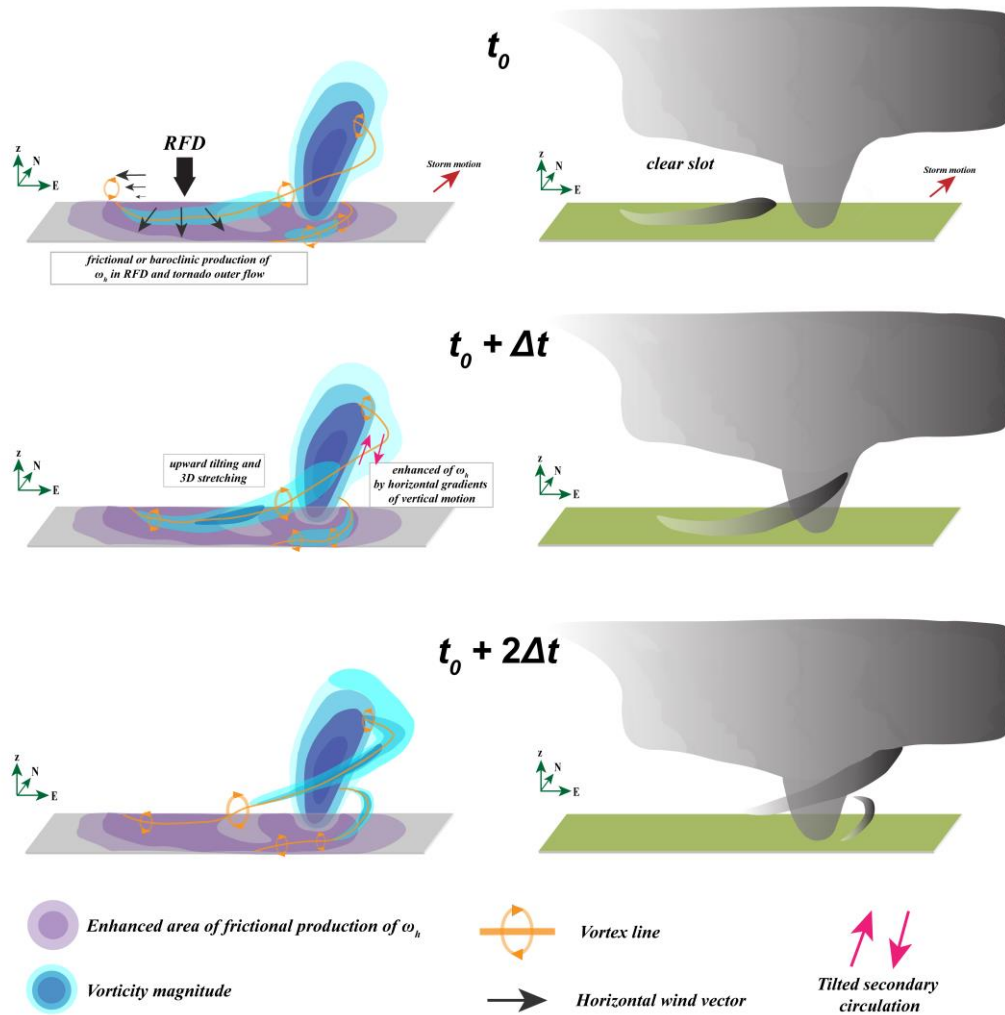


Fig. 4.20. Conceptual model of evolution of HVs in the simulation from initial time t_0 through $t_0 + 2\Delta t$, at Δt time increments. Left column: 3D vorticity magnitude isosurfaces shaded in blue. The vertically-oriented vortex represents an intensifying or mature tornado while slantwise, detached vortex tubes represent more horizontally-oriented vortices in the periphery of the tornado. Regions of enhanced frictional generation of horizontal vorticity in strong, near-ground horizontal wind embedded in the RFD outflow are shaded in purple. Magenta arrows in the middle panel show the tilted circulation on the forward side of the tornado. Representative vortex lines associated with the HVs are displayed in light orange, with circular arrows indicating their sense of rotation. Strong surface RFD flow is indicated by the curved black arrows. Right column: The cloud field associated with a tornado producing HVs consistent with the vorticity field displayed in the right column and visual observations. The RFD-related clear slot is annotated. The storm is moving to the northeast, as indicated by the red arrow the upper panel.

Finally, it is important to point out that the 1.5-order TKE-based subgrid-scale turbulence parameterization with a mixing length $(\Delta x \Delta y \Delta z)^{1/3}$ can result in relatively large vertical mixing relative to the vertical grid spacing. This would imply rather large vertical turbulence mixing and more efficient transfer of (negative) surface momentum flux (due to surface drag) upward into the flow above ground. The subgrid-scale turbulence parameterization near a rigid wall (Chow et al. 2005) and with a large grid aspect ratio (Xue et al. 2001; Nishizawa et al. 2015) are issues that can potentially affect near-ground tornado dynamics and deserve further investigation.

4.3.2 Behavior of trailing HVs based on the 30-m simulation

A combined analysis of videos of the 27 April 2011 Tuscaloosa EF4 tornado and 3D visualizations of a 30-m grid spacing simulation based on the same tornado reveals a distinct type of HV structure termed “trailing HV”. As the name indicates, this type of vortex trails the tornado and is attached to its right flank and immediately above the surface, producing visually impressive helical motions consistent with vorticity generation via surface friction or baroclinity along warm RFD internal boundaries. Unlike previously documented HVs, which are typically smaller than the tornado and move along with its outer flow, trailing HVs are larger and strong enough to interact with the tornado for longer periods and maintain a semi-stationary tornado-relative position, without being advected around and distorted significantly. An intriguing aspect of trailing HVs is that they occasionally display smaller vortices around them. The tail of these vortices leans outward with height while they move crosswise relative to the outer periphery of the trailing HV axis and rotate around the base of the tornado, such that their vertical component of vorticity is clockwise or anticyclonic. When reaching the forward sector of the tornado, they may evolve into spiral structures with the leading portion being advected upward into the tornado’s upper flow and contribute cyclonic vorticity to tornado circulation. Spiral structures are commonly observed in

tornadoes during vortex breakdown (Fiedler 2009; Dahl 2021). In the case of the small vortices discussed here, though, vortex breakdown dynamics seems unlikely to explain their spiral structures, since they do not appear to be rooted at the ground as vertical vortices and may be later advected upward. Rather, it seems plausible to assume that, based on the tornado videos and simulation visualizations, the spiraling structures result from the combined wind fields of the trailing HV and the tornado acting to deform the smaller vortices. To the authors' knowledge, this is the first study to document such vortical structures in the context of tornado dynamics.

Visualizations of the simulated three-dimensional vorticity magnitude field show that the trailing HV forms as an amalgamation of mainly streamwise HVs originating in the RFD near-surface outflow (presumably produced by frictional effects) west and south of the tornado. An internal convergence boundary attached to the east-southeast flank of the tornado acts as a corridor where the HVs accumulate, realign (with the flow turning into the direction of HV rotation axis so that the horizontal velocity and vorticity vectors become aligned), and are subsequently intensified via stretching of streamwise horizontal vorticity. The induced velocity field of neighboring quasi-parallel large HVs causes them to entangle and subsequently evolve into long intertwined vortices; this entangling process is the essence of the trailing HV structure. Furthermore, the vortex entangling process also explains the smaller, spiraling vortices observed in the videos of the Tuscaloosa tornado. The small vortices, initially quasi-horizontal, arise at the tail of the trailing HV and are twisted (i.e., tilted downward) by the trailing HV, such that their "heads" move underneath and along the trailing HV, while their tail becomes quasi-vertical and rotates clockwise. Analogous entangling of quasi-parallel vortices is known to occur in low-Reynolds-number simulations, but has not been extensively studied in the context of supercell or tornado dynamics.

A conceptual model summarizing proposed formation mechanisms of trailing HVs, as well as their relationship with the internal convergence boundary and smaller vortices is provided in Fig. 4.21.

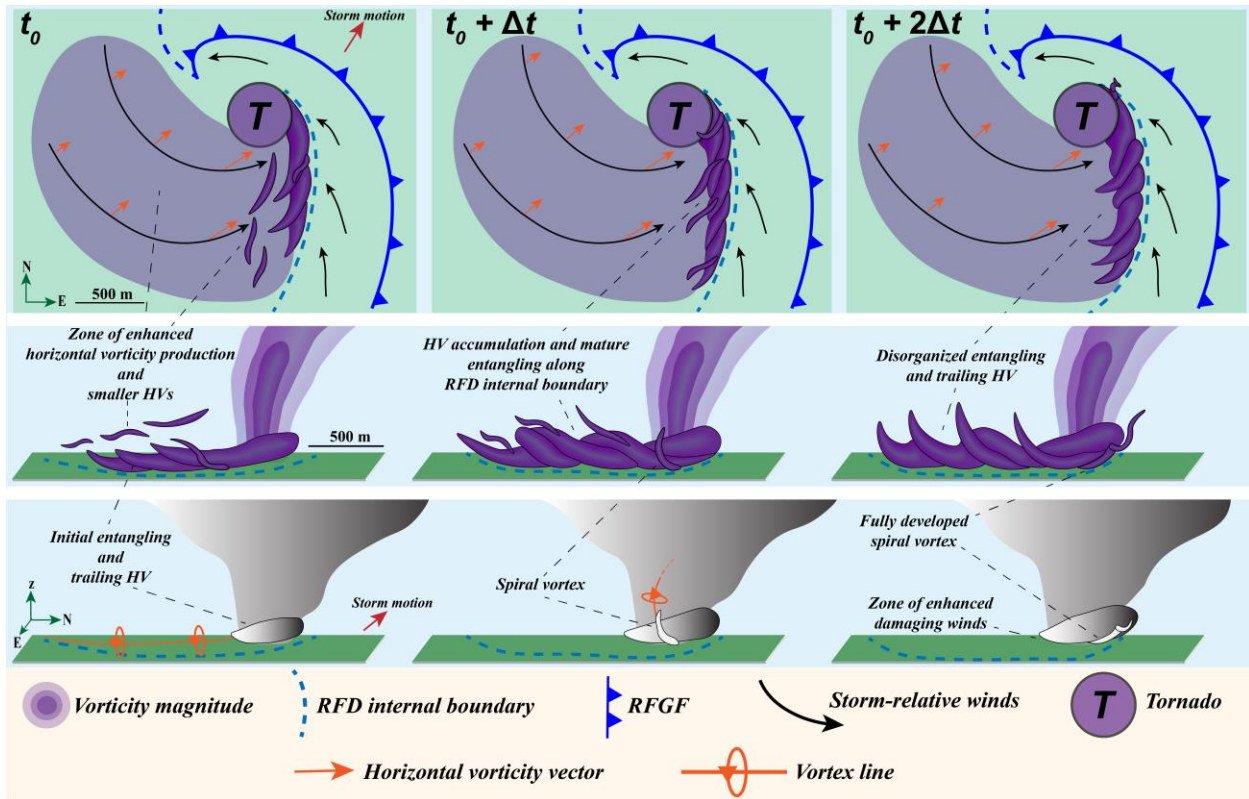


Fig. 4.21. Conceptual model for the evolution of the trailing HV and spiraling vortices as related to surrounding storm-scale features. Top panel: top view of the three-dimensional vorticity magnitude field. Middle panel: three-dimensional vorticity magnitude field viewed from the northeast. Bottom panel: cloud field consistent with the visual observations viewed from the northeast. In all panels, time advances from the left to the right. All relevant symbols are defined in the bottom section of the figure. At t_0 , predominantly crosswise horizontal vorticity which is produced in the RFD outflow evolves into coherent HVs that align and accumulate in the vicinity of an internal boundary east-southeast of the tornado. As large and small HVs interact in that zone, their self-induced wind fields initiate an entangling process. By $t_0 + \Delta t$, the HVs have fully intertwined and grown into a complex vortex entanglement, visually observed as a large helical HV. As the entangling continues, some smaller HVs as well as the tails of the larger HVs may bend downward, producing small spiraling anticyclonic vortices in the outer edge of the HV. By $t_0 + 2\Delta t$, the entangling begins to disorganize, as seen by the increasingly distortion larger vortices composing the trailing HVs. Spiraling vortices continue to occur during this stage.

One of the videos of the Tuscaloosa tornado (Rosolowski's video) shows damage to structures near the region where a trailing HV tangents the tornado. An analysis of the low-level winds during the mature stage of the simulated trailing HV shows that the combined wind fields of the tornado's outer updraft and the upward branch of the trailing HV resemble a rotor-type circulation that potentially enhances upward and horizontal winds very close to the surface, where significant damage may result. Larger-scale rotor-type circulations have been observed in simulated quasi-linear convective systems (Schenkman et al. 2012) and tornadic supercells (Schueth et al. 2021) and are associated with enhanced upward motion and horizontal vorticity. It is possible that the trailing HV documented in this study represents an additional class of rotor circulation in severe storms.

Finally, a few considerations regarding real and simulated trailing HVs must be made. First, since this is the first study to document trailing HVs, their frequency of occurrence is unknown. Trailing HVs have a higher degree of coherency compared to smaller (turbulent) HVs, given their apparent association with internal RFD boundaries. It seems plausible to assume that similar structures eventually occur in other strong/violent tornadoes, but are not readily visualized as condensation tubes (when the pressure drop inside is not large enough, at least away from the tornado). It is also possible that such structures are simply too rare and go unreported in most situations. The ever-increasing availability of close-range mobile Doppler radar, as well as visual observations of tornadoes may eventually elucidate these concerns. Second, surface friction was implied as the most likely vorticity generation mechanism for trailing HVs. Nevertheless, it is known that the use of semi-slip lower boundary conditions in severe storm simulations is problematic, resulting in overestimates of near-ground horizontal vorticity in the storm's inflow due to insufficient resolved turbulence (Markowski and Bryan 2016), intrinsic artificial problem

of the GWB technique used herein (Davies-Jones 2021) and underestimation in the outflow due to violations of the Monin-Obukhov similarity assumptions (Markowski et al. 2019). The reasonable match between the visual observations of the trailing HVs and their simulated counterpart suggest that these issues, although present in the simulation, do not hamper the qualitative interpretation of the results presented in this study. Lastly, the results also underscore the importance of studying interactions between tornadoes and their nearby turbulent outflow (Takahashi et al. 2005). Further investigation of these processes can lead to a broader understanding of the spectrum of behaviors and structures that tornadoes display in nature. Detailed quantitative analyses of the vorticity sources of HVs and other related processes are underway and will be reported elsewhere.

Chapter 5: Summary and Future Work

In this dissertation, idealized, high-resolution numerical simulations of supercells conducted with the Advanced Regional Prediction System (ARPS) were performed with the objective of better understanding important characteristics of cyclic tornadogenesis and horizontal vortices (HVs) sometimes observed near tornadoes. Three simulations with grid spacings of 100-, 50-, and 30-m, respectively, were investigated: the 50-m simulation was used in the analysis of cyclic tornadogenesis, while the 30-m simulation was used to analyze the HVs; the 100-m simulation is an early version of the 50- and 30-m simulations, which used different model configurations and was also used to analyze several aspects of HVs. Considering that surface friction has been shown to play a significant role in the dynamics of tornadoes (including and in the generation of HVs), its effects have been included in all experiments via parameterized surface drag using a drag coefficient (C_d) = 0.028, corresponding to roughness length of 9.16 cm. Since surface friction tends to continuously slow down the wind profile near the surface, thus undesirably modifying the base-state environment as the storm evolves, the Geotriptic Wind Balance (GWB) method was used to mitigate this issue. This method allows an idealized numerical simulation to be initialized using an input arbitrary sounding (in this case, extracted from another model output dataset) and drag coefficient and remain in a three-way force balance between the horizontal pressure gradient, Coriolis, and frictional forces during the duration of the model integration. The 100-m experiment used a model-derived sounding from a 3-km grid spacing Weather Research and Forecasting (WRF) model ensemble-mean analysis of the 27 April 2011 EF4 Tuscaloosa tornado as initial condition. The 50- and 30-m experiments used a similar sounding, but with stronger environmental winds below 2 km AGL (obtained artificially via sensitivity experiments).

Cyclic tornadogenesis is investigated in the 50-m simulation to address how the evolution of the supercell at high resolution deviates from previous conceptual models of cyclic tornadogenesis/mesocyclogenesis, particularly, how different tornado cycles affect each other subsequently. Four tornadoes developed cyclically in the simulated supercell during the 16200 s (4 h 30 min) duration of model time integration. The characteristics of each tornado varied significantly from cycle to cycle, as did the supercell structure associated with each of them. Despite these differences, the supercell did produce tornadoes at relatively regular intervals, with an average cycling frequency of 35.2 min, well within the range found for other numerically simulated or observed supercells. Tornadoes 1, 2, and 4 attain EF5 strength (though tornadoes 2 and 4 only reach such intensity briefly), while one tornado 3 only briefly attained EF3 intensity and evolved in rather different way than the other tornadoes. The main reason for the remarkable differences between each tornado cycle are related to the transition of supercell from an originally “classic” morphology to a high-precipitation (HP) mode. Tornado 1 developed during the “classic phase” of the supercell, remaining removed from the strongest precipitation core of the storm and colder outflow for several minutes. When the tornado’s parent low-level updraft occluded, tornado 1 finally become encircled in precipitation, initially intensifying (attaining peak strength), as it moved underneath its parent midlevel updraft, but later dissipated embedded in rain and outflow. After tornado 1 decayed, a large amount of precipitation was produced in the rear-flank of the storm, which was rapidly advected into the low-level updraft associated with developing tornado 2, causing it to occlude as it formed. As tornado 2 decayed, a large surface circulation persisted for several minutes embedded in precipitation. As tornado 3 formed, it was quickly ingested by the lingering low-level circulation of tornado 2, such that the tornado never underwent drastic intensification under an organized low-level updraft for a prolonged period as did the other

tornadoes. After the dissipation of tornado 3, the supercell reorganized once again to produce tornado 4, which occluded, intensified rapidly, and decayed embedded in precipitation similar to tornado 2. The increasingly disorganized and HP character of the supercell is partially attributed to a complex evolution of the storm's midlevel updrafts. Unlike classic cyclic mesocyclogenesis conceptual models, the occluded midlevel updrafts in the simulated supercell often merged with newly developed updrafts, either bearing a new tornado or triggered along the southern extent of the surface outflow boundary. This induced a convoluted distribution of midlevel downdrafts that tended to produce increasing amounts of precipitation at the storm's rear flank, and closer to developing tornadoes. All tornado cycles were preceded and developed southwest of low-pressure lobes (LPLs) located in the inflow sector of the tornadoes. These LPLs form due to accelerating low-level inflow into the intensifying tornadic updrafts. These structures were associated with zones of enhanced near-surface streamwise environmental vorticity, suggesting that the supercell can locally intensify the surrounding vorticity field and further strengthen its low-level updrafts dynamically.

Interactions between tornadoes and HVs were investigated first in the 100-m simulation. Despite the relatively coarse grid spacing for resolving fine-scale structures, important insights regarding HV-tornado interactions were found. By visualizing and comparing the simulated 3D vorticity magnitude field to visual observations of the real Tuscaloosa tornado, it was shown that HVs usually appear within the rear-flank downdraft (RFD) or the outer tornadic flow at low levels and on the back and right sectors of the tornado (in a tornado-relative sense). As the HVs are lifted in updrafts outside the tornado, they encircle the tornado, with larger HVs maintain the shapes and position relative to the tornado, while small HVs are quickly distorted by surrounding turbulent flow. HVs located farther from the tornado (in less turbulent flow) may maintain their structure

for longer periods. A closer inspection of a large HV interacting with the simulated tornado reveals that HVs are advected toward the forward sector of the tornado with time, eventually coupling with the forward portion of the secondary circulation of the tornado, which is distorted by the tornado fast forward motion. When this occurs, the vortex aligns azimuthally with the outer tornado flow, sometimes developing into a downward-bending or U-shaped structure. Abrupt acceleration of the air into the HV at this stage may cause enough cyclostrophic pressure drop in its core and induce condensation formation. The apparently passive behavior of HVs relative to the tornado in the 100-m simulation is representative of most HVs observed in real tornadoes. Analysis of the near-surface vorticity field around HVs and their typical sense of rotation in visual observations show that they emerged from strong crosswise horizontal vorticity presumably produced via surface drag, baroclinity along warm RFD internal surges (RFDISs), or a combination of both.

Further analyses of tornado-HV interactions were conducted using the 30-m simulation and additional visual observations of the Tuscaloosa tornado. This combined analysis revealed a type of HV that has different characteristics from the ones described above, which was referred to as “trailing HV”, as this vortex closely trailed the right flank of the of the fast-moving tornado. Trailing HVs differed from regular HVs particularly because they were much larger, more intense, last longer, and maintain their tornado-relative position for longer periods. Nonetheless, the sense of rotation of trailing HVs was the same as their smaller counterparts, possibly a result of frictionally generated crosswise horizontal vorticity within the storm’s rear-flank outflow. Interestingly, smaller vortices formed in the tail end of the trailing HV and moved along its outer edge and around the base of the tornado. These small vortices, initially quasi-horizontally oriented, were tilted downward when moving along the trailing HV outer portion, such that their tails

pointed upward producing anticyclonic (clockwise) vertical vorticity. One of the small vortices developed a spiral structure at its tail end that was hypothesized to result from deformation or some instability induced by sharp velocity gradients between the tornado and the trailing HV. The vortical structure seen in visualizations of the 3D vorticity field of the 30-m simulation that is thought to be model-equivalent of the visually observed trailing HV for as horizontal vortex tubes formed in the rear-flank outflow within near-ground crosswise horizontal vorticity accumulated along an RFD internal boundary adjacent to the east-southeast flank of the tornado. When accumulating, the vortex tubes entangled, giving rising to a “spaghetti”-like structure; occasionally, smaller vortices at the tail end of the trailing HV were depleted and distorted in a similar way as the observed spiral vortices previously mentioned. Along the RFD internal boundary, horizontal vorticity vectors aligned with the local velocity vectors producing an elongated band of horizontal streamwise vorticity that was stretched in the confluent flow. Cross sections taken in the sector where the trailing HV tangents the tornado revealed its rotor-like structure analogous to other rotors observed in supercells and quasi-linear convective systems. These cross sections, coupled with a close-range video of the trailing HV, suggested that its interaction with the tornado may produce locally enhanced winds speeds, though more quantitative analyses are needed in order to make more definitive statements about this feature.

The work presented in this dissertation, though essentially qualitative, adds relevant components to our understanding of tornadic storms. In particular, the LPL structure and its relationship with tornado cycling, must be further investigated. How often and what under circumstances is the appearance of an LPL associated with tornado formation? These questions could not be addressed in the current single (50-m) simulation because all mesocyclone cycles do produce tornadoes. Ensemble simulations similar to those of Coffey et al. (2017) and Markowski

(2020) using other initial soundings can be used to address these questions. Another interesting feature related to the LPLs is the band of enhanced environmental streamwise vorticity near the surface. Observational studies have documented areas of enhanced storm-relative helicity in the inflow sector of tornadic supercells (Wade et al. 2018). Acceleration of inflow into the low-level updraft seems to be of primary importance for generating this type structure. In addition, surface friction is likely to play a significant role in its development due to its proximity to the surface (Dowell and Bluestein 2002a). Future quantitative investigations of this simulation can employ vorticity budget analyses along trajectories to determine the formation mechanisms of these vorticity bands and their impacts on tornadogenesis. This is also an opportunity to address the issues raised by Davies-Jones (2021), so that it is possible to determine how much of the vorticity in and around the storm is physical or produced by spurious sources. Finally, future work should also investigate more objectively the interactions between HVs and tornadoes. In low-Reynolds number simulations of isotropic turbulence, small-scale vortex filaments (so-called “worms”) are known to induce instabilities on larger columnar vortices (Takahashi et al. 2005). To which extent an analogy can be made regarding tornadoes and HVs is unknown. Perhaps highly idealized “toy” model simulations can be used to address this question and the vortex entangling process by which trailing HVs develop.

References

- Adlerman, E. J., and K. K. Droegemeier, 2000: A numerical simulation of cyclic tornadogenesis. *Preprints, 20th Conf. on Severe Local Storms, Orlando, FL, Amer. Meteor. Soc.*
- Adlerman, E. J., and K. K. Droegemeier, 2002: The sensitivity of numerically simulated cyclic mesocyclongenesis to variations in model physical and computational parameters. *Mon. Wea. Rev.*, **130**, 2671-2691.
- Adlerman, E. J., and K. K. Droegemeier, 2005: The dependence of numerically simulated cyclic mesocyclongenesis upon environmental vertical wind shear. *Mon. Wea. Rev.*, **133**, 3595-3623.
- Adlerman, E. J., K. K. Droegemeier, and R. Davies-Jones, 1999: A Numerical Simulation of Cyclic Mesocyclongenesis. *Journal of the Atmospheric Sciences*, **56**, 2045-2069.
- Agee, E., and E. Jones, 2009: Proposed conceptual taxonomy for proper identification and classification of tornado events. *Wea. and Forecasting*, **24**, 609-617.
- Agee, E. M., 2014: A Revised Tornado Definition and Changes in Tornado Taxonomy. *Weather and Forecasting*, **29**, 1256-1258.
- Agee, E. M., J. T. Snow, and P. R. Clare, 1976: Multiple vortex features in the tornado cyclone and the occurrence of tornado families. *Mon. Wea. Rev.*, **104**, 552-563.
- Ashley, W. S., A. M. Haberlie, and J. Strohm, 2019: A Climatology of Quasi-Linear Convective Systems and Their Hazards in the United States. *Weather and Forecasting*, **34**, 1605-1631.
- Atkins, N. T., M. L. Weisman, and L. J. Wicker, 1999: The Influence of Preexisting Boundaries on Supercell Evolution. *Mon. Wea. Rev.*, **127**, 2910-2927.
- Atkins, N. T., K. M. Butler, K. R. Flynn, and R. M. Wakimoto, 2014: An integrated damage, visual, and radar analysis of the 2013 Moore, Oklahoma, EF5 tornado. *Bulletin of the American Meteorological Society*, **95**, 1549-1561.

Atkins, N. T., J. M. Arnott, R. W. Przybylinski, R. A. Wolf, and B. D. Ketcham, 2004: Vortex Structure and Evolution within Bow Echoes. Part I: Single-Doppler and Damage Analysis of the 29 June 1998 Derecho. *Mon. Wea. Rev.*, **132**, 2224-2242.

Bai, L., and Coauthors, 2017: An Integrated Damage, Visual, and Radar Analysis of the 2015 Foshan, Guangdong, EF3 Tornado in China Produced by the Landfalling Typhoon Mujigae (2015). *Bulletin of the American Meteorological Society*, **98**, 2619-2640.

Barnes, S. L., 1978a: Oklahoma thunderstorms on 29-30 April 1970. Part II: Radar-observed merger of hook echoes. *Mon. Wea. Rev.*, **106**, 685-696.

——, 1978b: Oklahoma thunderstorms on 29-30 April 1970. Part I: Morphology of a tornadic storm. *Mon. Wea. Rev.*, **106**, 673-684.

Beck, J., and C. Weiss, 2013: An Assessment of Low-Level Baroclinity and Vorticity within a Simulated Supercell. *Monthly Weather Review*, **141**, 649-669.

Beck, J. R., J. L. Schroeder, and J. M. Wurman, 2006: High-Resolution Dual-Doppler Analyses of the 29 May 2001 Kress, Texas, Cyclic Supercell. *Monthly Weather Review*, **134**, 3125-3148.

Betten, D. P., M. I. Biggerstaff, and C. L. Ziegler, 2018: Three-dimensional storm structure and low-level boundaries at different stages of cyclic mesocyclone evolution in a high-precipitation tornadic supercell. *Advances in Meteorology*, **2018**.

Bluestein, H. B., 1985: The formation of a "landspout" in a "broken-line" squall line in Oklahoma. *14th Conf. on Severe Local Storms, American Meteorological Society*.

Bluestein, H. B., 2009: The Formation and Early Evolution of the Greensburg, Kansas, Tornadic Supercell on 4 May 2007. *Weather and Forecasting*, **24**, 899-920.

Bluestein, H. B., M. M. French, J. C. Snyder, and J. B. Houser, 2016: Doppler radar observations of anticyclonic tornadoes in cyclonically rotating, right-moving supercells. *Monthly Weather Review*, **144**, 1591-1616.

Bluestein, H. B., K. J. Thiem, J. C. Snyder, and J. B. Houser, 2018: The Multiple-Vortex Structure of the El Reno, Oklahoma, Tornado on 31 May 2013. *Monthly Weather Review*, **146**, 2483-2502.

———, 2019: Tornadogenesis and Early Tornado Evolution in the El Reno, Oklahoma, Supercell on 31 May 2013. *Monthly Weather Review*, **147**, 2045-2066.

Bluestein, H. B., M. M. French, R. L. Tanamachi, S. Frasier, K. Hardwick, F. Junyent, and A. L. Pazmany, 2007a: Close-Range Observations of Tornadoes in Supercells Made with a Dual-Polarization, X-Band, Mobile Doppler Radar. *Monthly Weather Review*, **135**, 1522-1543.

Bluestein, H. B., C. C. Weiss, M. M. French, E. M. Holthaus, R. L. Tanamachi, S. Frasier, and A. L. Pazmany, 2007b: The Structure of Tornadoes near Attica, Kansas, on 12 May 2004: High-Resolution, Mobile, Doppler Radar Observations. *Monthly Weather Review*, **135**, 475-506.

Bluestein, H. B., and Coauthors, 2013: Observations of the Boundary Layer near Tornadoes and in Supercells Using a Mobile, Collocated, Pulsed Doppler Lidar and Radar. *Journal of Atmospheric and Oceanic Technology*, **31**, 302-325.

Boyer, C. H., and J. M. L. Dahl, 2020: The Mechanisms Responsible for Large Near-Surface Vertical Vorticity within Simulated Supercells and Quasi-Linear Storms. *Monthly Weather Review*, **148**, 4281-4297.

Brandes, E. A., 1984: Vertical vorticity generation and mesocyclone sustenance in tornadic thunderstorms: The observational evidence. *Mon. Wea. Rev.*, **112**, 2253-2269.

Brandes, E. A., and R. P. D.-J. B. C. Johnson, 1988: Streamwise vorticity effects on supercell morphology and persistence. *J. Atmos. Sci.*, **45**, 947-963.

Britt, K. C., P. S. Skinner, P. L. Heinselman, and K. H. Knopfmeier, 2020: Effects of Horizontal Grid Spacing and Inflow Environment on Forecasts of Cyclic Mesocyclogenesis in NSSL's Warn-on-Forecast System (WoFS). *Weather and Forecasting*, **35**, 2423-2444.

Brooks, H. E., J. W. Lee, and J. P. Craven, 2003: The spatial distribution of severe thunderstorm and tornado environments from global reanalysis data. *Atmos. Res.*, **67-68**, 73-94.

Brown, J. M., and K. R. Knupp, 1980: The Iowa cyclonic-anticyclonic tornado pair and its parent thunderstorm. *Mon. Wea. Rev.*, **108**, 1626-1646.

Browning, K. A., 1964: Airflow and precipitation trajectories within severe local storms which travel to the right of the mean winds. *J. Atmos. Sci.*, **21**, 634-639.

Browning, K. A., and F. H. Ludlam, 1962: Airflow in convective storms. *Quart. J. Roy. Meteor. Soc.*, **88**, 117- 135.

Browning, K. A., and R. J. D. and, 1963: Airflow and structure of a tornadic storm. *J. Atmos. Sci.*, **20**, 533-545.

Burgess, D. W., V. T. Wood, and R. A. Brown, 1982: Mesocyclone evolution statistics. *Preprints, Twelfth Conference on Severe Local Storms*, San Antonio, TX, Amer. Meteor. Soc., Boston, 422-424.

Byers, H. R., and R. R. Braham, 1949: The Thunderstorm: Report of the Thunderstorm Project, 287 pp.

Chow, F., R. Street, M. Xue, and J. Ferziger, 2005: Explicit filtering and reconstruction turbulence modeling for large-eddy simulation of neutral boundary layer flow. *Journal of the Atmospheric Sciences*, **62**, 2058-2077.

Church, C., D. Burges, C. Doswell, and R. Davies-Jones, Eds., 1993: *The Tornado: Its Structure, Dynamics, Prediction, and Hazards*. American Geophysical Union, 637 pp.

Church, C. R., J. T. Snow, G. L. Baker, and E. M. Agee, 1979: Characteristics of Tornado-Like Vortices as a Function of Swirl Ratio: A Laboratory Investigation. *Journal of Atmospheric Sciences*, **36**, 1755-1776.

Coffer, B. E., and M. D. Parker, 2015: Impacts of increasing low-level shear on supercells during the early evening transition. *Monthly Weather Review*, **143**, 1945-1969.

Coffer, B. E., and M. D. Parker, 2017: Simulated supercells in nontornadic and tornadic VORTEX2 environments. *Mon. Wea. Rev.*, **145**, 149–180.

Coffer, B. E., and M. D. Parker, 2018: Is there a "tipping point" between simulated nontornadic and tornadic supercells in VORTEX2 environments? *Monthly Weather Review*, **146**, 2667-2693.

Coffer, B. E., M. D. Parker, J. M. L. Dahl, L. J. Wicker, and A. J. Clark, 2017: Volatility of tornadogenesis: An ensemble of simulated nontornadic and tornadic supercells in VORTEX2 environments. *Monthly Weather Review*, **145**, 4605-4625.

Coffer, B. E., M. D. Parker, R. L. Thompson, B. T. Smith, and R. E. Jewell, 2019: Using Near-Ground Storm Relative Helicity in Supercell Tornado Forecasting. *Weather and Forecasting*, **34**, 1417-1435.

Dahl, J. M. L., 2015: Near-ground rotation in simulated supercells: On the robustness of the baroclinic mechanism. *Monthly Weather Review*, **143**, 4929–4942.

———, 2021: Centrifugal Waves in Tornado-like Vortices: Kelvin's solutions and their Applications to Multiple-Vortex Development and Vortex Breakdown. *Monthly Weather Review*.

Dahl, J. M. L., M. D. Parker, and L. J. Wicker, 2014: Imported and storm-generated near-ground vertical vorticity in a simulated supercell. *Journal of the Atmospheric Sciences*, **71**, 3027-3051.

Darkow, G. L., and J. C. Roos, 1970: Multiple tornado producing thunderstorms and their apparent cyclic variations in intensity. Preprints, . *14th Conf. on Radar Meteorology*, Tucson, AZ, Amer. Meteor. Soc., 305–308.

Davidson, P. A., 2015: *Turbulence: an introduction for scientists and engineers*. Oxford university press.

Davies-Jones, R., 2008: Can a descending rain curtain in a supercell instigate tornadogenesis barotropically? *J. Atmos. Sci.*, **65**, 2469-2496.

Davies-Jones, R., 2021: Invented Forces in Supercell Models. *Journal of the Atmospheric Sciences*.

Davies-Jones, R. P., 1984: Streamwise vorticity: The origin of updraft rotation in supercell storms. *J. Atmos. Sci.*, **41**, 2991-3006.

———, 2015: A review of supercell and tornado dynamics. *Atmospheric Research*, **158–159**, 274–291.

Davies-Jones, R. P., and H. Brooks, 1993: Mesocyclogenesis from a theoretical perspective. *The Tornado: Its Structure, Dynamics, Prediction, and Hazards*, C. R. Church, Ed., Amer. Geophys. Union Press, 105-114.

Davies-Jones, R. P., R. J. Trapp, and H. B. Bluestein, 2001: Tornadoes and tornadic storms. *Severe Convective Storms*, C. A. Doswell, III, Ed., Amer. Meteor. Soc., 167-222.

Dawson, D. T., B. Roberts, and M. Xue, 2019: A Method to Control the Environmental Wind Profile in Idealized Simulations of Deep Convection with Surface Friction. *Monthly Weather Review*, **147**, 3935-3954.

Dawson, D. T., M. Xue, J. A. Milbrandt, and A. Shapiro, 2015: Sensitivity of Real-Data Simulations of the 3 May 1999 Oklahoma City Tornadic Supercell and Associated Tornadoes to

Multimoment Microphysics. Part I: Storm- and Tornado-Scale Numerical Forecasts. *Mon. Wea. Rev.*, **143**, 2241-2265.

Dawson, D. T., II, M. Xue, J. A. Milbrandt, and M. K. Yau, 2010: Comparison of evaporation and cold pool development between single-moment and multi-moment bulk microphysics schemes in idealized simulations of tornadic thunderstorms. *Mon. Wea. Rev.*, **138**, 1152-1171.

Doswell, C. A., III, and D. W. Burgess, 1993: Tornadoes and tornadic storms: A review of conceptual models. *The Tornado: Its Structure, Dynamics, Prediction, and Hazards, Geophys. Monogr.*, Amer. Geophys. Union, 75-88.

Dowell, D. C., and H. B. Bluestein, 2002a: The 8 June 1995 McLean, Texas, Storm. Part II: Cyclic Tornado Formation, Maintenance, and Dissipation. *Monthly Weather Review*, **130**, 2649-2670.

———, 2002b: The 8 June 1995 McLean, Texas, Storm. Part I: Observations of Cyclic Tornadogenesis. *Monthly Weather Review*, **130**, 2626-2648.

Edwards, R., J. G. LaDue, J. T. Ferree, K. Scharfenberg, C. Maier, and W. L. Coulbourne, 2013: Tornado Intensity Estimation: Past, Present, and Future. *Bulletin of the American Meteorological Society*, **94**, 641-653.

Fiedler, B., 2009: Suction vortices and spiral breakdown in numerical simulations of tornado-like vortices. *Atmospheric Science Letters*, **10**, 109-114.

Finley, C. A., L. Orf, B. D. Lee, and R. B. Wilhelmson, 2018: High-Resolution Simulation of a Violent Tornado in the 27 April 2011 Outbreak Environment. *29th Conf. on Severe Local Storms*, Stowe, VT, Amer. Meteor. Soc.

Fischer, J., and J. M. L. Dahl, 2020: The Relative Importance of Updraft and Cold Pool Characteristics in Supercell Tornadogenesis Using Highly Idealized Simulations. *Journal of the Atmospheric Sciences*, **77**, 4089-4107.

Flournoy, M. D., M. C. Coniglio, E. N. Rasmussen, J. C. Furtado, and B. E. Coffey, 2020: Modes of Storm-Scale Variability and Tornado Potential in VORTEX2 Near- and Far-Field Tornadic Environments. *Monthly Weather Review*, **148**, 4185-4207.

Forbes, G. S., and R. M. Wakimoto, 1983: A concentrated outbreak of tornadoes, downbursts and microbursts, and implications regarding vortex classification. *Mon. Wea. Rev.*, **111**, 220-235.

French, M. M., and D. M. Kingfield, 2019: Dissipation Characteristics of Tornadic Vortex Signatures Associated with Long-Duration Tornadoes. *Journal of Applied Meteorology and Climatology*, **58**, 317-339.

French, M. M., P. S. Skinner, L. J. Wicker, and H. B. Bluestein, 2015: Documenting a Rare Tornado Merger Observed in the 24 May 2011 El Reno–Piedmont, Oklahoma, Supercell. *Monthly Weather Review*, **143**, 3025-3043.

French, M. M., H. B. Bluestein, D. C. Dowell, L. J. Wicker, M. R. Kramar, and A. L. Pazmany, 2008: High-Resolution, Mobile Doppler Radar Observations of Cyclic Mesocyclogenesis in a Supercell. *Monthly Weather Review*, **136**, 4997-5016.

Fujita, T. T., 1971: A proposed characterization of tornadoes and hurricanes by area and intensity. Dept. of Geophysical Sciences, University of Chicago SMRP Res. Paper 91, 42 pp.

———, 1981: Tornadoes and downbursts in the context of generalized planetary scales. *J. Atmos. Sci.*, **38**, 1511-1534.

Fujita, T. T., and H. Grandoso, 1968: Split of a thunderstorm into anticyclonic and cyclonic storms and their motion as determined from numerical model experiments. *J. Atmos. Sci.*, **25**, 4164-39.

Fujita, T. T., D. L. Bradbury, and C. F. V. Thullenar, 1970: Palm Sunday tornadoes of April 11, 1965. *Mon. Wea. Rev.*, **98**, 29-69.

Glickman, T. S., Ed., 2000: *Glossary of Meteorology, 2nd Edition*. American Meteorological Society, 855 pp.

Goldacker, N. A., and M. D. Parker, 2021: Low-level Updraft Intensification in Response to Environmental Wind Profiles. *Journal of the Atmospheric Sciences*.

Golden, J. H., 1971: Waterspouts and tornadoes over south Florida. *Mon. Wea. Rev.*, **99**, 146-154.

Grasso, L. D., and W. R. Cotton, 1995: Numerical simulation of a tornado vortex. *J. Atmos. Sci.*, **52**, 1192-1203.

Griffin, C. B., D. J. Bodine, J. M. Kurdzo, A. Mahre, and R. D. Palmer, 2019: High-Temporal Resolution Observations of the 27 May 2015 Canadian, Texas, Tornado Using the Atmospheric Imaging Radar. *Monthly Weather Review*, **147**, 873-891.

Grzych, M. L., B. D. Lee, and C. A. Finley, 2007: Thermodynamic analysis of supercell rear-flank downdrafts from project ANSWERS. *Mon. Wea. Rev.*, **135**, 240-246.

Guchte, A. V., and J. M. L. Dahl, 2018: Sensitivities of Parcel Trajectories beneath the Lowest Scalar Model Level of a Lorenz Vertical Grid. *Monthly Weather Review*, **146**, 1427-1435.

Hirth, B. D., J. L. Schroeder, and C. C. Weiss, 2008: Surface analysis of the rear-flank downdraft outflow in two tornadic supercells. *Mon. Wea. Rev.*, **136**, 2344-2363.

Houser, J. L., H. B. Bluestein, and J. C. Snyder, 2015: Rapid-Scan, Polarimetric, Doppler Radar Observations of Tornadogenesis and Tornado Dissipation in a Tornadic Supercell: The “El Reno, Oklahoma” Storm of 24 May 2011. *Monthly Weather Review*, **143**, 2685-2710.

———, 2016: A finescale radar examination of the tornadic debris signature and weak-echo reflectivity band associated with a large, violent tornado. *Monthly Weather Review*, **144**, 4101-4130.

Jiménez, J., A. A. Wray, P. G. Saffman, and R. S. Rogallo, 1993: The structure of intense vorticity in isotropic turbulence. *Journal of Fluid Mechanics*, **255**, 65-90.

Johnson, K. W., P. S. Ray, B. C. Johnson, and R. P. Davies-Jones, 1987: Observations related to the rotational dynamics of the 20 May 1977 tornadic storms. *Mon. Wea. Rev.*, **115**, 2463-2478.

Karstens, C. D., W. A. Gallus, B. D. Lee, and C. A. Finley, 2013: Analysis of Tornado-Induced Tree Fall Using Aerial Photography from the Joplin, Missouri, and Tuscaloosa?Birmingham, Alabama, Tornadoes of 2011. *Journal of Applied Meteorology and Climatology*, **52**, 1049-1068.

Klemp, J. B., 1987: Dynamics of tornadic thunderstorms. *Annul Rev. Fluid. Mech.*, **19**, 369-402.

Klemp, J. B., and R. B. Wilhelmson, 1978a: The simulation of three-dimensional convective storm dynamics. *J. Atmos. Sci.*, **35**, 1070-1096.

——, 1978b: Simulations of right- and left-moving thunderstorms produced through storm splitting. *J. Atmos. Sci.*, **35**, 1097-1110.

Klemp, J. B., and M. L. Weisman, 1983: The dependence of convective precipitation patterns on vertical wind shear. *Preprints, 21st Conf. on Radar Meteorology*, Edmonton, Amer. Meteor. Soc., 44-49.

Klemp, J. B., and R. Rotunno, 1983: A study of the tornadic region within a supercell thunderstorm. *J. Atmos. Sci.*, **40**, 359-377.

Knupp, K. R., and Coauthors, 2014: Meteorological Overview of the Devastating 27 April 2011 Tornado Outbreak. *Bulletin of the American Meteorological Society*, **95**, 1041-1062.

Kosiba, K., J. Wurman, Y. Richardson, P. M. Markowski, P. Robinson, and J. Marquis, 2013: Genesis of the Goshen County, Wyoming tornado on 05 June 2009 during VORTEX2. *Mon. Wea. Rev.*, **141**, 1157-1181.

Kosiba, K. A., and J. Wurman, 2013: The Three-Dimensional Structure and Evolution of a Tornado Boundary Layer. *Weather and Forecasting*, **28**, 1552-1561.

Lee, B. D., and R. B. Wilhelmson, 1997a: The numerical simulation of non-supercell tornadogenesis. Part I: Initiation and evolution of pretornadic mesocyclone circulations along a dry outflow boundary. *J. Atmos. Sci.*, **54**, 32-60.

———, 1997b: The numerical simulation of non-supercell tornadogenesis. Part II: Evolution of a family of tornadoes along a weak outflow boundary. *J. Atmos. Sci.*, **54**, 2387-2415.

Lee, B. D., C. A. Finley, and T. M. Samaras, 2011: Surface analysis near and within the Tipton, Kansas, tornado on 29 May 2008. *Mon. Wea. Rev.*, **139**.

Lee, B. D., C. A. Finley, and C. D. Karstens, 2012: The Bowdle, South Dakota, cyclic tornadic supercell of 22 May 2012: Surface analysis of rear-flank downdraft evolution and multiple internal surges. *Mon. Wea. Rev.*, in press.

Leibovich, S., and K. Stewartson, 1983: A sufficient condition for the instability of columnar vortices. *J. Fluid Mech.*, **126**, 335–356.

Lemon, L. R., and C. A. Doswell, 1979: Severe thunderstorm evolution and mesocyclone structure as related to tornadogenesis. *Mon. Wea. Rev.*, **107**, 1184-1197.

Lerach, D. G., and W. R. Cotton, 2012: Comparing aerosol and low-level moisture influences on supercell tornadogenesis: Three-dimensional idealized simulations. *Journal of the Atmospheric Sciences*, **69**, 969-987.

Lerach, D. G., B. J. Gaudet, and W. R. Cotton, 2008: Idealized simulations of aerosol influences on tornadogenesis. *Geophys. Res. Letters*, **35**, L23806.

Lewellen, D. C., and W. S. Lewellen, 2007: Near-Surface Intensification of Tornado Vortices. *Journal of the Atmospheric Sciences*, **64**, 2176-2194.

Li, S., S. Jaroszynski, S. Pearse, L. Orf, and J. Clyne, 2019: VAPOR: A Visualization Package Tailored to Analyze Simulation Data in Earth System Science. *Atmosphere*, **10**, 488.

Lin, Y.-L., R. D. Farley, and H. D. Orville, 1983: Bulk parameterization of the snow field in a cloud model. *J. Climat. Appl. Meteor.*, **22**, 1065-1092.

Locatelli, J. D., M. T. Stoelinga, and P. V. Hobbs, 2002: A New Look at the Super Outbreak of Tornadoes on 3-4 April 1974. *Mon. Wea. Rev.*, **130**, 1633-1651.

Mansell, E. R., C. L. Ziegler, and E. C. Bruning, 2010: Simulated electrification of a small thunderstorm with two-moment bulk microphysics. *Journal of the Atmospheric Sciences*, **67**, 171-194.

Markowski, P., and Coauthors, 2012a: The pretornadic phase of the Goshen County, Wyoming, supercell of 5 June 2009 intercepted by VORTEX2. Part II: Intensification of low-level rotation. . *Mon. Wea. Rev.*, **140**, 2916-2938.

Markowski, P., and Coauthors, 2012b: The pretornadic phase of the Goshen County, Wyoming, supercell of 5 June 2009 intercepted by VORTEX2. Part I: Evolution of kinematic and surface thermodynamic fields. *Mon. Wea. Rev.*, **140**, 2887-2915.

Markowski, P., Y. Richardson, J. Marquis, J. Wurman, K. Kosiba, P. Robinson, D. Dowell, E. Rasmussen, and R. Davies-Jones, 2012: The pretornadic phase of the Goshen County, Wyoming, supercell of 5 June 2009 intercepted by VORTEX2. Part II: Intensification of low-level rotation. . *Mon. Wea. Rev.*, **140**, 2916-2938.

Markowski, P. M., 2002: Hook echoes and rear-flank downdrafts: A review. *Mon. Wea. Rev.*, **130**, 852-876.

Markowski, P. M., 2016: An Idealized Numerical Simulation Investigation of the Effects of Surface Drag on the Development of Near-Surface Vertical Vorticity in Supercell Thunderstorms. *Journal of the Atmospheric Sciences*, **73**, 4349-4385.

——, 2020: What is the Intrinsic Predictability of Tornadic Supercell Thunderstorms? *Monthly Weather Review*, **148**, 3157-3180.

Markowski, P. M., and Y. Richardson, 2009: Tornadogenesis: Our current understanding, forecasting considerations, and questions to guide future research. *Atmos. Res.*, **93**, 3-10.

Markowski, P. M., and Y. Richardson, 2010: *Mesoscale Meteorology in Midlatitudes*. Wiley-Blackwell, 430 pp.

Markowski, P. M., and Y. P. Richardson, 2014: The Influence of Environmental Low-Level Shear and Cold Pools on Tornadogenesis: Insights from Idealized Simulations. *Journal of the Atmospheric Sciences*, **71**, 243-275.

Markowski, P. M., and G. H. Bryan, 2016: LES of Laminar Flow in the PBL: A Potential Problem for Convective Storm Simulations. *Monthly Weather Review*, **144**, 1841-1850.

Markowski, P. M., E. Rasmussen, and J. Straka, 1998: The occurrence of tornadoes in supercells interacting with boundaries during VORTEX-95. *Wea. and Forecasting*, **13**, 852-859.

Markowski, P. M., J. M. Straka, and E. N. Rasmussen, 2002: Direct surface thermodynamic observations within the rear-flank downdrafts of nontornadic and tornadic supercells. *Mon. Wea. Rev.*, **130**, 1692-1721.

Markowski, P. M., J. M. Straka, and E. N. Rasmussen, 2003a: Tornadogenesis Resulting from the Transport of Circulation by a Downdraft: Idealized Numerical Simulations. *J. Atmos. Sci.*, **60**, 795-823.

Markowski, P. M., N. T. Lis, D. D. Turner, T. R. Lee, and M. S. Buban, 2019: Observations of Near-Surface Vertical Wind Profiles and Vertical Momentum Fluxes from VORTEX-SE 2017: Comparisons to Monin-Obukhov Similarity Theory. *Monthly Weather Review*, **147**, 3811-3824.

Markowski, P. M., E. Rasmussen, J. Straka, R. Davies-Jones, Y. Richardson, and R. J. Trapp, 2008: Vortex lines within low-level mesocyclones obtained from pseudo-dual-Doppler radar observations. *Mon. Wea. Rev.*, **136**, 3513-3535.

Markowski, P. M., C. Hannon, J. Frame, E. Lancaster, A. Pietrycha, R. Edwards, and R. L. Thompson, 2003b: Characteristics of vertical wind profiles near supercells obtained from the Rapid Update Cycle. *Wea. and Forecasting*, **18**, 1262-1272.

Marquis, J., Y. Richardson, P. Markowski, D. Dowell, and J. Wurman, 2011: Tornado maintenance investigated with high-resolution dual-Doppler and EnKF analysis. *Mon. Wea. Rev.*, **140**, 3-27.

Marquis, J., Y. Richardson, P. Markowski, D. Dowell, and J. Wurman, 2012: Tornado Maintenance Investigated with High-Resolution Dual-Doppler and EnKF Analysis. *Mon. Wea. Rev.*, **140**, 3-27.

Marquis, J., Y. Richardson, P. Markowski, J. Wurman, K. Kosiba, and P. Robinson, 2016: An Investigation of the Goshen County, Wyoming, Tornadic Supercell of 5 June 2009 Using EnKF Assimilation of Mobile Mesonet and Radar Observations Collected during VORTEX2. Part II: Mesocyclone-Scale Processes Affecting Tornado Formation, Maintenance, and Decay. *Monthly Weather Review*, **144**, 3441-3463.

Marwitz, J. D., 1972a: The structure and motion of severe hailstorms. Part I: Supercell storms. *J. Appl. Meteor.*, **11**, 166-179.

- , 1972b: The structure and motion of severe hailstorms. Part II: Multi-cell storms. *J. Appl. Meteor.*, **11**, 180-188.
- , 1972c: The structure and motion of severe hailstorms. Part III: Severely sheared storms. *J. Appl. Meteor.*, **11**, 189-201.
- Mashiko, W., 2016a: A numerical study of the 6 May 2012 Tsukuba City supercell tornado. Part I: Vorticity sources of low-level and midlevel mesocyclones. *Monthly Weather Review*, **144**, 1069-1092.
- , 2016b: A numerical study of the 6 May 2012 Tsukuba City supercell tornado. Part II: Mechanisms of tornadogenesis. *Monthly Weather Review*, **144**, 3077-3098.
- Mashiko, W., H. Niino, and K. Teruyuki, 2009: Numerical simulations of tornadogenesis in an outer-rainband minisupercell of typhoon Shanshan on 17 September 2006. *Mon. Wea. Rev.*, **137**, 4238-4260.
- Moeng, C.-H., and J. C. Wyngaard, 1988: Spectral analysis of large-eddy simulations of the convective boundary layer. *J. Atmos. Sci.*, **45**, 3573-3587.
- Moller, A. R., C. A. D. III, and R. Przybylinski, 1990: High precipitation supercells: A conceptual model and documentation. *Preprints, 16th Conf. on Severe Local Storms*, Kananaskis Park, AB, Canada, Amer. Meteor. Soc., 52-57.
- Moller, A. R., C. A. Doswell, III, M. P. Foster, and G. R. Woodall, 1994: The operational recognition of supercell environments and storm structures. *Wea. Forecasting*, **9**, 327-347.
- Nascimento, E. d. L., G. Held, and A. M. Gomes, 2014: A multiple-vortex tornado in southeastern Brazil. *Monthly Weather Review*, **142**, 3017-3037.

Nishizawa, S., H. Yashiro, Y. Sato, Y. Miyamoto, and H. Tomita, 2015: Influence of grid aspect ratio on planetary boundary layer turbulence in large-eddy simulations. *Geosci. Model Dev.*, **8**, 3393-3419.

Nolan, D. S., 2012: Three-dimensional instabilities in tornado-like vortices with secondary circulations. *J. Fluid Mech.*, **711**, 61–100.

Nolen, R. H., 1959: A radar pattern associated with tornadoes. *Bull. Amer. Meteor. Soc.*, **40**, 277-279.

Oliveira, M. I., M. Xue, B. Roberts, and L. J. Wicker, 2019: Horizontal vortex tubes near tornadoes: three-dimensional structure and dynamics. *Atmosphere*, **10**, 716.

Orf, L., 2019: A Violently Tornadic Supercell Thunderstorm Simulation Spanning a Quarter-Trillion Grid Volumes: Computational Challenges, I/O Framework, and Visualizations of Tornadogenesis. *Atmosphere*, **10**, 578.

Orf, L., R. Wilhelmson, B. Lee, C. Finley, and A. Houston, 2017: Evolution of a long-track violent tornado within a simulated supercell. *Bulletin of the American Meteorological Society*, **98**, 45-68.

Parker, M. D., 2012: Impacts of Lapse Rates on Low-Level Rotation in Idealized Storms. *Journal of the Atmospheric Sciences*, **69**, 538-559.

Parker, M. D., and J. M. L. Dahl, 2015: Production of Near-Surface Vertical Vorticity by Idealized Downdrafts. *Monthly Weather Review*, **143**, 2795-2816.

Pauley, R. L., and J. T. Snow, 1988: On the Kinematics and Dynamics of the 18 July 1986 Minneapolis Tornado. *Monthly Weather Review*, **116**, 2731-2736.

Pazmany, A. L., J. B. Mead, H. B. Bluestein, J. C. Snyder, and J. B. Houser, 2013: A mobile rapid-scanning x-band polarimetric (RaXPoL) Doppler radar system. *Journal of Atmospheric and Oceanic Technology*, **30**, 1398-1413.

Potvin, C. K., K. L. Elmore, and S. J. Weiss, 2010: Assessing the Impacts of Proximity Sounding Criteria on the Climatology of Significant Tornado Environments. *Weather and Forecasting*, **25**, 921-930.

Rasmussen, E., 2003: Refined supercell and tornado forecast parameters. *Wea. and Forecasting*, **18**, 530-535.

Rasmussen, E., and D. O. Blanchard, 1998: A baseline climatology of sounding-derived supercell and tornado forecast parameters. *Wea. and Forecasting*, **13**, 1148-1164.

Rasmussen, E. A., J. M. Straka, R. P. Davies-Jones, C. E. D. III, F. Carr, M. Eilts, and D. R. MacGorman, 1994: Verification of the Origins of Rotation in Tornadoes Experiment: VORTEX. *Bull. Amer. Meteor. Soc.*, **75**, 1-12.

Rasmussen, E. N., S. Richardson, J. M. Straka, P. M. Markowski, and D. O. Blanchard, 2000: The association of significant tornadoes with a baroclinic boundary on 2 June 1995. *Mon. Wea. Rev.*, **128**, 174-191.

Ray, P. S., and Coauthors, 1981: The morphology of severe tornadic storms on 20 May 1977. *J. Atmos. Sci.*, **38**, 1643-1663.

Roberts, B., 2017: The Role of Surface Drag in Supercell Tornadogenesis and Mesocyclogenesis: Studies Based on Idealized Numerical Simulations, School of Meteorology, University of Oklahoma, 164 pp.

Roberts, B., and M. Xue, 2017: The role of surface drag in mesocyclone intensification leading to tornadogenesis within an idealized supercell simulation. *J. Atmos. Sci.*, **74**, 3055-3077.

Roberts, B., M. Xue, and D. T. Dawson, 2020: The Effect of Surface Drag Strength on Mesocyclone Intensification and Tornadogenesis in Idealized Supercell Simulations. *Journal of the Atmospheric Sciences*, **77**, 1699-1721.

Roberts, B., M. Xue, A. D. Schenkman, and I. Daniel T. Dawson, 2016: The role of surface drag in tornadogenesis within an idealized supercell simulation. *J. Atmos. Sci.*, **73**, 3371–3395.

Rotunno, R., 1979: A study in tornado-like vortex dynamics. *J. Atmos. Sci.*, **36**, 140-155.

———, 1981: On the evolution of thunderstorm rotation. *Mon. Wea. Rev.*, **109**, 171-180.

Rotunno, R., and J. B. Klemp, 1982: The influence of the shear-induced pressure gradient on thunderstorm motion. *Mon. Wea. Rev.*, **110**, 136-151.

———, 1985: On the rotation and propagation of simulated supercell thunderstorms. *J. Atmos. Sci.*, **42**, 271-292.

Rotunno, R., P. M. Markowski, and G. H. Bryan, 2017: “Near Ground” Vertical Vorticity in Supercell Thunderstorm Models. *Journal of the Atmospheric Sciences*, **74**, 1757-1766.

Schenkman, A. D., M. Xue, and A. Shapiro, 2012: Tornadogenesis in a simulated mesovortex within a mesoscale convective system. *J. Atmos. Sci.*, **69**, 3372-3390.

Schenkman, A. D., M. Xue, and M. Hu, 2014: Tornadogenesis in a high-resolution simulation of the 8 May 2003 Oklahoma City supercell. *J. Atmos. Sci.*, **71**, 130-154.

Schenkman, A. D., M. Xue, and D. T. Dawson, II, 2016: The cause of internal outflow surges in a high-resolution simulation of the 8 May 2003 Oklahoma City tornadic supercell. *J. Atmos. Sci.*, **73**, 353-370.

Schlesinger, R. E., 1973: A numerical model of deep moist convection. Part I. Comparative experiments for variable ambient moisture and wind shear. *J. Atmos. Sci.*, **30**, 835-856.

Schueth, A., C. Weiss, and J. M. L. Dahl, 2021: Comparing Observations and Simulations of the Streamwise Vorticity Current and the Forward-Flank Convergence Boundary in a Supercell Storm. *Monthly Weather Review*, **149**, 1651-1671.

Shabbot, C. J., and P. M. Markowski, 2006: Surface in situ observations within the outflow of forward-flank downdrafts of supercell thunderstorms. *Mon. Wea. Rev.*, **2006**, 1422-1441.

Skamarock, W. C., and J. B. Klemp, 1992: The stability of time-split numerical methods for the hydrostatic and nonhydrostatic elastic equations. *Mon. Wea. Rev.*, **120**, 2109-2127.

Skinner, P. S., C. C. Weiss, J. L. Schroeder, L. J. Wicker, and M. I. Biggerstaff, 2011: Observations of the Surface Boundary Structure within the 23 May 2007 Perryton, Texas, Supercell. *Mon. Wea. Rev.*, **139**, 3730-3749.

Skinner, P. S., C. C. Weiss, L. J. Wicker, C. K. Potvin, and D. C. Dowell, 2015: Forcing Mechanisms for an Internal Rear-Flank Downdraft Momentum Surge in the 18 May 2010 Dumas, Texas, Supercell. *Mon. Wea. Rev.*, **143**, 4305-4330.

Skinner, P. S., C. C. Weiss, M. M. French, H. B. Bluestein, P. M. Markowski, and Y. P. Richardson, 2014: VORTEX2 Observations of a Low-Level Mesocyclone with Multiple Internal Rear-Flank Downdraft Momentum Surges in the 18 May 2010 Dumas, Texas, Supercell. *Monthly Weather Review*, **142**, 2935-2960.

Smith, B. T., R. L. Thompson, J. S. Grams, C. Broyles, and H. E. Brooks, 2012: Convective Modes for Significant Severe Thunderstorms in the Contiguous United States. Part I: Storm Classification and Climatology. *Weather and Forecasting*, **27**, 1114-1135.

Snook, N., and M. Xue, 2008: Effects of microphysical drop size distribution on tornadogenesis in supercell thunderstorms. *Geophys. Res. Letters*, **35**, L24803, doi:24810.21029/22008GL035866.

Snook, N., M. Xue, and Y. Jung, 2019: Tornado-resolving ensemble and probabilistic predictions of the 20 May 2013 Newcastle-Moore EF5 tornado. *Mon. Wea. Rev.*, Conditionally accepted.

Straka, J. M., E. N. Rasmussen, R. P. Davies-Jones, and P. M. Markowski, 2007: An observational and idealized numerical examination of low-level counter-rotating vortices in the rear flank of supercells. *Electronic J. Severe Storms Meteor.*, **2** (8), 1-22.

Takahashi, N., H. Ishii, and T. Miyazaki, 2005: The influence of turbulence on a columnar vortex. *Physics of Fluids*, **17**, 035105.

Tanamachi, R. L., P. L. Heinselman, and L. J. Wicker, 2015: Impacts of a Storm Merger on the 24 May 2011 El Reno, Oklahoma, Tornadic Supercell. *Weather and Forecasting*, **30**, 501-524.

Tanamachi, R. L., L. J. Wicker, D. C. Dowell, H. B. Bluestein, D. T. Dawson, II, and M. Xue, 2013: EnKF Assimilation of High-Resolution, Mobile Doppler Radar Data of the 4 May 2007 Greensburg, Kansas, Supercell into a Numerical Cloud Model. *Mon. Wea. Rev.*, **141**, 625-648.

Tao, T., and T. Tamura, 2020: Numerical Study of the 6 May 2012 Tsukuba Supercell Tornado: Vorticity Sources Responsible for Tornadogenesis. *Monthly Weather Review*, **148**, 1205-1228.

Tao, W.-K., and J. Simpson, 1991: The Goddard cumulus ensemble model. Part I: Model description. *Terr. Atmos. Oceanic Sci.*, **4**, 35-72.

Taszarek, M., J. T. Allen, T. P??ik, K. A. Hoogewind, and H. E. Brooks, 2020: Severe Convective Storms across Europe and the United States. Part II: ERA5 Environments Associated with Lightning, Large Hail, Severe Wind, and Tornadoes. *Journal of Climate*, **33**, 10263-10286.

Vasiloff, S. V., E. A. Brandes, R. P. Davies-Jones, and P. S. Ray, 1986: An investigation of the transition from multicell to supercell storms. *J. Climate Appl Meteor.*, **25**, 1022-1036.

Wade, A. R., M. C. Coniglio, and C. L. Ziegler, 2018: Comparison of Near- and Far-Field Supercell Inflow Environments Using Radiosonde Observations. *Monthly Weather Review*, **146**, 2403-2415.

Wakimoto, R. M., and J. W. Wilson, 1989: Non-supercell tornadoes. *Mon. Wea. Rev.*, **117**, 1113-1140.

Wakimoto, R. M., H. Cai, and H. V. Murphey, 2004: The Superior, Nebraska, Supercell During BAMEX. *Bulletin of the American Meteorological Society*, **85**, 1095-1106.

Weisman, M. L., 1993: The genesis of severe long-lived bow-echoes. *J. Atmos. Sci.*, **50**, 645-670.

Weisman, M. L., and J. B. Klemp, 1982: The dependence of numerically simulated convective storms on vertical wind shear and buoyancy. *Mon. Wea. Rev.*, **110**, 504-520.

———, 1984: The structure and classification of numerically simulated convective storms in directionally varying wind shears. *Mon. Wea. Rev.*, **112**, 2479-2498.

Weisman, M. L., and C. A. Davis, 1998: Mechanisms for the generation of mesoscale vortices within quasi-linear convective systems. *J. Atmos. Sci.*, **55**, 2603-2622.

Wicker, L. J., and R. B. Wilhelmson, 1995: Simulation and analysis of tornado development and decay within a three-dimensional supercell thunderstorm. *J. Atmos. Sci.*, **52**, 2675-2703.

Wienhoff, Z. B., H. B. Bluestein, D. W. Reif, R. M. Wakimoto, L. J. Wicker, and J. M. Kurdzo, 2020: Analysis of Debris Signature Characteristics and Evolution in the 24 May 2016 Dodge City, Kansas, Tornadoes. *Monthly Weather Review*, **148**, 5063-5086.

Wilhelmson, R. B., and J. B. Klemp, 1978: A numerical study of storm splitting that leads to long-lived storms. *J. Atmos. Sci.*, **35**, 1975-1986.

———, 1981: A three-dimensional numerical simulation of splitting severe storms on 3 April 1964. *J. Atmos. Sci.*, **38**, 1581-1600.

WSEC, 2006: A recommendation for an Enhanced Fujita Scale (EF-Scale). *Texas Tech University Wind Science and Engineering Center Rep*, 95 pp.

Wu, J.-Z., H.-Y. Ma, and M.-D. Zhou, 2007: *Vorticity and vortex dynamics*. Springer Science & Business Media.

Wurman, J., and K. Kosiba, 2013: Finescale Radar Observations of Tornado and Mesocyclone Structures. *Weather and Forecasting*, **28**, 1157-1174.

Wurman, J., Y. Richardson, C. Alexander, S. Weygandt, and P. F. Zhang, 2007: Dual-Doppler and single-Doppler analysis of a tornadic storm undergoing mergers and repeated tornadogenesis. *Mon. Wea. Rev.*, **135**, 736-758.

Wurman, J., D. Dowell, Y. Richardson, P. Markowski, D. Burges, L. Wicker, and H. Bluestein, 2012: The Second Verification of the Origins of Rotation in Tornadoes Experiment: VORTEX2. *Bull. Amer. Meteor. Soc.*, Accepted with minor revision.

Xu, X., M. Xue, and Y. Wang, 2015: The genesis of mesovortices within a real data simulation of a bow echo system. *J. Atmos. Sci.*, **72**, 1963-1986.

Xue, M., K. K. Droegemeier, and V. Wong, 2000: The Advanced Regional Prediction System (ARPS) - A multi-scale nonhydrostatic atmospheric simulation and prediction model. Part I: Model dynamics and verification. *Meteor. Atmos. Phy.*, **75**, 161-193.

Xue, M., M. Hu, and A. D. Schenkman, 2014: Numerical Prediction of the 8 May 2003 Oklahoma City Tornadic Supercell and Embedded Tornado Using ARPS with the Assimilation of WSR-88D Data. *Wea. Forecasting*, **29**, 39-62.

Xue, M., K. K. Droegemeier, V. Wong, A. Shapiro, and K. Brewster, 1995: *ARPS Version 4.0 User's Guide*. [Available at <http://www.caps.ou.edu/ARPS>], 380 pp.

Xue, M., D.-H. Wang, J.-D. Gao, K. Brewster, and K. K. Droegemeier, 2003: The Advanced Regional Prediction System (ARPS), storm-scale numerical weather prediction and data assimilation. *Meteor. Atmos. Phy.*, **82**, 139-170.

Xue, M., and Coauthors, 2001: The Advanced Regional Prediction System (ARPS) - A multi-scale nonhydrostatic atmospheric simulation and prediction model. Part II: Model physics and applications. *Meteor. Atmos. Phys.*, **76**, 143-165.

Yao, D., Z. Meng, and M. Xue, 2019: Genesis, maintenance and demise of a simulated tornado and the evolution of its preceding descending reflectivity core (DRC). *Atmosphere*, 10236; doi:10.13390/atmos10050236.

Yokota, S., H. Niino, H. Seko, M. Kunii, and H. Yamauchi, 2018: Important factors for tornadogenesis as revealed by high-resolution ensemble forecasts of the tsukuba supercell tornado of 6 May 2012 in Japan. *Monthly Weather Review*, **146**, 1109-1132.

Yussouf, N., D. C. Dowell, L. J. Wicker, K. H. Knopfmeier, and D. M. Wheatley, 2015: Storm-Scale Data Assimilation and Ensemble Forecasts for the 27 April 2011 Severe Weather Outbreak in Alabama. *Monthly Weather Review*, **143**, 3044-3066.